Charge Density Wave Order in Cuprate Superconductors Studied by Resonant Soft X-ray Scattering

by

Andrew Achkar

A thesis
presented to the University of Waterloo
in fulfillment of the
thesis requirement for the degree of
Doctor of Philosophy
in
Physics

Waterloo, Ontario, Canada, 2015

This thesis consists of material all of which I authored or co-authored: see Statement of Contributions included in the thesis. This is a true copy of the thesis, including any required final revisions, as accepted by my examiners.

I understand that my thesis may be made electronically available to the public.

Statement of Contributions

This thesis is based in large part on three published papers (Refs. [1, 2, 3]) and one paper in the submission stage, currently available as a pre-print that predates this writing,[4] all of which I am first author on. The content from these papers is found in Chapters 3, 4, 6, and 5, respectively. In all cases, I wrote significant portions of the manuscripts, working in tandem with my supervisor and incorporating feedback from co-authors and/or anonymous referees. I performed the majority of the experiments, data analysis and figure preparation presented therein. The content of these chapters has mostly been left in their published forms, except for Chapter 5, which contains new data and additional analysis not contained in Ref. [4]. Some minor alterations, such as providing section headings and moving supplementary sections to more suitable locations, were made to provide better structure to the thesis. All other chapters and appendices were written solely by myself for this thesis.

Abstract

Cuprate high temperature superconductors have been the subject of intense investigation since their discovery in 1986. The nature of the pairing mechanism in these unconventional superconductors does not seem to be mediated by phonons, as in conventional superconductors, and thus remains a puzzle. The superconducting phase emerges from doping holes (or electrons) into the CuO_2 planes of an anti-ferromagnetic Mott insulator, producing a wealth of electronic ordering phenomena in many of the cuprate families. One of these phases is an incommensurate charge ordered state, known since the mid 90's to occur in La-based cuprates along with incommensurate spin ordering and compete with superconductivity. Recent advances in experimental capabilities, notably the ability to perform resonant diffraction experiments with soft x-rays, which can be made sensitive to holes in Cu $3d$ and O $2p$ orbitals, have provided new opportunities to learn about these charge ordered states. The study of charge order in cuprate superconductors by resonant soft x-ray scattering is the subject of this thesis. The main results are as follows.

The energy dependence of the resonant scattering intensity sensitive to holes in Cu $3d_{x^2-y^2}$ and O $2p_{x,y}$ orbitals was shown to result from modulated orbital energy levels rather than directly due to charge modulations. This is notable, as prior interpretations of this scattering signature were taken as direct evidence for a sizeable charge modulation, whereas this result indicates considerably smaller modulation amplitudes. The applicability of this model was first demonstrated for $La_{1.475}Nd_{0.4}Sr_{0.125}CuO_4$, but subsequently validated for $YBa_2Cu_3O_{6+x}$ as well. This commonality hinted at a largely similar type of charge ordering in these different families, despite important structural and compositional differences. Moreover, the applicability of this model in $YBa_2Cu_3O_{6+x}$, along with studies of the temperature and momentum dependence of the scattering signature, demonstrated that the chain layer of $YBa_2Cu_3O_{6+x}$, which supports its own type of order involving full and empty CuO chains, was not responsible for the observed charge order and argued for it being an intrinsic property of the CuO_2 planes. This crucial distinction has now helped to affirm charge order as a generic feature of hole-doped cuprates. This point has since been further established by the observation of charge ordering in other cuprate families.

More recently, there has been a great deal of interest in determining the symmetry of the charge density waves, as theory has predicted a d type symmetry on the O $2p_{x,y}$ bonds surrounding Cu sites. To address this, an experiment on $La_{1.875}Ba_{0.125}CuO_4$ involving a special scattering geometry was performed. The relative d and s' symmetry components were determined by modelling of the polarization and geometry dependence of the scattering intensity and mapping this to a theoretical construct to provide quantifiable symmetry components. This revealed a dominant s' symmetry, in contrast to d symmetry

in other cuprate families recently identified by scanning tunnelling microscopy. The strong incommensurate spin order in $La_{2-x}Ba_xCuO_4$ was argued to play a role in favouring this symmetry arrangement.

The role of disorder in the charge density wave order seen in $YBa_2Cu_3O_{6+x}$ was also investigated. Rather than introducing substitutional impurities, disorder was modified by intentionally destroying the chain order. A special experimental procedure was used to ensure the comparability of the scattering intensities and peak positions allowing for subtle differences to be identified reliably. This experiment revealed that the presence of ordered chains in $YBa_2Cu_3O_{6+x}$ enhances the scattering intensity from charge density waves in the CuO_2 planes, but has no impact on the correlation length, incommensurability and temperature evolution of the charge density wave order, possibly by altering the balance between superconducting and charge density wave order parameters.

Finally, resonant scattering studies of $YBa_2Cu_3O_{6+x}$ for a number of compositions were undertaken to expand upon the known doping evolution of important characteristics of the charge density wave order, such as the onset temperature, correlation length and incommensurability. New phase diagrams were constructed revealing additional details of their doping dependence. Notably, charge density wave order is observed at $p = 0.058$ in a sample very near the low-p limit of the superconducting dome. This argues to extend the dome of charge order down to $p \sim 0.05$, roughly where superconductivity ceases. This further demonstrates the existence of coexisting spin and charge density waves in the $0.05 < p < 0.08$ region of the phase diagram. Differences in the doping dependence of the charge order aligned with the a and b crystal axes were also identified by this study, suggesting two partially overlapping domes and possibly faster extinction of the charge density wave order along a due to competition with incommensurate spin density waves also aligned with a in the low doping regime.

Acknowledgements

I would like to first thank my supervisor David Hawthorn for the opportunity he gave me to lead these projects. He was always there when I had run out ideas or needed extra motivation. He spent many long hours with me at the experimental beamline, both when things succeeded and when they failed. He always raised the bar, whether it meant improving a measurement, refining my analysis procedures, improving a presentation, or encouraging me to try something difficult because of an untapped potential for discovery. Without a doubt, his guidance helped me to exceed my potential.

I would also like to thank all the people who, at various times, have participated in the experiments themselves: Feizhou He (beamline scientist) and Ronny Sutarto (research associate), who have both gone beyond the call of duty too many times to recall, David Muir, who helped me fix problems with the beamline on many occasions, Xiaopan Mao and Christopher McMahon, my lab mates, who have both felt the chill of Saskatoon in the winter and know the joy of orienting a crystal at 4 AM, and Yiting Qian and Martin Zwiebler, who participated in a few of the experiments.

I would also like to thank all of the people who have had an indirect, yet important impact on the success of my research, either through discussions, hands-on training or friendship: Hiruy Haile, for helping me machine awesome things, Luke Yaraskavitch and John Dunn, for teaching me about sample polishing and what low temperature physics really means, Mike Wesolowski for moving to Saskatoon and being a friendly (and wise) face whenever I visit, Jordan Thompson and Stephen Inglis, for insightful theoretical discussions and plenty of memorable times, Behnam Javanparast, Lauren Hayward, David Pomaranski, Chad Daley, Alex Day, Hao Zhihao, and Bohdan Kulchytskyy, for making life as a grad student enjoyable, through daily lunches at Grad House and frequent coffee breaks. Special mention goes to "sir" Gregory J. McLeod and James Parrish, since they *insisted* they be mentioned (thanks for keeping it classy guys).

To my family, I thank you for your unwavering support in every venture I take on. Dad, seriously it's impressive that you read through my papers. Mom, merci pour l'amour et la patience que tu me donnes, en tous temps. Alex, no it's still not freakin' laser beams mounted on sharks' heads, but close enough.

To Halle Revell, who supported me through all the late nights, long trips, working weekends, endless rants, missed deadlines, missed Valentine's days and regularly occurring obsessions — you are my moral compass, my best friend and the love of my life. From the bottom of my heart, thank you.

Dedication

To Halle Revell, for approving my proposal without sending it out for peer review. I love you.

Table of Contents

List of Tables

List of Figures

Chapter 1

Introduction

1.1 Foreward

As explained on page iii, chapters 3-6 are structured as standalone publications. It should therefore be possible to read these chapters independently, in any order. However, from such a reading it might be difficult to place the significance of their content into a broader context. This chapter will thus serve to provide such a broader context. Additionally, to non-specialists, the technique of resonant soft x-ray scattering may be unfamiliar. Chapter 2 will thus review resonant soft x-ray scattering, aiming to provide a suitable theoretical framework and general methodological details that underpin the experiments and analyses presented in the following chapters.

1.2 Historical context

1.2.1 High temperature superconductivity

High temperature superconductivity (HTSC) in the copper oxides (cuprates) was discovered in 1986.[5] In many ways, this discovery defied conventional thinking about superconductivity. For one, their record high critical transition temperatures (T_c) could not readily be explained by the phonon mediated electron pairing mechanism used with great success to describe conventional superconductors in the Migdal-Eliashberg extension of Bardeen-Cooper-Schrieffer (BCS) theory[6, 7, 8] Moreover, the pairing gap Δ was shown to d-wave symmetry in the cuprates, rather than isotropic s-wave symmetry, with nodes

and sign changes occurring at diagonal wavevectors in momentum space (see Fig. 1.1).[9] Additionally, the crystal structure and and phase diagrams of the cuprates contradicted the famous Matthias rules, which said that to increase T_c one should search for cubic crystals, preferably d-electron metals with an odd number of valence electrons, that were should not exhibit magnetic phases or metal-insulator transitions.[10] Instead, cuprates have layered crystal structures with quasi two-dimensional CuO_2 planes (see Fig. 1.2) and a complex phase diagram (see Fig. 1.3) that includes both magnetic order and metal-insulator transitions.[11, 12] Also unexpectedly, at temperatures just above T_c the cuprates do not exhibit normal Fermi-liquid behaviour, instead retaining a partially gapped Fermi surface up to the 'pseudogap' transition temperature T^*.[13, 14] That these phenomena could not readily be explained by the very successful BCS theory sparked a flurry of activity to resolve this astounding mystery.

Despite nearly three decades of intensive research, and more than 100,000 research papers on the subject,[15] the mechanism for HTSC in the cuprates remains unclear. Although this may seem discouraging, we should not forget that 1) it took nearly 50 years for BCS theory to emerge (1957) after conventional superconductivity was discovered in 1911,[16] 2) cuprates still hold the record for the highest T_c, despite seven new classes of superconductors having been discovered since 1986,[17] and 3) that there is still great potential if this problem can be solved.

This potential is largely associated with the ultimate goal of developing *room temperature* superconductors. These would have immense societal benefit, for instance by bringing

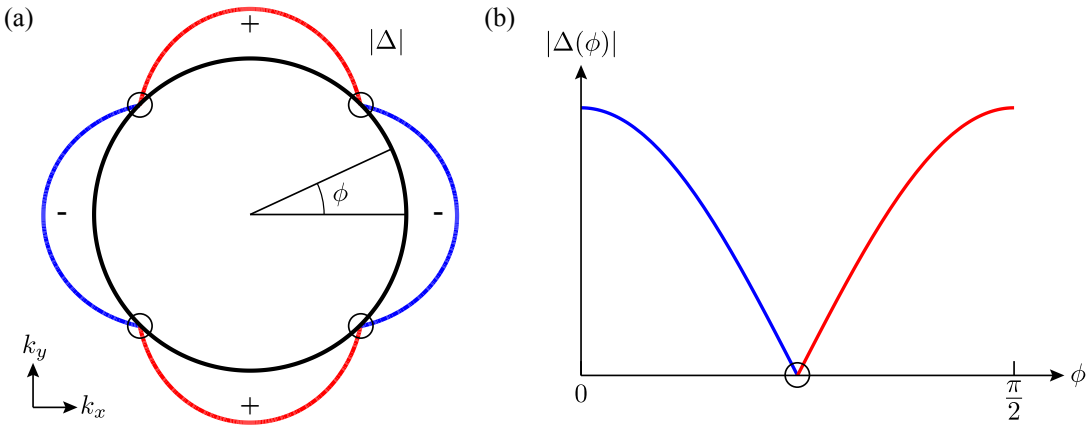

Figure 1.1 – Gap function in unconventional d-wave superconductors. (a) The d-wave gap in momentum space. (b) Magnitude of the gap function versus polar angle ϕ. The gap function in a conventional superconductor is constant as a function of ϕ (s-wave symmetry).

economic viability to current applications that require liquid helium cooling (e.g., magnetic resonance imaging, magnetically levitating trains), enabling new categories of devices (e.g., high performance computing, electronic devices), and potentially mitigating the energy crisis with efficient power transmission and generation equipment.[18] The potential is also rooted in the mere recognition that, regardless of whether the HTSC problem can be solved,

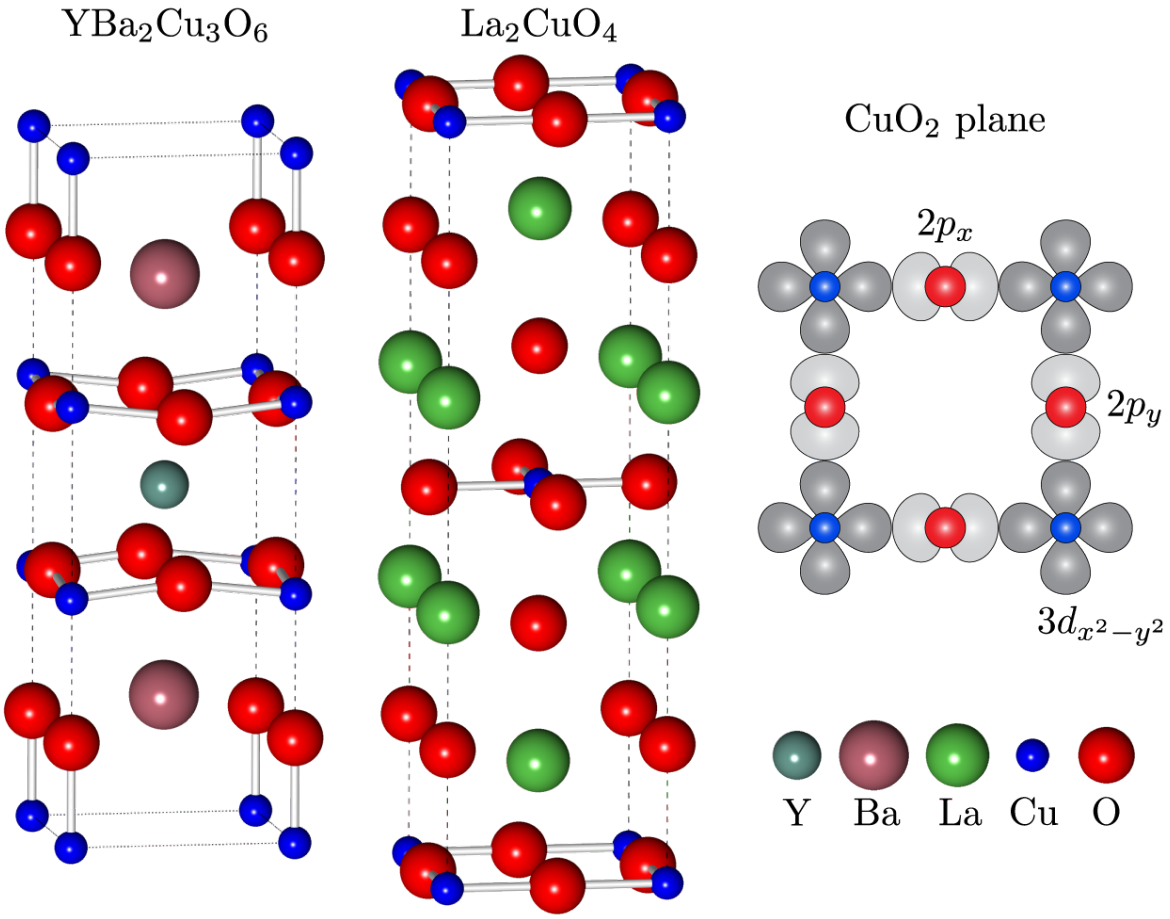

Figure 1.2 – Crystal structure of cuprate superconductors. The parent compounds $YBa_2Cu_3O_6$ and La_2CuO_4 are shown. High-T_c superconductivity is achieved by hole doping the CuO_2 planes of these compounds. For La_2CuO_4, La is substituted with Sr or Ba and optionally co-doped with Nd or Eu. For $YBa_2Cu_3O_{6+x}$, O atoms are added, fitting most naturally in the top and bottom CuO_x layers. The common structural unit is the CuO_2 plane, whose electronic states near E_F have Cu $3d_{x^2-y^2}$ and O $2p_{x,y}$ character.

the theoretical and experimental tools developed for it may likely be used to study and understand other complex materials with untold potential applications.

1.2.2 The cuprate phase diagram

Besides being unconventional high-T_c superconductors, cuprates have drawn a great deal of attention due the wide variety of *other* phenomena they exhibit.[19, 20] The basic building block for all of this is the CuO_2 plane (see Fig. 1.2), which is common to all cuprates. Beginning with a 'parent' compound, chemical substitution can be used to dope the CuO_2 plane, by either adding or removing electrons. Cuprates can be made superconducting by electron doping or hole doping. I will focus on hole doped cuprates in this thesis.

A typical phase diagram for a generic hole doped cuprate is schematically illustrated in Fig. 1.3. The hole doping p denotes the number of holes per Cu atom in the CuO_2 planes. It contains 1) the antiferromagnetic (AF) Mott (charge-transfer) insulating phase of the parent compound up to $p \approx 0.05$, 2) the pseudogap up to a critical value of p_c (not shown, since its value is controversial), 3) an unusual metallic phase, and 4) a dome-shaped region of d-wave superconductivity (d-SC). In Fig. 1.3, there is also a fifth phase: a region of charge density wave (CDW) order centered around $p = \frac{1}{8}$, and coinciding with the wiggle in T_c. This phase has only recently (2012) been recognized as a *generic* part of the cuprate phase diagram,[22, 23, 24] despite charge "stripe" ordering having been observed in La-based cuprates as early as 1995.[25]

1.2.3 Prior studies of the cuprates

The rich cuprate phase diagram has motivated a vast range of experimental and theoretical studies, which is well beyond the scope of this thesis to fully cover. To give a sense of the scale of this effort, I will instead provide a brief, and by no means complete, sampling of the various methods used to study these phenomena and establish some of their properties. Where possible, citations to topical reviews or seminal works are given.

The cuprates have been studied by numerous experimental probes, including angle-resolved photoemission spectroscopy,[26, 14] to study the Fermi surface and energy dispersion, neutron and x-ray scattering,[27, 28, 29] to study spin and charge order, scanning tunnelling microscopy,[30] for nanoscale imaging, localized spectroscopy, studies of disorder and investigations of charge order, nuclear magnetic resonance,[31, 32] used to infer the presence of the pseudogap and charge order, and electron energy-loss and x-ray absorption spectroscopy,[33] to identify the electronic structure of states near the Fermi

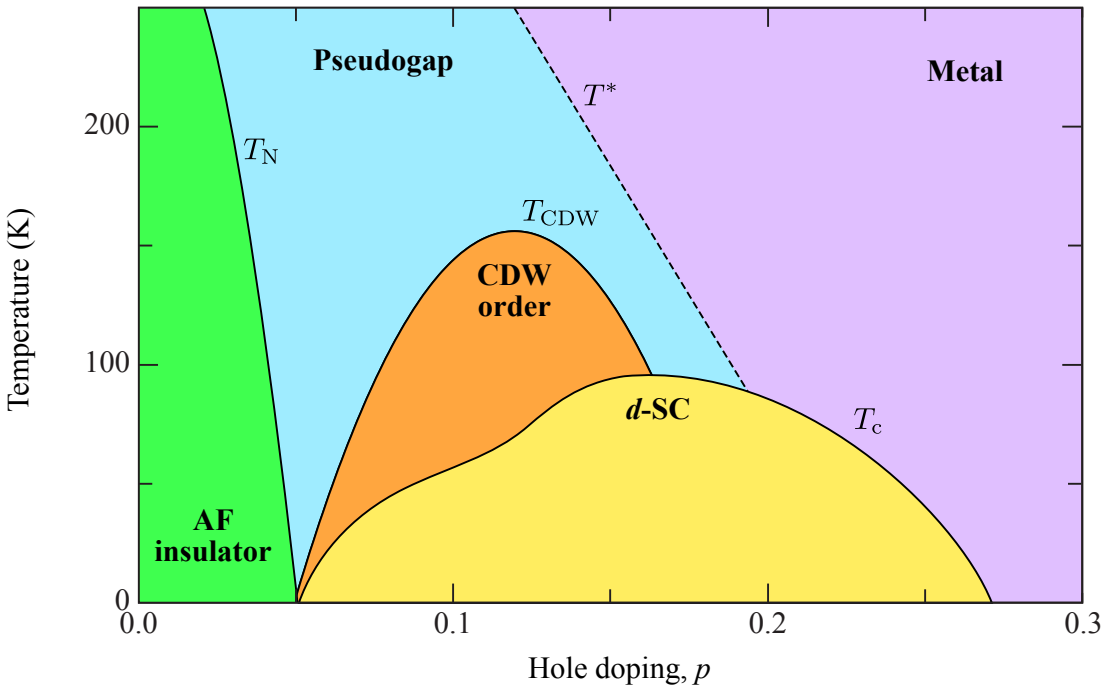

Figure 1.3 – Schematic phase diagram for hole doped cuprate superconductors. The parent compound with hole doping $p = 0$ is a Mott (charge-transfer) insulator with AF order at temperatures below the Néel temperature T_N. As holes are doped into the system, the insulating phase is quickly destroyed by $p \approx 0.05$ and a dome-shaped d-wave superconductivity (d-SC) phase forms. Wiggles (or anomalous suppressions) in T_c appear near $p = \frac{1}{8}$, coincident with CDW order, which onsets at T_{CDW}. The line T^* tracks the opening of a pseudogap in the energy dispersion and in this case intersects the T_c dome above optimal doping, defined as where T_c is maximal ($p \approx 0.16$). T_c and T_{CDW} are representative of $YBa_2Cu_3O_{6+x}$. Figure adapted from Ref. [21].

energy. Cuprates have also been thoroughly characterized through measurements of optical conductivity,[34] thermal conductivity,[35] transport,[36], the Hall effect,[37] the Nernst effect,[38] and quantum oscillations,[39, 40, 41] helping to identify, for example: the insulating state of the parent compound, that the gap has nodes across the phase diagram, an unusual linear in T resistivity near optimum doping, the sign of the charge carriers, the persistence of vortex excitations above T_c, and that there exists a closed Fermi surface across the full phase diagram. There has also been a great deal of experimental effort to study cuprate crystal structure and electronic structures,[11, 12, 42, 43] crystal growth properties,[44, 45, 46] and the influence of defects on T_c.[47, 48, 49]

Theoretical efforts to describe the physics of the CuO_2 plane have frequently taken the Hubbard,[12, 50, 51] $t-J$,[52] spin-fermion,[53, 54], or Landau [55, 56] model as a starting point. A variety of exotic states of matter and pairing mechanisms have been proposed to describe the cuprate phase diagram or its d-SC, such as resonating valence bonds,[57] loop currents,[58], 'intertwined' orders,[59, 60] pair-density waves,[61], nematic Fermi fluids,[62], and most recently Ampearan pairing.[63] Numerical techniques such as quantum Monte Carlo,[64, 65, 66] density matrix renormalization group,[67, 68] exact diagonalization,[69] and dynamical mean field theory,[70] have also been developed to handle the strong electronic correlations of these models.

An area of particularly intense focus in hole doped cuprates has naturally been the puzzling pseudogap phase. Historically speaking, two prevailing notions were that either i) the pseudogap is a signature of pre-formed Cooper pairs or ii) it arises from doping a Mott insulator.[71] As mentioned previously, generic CDW order is now a part of the cuprate phase diagram, due to the unambiguous identification of CDW order in $YBa_2Cu_3O_{6+x}$ by x-ray diffraction,[22, 23] and other cuprate families.[41, 72, 73, 74] This provides an additional twist to the story of the pseudogap and HTSC, since the CDW order is found in the underdoped regime of hole doped cuprates, it onsets at temperatures between T^* and T_c, and it clearly *competes* with superconductivity. This competition manifests itself in two ways. First, T_c suppressed where the CDW order is strongest. Second, it has been shown from x-ray diffraction that when a sample transitions into the superconducting state, the CDW order weakens, but that if a magnetic field is used to suppress the SC, the CDW order regains in strength.[23] The consequence is that theories now need to find ground states that involve both d-wave superconductivity and CDW order, out of which a better understanding of the pseudogap may arise. Already efforts have been made in this regard.[54, 75, 60]

This phase of CDW order is the main focus of this thesis, in large part due to its role in competing with superconductivity, its presence in the pseudogap phase and also many other questions regarding its nature, highlighted in the next section.

1.3 Motivations and main results

I will now cover the motivations for the different studies presented in this thesis. This section will also serve as an executive summary, highlighting the main results of those studies, some of which motivated or guided later studies. In the broadest sense, my motivation prior to 2012 was to clarify the nature of stripe order in La-based cuprates, given differences between model calculations and experimental data that suggested an incomplete explanation.

Following the 2012 discovery of CDW order in $YBa_2Cu_3O_{6+x}$, my focus naturally shifted to identifying whether this CDW order was intrinsic to the CuO_2 planes and what similarities it may share with La-based cuprates. This led to my most recent study comparing the orbital symmetry of the CDW states in $La_{1.875}Ba_{0.125}CuO_4$ and $YBa_2Cu_3O_{6.67}$.

1.3.1 CDW order in La-based cuprates

Prior to 2012, CDW order in the cuprates had only been seen, by diffraction techniques, in La-based cuprates.[76] These compounds were shown to exhibit both static spin *and* charge ordering.[25] However, this spin and charge order was generally attributed to structural peculiarities unique to the La-based cuprates,[77, 78, 79, 80] and therefore not taken as evidence for universal CDW order in cuprate superconductors. At this time, there was also evidence for density wave order in cupric oxychloride and Bi-based cuprates, as revealed by scanning tunnelling microscopy,[81, 82] but diffraction techniques did not find any signatures of charge order in those materials.[83] In addition, a search for static CDW order in $YBa_2Cu_3O_{6+x}$ by resonant soft x-ray scattering also reported a null result.[84] This state of affairs seemed to support the notion that CDW order was confined to certain compounds, attributable to particulars of their crystal structure.

I mention this because my research on the cuprates began in late 2009, at which time the ubiquitous nature of CDW order in the cuprates was not yet known. It was natural then to focus on the charge order in La-based cuprates. What was known about this static charge order came from neutron scattering,[25, 85, 86, 87, 88, 89, 90, 91] hard x-ray diffraction,[92, 93, 87, 94] and resonant soft x-ray scattering,[95, 96] in the La-based cuprates with hole doping near $p = \frac{1}{8}$.

1.3.1.1 Evidence for stripes: neutron and hard x-ray scattering

Neutron and hard x-ray scattering measurements in $La_{1.48}Nd_{0.4}Sr_{0.12}CuO_4$ found incommensurate charge and spin peaks in the vicinity of fundamental Bragg peaks, but split from these by amounts δ_{charge} and δ_{spin} and following the relation $\delta_{\text{charge}} = 2\delta_{\text{spin}}$.[25, 92] These observations were argued to be consistent with "stripes" of static spin and charge, as depicted in Fig. 1.4. In this standard stripe model, for a hole doping of $p = \frac{1}{8}$ and at sufficiently low temperature, the holes arranges periodically into parallel, unidirectional "rivers" of charge, each containing an average of 0.5 holes/Cu. The holes are mobile within each stripe. Between stripes, the hole doping is 0 as in the undoped AF parent compound. The stripes act as anti-phase domain walls for the AF order.

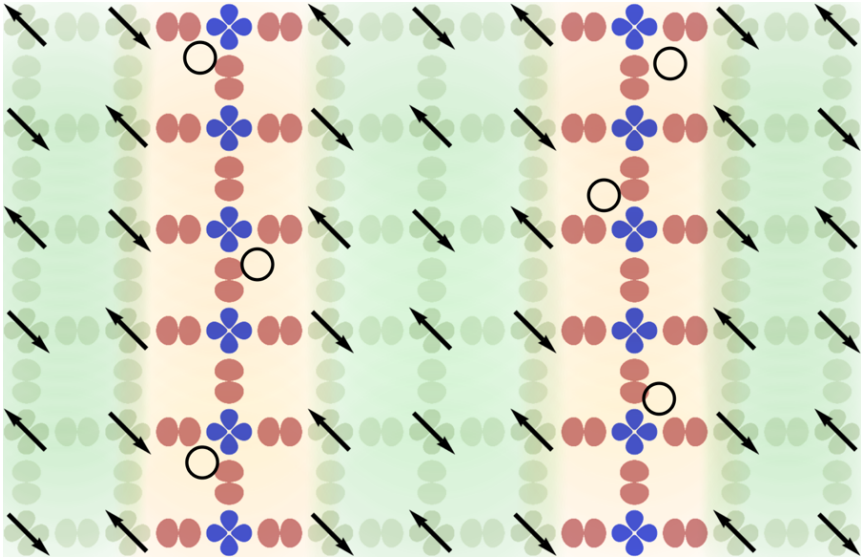

Figure 1.4 – Standard picture of commensurate spin and charge stripe order in La-based cuprates for $p = \frac{1}{8}$. Mobile holes (open circles) segregate into unidirectional stripes (light orange) with an average doping of 0.5 holes/Cu within each stripe. The stripes have a period of 4 times the lattice spacing. Regions between stripes (light green) are undoped and form AF order.

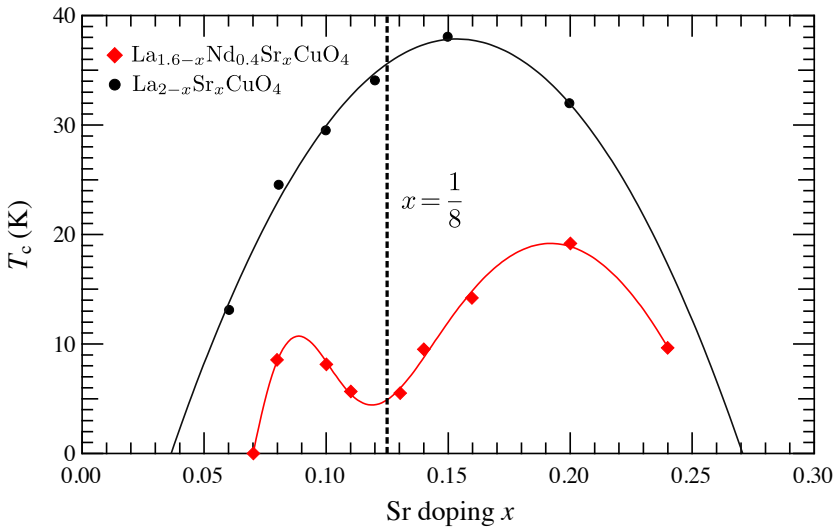

Figure 1.5 – Impact of "$\frac{1}{8}$-anomaly" on T_c in Nd-doped $La_{2-x}Sr_xCuO_4$. Doping Nd into $La_{2-x}Sr_xCuO_4$ dramatically reduces T_c, particularly near $x = p = \frac{1}{8}$. A similar effect occurs natively in $La_{2-x}Ba_xCuO_4$.[97] Data from Ref. [86]. Lines are guides to the eye.

At around the same $p = \frac{1}{8}$ doping, certain La-based cuprates exhibit a very strong suppression of T_c. Fig. 1.5 illustrates this effect, frequently referred to as the "$\frac{1}{8}$-anomaly",[97] for Nd-doped $La_{2-x}Sr_xCuO_4$. Competition between the stripes and superconductivity seemed to be a likely explanation for this anomaly,[86] bringing a great deal of attention to the role of charge inhomogeneity in the CuO_2 planes. This is because, despite being only known to occur in La-based cuprates (at the time), this competition may hold important clues to unlocking higher T_c in related compounds.

Yet, even as of 2009, the question of how this charge inhomogeneity manifests itself was not truly resolved. One issue was that scattering experiments were unable to identify higher harmonic diffraction peaks.[94, 80] These peaks are seen in the nickelates,[98] which have analogous stripe order, and thus would also be expected in the cuprates if the standard stripe picture applied. One possibility could be that the charge inhomogeneity forms sinusoidal modulations rather than stripe-like order. In principle, this could describe the diffraction patterns while also accounting for the absence of higher harmonics, but an important question then follows: how should one detect these sinusoidal charge modulations? Unfortunately, both neutron scattering, which is sensitive to the atomic nuclei, and hard x-ray diffraction, which is sensitive to the total electron density (of which only a small fraction is affected by the doped holes) away from an absorption edge, are only indirectly sensitive to such charge modulations through their associated atomic displacements.

1.3.1.2 A new approach: resonant soft x-ray scattering

In recognition of this problem, new instruments for resonant soft x-ray scattering (RSXS) at low temperature were developed. Resonant scattering refers to x-ray diffraction with a photon energy that corresponds to an x-ray absorption edge.[99] In contrast to x-ray diffraction far from an absorption edge, which is generally sensitive to the total electron density, diffraction at an absorption edge causes a core electron to transition into a higher energy unoccupied state before decaying back to the ground state. This resonant process greatly enhances the sensitivity of the scattering to *particular* electrons (not *all* electrons), providing element specificity as well as sensitivity to valence state and orbital orientation (this is discussed further in Chapter 2). The so-called 'soft' x-rays correspond to lower photon energies (e.g., 100 to 2000 eV) and shorter penetration lengths than 'hard' x-rays (greater than 10 keV) that are commonly used for crystallography and medical imaging.

Designing a scattering instrument for use with soft x-rays poses many technological challenges, namely caused by the need to operate a diffractometer in a high vacuum environment. Early demonstrations date back to 1988,[100] but were limited in that cooling

was not possible and that rotation of the polarization vector required rotating the scattering chamber around the beam axis. In the early 2000's a number of new diffractometer designs were implemented, providing temperature control and operating at more modern soft x-ray beamlines.[101, 102, 103] These later systems enabled the first studies of stripe ordered cuprates by RSXS.

Soft x-rays are particularly important for studying the CuO_2 planes in the cuprates since the O K and Cu L absorption edges are in this energy range. For the cuprates, hole doping the the CuO_2 planes influences the O K edge pre-edge structure, and the higher-energy side of the Cu $L_{3,2}$ edges,[104] by namely producing holes in states with Cu $3d_{x^2-y^2}$ and O $2p_{x,y}$ orbital character.[105] It was later pointed out that RSXS at the O K edge in particular should provide a dramatically enhanced sensitivity to spatial modulations in hole density.[102]

This technique was used to analyze the photon energy dependence of scattering from O sites in the CuO_2 planes of the spin and charge ordered cuprate $La_{2-x}Ba_xCuO_4$.[95] The conclusions of Ref. [95] are largely in agreement with the conventional stripe picture and suggested that the stripes were half-filled, separating regions of minimal charge. However, a close inspection of calculated resonance profile (i.e., the energy dependence of the resonant scattering intensity), upon which such conclusions are contingent, reveals a rather unsatisfying match to the experimental result. In particular, the experimental scattering profile at the O K pre-edge has two peaks: a prominent peak located just above E_F, associated with the mobile carriers (holes), and a smaller peak at slightly higher photon energy associated with the upper Hubbard band. The calculated profile in Ref. [95] is a single, broad peak, that encompasses the appropriate energy range, but captures neither of these fine details.

An effort to address this shortcoming was made by a different group in a later RSXS study of $La_{2-x-y}Eu_ySr_xCuO_4$.[96] Here, a revised model calculation of the O K pre-edge resonance profile produces two peaks at the appropriate energies. However, the calculated weight in the second peak is considerably larger than the experimental result. Additionally, the calculated resonance profile at the Cu L_3 edge was much wider than the observation, essentially mirroring the x-ray absorption profile rather than the scattering profile. These two shortcomings suggested that the underlying origin for the resonant scattering signal, and thus the nature of the charge inhomogeneity, was still not resolved.

This problem was a major motivation to study $La_{1.475}Nd_{0.4}Sr_{0.125}CuO_4$ by RSXS. As is shown in Ref. [1] (here Chapter 3), a detailed study of its resonance profiles at the O K and Cu $L_{3,2}$ edges was compared to three model calculations. The first two models followed conventional practice,[95, 96] and treated the scattering as arising from changes

in local doping (valence) for O sites and atomic positions for Cu site. With these models, a similar level of agreement to the previous calculations in Ref. [96] was found, failing to entirely reproduce the observed resonance profiles.

To address this, a third model was developed. It operates on the basis that the resonant transition energy, which relates to the orbital energy levels of the scatterers, is spatially modulated by an amount $\pm\Delta E$, so it is called the *energy shift* model. Calculations of the O K and Cu $L_{3,2}$ resonance profiles using the energy shift model (with $\Delta E < 0.2$ eV) are in excellent agreement with the data. An important feature of this model is that it does not explicitly include modulations in local hole doping (these imply an associated change in spectral weight, as shown by x-ray absorption;[105] for the energy shift model, all sites have the same spectral weight). It is therefore at odds with the standard stripe picture. Instead, its good match to the data is interpreted as a signature of a more subtle modulation in electronic structure, either induced by *small* charge density modulations and possibly consistent with a theoretically predicted valence bond order,[106] or arising from a more exotic type of electronic order.

1.3.2 CDW order in $YBa_2Cu_3O_{6+x}$

When CDW order was found in $YBa_2Cu_3O_{6+x}$,[22, 23] it was unclear whether this CDW order was intrinsic to the CuO_2 planes or related to the periodic ordering of O atoms in the partially filled CuO_x chain layer. The chain layer in $YBa_2Cu_3O_{6+x}$ forms well-known arrangements of CuO chains, depending on the oxgyen content x.[107, 108, 109, 110, 111] For example, when $x \approx 0.75$, the chain layer can order with an ortho-III configuration. This refers to CuO_x chains arranged in a full-full-empty pattern, as depicted in Fig. 1.6. This was a crucial point to address, since if the observed CDW order were attributable to the chain ordering, then this CDW order may simply be a mere peculiarity of the crystal structure of $YBa_2Cu_3O_{6+x}$, akin to the La-based cuprates. Conversely, if this order could be shown to belong to the CuO_2 planes and not depend on the chain ordering, then since $YBa_2Cu_3O_{6+x}$ is often considered *the* benchmark 'clean' cuprate, it may be possible to establish CDW order as generic to the cuprate phase diagram.

This motivated a RSXS study of the resonance profile at different wavevectors: 1) $\boldsymbol{Q}_{\mathrm{CDW},H} = (0.31\ 0\ L)$ and $\boldsymbol{Q}_{\mathrm{CDW},K} = (0\ 0.31\ L)$, corresponding to the newly found CDW order, and 2) $\boldsymbol{Q}_{\mathrm{O}} = (H_{\mathrm{O}}\ 0\ L)$, corresponding approximately to the inverse of the chain order periodicity. A simple hypothesis was that if this CDW order was similar to the charge order in La-based cuprates, then it should be possible to describe its resonance profile with the energy shift model. Validation would then strongly argue that the CDW order resides in

the CuO_2 planes and is not tied to O order in the chains. A second hypothesis was that the resonance profile of $\boldsymbol{Q}_{\mathrm{O}}$ should be consistent with a periodic modulation in Cu valence,[84] and thus differ significantly from that of $\boldsymbol{Q}_{\mathrm{CDW}}$ in its energy, photon polarization and temperature dependence. Both hypotheses were confirmed in Ref. [2] (here Chapter 4), illustrating that the CDW order and O chain order are distinct.

Another important question regarding the CDW order in $YBa_2Cu_3O_{6+x}$ relates to the possible role of disorder in setting the CDW length scale, or correlation length. It is generally believed that this can occur in two inequivalent ways: i) either disorder pins charge density fluctuations to produce short-range static order or ii) disorder disrupts what would otherwise be long-range order.[112, 113, 114] In $YBa_2Cu_3O_{6+x}$, the most influential defects reside in the CuO_x chain layer.[48] $YBa_2Cu_3O_{6+x}$ crystals are otherwise very pure and stoichiometric.[45] The previously mentioned ortho phases (e.g., o-II, o-III, o-V, o-VIII) are typically formed with care in a long annealing process,[115] yet they can also be destroyed by a simple procedure of heating the samples to modest temperatures and subsequently quench cooling them to prevent ortho phase formation. This procedure provides a unique means of investigating the role of disorder in $YBa_2Cu_3O_{6+x}$, without the need to chemically alter the sample composition nor even remove the sample from the diffractometer, thus minimizing uncontrolled variables that may influence T_c, the CDW order, or the reproducibility of the measurement.

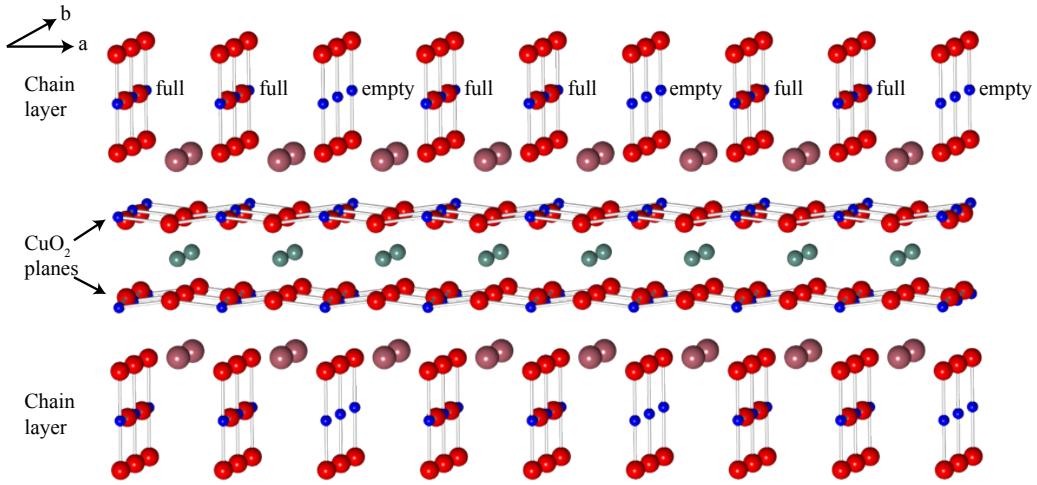

Figure 1.6 – An expanded view of $YBa_2Cu_3O_{6.75}$ showing three periods of ortho-III ordering in the chain layer. Doped oxygen atoms form CuO chains that run along the b axis and these chains go from being full to full and then to empty along the a axis.

In Ref. [3] (here Chapter 6), this approach revealed that disordering the chains reduced the CDW scattering intensity while not affecting the CDW correlation length, incommensurability or temperature dependence. Although the interpretation is not clear-cut and future work is needed to sort it out, this can be argued not to result from either of the above mentioned mechanisms, which may be more suited to scenarios where disorder plays a stronger role. Rather, this finding may be indicative of an intrinsic CDW length scale, possibly set by competition with superconductivity in the CuO_2 planes.

1.3.3 Orbital symmetry of CDW order

An important point made in certain theories is that the CDW order can take on different orbital symmetries.[106, 75, 54] One example is a d symmetry state where charge density is minimal on Cu sites but has locally different sign on the bonds between the Cu sites (i.e., the O sites) that run along the a and b axes of the CuO_2 plane.[106] This prompted a need to identify this orbital symmetry experimentally to constrain the theoretical models. Shortly thereafter, an examination of existing scanning tunnelling microscopy data, using a novel analysis method, identified a dominant d form factor, as favoured in the theory, in $Bi_2Sr_2CaCu_2O_{8+\delta}$ (Bi-2212) and $Ca_{2-x}Na_xCuO_2Cl_2$ (Na-CCOC).[116] A d form factor was also reported in $YBa_2Cu_3O_{6+x}$ and $Bi_2Sr_{2-x}La_xCuO_{6+\delta}$ by means of RSXS at the Cu L_3 edge in a special scattering geometry, interpreted at first by means of microscopic model of the CDW order,[117] and later by means of a model quite similar to one presented in Ref. [4] (here Chapter 5).[1]

These theoretical predictions also prompted me to investigate the orbital symmetry of CDW order. In particular, I aimed to study whether the CDW orbital symmetry would also have a d form factor in the La-based cuprates. Employing a similar scattering geometry as in Ref. [117], a study of $La_{1.875}Ba_{0.125}CuO_4$ was performed to address this question. An important difference in methodology was that resonant scattering was performed at the O K edge as well as the Cu L edge. For the O K edge, a mapping between the experimental observables and a theoretical parametrization of bond order, that allows for mixed orbital symmetries,[75] was developed in order to quantify the proportion of d and s' CDW symmetry components. It was found that $La_{1.875}Ba_{0.125}CuO_4$ has a CDW orbital symmetry dominated by an s' component for the O atoms in the CuO_2 planes, as will be shown in Chapter 5. This further distinguishes the La-based cuprates from other cuprates.

An intriguing possibility is that this s' symmetry CDW order in LBCO is more compatible with static spin order than CDW order with d symmetry. This possibility may

[1] Ref. [117] does not yet contain this revised analysis, which is known to me by private communication.

be supported by theory. For instance, a recent calculation for a three-orbital model finds a similar d to s' proportion when the system develops both static spin and charge order,[118] whereas models that do not form static spin order exhibit dominant d orbital symmetry.[119, 75, 54, 120, 121]

Chapter 2

Resonant soft x-ray scattering

2.1 Overview

Resonant soft x-ray scattering (RSXS) is a technique that extends conventional x-ray diffraction (XRD) beyond the study of atomic positions in order to gain element, site, valence and orbital specific information about ordered states of matter. This specificity is gained by tuning the photon energy to an x-ray absorption edge, providing sufficient energy to excite an inner-shell core electron into an empty valence state and altering the anomalous components of the atomic scattering form factor such that it depends strongly on photon energy, photon polarization and the electronic environment of the scatterers. This resonant effect enhances the scattering amplitude, making it possible to detect weak ordering signatures, and embeds a wealth of information about the charge, spin and orbital degrees of freedom of the electronic order into the scattering process. In transition metal (TM) oxides, most of the interesting physics occurs at low energies, near the Fermi level of the transition metal ion. These low-lying empty states can be probed using soft x-rays ($\hbar\omega$ ~50-2000 eV) which can resonantly excite the strong $2p \rightarrow 3d$, $3d \rightarrow 4f$, and $4d \rightarrow 5f$ dipole-allowed transitions of TM ions. In contrast, hard x-rays ($\hbar\omega > 10$ keV) are less useful for transition metal ions, since they probe the $4p$ states well above the Fermi energy via the $1s \rightarrow 4p$ transition.

Over the past two decades, the impact and importance of RSXS has grown significantly thanks to numerous advances in instrumentation and the theory of the resonant scattering.[122] Third generation synchrotrons have provided simple control of the incident photon energy and polarization (thanks to elliptically polarizing undulators [123]), while providing very high photon flux, excellent energy resolution (eg. a resolution of

$\Delta E \sim 0.1$ eV at $E = 1000$ eV is typical at most soft x-ray beamlines), better electron orbit stability and improved x-ray beam focusing properties.[124] Notable advances in the theory of resonant scattering have included the discovery of polarization dependence to anomalous scattering,[125] the appearance of forbidden reflections due to anisotropic x-ray susceptibility in crystals,[126] the theoretical description of magnetic resonant x-ray diffraction,[127, 99] and the development of frameworks to calculate resonant inelastic x-ray scattering spectra.[128, 129]

In this chapter, fundamental aspects of elastic RSXS will be presented. A theoretical treatment tailored to supplement the following chapters is presented in section 2.2. More exhaustive reviews of the theory of resonant scattering are available.[130, 131, 132, 133, 134, 135, 136, 28] Experimental details particular to the REIXS beamline at the Canadian Light Source will be discussed in section 2.3.

2.2 Basic theory of resonant elastic x-ray scattering

2.2.1 Diffraction

The diffraction of x-rays by crystals, structures composed of periodic arrangements of atoms that form a Bravais lattice,[137] was discovered in 1912 and has had an immeasurable impact on a vast array of disciplines.[138, 139] When a plane wave of the form $e^{i\boldsymbol{k}\cdot\boldsymbol{r}}$ is incident on periodic lattice of atoms, each atom causes a scattered radial wave of the form $fe^{i\boldsymbol{Q}\cdot\boldsymbol{r}}/r$ (for non-zero scattering angle),[140] where f is the atomic scattering form factor of the scattering atom. In a classical picture, this coincides with the incident wave causing an electron to vibrate and behave like a dipole that emits a radial wave with a scattering amplitude of f. Far from the scatterer, the emitted radial wave can be approximated by a plane wave. Constructive interference of many of such emitted plane waves from atoms in a lattice occurs when the difference in path length for plane waves arising from crystal planes that are separated by a distance d is an integer multiple of the wavelength. This describes the famous Bragg formulation of diffraction,[141] governed by the equation $n\lambda = 2d_{HKL}\sin\theta$, where λ is the x-ray wavelength, d_{HKL} is the interplanar separation (for a given set of lattice planes with Miller indices H, K, and L), θ is the scattering angle and n is the order of the interference.

Alternatively, it is possible to sum the emitted plane waves keeping track of their relative phases and arrive at the Laue condition for diffraction, $\boldsymbol{k}' - \boldsymbol{k} = \boldsymbol{G}$, where $\boldsymbol{G}$ is a vector of the reciprocal lattice.[142] The Laue formulation is more useful when dealing with

diffraction from a single crystal composed of multiple atom types, and it is more explicitly written as a set of three simultaneous equations.[142]

$$\begin{aligned} \boldsymbol{a}_1 \cdot (\boldsymbol{k}' - \boldsymbol{k}) &= 2\pi H \\ \boldsymbol{a}_2 \cdot (\boldsymbol{k}' - \boldsymbol{k}) &= 2\pi K \\ \boldsymbol{a}_3 \cdot (\boldsymbol{k}' - \boldsymbol{k}) &= 2\pi L \end{aligned} \tag{2.1}$$

Here, $\boldsymbol{a}_1$, $\boldsymbol{a}_2$ and $\boldsymbol{a}_3$ are the primitive vectors of the crystal lattice and H, K and L are Miller indices for a reciprocal lattice vector $\boldsymbol{G}$ that satisfies $\boldsymbol{G} = H\boldsymbol{b}_1 + K\boldsymbol{b}_2 + L\boldsymbol{b}_3$, where $\boldsymbol{b}_1$, $\boldsymbol{b}_2$ and $\boldsymbol{b}_3$ are the basis vectors for the reciprocal lattice.[143]

To account for the rotation of the crystal, and simplifying the problem to consider only cubic, tetragonal or orthorhombic lattices, it is useful to write $\boldsymbol{a}_{(1,2,3)} = (a, b, c)R.\boldsymbol{O}_{(a,b,c)}$, where a, b and c are lattice constants, $\boldsymbol{O}_{(a,b,c)}$ are the initial orientation vectors of the crystal axes in the diffractometer frame (eg. for a horizontal scattering geometry, $\hat{x}$=primary beam direction, $\hat{z}$=vertical direction, $\hat{y}$=perpendicular to $\hat{x}$ and $\hat{z}$ in horizontal plane) and R is a rotation matrix that rotates the crystal axes by the diffractometer's rotations (eg. $R = R_{\theta_s} \cdot R_\chi \cdot R_\phi$). If one eliminates ϕ and χ rotations and considers only horizontal plane scattering, then it is possible to show that for a crystal with initial orientation $\boldsymbol{O}_a = -\hat{x}$ and $\boldsymbol{O}_b = \hat{y}$, the sample rotation angle θ_s and the detector angle 2θ are related to $\boldsymbol{Q} = 2\pi(H/a, K/b)$ according to:

$$2\theta = 2\sin^{-1}\left(\frac{hc}{2E}\sqrt{\left(\frac{H}{a}\right)^2 + \left(\frac{K}{b}\right)^2}\right) \tag{2.2}$$

$$\theta_s = \theta - \tan^{-1}\left(\frac{H}{K}\frac{b}{a}\right), \tag{2.3}$$

where h is Planck's constant, c is the speed of light in vacuum and E is photon energy.[1] Equations 2.2 and 2.3 are very useful for RSXS, since soft x-ray diffractometers typically operate in a 2-circle mode (fixed χ and ϕ) with the detector kept in the scattering plane. However, use of Eq. 2.1 can in principle be used to calculate scattering geometries for H, K and L indices in 3- and 4- circle modes. In practice, many diffractometers are typically running the scientific diffraction software **spec**, that includes a program called **fourc**.[144] This program implements a general form of Eq. 2.1, based on previously established calculations,[145] that can automatically calculate appropriate scattering geometries for requested reciprocal lattice vectors, provided that the crystal parameters and initial crystal orientation are set correctly.

[1] See Section A.1 for a derivation of these equations.

As mentioned previously, the Laue formulation consists of summing up the plane waves emitted by all the atoms in a crystal. This approach is useful as it provides a way to calculate the scattering intensity as a function of $\boldsymbol{Q}$, the incident and emitted photon polarization vectors $\boldsymbol{\epsilon}$ and $\boldsymbol{\epsilon}'$, and the photon energy $E = \hbar\omega$. Assuming (for now) that the quantum mechanical light-matter interaction that occurs when a plane wave interacts with an atom in a crystal can be fully captured by the atomic scattering form factor $f \to f(\omega, \boldsymbol{\epsilon}, \boldsymbol{\epsilon}')$, it is possible to write down an expression for the scattering intensity in terms of this sum.[135, 28]

$$I(\boldsymbol{Q}, \omega, \boldsymbol{\epsilon}, \boldsymbol{\epsilon}') \propto \left| \sum_j f_j(\omega, \boldsymbol{\epsilon}, \boldsymbol{\epsilon}') e^{i\boldsymbol{Q}\cdot\boldsymbol{R}_j} \right|^2 \tag{2.4}$$

In Eq. 2.4, the sum is over all atomic sites j, with atomics positions denoted by $\boldsymbol{R}_j$. Following others, it is illustrative to index the coordinate system differently. If $\boldsymbol{R}_j$ is instead written as $\boldsymbol{C}_m + \boldsymbol{r}_j$, where $\boldsymbol{C}_m$ points to the center of unit cell m and $\boldsymbol{r}_j$ locates the atoms within the unit cell relative to $\boldsymbol{C}_m$, then the scattering intensity can be separated into two components: a unit cell structure factor $F(\omega, \boldsymbol{\epsilon}, \boldsymbol{\epsilon}')$ and a lattice component $L(\boldsymbol{Q})$.

$$\begin{aligned} I(\boldsymbol{Q}, \omega, \boldsymbol{\epsilon}, \boldsymbol{\epsilon}') &\propto \left| \sum_{m,j} f_j(\omega, \boldsymbol{\epsilon}, \boldsymbol{\epsilon}') e^{i\boldsymbol{Q}\cdot(\boldsymbol{C}_m + \boldsymbol{r}_j)} \right|^2 \\ &= \left| \sum_j f_j(\omega, \boldsymbol{\epsilon}, \boldsymbol{\epsilon}') e^{i\boldsymbol{Q}\cdot\boldsymbol{r}_j} \right|^2 \times \left| \sum_m e^{i\boldsymbol{Q}\cdot\boldsymbol{C}_m} \right|^2 \\ &= |F(\omega, \boldsymbol{\epsilon}, \boldsymbol{\epsilon}')|^2 \times |L(\boldsymbol{Q})|^2 \end{aligned} \tag{2.5}$$

The lattice component has to do with interference of scattering arising from different unit cells whereas the unit cell structure factor describes interference coming from within the unit cell. In the limit that the number of unit cells goes to infinity, all the cells will scatter coherently (in phase) and $L(\boldsymbol{Q}) \propto \sum_{\boldsymbol{G}} \delta(\boldsymbol{Q} - \boldsymbol{G})$,[28, 140] which is a convenient way to arrive at the Laue condition (scattering occurs when $\boldsymbol{Q} = \boldsymbol{G}$).[2] This procedure also shows that for long range order, one only needs to calculate the unit cell structure factor in order to calculate the scattering intensity function.

[2] This derivation is shown neatly in Ref. [140], section 3.2.4.

2.2.2 Quantum mechanical origin of resonant scattering

The quantum mechanical origin of resonant scattering traces back to the interaction between an electromagnetic field and a Dirac (spin-1/2) particle. The general approach for finding the scattering amplitude is to treat either the Schrödinger Hamiltonian, the Schrödinger-Pauli Hamiltonian or the Dirac Hamiltonian, up to second order in perturbation theory.[146, 147, 135] To capture the interaction of an electron with the electromagnetic field, the momentum operator $\boldsymbol{p}$ is replaced with $\boldsymbol{p} - e\boldsymbol{A}/c$, where $\boldsymbol{A}$ is the vector potential of a quantized, time-dependent radiation field.

The approach I follow (as in Refs. [146, 148, 135]) is to consider the low energy limit ($E_{\text{x-ray}} \ll mc^2 \simeq 511$ keV) of the Dirac Hamiltonian given by:

$$\mathcal{H}_D = \beta mc^2 + eV(\boldsymbol{r}) + c\boldsymbol{\alpha} \cdot [\boldsymbol{p} - e\boldsymbol{A}(\boldsymbol{r}, t)]\,, \tag{2.6}$$

where β and $\boldsymbol{\alpha}$ are 4×4 Hermitian matrices (see Ref. [149] Sec. 3-2 or Ref. [150] for their properties), $\boldsymbol{s}_i$ is the electron spin, $V(\boldsymbol{r})$ is the vector potential, and m is the electron mass. This approach is appropriate for scattering at almost all x-ray absorption edges (especially for soft x-rays $E_{\text{x-ray}} < 2$ keV). It also has the benefit of resolving all the dominant resonant and non-resonant magnetic and non-magnetic terms that contribute to the scattering cross-section. It has been shown that Eq. 2.6 leads to the following matter-radiation interaction Hamiltonian, $\mathcal{H}_{\text{int}} = \mathcal{H}_1 + \mathcal{H}_2 + \mathcal{H}_3 + \mathcal{H}_4$, when small relativistic corrections are dropped.[146, 148, 135] The sum is over electrons labeled by index i.

$$\mathcal{H}_1 = +\sum_i \frac{e^2}{2mc^2} \left[\boldsymbol{A}(\boldsymbol{r}_i, t)\right]^2 \tag{2.7}$$

$$\mathcal{H}_2 = -\sum_i \frac{e^2\hbar}{2m^2c^4} \boldsymbol{s}_i \left[\partial_t \boldsymbol{A}(\boldsymbol{r}_i, t) \times \boldsymbol{A}(\boldsymbol{r}_i, t)\right] \tag{2.8}$$

$$\mathcal{H}_3 = -\sum_i \frac{e}{mc} \left[\boldsymbol{A}(\boldsymbol{r}_i, t) \cdot \boldsymbol{p}_i\right] \tag{2.9}$$

$$\mathcal{H}_4 = -\sum_i \frac{e\hbar}{mc} \boldsymbol{s}_i \cdot \left[\boldsymbol{\nabla} \times \boldsymbol{A}(\boldsymbol{r}_i, t)\right] \tag{2.10}$$

Restricting our discussion to elastic scattering, we now consider how scattering events can occur through $\mathcal{H}_{\text{int}}$. An elastic scattering process can be defined as the interaction of a photon $(\boldsymbol{\epsilon}, \boldsymbol{k})$ with the electron system in a state $|G\rangle$ that results in the emission of a photon $(\boldsymbol{\epsilon}', \boldsymbol{k}')$ and leaves the system in the final state $|G\rangle$ (for an elastic process $|\boldsymbol{k}| = |\boldsymbol{k}'|$). This can occur most simply by an interaction that absorbs (annihilates) the photon $(\boldsymbol{\epsilon}, \boldsymbol{k})$

and then emits a new photon $(\boldsymbol{\epsilon}', \boldsymbol{k}')$ without causing any electronic transitions. Elastic scattering can also occur in cases where the absorption causes the electron to transition out of state $|G\rangle$ into an intermediate state $|I\rangle$ which subsequently decays back to $|G\rangle$ by emitting a photon. The former process is called non-resonant scattering and the latter is called resonant scattering.

We can understand these cases explicitly by checking how the four terms in $\mathcal{H}_{\text{int}}$ act upon $|G\rangle$. To do this, we introduce a general quantized vector potential as an expansion in plane waves (with the Coulomb gauge $\boldsymbol{\nabla} \cdot \boldsymbol{A} = 0$), given by

$$\boldsymbol{A}(\boldsymbol{r}, t) = \sum_{\boldsymbol{k},\mu} \sqrt{\frac{hc}{V|\boldsymbol{k}|}} \left(a_{\boldsymbol{k},\mu} \boldsymbol{\epsilon}_\mu(\boldsymbol{k}) e^{i(\boldsymbol{k}\cdot\boldsymbol{r} - \omega_{\boldsymbol{k}} t)} + a^\dagger_{\boldsymbol{k},\mu} \boldsymbol{\epsilon}_\mu(\boldsymbol{k}) e^{-i(\boldsymbol{k}\cdot\boldsymbol{r} - \omega_{\boldsymbol{k}} t)} \right), \tag{2.11}$$

where V is the volume of the quantization box and $a^\dagger_{\boldsymbol{k}}$ and $a_{\boldsymbol{k}}$ are, respectively, photon creation and annihilation operators that operate on photons with wavevector $\boldsymbol{k}$ and mode μ.[148] The mode is conventionally represented by unit vectors that are either parallel to the scattering plane (π-polarization) or perpendicular to the scattering plane (σ-polarization) and in both cases perpendicular to the incident/scattered wave propagation directions.

The significance of Eq. 2.11 is that the vector potential is linear in the creation and annihilation operators, which means that it must operate twice on $|G\rangle$ in order for elastic scattering to occur.[3] Hence, the terms $\mathcal{H}_1$ and $\mathcal{H}_2$, which are both quadratic in $\boldsymbol{A}$, will contribute in first order to elastic scattering. To calculate the transition rate and ultimately the scattering cross-section, we first need calculate the matrix elements $M_1 = \langle G|\mathcal{H}_1|G\rangle$ and $M_2 = \langle G|\mathcal{H}_2|G\rangle$.[151, 152, 148, 135, 28]

To obtain the dominant scattering contributions of $\mathcal{H}_3$ and $\mathcal{H}_4$, which are both linear in $\boldsymbol{A}$, second order perturbation theory is needed. Following others,[148, 135] the expression for the matrix elements $M_3 + M_4$ is given by

$$M_3 + M_4 = \sum_n \frac{\langle G|\mathcal{H}_3^* + \mathcal{H}_4^*|I_n\rangle\langle I_n|\mathcal{H}_3 + \mathcal{H}_4|G\rangle}{\hbar\omega_{\boldsymbol{k}} - (E_n - E_g) + i\frac{\Gamma}{2}}, \tag{2.12}$$

where the system transitions from a ground state $|G\rangle$ with energy E_g into all n accessible intermediate states $|I_n\rangle$ with energy E_n and lifetime $\simeq \hbar/\Gamma$. The number of transitions

[3] To see why, simply consider that $(a + a^\dagger)$ acting on the vacuum state $|0\rangle$ gives $|0\rangle + |1\rangle$ and therefore does not preserve the number of photons. In contrast, $(a + a^\dagger)^2$ has four terms and when acting on $|0\rangle$ one of these terms that will first annihilate and then create a photon, as needed for scattering. It also has a term that will first create and then annihilate a photon and two terms that create/annihilate ± 2 photons, but these extra terms do not correspond to scattering.

per unit time w is then given by Fermi's golden rule and can be evaluated as

$$\begin{aligned} w &= \frac{2\pi}{\hbar} \left| M_1 + M_2 + M_3 + M_4 \right|^2 \delta(\hbar\omega_{\boldsymbol{k}} - \hbar\omega_{\boldsymbol{k}'}) \\ &= \frac{2\pi}{\hbar} \left| \langle G|\mathcal{H}_1 + \mathcal{H}_2|G\rangle + \sum_n \frac{\langle G|\mathcal{H}_3^* + \mathcal{H}_4^*|I_n\rangle\langle I_n|\mathcal{H}_3 + \mathcal{H}_4|G\rangle}{\hbar\omega_{\boldsymbol{k}} - (E_n - E_g) + i\frac{\Gamma}{2}} \right|^2 \delta(\hbar\omega_{\boldsymbol{k}} - \hbar\omega_{\boldsymbol{k}'}). \end{aligned} \tag{2.13}$$

This general expression can be used to calculate all the dominant contributions of charge and magnetic scattering for both resonant and non-resonant processes. While magnetic x-ray scattering is a deep and interesting subject, the studies contained within this thesis rely on charge scattering, so for simplicity I will now drop the terms M_2 and M_4 that contain the spin $\boldsymbol{s}$ (see Refs. [153, 127, 99, 154, 148, 135] for more on magnetic x-ray scattering). Using Eq. 2.11, the matrix elements M_1 and M_3 become

$$\begin{aligned} M_1 &= \langle G| \sum_i \frac{e^2}{2m} \left[\boldsymbol{A}(\boldsymbol{r}_i, t)\right]^2 |G\rangle \\ &= \frac{hc}{V|\boldsymbol{k}|} \frac{e^2}{mc^2} (\boldsymbol{\epsilon}_{\mu'}^* \cdot \boldsymbol{\epsilon}_{\mu}) \sum_i \langle G| e^{i(\boldsymbol{k}-\boldsymbol{k}')\cdot\boldsymbol{r}_i} |G\rangle \end{aligned} \tag{2.14}$$

$$\begin{aligned} M_3 &= \sum_n \frac{\langle G| \sum_i \frac{e}{mc} \left[\boldsymbol{A}^*(\boldsymbol{r}_i, t) \cdot \boldsymbol{p}_i^*\right] |I_n\rangle\langle I_n| \sum_i \frac{e}{mc} \left[\boldsymbol{A}(\boldsymbol{r}_i, t) \cdot \boldsymbol{p}_i\right] |G\rangle}{\hbar\omega_{\boldsymbol{k}} - (E_n - E_g) + i\frac{\Gamma}{2}} \\ &= \frac{hc}{V|\boldsymbol{k}|m} \frac{e^2}{mc^2} \sum_n \frac{\langle G| \sum_{j=1}^N \boldsymbol{\epsilon}_{\boldsymbol{\mu}'}^{\prime *} \cdot \boldsymbol{p}_j e^{-i\boldsymbol{k}'\cdot\boldsymbol{r}_j} |I_n\rangle\langle I_n| \sum_{j'=1}^N \boldsymbol{\epsilon}_{\boldsymbol{\mu}} \cdot \boldsymbol{p}_{j'} e^{i\boldsymbol{k}\cdot\boldsymbol{r}_{j'}} |G\rangle}{\hbar\omega_{\boldsymbol{k}} - (E_n - E_g) + i\frac{\Gamma}{2}} \end{aligned} \tag{2.15}$$

as shown in Ref. [148].

Given these matrix elements, the differential cross-section (i.e., the probability that a photon is scattered into a given solid angle $\mathrm{d}\Omega$) can be calculated using the relations

$$\frac{\mathrm{d}^2\sigma}{\mathrm{d}E\mathrm{d}\Omega} = \frac{w\rho(E)}{c/V}, \text{ and } \rho(E) = \frac{V}{(2\pi)^3} \frac{E^2}{\hbar^3 c^3} \tag{2.16}$$

where $\rho(E)$ is the density of photon states (in the quantization box of volume V) with energy that satisfies $\hbar\omega_{\boldsymbol{k}} \leq \hbar\omega_{\boldsymbol{k}'} + \mathrm{d}E$.[153, 148] Substitution of the matrix elements into Eq. 2.13 and integration over energy (whereby the delta function ensures that only the

elastic scattering is included) gives

$$\frac{\mathrm{d}\sigma}{\mathrm{d}\Omega} = r_0^2 \left| (\boldsymbol{\epsilon}^*_{\mu'} \cdot \boldsymbol{\epsilon}_\mu) \sum_i \langle G| e^{i(\boldsymbol{k}-\boldsymbol{k}')\cdot \boldsymbol{r}_i} |G\rangle \right. \\ \left. + \sum_n \frac{\langle G| \sum_{j=1}^N \boldsymbol{\epsilon}'^*_{\boldsymbol{\mu}'} \cdot \boldsymbol{p}_j e^{-i\boldsymbol{k}'\cdot \boldsymbol{r}_j} |I_n\rangle \langle I_n| \sum_{j'=1}^N \boldsymbol{\epsilon}_{\boldsymbol{\mu}} \cdot \boldsymbol{p}_{j'} e^{i\boldsymbol{k}\cdot \boldsymbol{r}_{j'}} |G\rangle}{\hbar\omega_{\boldsymbol{k}} - (E_n - E_g) + i\frac{\Gamma}{2}} \right|^2 \tag{2.17}$$

where $r_0 = e^2/(mc^2)$ is the classical electron radius. Note that the quantization box volume V is not present in this observable and all the pre-factors except r_0 have canceled out. It is now apparent that the first term is simply Thomson scattering, which has the usual polarization factor $(\boldsymbol{\epsilon}^*_{\mu'} \cdot \boldsymbol{\epsilon}_\mu)^2$ and is proportional to the square of the Fourier transform $F(\boldsymbol{Q})$ of the electron density $\rho(\boldsymbol{r})$, defined by

$$F(\boldsymbol{Q}) = \sum_i \langle G| e^{i\boldsymbol{Q}\cdot \boldsymbol{r}_i} |G\rangle = \int \mathrm{d}\boldsymbol{r} e^{i\boldsymbol{Q}\cdot \boldsymbol{r}} \rho(\boldsymbol{r}). \tag{2.18}$$

The second term is the resonant charge scattering differential cross-section. This term can be further simplified if one takes the electric dipole approximation whereby the exponential term in Eq. 2.17 is expanded as $e^{-i\boldsymbol{k}\cdot \boldsymbol{r}_j} \sim (1 + i\boldsymbol{k}\cdot \boldsymbol{r}_j - (\boldsymbol{k}\cdot \boldsymbol{r}_j)^2/2 + \dots)$, keeping as many terms as needed for describing a particular process. For the resonant processes discussed here, only the first term contributes significantly. Multipole analysis involves keeping additional terms and has been covered in Refs. [153, 99, 130, 131, 135].

Keeping just the first term in the dipole approximation, the resonant scattering cross-section can be further simplified by replacing the momentum operator according to $\boldsymbol{p} = \frac{m}{i\hbar}[\boldsymbol{r}, H_{el}] = \frac{m}{i\hbar}\boldsymbol{r}(E_n - E_g)$, where H_{el} is the electron Hamiltonian that gives the energies of the ground and intermediate states. Using this commutator identity and dropping all pre-factors, the differential cross-section for electric dipole resonant scattering can be written

$$\left(\frac{\mathrm{d}\sigma}{\mathrm{d}\Omega}\right)_{\text{res.}} \propto \left| \sum_n \frac{\langle G| \boldsymbol{\epsilon}'^*_{\boldsymbol{\mu}'} \cdot (\sum_j \boldsymbol{r}_j) |I_n\rangle \langle I_n| \boldsymbol{\epsilon}_{\boldsymbol{\mu}} \cdot (\sum_j \boldsymbol{r}_j) |G\rangle}{\hbar\omega_{\boldsymbol{k}} - (E_n - E_g) + i\frac{\Gamma}{2}} \right|^2. \tag{2.19}$$

To illustrate the use of Eq. 2.19, it can further be shown (see Refs. [99, 131, 148]), that in the special case of atoms treated as free ions with spherical symmetry that is only broken by their magnetic moment, the differential cross-section simplifies to

$$\left(\frac{\mathrm{d}\sigma}{\mathrm{d}\Omega}\right)_{\text{res.}} \propto \left| \sum_n \left[(\boldsymbol{\epsilon}'^*_{\boldsymbol{\mu}'} \cdot \boldsymbol{\epsilon}_{\boldsymbol{\mu}}) F^{(0)} - i(\boldsymbol{\epsilon}'^*_{\boldsymbol{\mu}'} \times \boldsymbol{\epsilon}_{\boldsymbol{\mu}}) \cdot \boldsymbol{z}_n F^{(1)} + (\boldsymbol{\epsilon}'^*_{\boldsymbol{\mu}'} \cdot \boldsymbol{z}_n)(\boldsymbol{\epsilon}_{\boldsymbol{\mu}} \cdot \boldsymbol{z}_n) F^{(2)} \right] \right|^2, \tag{2.20}$$

where the functions $F^{(0,1,2)}$ (as defined in Ref. [131], not to be confused with $F(\boldsymbol{Q})$) are related to the radial wave functions of the atomic states (in terms of spherical harmonics) and $\boldsymbol{z}_n$ is a unit vector in the direction of the magnetic moment of the n^{th} ion.[4] It may be surprising that although we previously dropped the terms with an explicit spin term, there is a reappearance of magnetic scattering here in the second and third terms of Eq. 2.20. This comes from the Pauli exclusion principle. Since the resonant scattering cross-section depends on the availability of states into which the core electron can transition and since the electron's spin is conserved during the transition, the transition rate will depend on whether the core electron has the same spin or opposite spin as the unoccupied state.[148] These unexpected resonant magnetic scattering terms are important, as they can be used to explain x-ray magnetic dichroism effects in x-ray absorption spectroscopy,[155, 156] and also do contribute to resonant magnetic x-ray scattering effects.

The specific case of a free ion with spherical symmetry is, however, not general nor always appropriate. Many ions in real crystals can have their spherical symmetry broken due to their electronic environment (e.g., octahedral, tetragonal or orthorhombic coordination) in addition to perhaps having a local magnetic moment. Such anisotropy often translates to magneto-optical effects, which will influence how an atom scatters light of a given polarization. Instead of representing the interaction term by a scalar quantity (complex or otherwise) a Cartesian tensor can be used.[125, 126]

An elegant treatment of this problem for x-ray scattering was recently presented.[157] With the atomic scattering form factor denoted as a tensor $\widehat{f}$ rather than a scalar quantity, the differential cross-section, or measured scattering intensity, is given by

$$I \propto \frac{\mathrm{d}\sigma}{\mathrm{d}\Omega} \propto \left| \sum_j \left(\boldsymbol{\epsilon}'^{*}_{\boldsymbol{\mu}'} \cdot \widehat{f}_j \cdot \boldsymbol{\epsilon}_{\boldsymbol{\mu}} \right) e^{i\boldsymbol{Q}\cdot\boldsymbol{r}_j} \right|^2 , \tag{2.21}$$

where the scattering tensor $\widehat{f}_j$ at atomic site j can be written, in the lowest possible symmetry (i.e., triclinic) and dropping the site index, as

$$\widehat{f}(\omega) = \begin{pmatrix} f_{xx}(\omega) & f_{yx}(\omega) & f_{zx}(\omega) \\ f_{xy}(\omega) & f_{yy}(\omega) & f_{zy}(\omega) \\ f_{xz}(\omega) & f_{yz}(\omega) & f_{zz}(\omega) \end{pmatrix} . \tag{2.22}$$

The components of $\widehat{f}_j$ depend on photon energy and are complex. For systems with either cubic, tetragonal or orthorhombic symmetry, charge scattering contributions will

[4] Had we carried out the calculation including the matrix element M_4, we would have found an extra contribution to the charge scattering term proportional to $(\boldsymbol{\epsilon}' \cdot \boldsymbol{\epsilon})$; however, it turns out this correction is less than 1% of the above term so it is safe to neglect.[135]

only appear on the diagonal of this tensor but magnetic scattering contributions can appear on and off-diagonal and will generally depend on the direction of the local magnetization and the crystal symmetry.[157] These diagonal charge terms will play a crucial role in Chapter 5, where the crystal symmetry and absence of sensitivity to magnetic order give a tensor of the form

$$\widehat{f}_{\text{charge}} = \begin{pmatrix} f_{xx} & 0 & 0 \\ 0 & f_{yy} & 0 \\ 0 & 0 & f_{zz} \end{pmatrix}. \tag{2.23}$$

The tensorial representation of the scattering form factor has gained significance as the RSXS technique becomes more accessible and is used to study materials with increasingly complex magnetic structures or anisotropic crystal structures. However, prior to this development (and in cases where a full tensor is not needed) the complex, yet non-tensorial, atomic scattering form factor was (and is) used to calculate scattering intensities. I will now relate the atomic scattering form factor to the differential cross-section, show how it relates to the scattering tensor and highlight a practical, yet powerful, method of modelling resonant scattering processes.

2.2.3 Atomic scattering form factor

The relation between the differential cross-section and the atomic scattering form factor (also called the scattering length or scattering amplitude) is defined as

$$\frac{\mathrm{d}\sigma}{\mathrm{d}\Omega} = |f|^2 . \tag{2.24}$$

This comes simply from the definition that the scattered wave will have its amplitude reduced by a factor of f as compared to the incident wave. Comparing Eq. 2.24 to Eq. 2.17, we can see that f can be decomposed into 3 terms[5]

$$\begin{aligned} f &= f^{\mathrm{T}} + f' + if'' \\ f(\omega, \boldsymbol{\epsilon}, \boldsymbol{\epsilon}') &= f^{\mathrm{T}}(\boldsymbol{\epsilon}, \boldsymbol{\epsilon}') + f'(\omega, \boldsymbol{\epsilon}, \boldsymbol{\epsilon}') + if''(\omega, \boldsymbol{\epsilon}, \boldsymbol{\epsilon}'), \end{aligned} \tag{2.25}$$

where f^{T} is the usual non-resonant Thomson form factor and $f' + if''$ is the anomalous scattering form factor (also called the dispersion correction). The first line in Eq. 2.25 is a shorthand form whereas the second line shows which terms depend explicitly on polarization and/or energy. While f^{T} is simply proportional to the number of electrons, we see

[5] Actually a fourth term, f^{M} should appear in Eq. 2.25, corresponding to the non-resonant magnetic scattering that would have been included if the matrix element M_2 wasn't dropped.

that $f' + if''$ comes from the second order perturbation in $\mathcal{H}_3$, producing a photon energy dependent, complex quantity with a damped pole (resonance) at $\hbar\omega = E_n - E_g$. In this way, the atomic scattering form factor is clearly divided into a non-resonant and resonant contribution, both of which derive from the quantum mechanical interaction of an electromagnetic plane wave with an electron, as detailed in the previous section. Comparing terms in Eq. 2.4 and Eq. 2.21, it is apparent that f and $\widehat{f}$ are related by

$$f(\omega, \boldsymbol{\epsilon}, \boldsymbol{\epsilon}') = \left(\boldsymbol{\epsilon}'^{*}_{\boldsymbol{\mu}'} \cdot \widehat{f} \cdot \boldsymbol{\epsilon}_{\boldsymbol{\mu}}\right), \tag{2.26}$$

clarifying the link between the traditional atomic scattering form factor and the more general tensor representation.

If we suppose that we are dealing with spherical symmetry ($\widehat{f} = fI_3$, where I_3 is the identity matrix) and an isolated atom, then it is possible to calculate f' and f'' for all the elements. This problem has been studied extensively, and the most complete and currently the "best" tabulation of such theoretical calculations for elements $Z = 1-92$ in the energy range $E = 1 - 10$ eV to $0.4 - 1$ MeV is given by combining the tables in Refs. [158, 159]. It is possible to obtain this data using the online resource at Ref. [160]. An empirical tabulation of the atomic scattering form factor is given in Ref. [161], which can also be accessed online.[162] For offline access, I have created a Mathematica notebook that loads these databases and can then provide f' and f'' for all the elements and arbitrary photon energy (this is posted publicly online, see Ref. [163]).

While the empirical and theoretical tabulations are largely convergent, there can be sizeable differences, particularly at very low photon energy $E < 100$ eV and in the near-edge regions. For an example of such differences, and to establish a general idea for how f depends on photon energy, Fig. 2.1 shows f' and f'' for Cu and O in the soft x-ray regime. The imaginary component (f'') has notable "step-like" features and the real part (f') has "poles" that coincide with these steps.

The so-called edge-steps come from an instantaneous jump in the $|G\rangle \to |I\rangle$ transition probability of the free-atom. If one has familiarity with x-ray absorption spectroscopy, it becomes apparent that f'' is related to the x-ray absorption cross-section. In fact, this comes from the terms in $\mathcal{H}_3$ that annihilate the incident photon but do not create a scattered photon,[28] and we can then identify that the differential cross-section for x-ray absorption is

$$\frac{\mathrm{d}\sigma_{\mathrm{abs}}}{\mathrm{d}\Omega} = \frac{4\pi}{k} f''. \tag{2.27}$$

This relation defines the optical theorem,[164, 147] an important consequence of which is that the real and imaginary parts of the scattering amplitude satisfy the famous Kramers-Kronig dispersion relations.[165]

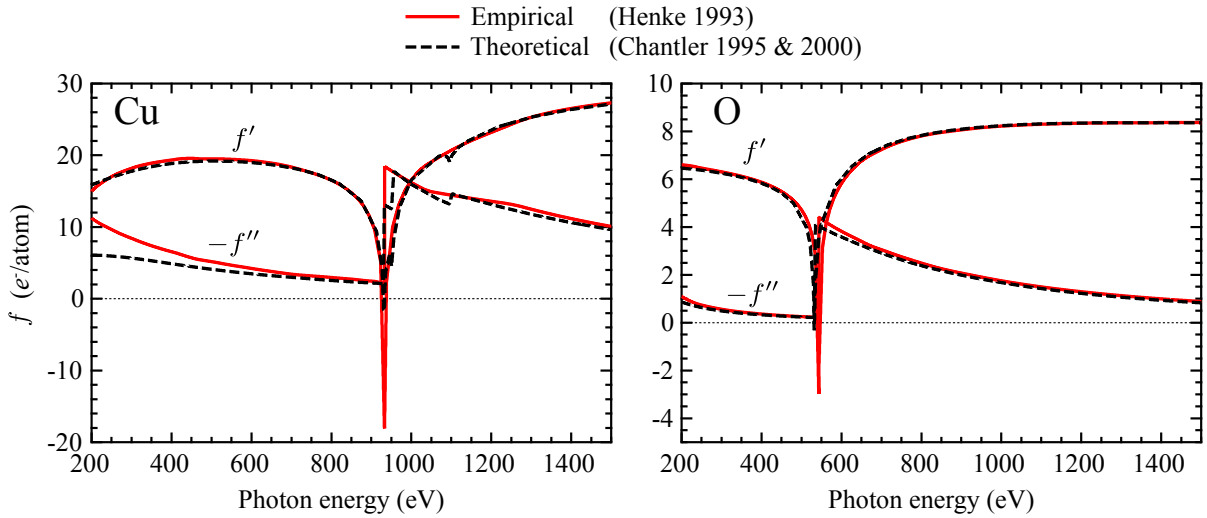

Figure 2.1 – The real and imaginary parts of the atomic scattering form factor for Cu (left) and O (right) tabulated for photon energies in the soft x-ray regime. The discontinuous jumps in f'' correspond to x-ray absorption edges. A finite-width pole (resonance) in f' occurs at the edges. Two sources are compared. The empirical data is interpolated from the available data in Ref. [161]. The theoretical data is from Ref. [158]

2.2.3.1 Kramers-Kronig dispersion relations

The Kramers-Kronig dispersion relations are

$$f'(E) = \frac{2}{\pi}\,\mathcal{P}\int_0^\infty \frac{E' f''(E)}{E'^2 - E^2}\mathrm{d}E' \tag{2.28}$$

$$f''(E) = -\frac{2E}{\pi}\,\mathcal{P}\int_0^\infty \frac{f'(E)}{E'^2 - E^2}\mathrm{d}E' \tag{2.29}$$

where the integral $\mathcal{P}\int$ denotes a Cauchy principal value integral. These are causal relations, strictly referring to the fact that a scattering event must first be preceded by an incident wave interacting with the scatterer.[165] The power of these relations is that it is generally possible to measure the x-ray absorption cross-section (eg., with an x-ray transmission experiment), and thus to empirically determine f'' as a function of energy. Given this, one can use Eq. 2.28 to determine $f'(E)$ and thus determine both f' and f'' from an x-ray absorption measurement. This is what was done in Ref. [161] to tabulate f'. Even in the case that a scattering tensor $\widehat{f}$ is needed, it is possible to measure the x-ray absorption with

the polarization vector aligned with the different crystal axes and build up the scattering tensor from these components (see Ref. [84] for an example of this done for YBCO).

As a slightly technical point, there are various integration schemes that can be found in the literature to deal with the principal value integral (see Refs. [161, 158] for two examples). These techniques are designed to succeed over a wide energy range by performing different integrations depending on whether the energy is near or far from an absorption edge. They are also coded in low level languages to ensure high speed. For the Kramers-Kronig transforms presented in Chapters 3 and 4, it was not crucial to reproduce these features, so I opted to implement the numerical integration in Mathematica. The key feature is that the numerical integral can simply be performed with a single (high level) function call of the form:

$$f'[E] := Z + \frac{2}{\pi}\text{NIntegrate}\left[\frac{E' f''[E']}{E'^2 - E^2}, \{E', 0, E, \infty\}, \text{Method} \to \left\{\text{“PrincipalValue”}, \right.\right.$$
$$\left.\text{Method} \to \left\{\text{“AdaptiveMonteCarlo”}, \text{“BisectionDithering”} \to 1/8\right\}\right\},$$
$$\left.\text{MaxRecursion} \to 200\right],$$

providing numerous options to control how NIntegrate is evaluated. Note that I have included the atomic number Z in this calculation to match the NIST definition for the real part of f, which includes the low-$\boldsymbol{Q}$ limit of f^{T} (given simply by Z)[6]. To test this method, I calculated f' from the tabulated values of f'' for a variety of elements and compared them to the tabulated f' values. A few such calculations for O, Cu, C, K, Ba, and Pb are presented in Fig. 2.2. I have made the precise implementation used to generate these calculations publicly available at Ref. [166]. As can be seen, this method provides a very good approximation of the tabulated f' values over the full energy range.

The residuals do highlight that this integration method has difficulty converging at the absorption edges (where f'' is discontinuous). However, in a realistic use-case that I am considering, the tabulated near-edge values of f'' would be replaced by high resolution x-ray absorption data, such that the edge-jumps would either be smooth or small compared to the x-ray absorption near-edge structure. Consequently, this numerical integration method is generally quite reliable for the use case it targets. It is also worth pointing out the same integration strategy was used for all cases in Fig. 2.2, but it is very likely that better results can be achieved on a case-by-case basis by optimizing the strategy.

[6]This is approximate, as for very high energy a relativistic correction is needed, and Z should be replaced by $Z^* \approx Z - (Z/82.5)^{2.37}$, relevant for high Z elements.[161]

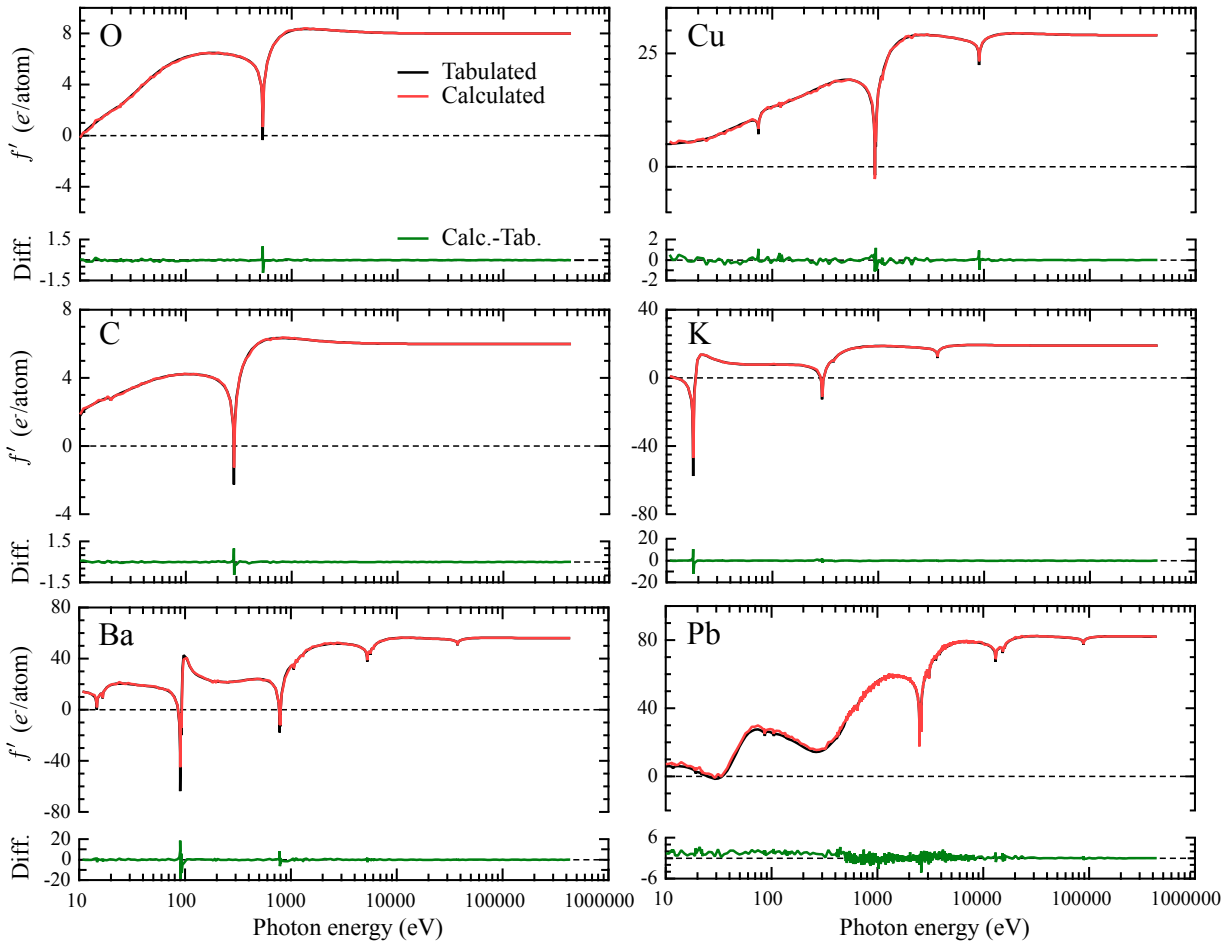

Figure 2.2 – The real part of $f = f' + if''$ for O, Cu, C, K, Ba, and Pb was calculated (red) and is compared to the tabulated values of f' (black) for free-atoms. Here, f' also includes the Thomson term f^{T}, which is approximately Z for low $\boldsymbol{Q}$. The numerical integration strategy used to evaluate the Kramers-Kronig transformation is described in the text. Minor convergence issues are noticeable at the edge-steps due to discontinuities in f'' there. The tabulated values of f' and f'' are from Refs. [158, 159], which are accessible online.[160]

While the existing methods and tabulated values are generally better and have been more thoroughly verified for free-atom calculations of f' than this approach, another important benefit of this method is that it is simple to build upon it to reliably calculate near-edge values of f' for non-free atoms with experimental x-ray absorption data as an

input. This is a tremendously useful tool for modelling resonant soft x-ray scattering, since the x-ray absorption cross-section is sensitive to the "true" electronic structure of a material and it is in many cases simple to measure at a synchrotron. In contrast, relying on a quantum mechanical formula akin to Eq. 2.17, requires the self-consistent determination of the ground state and all intermediate state wavefunctions that the core-electron can transition into, which for atoms in a crystal can quickly become a very complicated problem. This problem can be made tractable if one makes assumptions about the electronic structure and takes advantage of an existing software package to do the calculations (eg. CTM4XAS [167]). This is a great way to identify the origin of different features in x-ray absorption spectra. Yet, the calculations typically need to be validated against x-ray absorption data, so there is little benefit to using the calculations rather than XAS as an input to resonant scattering model calculations.

A general outline of how to use empirical x-ray absorption data along with the Kramers-Kronig numerical transformation method above is as follows (the calculations in Chapters 3 and 4 followed this procedure):

1. Convert XAS for element X in a multi-atom material to a form proportional to f''
   (a) Normalize XAS to $\sigma^{\text{abs}}_{\text{tot}} = \sigma^{\text{abs}}_{\text{X}} + \sigma^{\text{abs}}_{\text{other}}$ and then subact $\sigma^{\text{abs}}_{\text{other}}$, giving $\sigma^{\text{abs}}_{\text{X}}$
   (b) Calculate $\sigma^{\text{abs}}_{\text{X}} \times E \propto f'' = f''_{\text{data}}$
   (c) Normalize f''_{data} to the tabulated values f''_{tables}
2. Join f''_{data} and f''_{tables} together
3. Define a function f''_{interp} that linearly interpolates the values f''_{data} and f''_{tables}
4. Define f''_{interp} for energies outside the tabulated range as
   (a) $f''_{\text{interp}}(E < E_{\text{min}}) = f''(E_{\text{min}})$
   (b) $f''_{\text{interp}}(E > E_{\text{max}}) = f''(E_{\text{max}})(E/E_{\text{max}})^{-2}$
5. Evaluate Eq. 2.28 using f''_{interp} in the integrand.
   Modify NIntegrate strategy as needed.

With this approach, it is possible to fully determine the complex atomic scattering form factor for an element within a crystal structure that has a non-trivial electronic structure. Utilizing the polarization dependence of the x-ray absorption measurement, it is also possible to determine the individual elements of the more general scattering tensor to treat

scattering for a more complex system. Then, armed with some knowledge (or a reasonable guess) of how $\widehat{f}$ depends on site index j in Eq. 2.21, it is possible to calculate how the resonant scattering intensity should depend on photon energy, polarization and $\boldsymbol{Q}$. In this thesis, the photon energy dependence is studied for the cuprates $La_{1.475}Nd_{0.4}Sr_{0.125}CuO_4$ and $YBa_2Cu_3O_{6.75}$ in Chapters 3 and 4, respectively, and the polarization and $\boldsymbol{Q}$ dependence are evaluated for $La_{1.875}Ba_{0.125}CuO_4$ and $YBa_2Cu_3O_{6.67}$ in Chapter 5.

2.2.4 The polarization dependence in REXS

The polarization vectors are, in addition to the scattering tensor, an essential part of Eq. 2.21. They effectively provide sensitivity to the different elements of $\widehat{f}$. In Eq. 2.21, $\boldsymbol{\epsilon}$ and $\boldsymbol{\epsilon}'$ are labeled explicitly with an index μ (although it is often omitted for brevity), which denotes the mode. These modes can be represented by two basis vectors which are perpendicular to the wave propagation direction. The convention is to define the basis with two linear polarization vectors $\boldsymbol{\epsilon}_\sigma$ and $\boldsymbol{\epsilon}_\pi$, where $\boldsymbol{\epsilon}_\sigma$ is perpendicular to the scattering plane and $\boldsymbol{\epsilon}_\pi$ is parallel to it. One choice of basis that has its primary axes aligned with $\boldsymbol{Q}$, $\boldsymbol{k}+\boldsymbol{k}'$, and $\boldsymbol{k}\times\boldsymbol{k}'$ is depicted in Fig. 2.3.

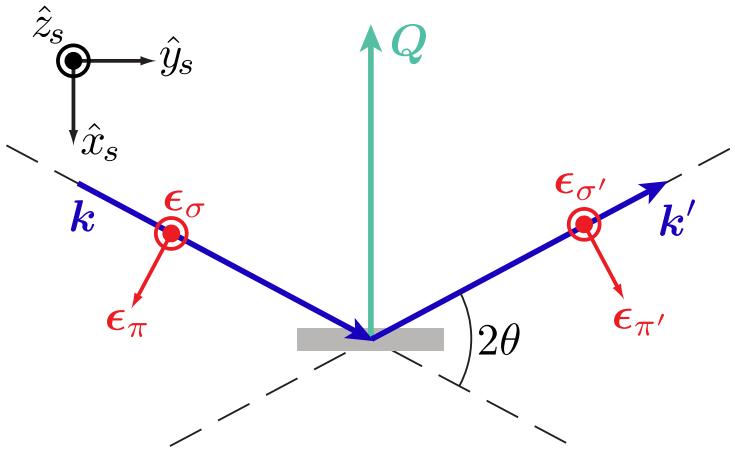

Figure 2.3 – Scattering geometry with reference frame chosen such that $\hat{x}_s \parallel (\boldsymbol{k}-\boldsymbol{k}')$, $\hat{y}_s \parallel (\boldsymbol{k}+\boldsymbol{k}')$, and $\hat{z}_s \parallel (\boldsymbol{k}\times\boldsymbol{k}')$. The angle between $\boldsymbol{k}$ and $\boldsymbol{k}'$ is defined as 2θ.

Formally, evaluation of Eq. 2.21 then requires summation over $\mu = \{\sigma, \pi\}$ and $\mu' = \{\sigma', \pi'\}$. There are four possibilities: $\sigma\sigma', \sigma\pi', \pi\sigma'$, and $\pi\pi'$. This can be represented as a

scattering matrix G (still at site j), given by

$$G_j = \begin{pmatrix} \boldsymbol{\epsilon}'^{*}_{\sigma'} \cdot \widehat{f}_j \cdot \boldsymbol{\epsilon}_{\sigma} & \boldsymbol{\epsilon}'^{*}_{\pi'} \cdot \widehat{f}_j \cdot \boldsymbol{\epsilon}_{\sigma} \\ \boldsymbol{\epsilon}'^{*}_{\sigma'} \cdot \widehat{f}_j \cdot \boldsymbol{\epsilon}_{\pi} & \boldsymbol{\epsilon}'^{*}_{\pi'} \cdot \widehat{f}_j \cdot \boldsymbol{\epsilon}_{\pi} \end{pmatrix}. \tag{2.30}$$

The scattering intensity is then $I \propto \left| \sum_{\mu,\mu'} \sum_j G_j e^{i\boldsymbol{Q}\cdot\boldsymbol{r_j}} \right|^2 = I_{\sigma\sigma'} + I_{\sigma\pi'} + I_{\pi\sigma'} + I_{\pi\pi'}$. Depending of the incident polarization and whether the polarization of the scattered rays can be discriminated, G can take on different forms. For example, if the incident light is σ or π polarized and an instrument is available to detect the outgoing light polarization, each scattering channel can be measured individually. More commonly (for soft x-ray beamlines), the incident polarization can be controlled but the outgoing polarization is unknown, leading to scattering that is either $I_{\sigma\sigma'} + I_{\sigma\pi'}$ or $I_{\pi\sigma'} + I_{\pi\pi'}$.

The case of Thomson scattering is particularly simple. For a spherically symmetric scatterer, we have $\widehat{f}_j \propto I_3$, ($I_3$ is the identity matrix). With polarization vectors defined as in Fig. 2.3

$$\boldsymbol{\epsilon}_{\sigma} = \begin{pmatrix} 0 \\ 0 \\ 1 \end{pmatrix} \quad \boldsymbol{\epsilon}_{\sigma'} = \begin{pmatrix} 0 \\ 0 \\ 1 \end{pmatrix} \tag{2.31}$$

$$\boldsymbol{\epsilon}_{\pi} = \begin{pmatrix} \cos\theta \\ -\sin\theta \\ 0 \end{pmatrix} \quad \boldsymbol{\epsilon}_{\pi'} = \begin{pmatrix} \cos\theta \\ \sin\theta \\ 0 \end{pmatrix}, \tag{2.32}$$

we find

$$G = \begin{pmatrix} 1 & 0 \\ 0 & \cos(2\theta) \end{pmatrix}, \tag{2.33}$$

by evaluation of Eq. 2.30. This reveals that only the $\sigma \to \sigma'$ and $\pi \to \pi'$ scattering channels are active for Thomson scattering. If the incident light is σ polarized, then $I^{\mathrm{T}}_{\sigma} = \left| f^{\mathrm{T}}(\boldsymbol{Q}) \right|^2$. For π polarization, we have $I^{\mathrm{T}}_{\pi} = \cos^2(2\theta) \left| f^{\mathrm{T}}(\boldsymbol{Q}) \right|^2$. For unpolarized incident light, the scattering intensity is the average $I^{\mathrm{T}}_{\mathrm{unpol.}} = (1/2)(1 + \cos^2(2\theta)) \left| f^{\mathrm{T}}(\boldsymbol{Q}) \right|^2$. This pre-factor is the well-known polarization factor for Thomson scattering. Notably, for unpolarized incident incident light, Thomson scattering produces polarized light.

For non-magnetic charge scattering, the scattering tensor $\widehat{f}_{\mathrm{charge}}$ (see Eq. 2.23) can be used, giving

$$G_{\mathrm{charge}} = \begin{pmatrix} f_{zz} & 0 \\ 0 & f_{xx}\cos^2(\theta) - f_{yy}\sin^2(\theta) \end{pmatrix}. \tag{2.34}$$

Similar to Thomson scattering, charge scattering only consists of $\sigma \rightarrow \sigma'$ and $\pi \rightarrow \pi'$ processes. This relation can be useful when comparing resonant scattering intensities for incident σ or π polarization, although generally one also needs to take the absorption of the incident and scattered photons into account, since for an anisotropic absorption/scattering tensor the absorption cross-section would differ for σ and π polarization.

2.3 Experimental methods

2.3.1 Beamline

The RSXS experiments presented in this thesis date back to early 2010,[7] and were all performed at the Canadian Light Source's REIXS (Resonant Elastic and Inelastic X-ray Scattering) 10ID-2 beamline using an in-vacuum four-circle diffractometer.[168] In synchrotron parlance, the REIXS beamline is referred to as 10ID-2, meaning that the insertion device (ID) is the second one installed on the 10^{th} straight section of the CLS's storage ring. The ID at REIXS is an elliptically polarizing undulator (EPU) with 43 poles having a 75 mm period and spanning 1.6 m. This EPU produces linearly polarized photons with energy $100 \rightarrow 3000$ eV or circularly polarized (left or right) photons with energy $100 \rightarrow 1000$ eV. For linear polarization, the angle of the polarization can be set arbitrarily.

The optical configuration of the REIXS beamline is shown schematically in Fig. 2.4. REIXS features a variable line spacing plane grating monochromator (VLS-PGM) with three gratings (Ni low energy, Au low energy, Au high energy) and four coatings (Ni, C, Si, Au) on the plane mirror. These can be chosen to optimize flux at photon energies spanning the full energy range of the beamline. A variable exit slit can be used to adjust energy resolution, giving maximal energy resolutions of 0.005 eV at 100 eV and 0.13 eV at 1000 eV. The size of the exit slit gap is typically set in the 10–50 μm range and is approximately proportional to flux. The beamline produces a flux of 5×10^{12} photons/s/0.1% bandwidth (for 100 mA ring current and 1000 eV). Since the incident flux I_0 depends on energy,

[7] Specifically, the data presented here was collected from February 2010 to January 2015, beginning shortly after the REIXS beamline and scattering endstation were put together. For context, the monochromator and EPU at REIXS were installed in November and December of 2007, respectively, and two years later the scattering chamber received its first light (June 2009) and the first spectrum was recorded (July 2009). The diffractometer was commissioned (characterization and testing) from August 2009 to April 2010 by many people, including myself. Some of this early work is presented in Chapter 3. The first access to general users was later made possible by letters of intent (specific proposals likely to succeed) in May 2010, followed soon thereafter by competitive proposals (January 2011).

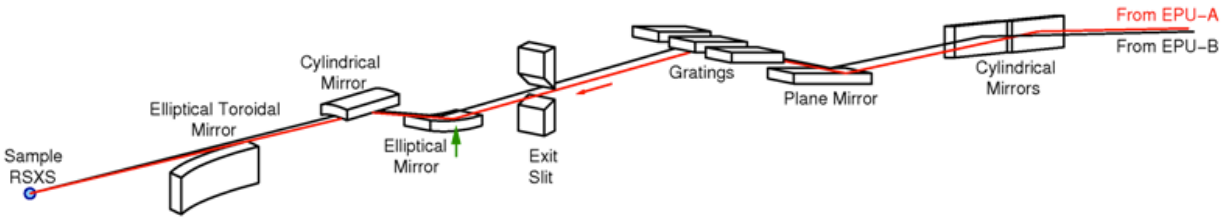

Figure 2.4 – Schematic of REIXS beamline showing novel x-ray optics configuration capable of sending spatially separated beams from two EPUs to the sample position simultaneously. Figure adapted from Ref. [169].

storage ring current and other beamline settings (grating, coating, exit slit gap, etc.), the electron yield from a high transmission Au mesh is used to record I_0 for normalization. The beam spot size at the sample position is width $\times$ height $\approx 250 \times 150$ μm. Note that in typical usage, light from only one of two EPUs is sent down the optical path for scattering, but that REIXS features an operating mode and optics capable of using the light from 10ID-1 (normally servicing the neighbouring soft x-ray spectromicroscopy beamline) and 10ID-2 simultaneously, such that two different light polarizations can be rapidly switched during a measurement.

The entire beamline is operated in ultra-high vacuum (UHV) conditions ($P < 10^{-9}$ Torr). This is firstly needed to ensure a long lifetime of the electron orbit in the storage ring, which the EPU is a part of. It is also quite important due to the use of soft x-rays, since even for modest pressures, the mean path length of soft x-rays can suffer dramatically.[8] Operating in UHV also reduces the amount of contaminants that can build up on optical elements of the beamline by limiting adsorption or potential condensation of gases such as water vapour onto these components. For samples that are heated and cooled in vacuum, this can also be quite important since certain measurements (e.g., electron yield or resonant reflectivity) can be sensitive to the topmost layers of the sample.

2.3.2 Diffractometer and detectors

The following discussion is an abbreviated summary of some of the essential aspects of the elastic scattering chamber and diffractometer design, which are covered thoroughly in Ref.

[8] See Section A.3 for a brief illustration of this point.

[168]. Some details here will differ due to modifications to the system that have occurred since Ref. [168] was published in July 2011.

The ∼1 m diameter stainless steel vacuum chamber pictured in Fig. 2.5 at the REIXS beamline houses an UHV 4-circle diffractometer (Fig. 2.6) consisting of a 2-circle goniometer mounted on a central θ ring and a detector arm mounted on a separate 2θ ring. The diffractometer is mounted on a separate subframe than the main scattering chamber and connected to it with flexible bellows, so that the diffractometer can be translated into the x-ray beam path independent of the main scattering chamber.

A load lock is used so samples can be transferred without venting the scattering chamber. The load lock has a garage for storage of up to 3 sample holders at a time. Sample holders are transferred into the scattering chamber using a magnetically coupled rack and pinion linear translator that uses a pincer mechanism to securely hold onto a small tab

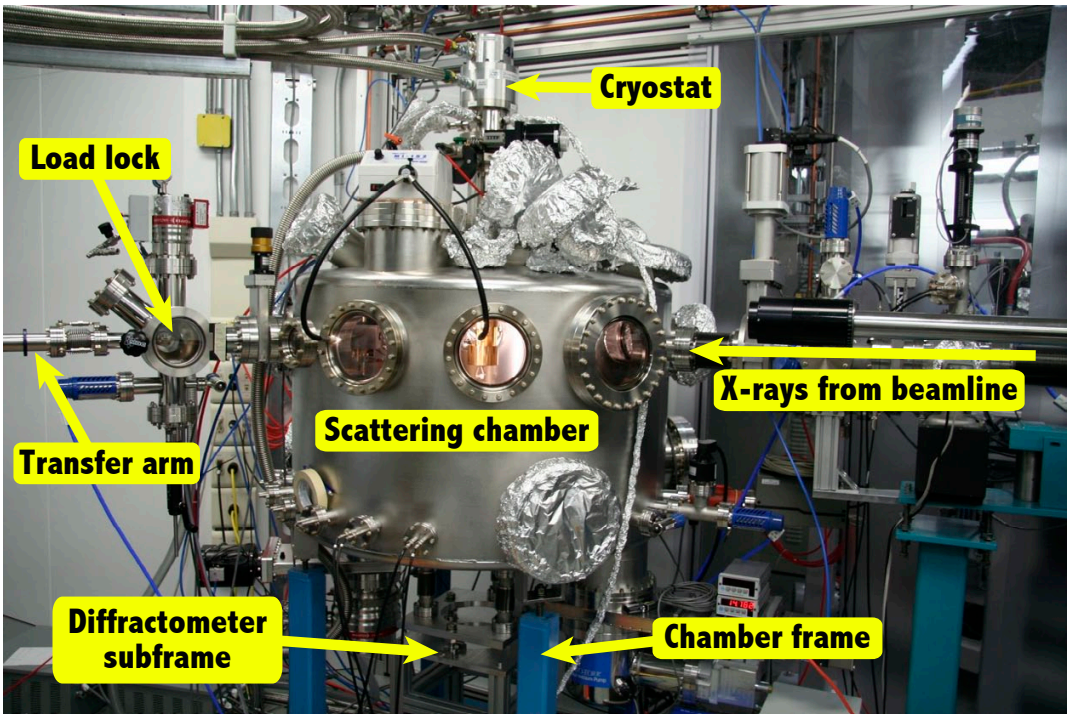

Figure 2.5 – The RSXS scattering chamber at the CLS's REIXS beamline. A polarized, monochromatic beam of soft x-rays from the beamline enter from the right and focus at the sample position, centred in the scattering chamber. A load lock is used to store samples and facilitate sample transfers. The closed-cycle cryostat is mounted on top of the scattering chamber.

on the sample holder. Gate valves are used to isolate the scattering chamber from the beamline and the load lock from the scattering chamber during sample transfers.

The load lock is pumped down with a 300 L/s Pfieffer turbopump and typically reaches 5×10^{-7} Torr in ~ 45 min or less, sufficiently low for transfers. The main chamber is pumped using a 700 L/s Pfieffer turbopump (backed by a triscroll roughing pump) and a CTI Cryotorr 8F cryopump. A closed-cycle cryostat is mounted on a differentially pumped rotatory feedthrough, located at the top of the chamber. The feedthrough is pumped in two stages by the triscroll pump and a 2 L/s ion pump. The pressure in the scattering chamber is usually better than 5×10^{-9} Torr. Pressure gauges include a cold cathode gauge, a hot filament ion gauge and a residual gas analyzer, for low pressure measurements, as well as thermocouple and convectron gauges for intermediate and high pressures, respectively.

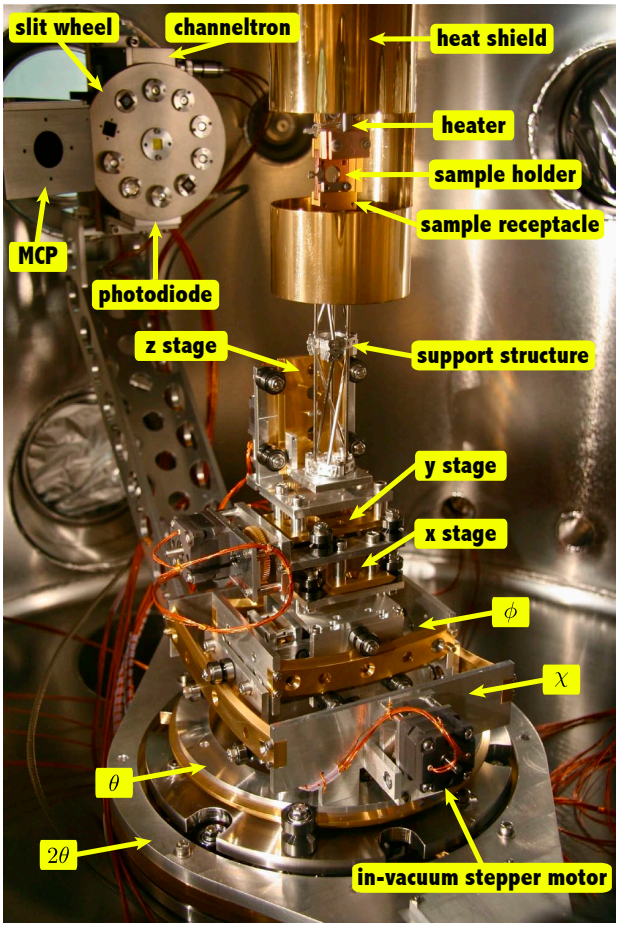

Figure 2.6 – The in-vacuum four-circle diffractometer at the CLS's REIXS beamline.

Sample translations up to ± 7.5 mm are accomplished with stacked x, y and z linear translation stages mounted on the goniometer. The θ and 2θ motions, originally supported motion ranges of $-25°$ to $+265°$, but due to instrument modifications and practical considerations, ranges of $-60°$ to $165°$ for θ and $-25°$ to $172°$ for 2θ are currently imposed. The ϕ and χ motions have (approximate) ranges of $\pm 7°$. These motions are primarily used to correct sample alignment but can also be used to expand the range of accessible $\boldsymbol{Q}$.

Cooling is achieved by connecting the cryostat's cold head to the sample receptacle with flexible copper braids (not seen in Fig. 2.6 since the braids are inside the heat shield). These braids damp vibrations from the cryostat and also reduce torsional forces if the cryostat

is stationary while θ is rotated (the cryostat can also be rotated to match θ rotations, keeping constant torsion on the support frame). Moreover, because the cooling elements are decoupled from the sample receptacle, their thermal expansion or contraction do not affect the sample position.

The sample receptacle is attached to a support structure, built with thin-walled stainless steel tubing, and mounted atop the translation stages of the goniometer. The support structure design minimizes thermal conduction between the sample holder (and receptacle) and the rest of the goniometer, reducing the heat load on the cryostat. It also limits thermal expansion of the support structure as the sample temperature is varied. For example, raising the temperature from 20 K to 298 K, thermal expansion accounts for just ~ 180 μm of sample displacement along the z-axis, as shown in Fig. 2.7.

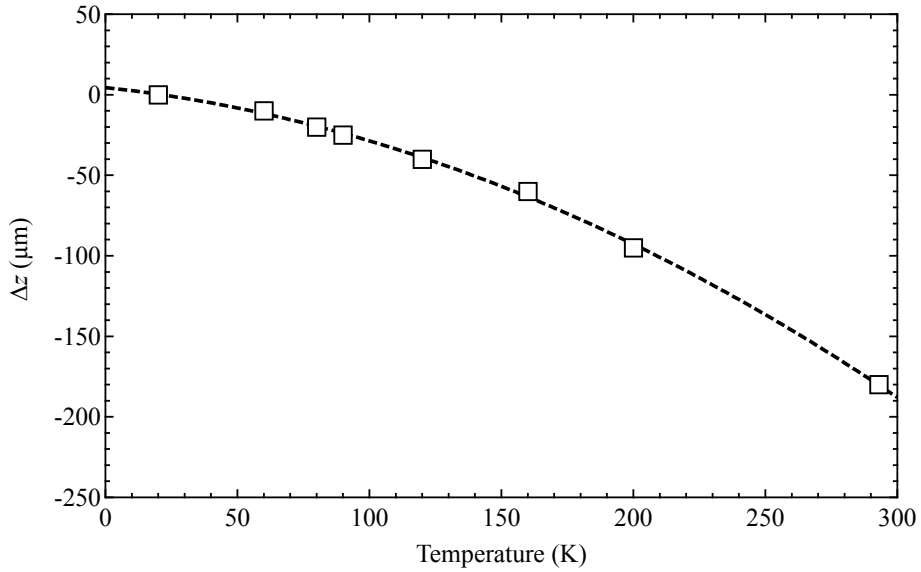

Figure 2.7 – The relative displacement $\Delta z = z(T) - z(20\text{ K})$ due to thermal expansion of the support structure, sample holder, and sample receptacle. The negative sign indicates that the z stage must be lowered to centre as temperature is increased. The dashed line is a polynomial fit providing a reasonable interpolation scheme for this temperature range.

With the configuration pictured in Fig. 2.6, a base temperature at the sample position of 18 K was possible during the 2009 to October 2013 timeframe. At the end of 2013 (October to November) a magnet assembly was installed on the sample receptacle, increasing the thermal load and raising the base temperature to ∼23 K. This base temperature may

be improved in the future with planned revisions to the heatshield design. Heating is accomplished with a 100 W Lakeshore HTR-25-1000 cartridge heater, which is thermally connected to the sample receptacle just above the sample holder position. A sapphire plate and ceramic hat washers are used to electrically isolate the heater from the sample holder assembly. The heater is sufficiently powerful to raise the sample temperature to 400 K with the cryostat in operation.

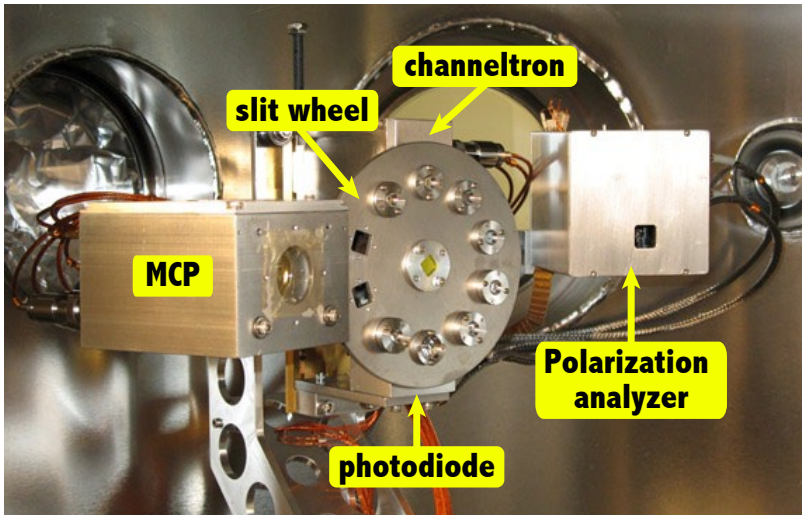

Figure 2.8 – Detector assembly in the RSXS scattering chamber

Four detectors are currently installed on the detector arm (Fig. 2.8): a micro-channel plate (MCP), a photodiode (PD), a channeltron (ChT) and a polarization analyzer. These are located at a radius of ∼29 cm from the sample position and are mounted to a structure that can be raised or lowered by 40 mm to place any of the detectors in the scattering plane. The MCP has a 25 mm diameter and provides 2D sensitive single-photon detection capability. A negatively charged grid is placed in front the MCP to capture positively charged ions (from ion gauges or possibly ejected from the sample). The front surface is also negatively biased to repel electrons from the surface. The ChT is a 10×10 mm detector that provides single photon sensitivity similar to the MCP but without 2D sensitivity. It has a similar biasing scheme as the MCP. The PD has a 10×10 mm active area, is sensitive to a very wide range of photon energies with a linear response for photon energies up to 5 keV and a high dynamic range (currents can range from 10^{-12} to 10^{-5} A, suitable for the high flux of the direct beam or an x-ray fluorescence measurement). A slit wheel allows the the selection of different slits (with width × height of 10×10 mm, 1×2 mm, 0.5×3

mm, 0.1×3 mm, or 0.1×1 mm) and thin Al or SiN filters to be placed in front of either the ChT or PD. The different slits give control over detector resolution and the filters can be used to block charged ions or reduce the detection of background fluorescence.

The polarization analyzer uses two PDs and a selection of 4 multilayers suited for different x-ray absorption edges (O K: 530 eV, Mn L: 645 eV, Ni L: 860 eV, and Cu L: 940 eV), which can be switched using two Attocube rotary actuators, to reflect the vertical and horizontal polarization components of the scattered light into one of the two PDs. This design is not well suited to studying weak scattering signatures (as seen in this thesis), since the intensity losses due to this multilayer reflectivity are extreme (97% for O K and 99.85% for Cu L), but it can be useful in reflectivity experiments, where at small angles the flux of scattered light can be very high.

2.3.3 Sample preparation

For successful RSXS experiments, it is essential to prepare samples with good surface quality and with an orientation that provides access to a chosen zone in reciprocal space. This is because, unlike hard x-ray scattering, the range of $\boldsymbol{Q}$ is very restricted and RSXS can be sensitive to surface effects. I will first discuss crystal orientation by Laue diffraction and then discuss crystal cleaving and polishing methods. Also, I will briefly describe the methods used to mount samples for RSXS measurements.

In many cases, the crystallographic orientation of as-grown crystals is not known. It is possible to determine the orientation with Laue diffraction. A typical configuration for Laue diffraction uses an x-ray tube with a tungsten target in order to produce a broad spectrum of x-rays. This broad spectrum of light can then readily satisfy Bragg's law (or the Laue condition) simultaneously for many crystal planes with different d_{hkl} and lead to a series of spots that can be recorded by photographic film. Laue diffraction can be measured in transmission (x-rays pass through a sample) or backscattering (x-rays are diffracted back towards x-ray tube) geometry. For the thick crystals studied in this thesis, backscattering geometry was more suitable. The backscattering geometry is depicted in Fig. 2.9.

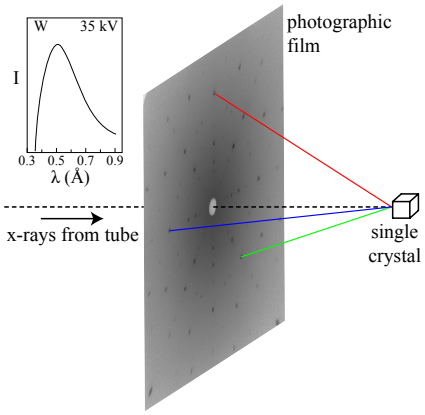

Figure 2.9 – Laue backscattering geometry for single crystal orientation.

A practical application is illustrated in Fig. 2.10. Here, Laue backscattering was used to orient an $La_{1.475}Nd_{0.4}Sr_{0.125}CuO_4$ (LNSCO) crystal boule with unknown orientation. First, a measurement on a cut surface was taken (left panels, Fig. 2.10). The orientation was solved using OrientExpress by indexing high symmetry points shown in the lower left panel of Fig. 2.10.[170] Angular corrections were calculated to orient the boule with the $a(b)$ axis perpendicular to the page and with c horizontal. A goniometer (see Fig. 2.11) was used to make these rotations and a subsequent Laue image (right panels, Fig. 2.10) confirmed the re-orientation.

The boule and goniometer were then transferred to a wire saw so that a cut could be made along the ab plane. The sample was then mounted on this flat surface so that subsequent cuts would produce tall samples with the c axis along the long side and a or b

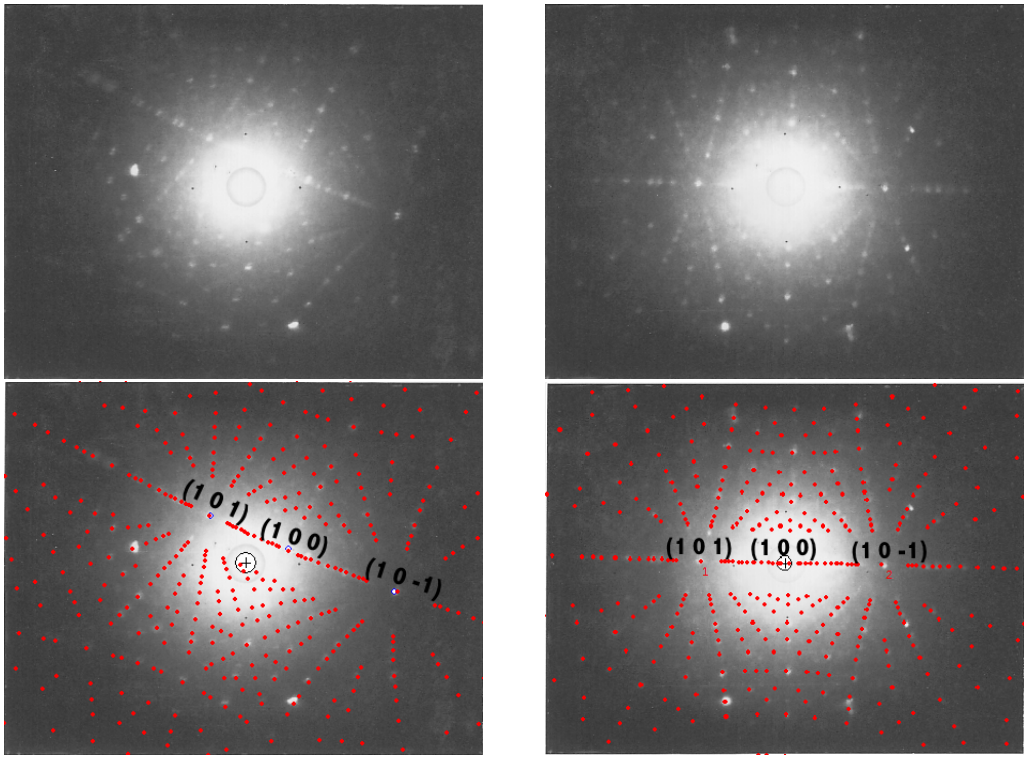

Figure 2.10 – Laue backscattering images taken on a cut surface of an LNSCO boule before (left) and after (right) orienting. The top row shows the Laue image as captured and the bottom row shows a superimposed Laue simulation obtained using OrientExpress.[170] (Simulation parameters: film to crystal distance: 35 mm, scattering geometry: 180°, space group: I4/mmm, lattice constants: $a=b=3.787$ Å, $c=13.24$ Å)

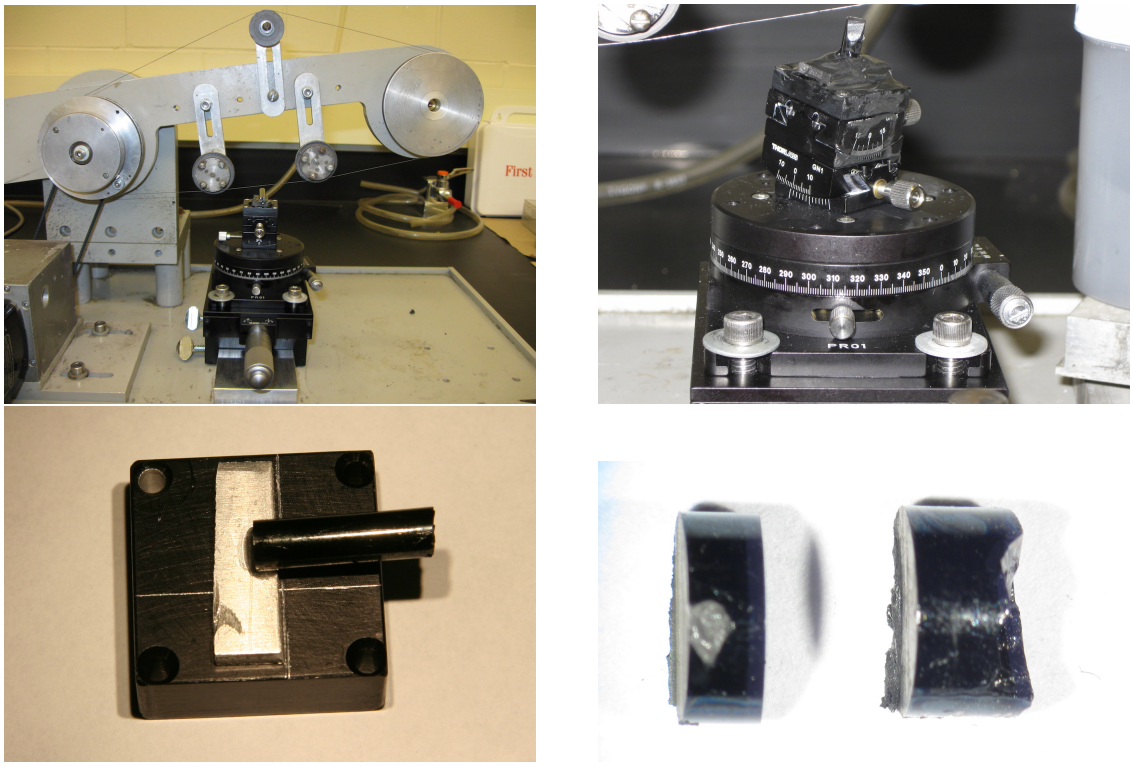

Figure 2.11 – A crystal boule of LNSCO was cut on a wire saw, first to expose a surface for Laue diffraction (top left), and then along a crystallographic plane (top right), for subsequent mounting (bottom left) and additional cuts (bottom right). The samples shown in the bottom right have the c axis out of the page and $a(b)$ along their width and length.

horizontal. The different cutting stages are illustrated in Fig. 2.11. These smaller pieces were then cut parallel to the flat edge,[9] and finally once more along the horizontal of this page, producing 4 tall samples with approximately square bases and dimensions in the range of $\sim 1.5 \times 1.5 \times 3$ mm to $\sim 2 \times 2 \times 3$ mm.

After orienting a crystal, the next important consideration is the condition of the surface. The wire saw achieves its cutting action by dragging a grit of boron carbide across the sample, producing a rough and highly textured surface, as shown in Fig. 2.12 (a), not

[9]The flat edge enables further Laue measurements to establish the *final* orientation of the crystal, as-mounted and ready for scattering. This is important, since small errors compound and it is rare to have a perfectly oriented crystal. Knowing approximately where to look in angle-space with the soft x-ray diffractometer can save a lot of time.

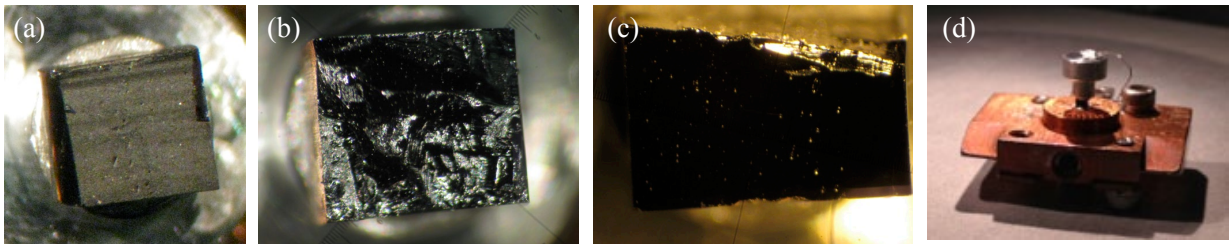

Figure 2.12 – (a)-(c) A sample of LNSCO with different surface conditions. (a) The rough surface results from cutting on the wire saw. (b) The shiny, bumpy surface results from fracturing in vacuum. (c) The flat, smooth, and shiny surface results from polishing (a piece broke off, giving it a trapezoidal shape). (d) An $La_{1.875}Ba_{0.125}CuO_4$ sample prepared for cleaving with a top post.

suitable for RSXS or XAS (due to surface damage and contamination). The load lock of the scattering chamber is equipped with a blade and anvil sample cleaver, which in this case was used to apply pressure to the sides of the sample and cause it to fracture in vacuum, producing a fresh surface [Fig. 2.12 (b)] for XAS and RSXS measurements.[10] It is also possible to cleave or fracture a sample by attaching a post at the top of the sample [Fig. 2.12 (d)]. An impact is then delivered to the top post and if the crystal is weaker than its bonds to the sample plate and top post, a fresh surface will be exposed. Besides cleaving, one can also polish a crystal to produce a smooth, flat surface [Fig. 2.12 (c)].

Polishing was performed in stages usually beginning with a 10 μm boron carbide powder, suspended in mineral oil, to obtain the primary grinding action. Water-based suspensions were avoided since cuprates are a bit hydroscopic. Using progressively finer powders (eg. "jeweler's rouge", $\sim$0.5 to 1.5 μm), the surface could be smoothed down gradually. The finishing stages used 0.3 and 0.05 μm lapping films. Given the delicate nature of the samples, this was all done by hand using a custom-built polishing assembly. The polishing direction could be aligned with a high-strength axis of the crystal to minimize the likelihood of fracturing. Despite this, parts of the samples did frequently fracture or break off (usually near the edges). A comparison of the surface conditions of two $YBa_2Cu_3O_{6+x}$ samples before and after polishing is shown in Fig. 2.13. The polished surfaces appeared smooth and mostly featureless at a magnification of 45$\times$ (noted by eye, not pictured here).

For detecting charge density wave order by RSXS in La-based cuprates, cleaving samples has typically been a necessary step. Cleaving in vacuum or in air are both viable approaches, with the former having the benefit of giving more reliable electron yield at the

[10] The pictured sample is oriented with its weak plane not aligned with the sample cleaver, so the surface results formally from a fracture, not a cleave. The terms are often used interchangeably.

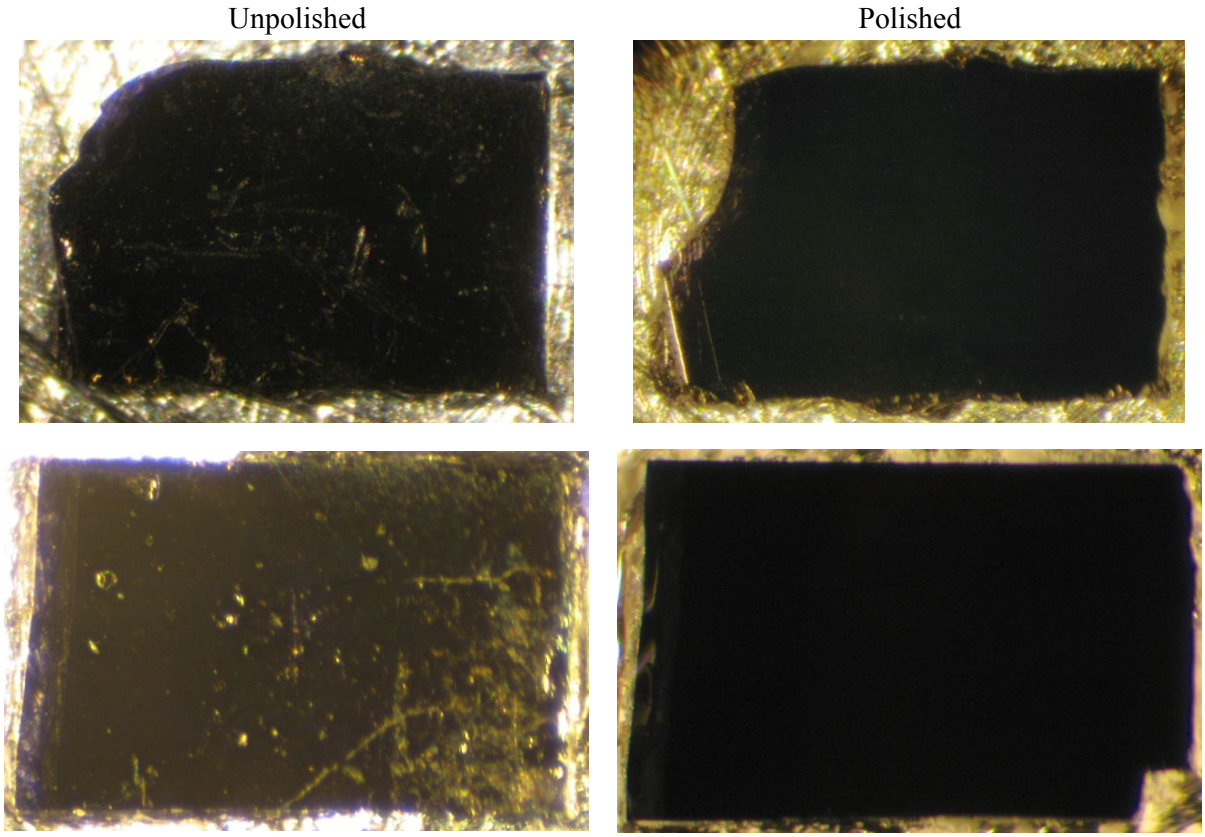

Figure 2.13 – Polishing $YBa_2Cu_3O_{6+x}$ samples. Left: unpolished samples. Right: after polishing. Polishing was performed in stages, as described in the text. The top row is a sample of $YBa_2Cu_3O_{6.335}$ and the bottom row is a sample of o-III ordered $YBa_2Cu_3O_{6.75}$. The polishing procedure succeeded in removing the surface imperfections. Although the polishing procedure was gentle, parts of both samples can be seen to have broken off.

expense of being a more difficult procedure. I have also had success detecting CDW order from a polished LNSCO surface. For $YBa_2Cu_3O_{6+x}$, polishing was useful for eliminating surface imperfections, but not essential for detecting the charge density wave order.

It is also important to have good electrical and thermal conductivity with the sample holder. Electrical contact can be made using silver epoxy (EPO-TEK H21D), high purity silver paint (SPI #5001-AB), silver paste (SPI #5063-AB) or carbon tape (SPI #05081-AB). For low temperatures or experiments with significant temperature cycling, the silver epoxy and paint are better choices, since they retain their strength and provide excellent

thermal and electrical conductivity. Silver epoxy forms a much stronger and more permanent bond than silver paint, making it suitable when samples are to be cleaved. Silver epoxy can be excessive for many applications, since removing it typically requires scraping with a scalpel and hours of sonication in acetone. In contrast, silver paint can be removed with a few minutes of sonication in acetone. For room temperature measurements, silver paste and carbon tape are good choices. Silver paste dissolves in acetone, with little need for sonication. Samples mounted on carbon tape can usually be removed simply with tweezers. Occasionally, carbon tape residue is left on the sample. The residue can be wiped off or dissolved in acetone.

Chapter 3

Spatially Modulated Orbital Energies in Cuprate Superconductors

This chapter has been adapted from Ref. [1].

3.1 Overview

A prevailing description of the stripe phase in underdoped cuprate superconductors is that the charge carriers (holes) phase segregate on a microscopic scale into hole rich and hole poor regions. Here, resonant elastic x-ray scattering measurements of stripe-ordered $La_{1.475}Nd_{0.4}Sr_{0.125}CuO_4$ at the Cu L and O K absorption edges are shown to identify an additional feature of stripe order. Analysis of the energy dependence of the scattering intensity reveals that the dominant signature of the stripe order is a spatial modulation in the energies of Cu $2p \rightarrow 3d$ and O $1s \rightarrow 2p$ resonant transitions rather than the large modulation of the charge density (valence) envisioned in the common stripe paradigm.

3.2 Introduction

Static stripe order in cuprates was first theoretically predicted by mean-field Hubbard model calculations [171, 172, 173, 174] and subsequently observed in lanthanum-based cuprates by neutron and x-ray diffraction[25, 85, 92, 94, 175, 95, 96]. Although still a matter of debate, more recent work has indicated that stripe-like density wave order is generic to the cuprates [82, 176, 177, 178, 179, 32] and plays a significant role in competing with or possibly causing superconductivity [59].

Microscopically, stripes in the cuprates have been widely described as rivers of charge—hole-rich antiphase domain walls that separate undoped antiferromagnetic regions. However, alternate models with different underlying physics, such as the valence bond solid (VBS), have also been proposed to explain stripe order [180, 19, 181]. VBS models involve singlet formation between neighbouring spins and, in contrast to other models of stripe order, may occur with a small modulation of the charge density [19].

Distinguishing which of these models is most relevant to stripe order in the cuprates is challenging since the models share many symmetries and experimental signatures. In particular, direct evidence for charge-density modulations, which may distinguish various models, has been elusive. Neutron and conventional x-ray scattering are only sensitive to lattice displacements. It is therefore only inferred indirectly that these lattice displacements are induced by modulations in charge density (valence). Resonant soft x-ray scattering (RSXS) offers a means to couple more directly to modulations in the electronic structure, including charge density modulations. By performing an x-ray diffraction measurement on resonance (at an x-ray absorption edge), the atomic scattering form factor $f(\omega)$ is enhanced and made sensitive to the valence, orbital orientation and spin state of specific elements. A key feature of RSXS is that the energy dependence of the scattering intensity through an absorption edge differs for lattice distortions, charge-density modulations or other forms of electronic ordering, providing a means to distinguish these different types of order.

In the cuprates, RSXS of the $(2\varepsilon, 0, L)$ charge density wave (CDW) superlattice peak has been measured in stripe-ordered $La_{2-x}Ba_xCuO_4$ (LBCO) [95], $La_{2-x-y}Eu_ySr_xCuO_4$ (LESCO)[96, 182] and $La_{1.475}Nd_{0.4}Sr_{0.125}CuO_4$ (LNSCO) [183] at the O K $(1s \rightarrow 2p)$ and Cu L $(2p \rightarrow 3d)$ absorption edges, which provide sensitivity to the O $2p$ and Cu $3d$ orbitals that are central to the physics of the cuprates. These measurements have been interpreted as direct evidence for a large valence modulation on the O sites [95]. Moreover, it is argued that a modulation of the valence occurs primarily on the O sites and not on the Cu sites, which are instead subject to lattice distortions induced by the valence modulation on the O sites [95, 96]. However, efforts to model the energy dependence of the scattering intensity

based on this picture are not truly reconciled with experiment, leaving this interpretation open to question [96].

In this chapter, the energy dependence of the resonant scattering at the O K and Cu L edges of LNSCO are presented. This energy dependence is modelled using x-ray absorption measurements to determine $f(\omega)$ at different sites in the lattice, a procedure that has proven effective in describing the scattering intensity of valence modulations in the chain layer of ortho-II $YBa_2Cu_3O_{6+\delta}$ (YBCO) [84]. Contrary to previous analysis of LESCO [96] and LBCO [95], it is shown that the resonant scattering intensity is best described by small energy shifts in the O $1s \rightarrow 2p$ and Cu $2s \rightarrow 3d$ transitions at different Cu and O sites rather than a valence modulation of O and a lattice displacement of Cu.

3.3 Results

3.3.1 Measurement

The measured intensity for scans through $\mathbf{Q} = (H,\ 0,\ 1.5)$ with the photon energy at the peak of the Cu L_3 absorption edge (931.3 eV) are presented in Fig. 3.1(b) (methods are described in section 3.5.1). Below the stripe-ordering transition temperature of ∼70 K, a clear superlattice peak is observed at $\mathbf{Q} = (2\varepsilon, 0, L) = (0.236, 0, 1.5)$. Above the stripe-ordering transition temperature, a large, smoothly varying fluorescence background is observed. To determine the photon energy dependence of the scattering intensity, H scans through the superlattice peak were performed at 22 K as a function of photon energy at $L = 1.5$ for Cu and $L = 0.2$ for O. The fluorescence background is fit and subtracted from each scan. The integrated intensity of the superlattice peak is then determined as a function of photon energy for the O K and Cu L edges [Fig. 3.1(c) and Fig. 3.1(d)]. The resulting spectra are qualitatively similar to previous measurements on LBCO [95] and LESCO [96]. Importantly, our measurements extend the previous Cu L edge measurements to include the L_2 edge, which proves valuable in distinguishing models for the stripe phase. An important feature of our measurement is that all scattering measurements are performed with the incident x-ray polarization along the b_o axis of the sample. As a result, the scattering intensity will be sensitive to only the O p_y and not the O p_x orbitals. Assuming doped holes go only into σ-bonded orbitals of O, this measurement geometry is only sensitive to half of the oxygen atoms; the site-centred and not the bond-centred oxygen. This fact simplifies the expression for the structure factor.

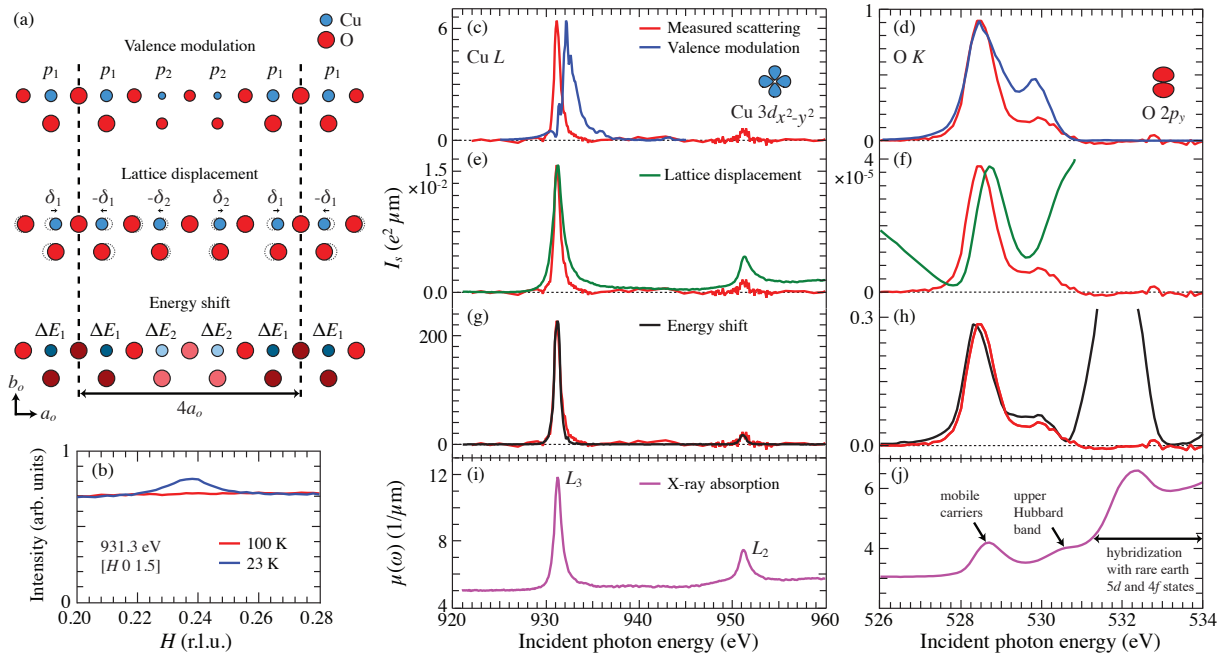

Figure 3.1 – Resonant scattering of 1/8 doped LNSCO at the Cu L and O K edges. (a) Schematic representations of bond-centred stripe ordering for the three models proposed to describe the resonant scattering energy dependence. (b) H scan through the CDW superlattice peak at (H, 0, 1.5) and at the peak of the Cu L_3 absorption edge [84]. (c)—(h) Scattering intensity as a function of photon energy through the Cu $L_{3,2}$ and O K absorption edges. The measured intensity (red line) is compared to the scattering intensity of valence modulation (blue line), lattice displacement (green line) and energy shift (black line) models of the stripe-ordering. The best agreement with experiment is for the energy shift model. (i) and (j) X-ray absorption $\mu(\omega)$ at the Cu $L_{3,2}$ (i) and O K (j) absorption edges measured using total electron yield.

3.3.2 Model calculations

The measured energy dependence of the scattering intensity is compared to three model calculations [see Fig. 3.1(a)]: 1. valence modulation, a spatial modulation in the valence of the Cu and O; 2. lattice displacement, a small displacement of the Cu and O atoms from their equilibrium positions outside the stripe-ordered phase; and 3. energy shift, a spatial modulation in the energy of the Cu $3d$ and O $2p$ states. The first two models essentially follow previous analysis of RSXS in LBCO and LESCO [95, 96].

The three models differ in the structure factor (described in section 3.5.2) and the energy dependence of the atomic scattering form factor $f(\omega)$. These two factors give

rise to a different energy dependence to the scattering intensity, $I_s(\omega)$. For the valence modulation model, $I_s(\omega) \propto |f(\omega, p_2) - f(\omega, p_1)|^2/\mu(\omega)$, where p_1 and p_2 are the local hole concentrations (valence) at different sites [see Fig. 3.1(a)] and $\mu(\omega)$ is the absorption coefficient. For the lattice displacement model, $f(\omega)$ is the same at each site for a given element and $I_s(\omega) \propto |f(\omega)|^2/\mu(\omega)$. Finally, for the energy shift model, $I_s(\omega) \propto |f(\hbar\omega + \Delta E) - f(\hbar\omega - \Delta E)|^2/\mu(\omega)$, similar to the valence modulation model but with an energy shift $\pm\Delta E$ at different sites instead of a modulation in valence. In all three models, the site specific $f(\omega, p_{1,2}, \Delta E)$ are determined from x-ray absorption measurements.

3.3.2.1 Valence modulation model

For the valence modulation model, x-ray absorption spectroscopy (XAS) on samples with different doping levels from Ref. [105] are used to determine $f(\omega, p_{1,2})$. This procedure found very good agreement between experiment and calculations for a modulation of the Cu valence in the chain layer of oxygen-ordered YBCO [84]. In lanthanum based cuprates, the key features of the O K edge XAS are two preedge peaks at 528.6 eV and 530.5 eV that are due to hybridization between Cu $3d$ and O $2p$ states and have been assigned to the mobile doped holes and the upper Hubbard band respectively [Fig. 3.1(j)] [104, 105, 184]. The intensities of these two peaks evolve strongly with doping, whereas the spectra at higher energy are doping independent and dominated by O $2p$ states hybridized with rare earth $5d$ and $4f$ states [185]. As argued in Ref. [96], the scattering intensity for a valence modulation of arbitrary magnitude can be modeled using XAS measured at two different dopings. Here $f_j(\omega)$ [Fig. 3.2(b)] and the scattering intensity expected for a valence modulation [Fig. 3.1(d)] is calculated from XAS in $La_{2-x}Sr_xCuO_4$ (LSCO) at $x = 0.07$ and 0.15 from Ref. [105], corresponding to a hole modulation of $\delta p = p_1 - p_2 = 0.08$. Although this calculation successfully produces two peaks at approximately the correct energies, it strongly overestimates the intensity of the peak at 529.9 eV [96]. A different choice of doping values to determine $f(\omega, p_{1,2})$ impacts the magnitude of the scattering, scaling it roughly as δp^2, and produces differences in the line shape (see Fig. 3.4). However, calculations using existing XAS data are all similarly inconsistent with the measured RSXS line shape.

A similar analysis, again using XAS from Ref. [105] to determine $f(\omega, p)$ [Fig. 3.2(a)], can be applied to the Cu L edge. The XAS for the Cu L edge exhibits two primary peaks at 931.3 eV and 951.3 eV corresponding to the L_3 and L_2 edges that are split by the spin-orbit coupling of the $2p$ core electrons. Focusing on the L_3 edge, the XAS is comprised of a peak (931.3 eV) and a shoulder (932.3 eV) that are associated with d^9 (a single hole in the $d_{x^2-y^2}$ orbital) and $d^9\underline{L}$ (doped holes that are primarily on the oxygen ligands)

ground states. Consistent with this assignment, the high energy shoulder evolves much more strongly with doping than the d^9 peak [105]. It follows that the predicted scattering intensity for a valence modulation of the Cu is peaked at the shoulder and not the peak of the XAS [Fig. 3.1(c)]. As discussed in Refs. [95, 96], this is in poor agreement with the energy dependence of the resonant scattering, which is peaked at the maximum of the XAS.

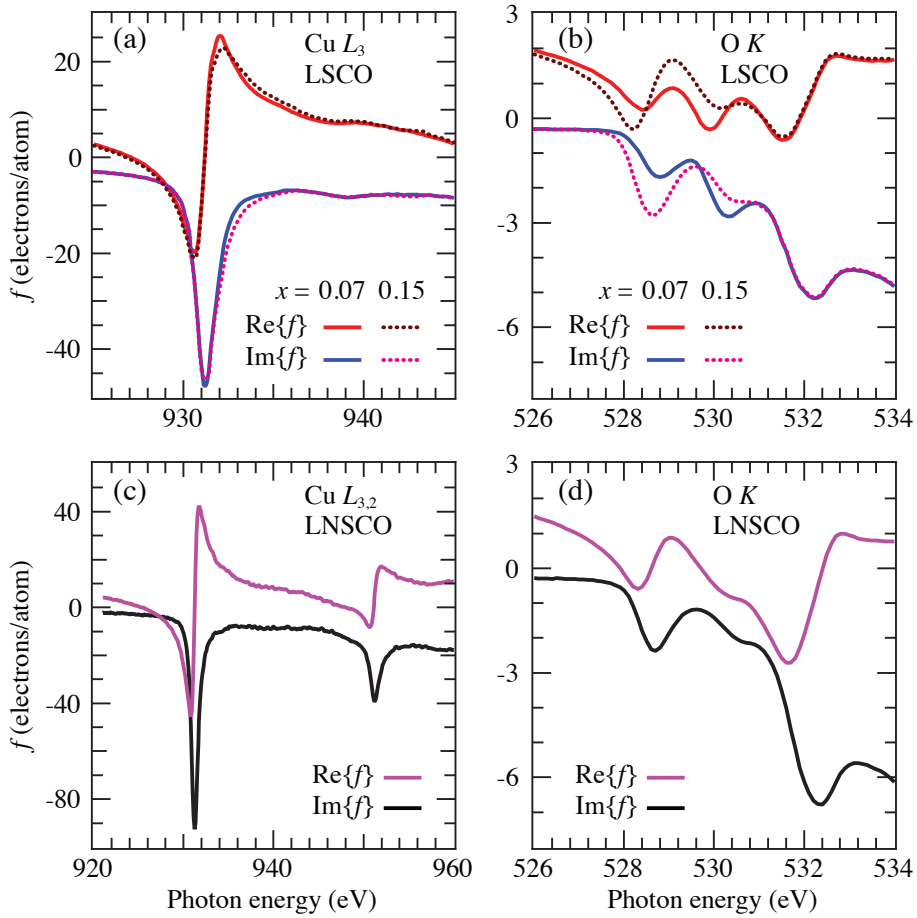

Figure 3.2 – The atomic scattering form factors $f(\omega)$ as a function of photon energy through the Cu L and O K absorption edges for (a), (b) $La_{2-x}Sr_xCuO_4$ ($x = 0.07$ and 0.15) and (c), (d) $La_{1.475}Nd_{0.4}Sr_{0.125}CuO_4$. $f(\omega)$ for LSCO is determined using XAS measurements from Ref. [105].

3.3.2.2 Lattice displacement model

Calculations based on the lattice displacement model [Fig. 3.1(e) and Fig. 3.1(f)] are also in poor agreement with experiment [here using XAS on our sample of LNSCO in Fig. 3.1(i) and Fig. 3.1(j) to determine $f(\omega)$ in Fig. 3.2(c) and Fig. 3.2(d)]. The lattice displacement model at the O K edge predicts large scattering intensity above and below the absorption edge that is not observed in experiment and, at the Cu L edge, scattering intensity that is broader in energy and has a smaller ratio of the L_3 to L_2 peaks than the measurement. The calculated magnitude of the scattering intensity assumes a 0.004 Å lattice displacement, as deduced from neutron scattering [85].

3.3.2.3 Energy shift model

Like the lattice displacement model, XAS on our sample of LNSCO [Fig. 3.1(i) and Fig. 3.1(j)] is used to determine $f(\omega)$ [Fig. 3.2(c) and Fig. 3.2(d)] for the energy shift model. For the two sites (1 and 2), $f(\omega)$ is shifted in energy by $\Delta E = \pm 0.1$ eV for both the O K and Cu L edges. In contrast to the lattice displacement and valence modulation models, the energy shift model is in very good agreement with experiment. At the Cu L edge, it captures the correct intensity ratio of the Cu L_3 and L_2 peaks, the correct width in energy of the scattering and the correct energy position of the maximum of the scattering intensity. Similarly, at the O K edge, the energy shift model reproduces the energy dependence of the preedge peak. It does not agree with the spectra at higher energy, predicting a large peak at 531.5 eV that is not observed. However, this apparent discrepancy can be reconciled if we interpret this as evidence that only the low energy states involving hybridization between the O $2p$ and Cu $3d$ states (and not the rare earth $5d$ and $4f$ states) are subject to these energy shifts. We also note that the choice of ΔE impacts the magnitude, which scales as ΔE^2, but not the energy dependence of the calculated scattering intensity, provided ΔE is less than the energy width of the XAS ($\sim$0.2 eV). As such, ΔE is neither determined in our analysis, nor should it be viewed as a fitting parameter.

3.4 Discussion

Our interpretation of the energy shifts is that they are induced by subtle spatial modulations of the local electronic structure. The energy levels of the unoccupied Cu $3d$ and O $2p$ states can be described by parameters such as the Cu onsite Coulomb repulsion (U_{dd}), the crystal field splitting parameters ($10Dq, Ds, Dt$), the charge transfer energy (Δ_{pd}) and

the Cu $3d$—O $2p$ hopping (t_{pd}) [104, 186, 187]. Small changes to these parameters can lead predominately to shifts in the Cu $3d$ and O $2p$ energy levels that would manifest themselves as energy shifts in $f(\omega)$ [188], unlike the large changes in the spectral weight distribution that are observed with doping [105]. Since the XAS and RSXS are sensitive to the Cu $2p \rightarrow 3d$ and O $1s \rightarrow 2p$ transitions, modulations of the Cu $2p$ and O $1s$ binding energies may also contribute to the energy shifts.

The agreement between the measured scattering intensity and this simple phenomenological model indicates that energy shifts are responsible for the dominant contribution to the resonant scattering intensity. In comparison, contributions arising from lattice displacements and valence modulations appear to be much less significant. This is reasonable for the lattice displacement model, given that the magnitude of the calculated scattering intensity is $\sim$4 orders of magnitude weaker than the energy shift model at both the O K and Cu L edges.[1]

In contrast, the valence modulation model (assuming $\delta p = 0.08$) is $\sim$4 times larger than the energy shift model at the O K edge. At the Cu L edge, the valence modulation model is $\sim$35 times weaker than the energy shift model at their respective peak values but is comparable in intensity at 932.3 eV, the peak energy of the valence model calculation. As such, unlike lattice displacements, we do not expect the energy shift contribution to dominate the scattering intensity for valence modulations of order $\delta p = 0.08$ or larger. This argues against a large valence modulation, such as those reported in Ref. [95], but does not rule out smaller valence modulations. However, even if negligibly small, one can infer that valence modulations must be nonzero, as they must occur for a spatial modulation of the Cu $3d$ (or $2p$) and O $2p$ (or $1s$) energies (i.e., the energy shifts provide indirect evidence for valence modulations). Placing a precise upper limit on the magnitude of the valence modulation is beyond the scope of the present work, requiring more sophisticated modelling. However, we note that the energy shift model has the same unoccupied spectral weight, and hence the same valence, for all sites in the stripe phase. As such, the resonant scattering line shapes, which are well described by the energy shift model alone, are consistent with a stripe phase that has a minimal but nonzero valence modulation.

The origin of these modulating energy levels and how they relate to the microscopic mechanism of stripe ordering is an open question. The energy shifts may simply be induced by small charge-density modulations or lattice displacements, yet still be the dominant signature in resonant scattering. Alternatively, they may be a more direct signature of the

[1] Since ΔE is unknown, for this analysis we compare to an arbitrarily chosen value of $\Delta E = 100$ meV, which serves as a reasonable upper limit value. Comparing to other values of ΔE involves scaling by $(\Delta E/(100\text{ meV}))^2$.

interactions underlying stripe order. For instance, these energy modulations may point to a VBS description of the stripe phase [180, 19, 181]. In the VBS picture, stripe order is driven by exchange interactions, which also induce lattice displacements and bond-centered charge order. However, the magnitude of bond-centered charge density modulations can be small, being screened by long-range Coulomb repulsions. This may provide an explanation for the lack of clear evidence for a valence modulation from resonant scattering. In contrast, the energy shifts that we have identified in RSXS may arise naturally out of a VBS, which involves a modulation of the bonding in the lattice.

Finally, our identification of energy shifts is likely applicable not only to CDW order in other cuprates (energy shifts were recently shown to also describe density wave order in YBCO [2]), but also to other transition oxides. For instance, recent first principles calculations have shown that several "charge" ordered transition metal oxides exhibit a site dependence to the energies of the electronic states but no site dependence to the total d orbital occupation [189], similar to our phenomenological energy shift model.

3.5 Supplementary information

3.5.1 Methods

Resonant soft x-ray scattering measurements were performed at the Canadian Light Source's REIXS beamline.[168] Single crystals of LNSCO, grown by the traveling-solvent floating zone method, were prepared with [100] and [001] faces and oriented such that scattering could be performed in the $\mathbf{Q} = (H, 0, L) = (2\pi/a_o, 0, 2\pi/c)$ plane. Here (H, K, L) is referenced to the high temperature tetragonal (HTT) unit cell, where a_o and b_o are aligned with the Cu-O bonds. For all measurements the incident light was σ-polarized along the b_o axis. The sample orientation was confirmed by detection of (0, 0, 4) and (1, 0, 3) Bragg reflections at 2.5 keV.[168] The sample was cleaved in vacuum to minimize surface contamination effects in the O K edge x-ray absorption spectroscopy (XAS). XAS at the Cu $L_{3,2}$ and O K edges was measured by total electron yield. Measurements of XAS [Fig. 3.1(i) and Fig. 3.1(j)] have been offset and scaled to calculated values of $\mu(\omega)$ from NIST [158] at the pre-edge and post-edge to express $\mu(\omega)$ in units of μm^{-1}. Via the optical theorem, $\text{Im}\{f_j(\omega)\}$ is linearly proportional to the absorption coefficient, $\mu(\omega)$, and $\text{Re}\{f_j(\omega)\}$ can be determined from $\text{Im}\{f_j(\omega)\}$ using Kramers-Kronig transformations. Accordingly, to determine $f(\omega)$ in electrons/atom (Fig. 3.2), measured XAS was scaled and extrapolated to high and low energy using tabulated calculations of $\text{Im}\{f(\omega)\}$ above and below the absorption edge.[158]

3.5.2 Structure factors

The three scattering models discussed in the text can be understood by a calculation of the structure factor S, which is written generally as

$$S = \sum_j f_j(\omega) e^{-i\boldsymbol{Q}\cdot(\boldsymbol{r}_j + \delta\boldsymbol{r}_j)} \tag{3.1}$$

where f_j is the atomic form factor at lattice position j, ω is the photon angular frequency, $\boldsymbol{Q}$ is the scattering vector, $\boldsymbol{r}_j$ is the position vector at j and $\delta\boldsymbol{r}_j$ is the displacement at j from the lattice position outside the stripe-ordered phase. The atomic form factor can also depend on additional parameters related to the electronic structure of the atom at j, such as the local charge density or energy level, and these factors are explicitly included for the respective models.

To determine the structure factor for the 3 models, we make several assumptions: 1. We take $\boldsymbol{Q} = 2\pi(\frac{1}{4a_o}, 0, \frac{L}{c})$. 2. We treat only a single CuO_2 plane for simplicity. 3. As mentioned in the text, because $\boldsymbol{\epsilon}_i \parallel b_o$, the scattering measurements at the O K edge are only sensitive to the O $2p_y$ states and thus only half of the O atoms enter into the structure factor. The relevant O have the same x positions as the Cu sites and thus share expressions for the scattering intensity. 4. Because the scattering intensity is measured to be very weak above and below the absorption edges, we assume that non-resonant terms in the scattering intensity calculation are negligible compared to the resonant contributions (ie. at the Cu edge we only include the Cu atoms in the structure factor).

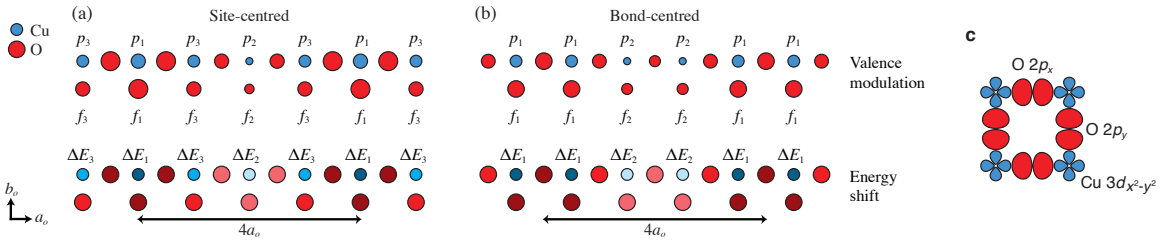

Figure 3.3 – **Stripe-ordering models** (a) and (b) Schematic representations of site-centred (a) and bond-centred (b) stripe-ordering for the valence modulation and energy shift models. (c) Illustration of the Cu $3d_{x^2-y^2}$ and O $2p_{x,y}$ orbitals of the CuO_2 plane. Only the O $2p_y$ orbitals are considered in the scattering models because of the experimental geometry and the incident polarization.

3.5.2.1 Valence modulation

The valence modulation model considers that the modulation of charge is due to differences in the local hole concentration at different O or Cu sites. In the case of a bond-centred stripe (Fig. 3.3(b)), there are two inequivalent sites in this case each with different local hole doping levels $p_1 = p + \delta p_1$ and $p_2 = p + \delta p_2$. The structure factor is thus given by

$$S = (1 + i) \left[f_2(\omega, p + \delta p_2) - f_1(\omega, p + \delta p_1) \right]. \tag{3.2}$$

As shown previously,[96] since the XAS is known to evolve roughly linearly with doping and $f_j(\omega)$ is proportional to the absorption coefficient, one can determine $f_j(\omega, p_j)$ with arbitrary doping p_j from a linear combination of $f(\omega)$ deduced from XAS at two Sr dopings, x, (in our calculation, $x = p = 0.07$ and $x = p = 0.15$), such that

$$f_{1,2}(\omega, p + \delta p_{1,2}) \approx f(\omega, p = 0.125) + \frac{f(\omega, x = 0.15) - f(\omega, x = 0.07)}{0.15 - 0.07} \delta p_{1,2} \tag{3.3}$$

and therefore the scattering intensity, $I_s = c|S|^2/\mu(\omega)$, (the division by $\mu(\omega)$ accounts for the energy dependent absorption of the incident and scattered x-rays) is given by

$$\begin{aligned} I_s &= \frac{c}{\mu(\omega)} \left| (1 + i) \frac{\delta p_2 - \delta p_1}{0.15 - 0.07} \left[f(\omega, x = 0.15) - f(\omega, x = 0.07) \right] \right|^2 \\ &= \frac{c}{\mu(\omega)} \left| f(\omega, x = 0.15) - f(\omega, x = 0.07)) \right|^2, \end{aligned} \tag{3.4}$$

where c is a constant. One can also use XAS at different Sr dopings, as shown in Fig. 3.4, to calculate the scattering intensity.

In the case of a site-centred stripe (Fig. 3.3(a)), there are three inequivalent sites, but the structure factor only depends on two sites owing to the cancellation of f_3 terms by symmetry:

$$S = i \left[f_2(\omega, p + \delta p_2) - f_1(\omega, p + \delta p_1) \right], \tag{3.5}$$

which gives the same scattering intensity as for a bond-centred stripe

$$I_s = \frac{c}{\mu(\omega)} \left| f(\omega, x = 0.15) - f(\omega, x = 0.07)) \right|^2. \tag{3.6}$$

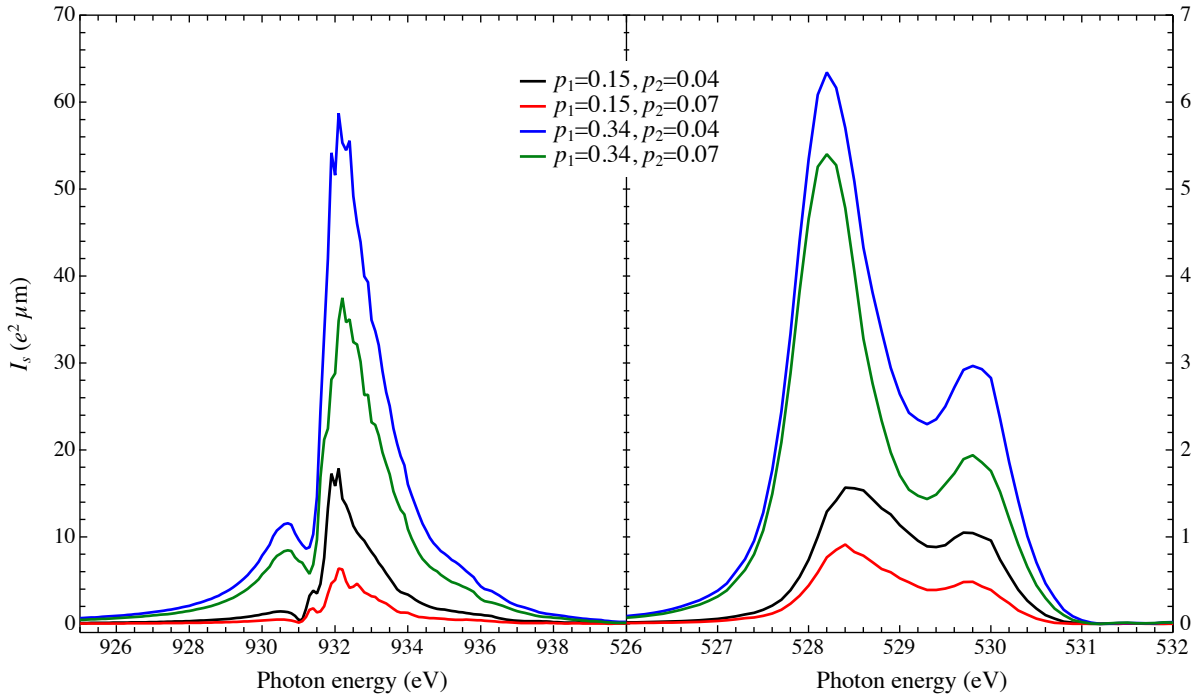

Figure 3.4 – **Valence modulation calculations** (a) and (b) Calculated scattering intensities at the Cu L_3 and O K edges for XAS from Ref. [105] at different dopings p_1 and p_2.

3.5.2.2 Energy shift

The energy shift model has the same periodicity as the valence modulation model for both site- and bond-centred stripes (Fig. 3.3(a) and Fig. 3.3(b)). The primary difference is that we replace the dependence on local hole doping with shifts of the energy levels, such that the structure factor is given by

$$S_{\text{bond-centred}} = (1+i)\left[f_2(\hbar\omega + \Delta E_2) - f_1(\hbar\omega + \Delta E_1)\right] \tag{3.7}$$

$$S_{\text{site-centred}} = i\left[f_2(\hbar\omega + \Delta E_2) - f_1(\hbar\omega + \Delta E_1)\right] \tag{3.8}$$

In our calculation, we set the magnitude of ΔE_j to 0.1 eV and $\Delta E_1 = -\Delta E_2$, but any value $0 < |\Delta E_j| \leq 0.2$ eV produces the same energy dependence. The scattering intensity can thus be written as

$$I_s = \frac{c}{\mu(\omega)}\left|f(\hbar\omega + \Delta E) - f(\hbar\omega - \Delta E)\right|^2 \tag{3.9}$$

for either a bond-centred or site-centred stripe.

3.5.2.3 Lattice displacement

Finally, for the lattice displacement model, f_j is the same at each site, but $r_j + \delta r_j$ is site-dependent. Considering a chain of 4 sites separated by a, the structure factor is given by

$$S = f(\omega)\left(e^{-\frac{i\pi\delta_1}{2a}} + e^{-\frac{i\pi(a+\delta_2)}{2a}} + e^{-\frac{i\pi(2a+\delta_3)}{2a}} + e^{-\frac{i\pi(3a+\delta_4)}{2a}}\right). \tag{3.10}$$

Expanding the exponential terms in series to first order (ie. for small displacements relative to the lattice spacing), we find

$$S = f(\omega)\frac{\pi}{2a}\left[(\delta_4 - \delta_2) + i(\delta_3 - \delta_1)\right] \tag{3.11}$$

which gives a scattering intensity that goes as

$$I_s = \frac{c}{\mu(\omega)}|f(\omega)|^2\frac{\pi^2}{4a^2}\left[(\delta_4 - \delta_2)^2 + (\delta_3 - \delta_1)^2\right] = \frac{c}{\mu(\omega)}|f(\omega)|^2. \tag{3.12}$$

This result holds if one includes higher order terms in the series expansion or if one considers a square lattice rather than a chain. Moreover, the magnitude of the displacements have no impact on the energy dependence of the calculated scattering intensity. Although we have depicted a bond-centred lattice displacement in Fig. 3.1(a), the generality of this result illustrates that we recover the same energy dependence to I_s for site-centred and bond-centred stripe models.

Chapter 4

Distinct Charge Orders in the Chains and Planes of Ortho-III-Ordered $YBa_2Cu_3O_{6+\delta}$

This chapter has been adapted from Ref. [2].

4.1 Overview

Recently, charge density wave (CDW) order in the CuO_2 planes of underdoped $YBa_2Cu_3O_{6+\delta}$ was detected using resonant soft x-ray scattering. An important question remains: is the chain layer responsible for this charge ordering? Here, we explore the energy and polarization dependence of the resonant scattering intensity in a detwinned sample of $YBa_2Cu_3O_{6.75}$ with ortho-III oxygen ordering in the chain layer. We show that the ortho-III CDW order in the chains is distinct from the CDW order in the planes. The ortho-III structure gives rise to a commensurate superlattice reflection at Q=[0.33 0 L] whose energy and polarization dependence agrees with expectations for oxygen ordering and a spatial modulation of the Cu valence in the chains. Incommensurate peaks at [0.30 0 L] and [0 0.30 L] from the CDW order in the planes are shown to be distinct in Q as well as their temperature, energy, and polarization dependence, and are thus unrelated to the structure of the chain layer. Moreover, the energy dependence of the CDW order in the planes is shown to result from a spatial modulation of energies of the Cu $2p$ to $3d_{x^2-y^2}$ transition, similar to stripe-ordered 214 cuprates.

4.2 Introduction

Direct evidence for charge density wave (CDW) order in $YBa_2Cu_3O_{6+\delta}$ (YBCO) was recently observed in high magnetic field using nuclear magnetic resonance [32] and in zero-field diffraction, first with resonant soft x-ray scattering (RSXS) [22] and subsequently with hard x-ray scattering [23]. Prior to these measurements, density wave order [190, 179] had been observed in 214 cuprates [$La_{2-x-y}(Ba,Sr)_x(Eu,Nd)_yCuO_4$] [25] as well as $Ca_{2-x}Na_xCuO_2Cl_2$ [82] and $Bi_2Sr_2CaCu_2O_{8+\delta}$ [191]. However, density wave order in YBCO—a material long considered a benchmark cuprate due to its low disorder and high $T_{c,\max} \simeq 94.2$ K—had only been inferred indirectly, being offered as an explanation for Hall effect measurements [177] and the electron pockets observed in quantum oscillation experiments [39, 192, 193]. The observation of density wave order in YBCO thus marks an important milestone in effortss to determine whether density wave order is generic to the cuprates while providing new opportunities to identify common features of CDW order in the cuprates.

RSXS is well suited to give direct insight into the nature of CDW order in YBCO. RSXS involves diffraction with the photon energy tuned through an x-ray absorption edge. This gives significant energy dependence to the atomic scattering form factor, $f(\omega)$, enhancing the scattering from weak ordering and providing sensitivity to the charge, spin and orbital occupation of specific elements. At the Cu L absorption edge, the scattering is sensitive to modulations in the unoccupied Cu $3d$ states that are central to the low energy physics of the cuprates [95, 96, 182, 183, 2]. The recent RSXS measurements of Ghiringhelli *et al.* at the Cu L absorption edge identified superlattice peaks at $Q = [0.31\ 0\ L]$ and $[0\ 0.31\ L]$ indicative of CDW order [22]. They also showed that the intensity of the superlattice reflections peak at $\sim T_c$ and decrease in intensity for $T < T_c$, providing a clear link between the density wave order and superconductivity [22]. Importantly, based on the energy dependence of the scattering intensity and the presence of peaks at H=0.31 and K=0.31 in a detwinned sample, Ghiringhelli *et al.* also demonstrate that the CDW superlattice peaks originate from modulations in the CuO_2 planes.

However, the possible role of the charge reservoir layer in stabilizing the CDW order is not yet clear. In YBCO, the charge reservoir for the CuO_2 planes is composed of CuO chains. The Cu sites in the chains (Cu1) and planes (Cu2) have different orbital symmetries and contribute differently to x-ray absorption spectroscopy (XAS) and RSXS measurements [194, 84]. In addition to making the structure orthorhombic ($a \neq b$), the chain layer can be oxygen ordered into a variety of "ortho" ordered phases [107, 111]. For instance, the ortho-III phase corresponds to a repeated pattern of full–full–empty ordering of oxygen in the chains [see Fig. 4.1(a)] that produces a commensurate superlattice peak at

[0.33 0 L], in close proximity to the [0.31 0 L] peaks observed in Ref. [22]. In addition, the chains may also be susceptible to CDW order along the chains (producing incommensurate peaks at [0 K L]) [195, 196, 197]. As such, the chains may act to stabilize CDW order in YBCO akin to the low-temperature tetragonal (LTT) structural phase stabilizing spin and charge stripes in stripe ordered 214 cuprates [25, 198].

In this chapter, RSXS measurements of a high purity, ortho-III ordered single crystal of $YBa_2Cu_3O_{6.75}$ (T_c=75.2 K, p=0.133) [45, 199] are shown to (a) confirm the in-plane origin of the incommensurate [0.30 0 L] CDW peak [1], (b) clarify its relation to the oxygen ordering in the chain layer, and (c) demonstrate a link to the microscopic origin of stripes in 214 cuprates. Analysis of the scattering intensities provides clear evidence that the [0.30 0 L] CDW peak has an energy, polarization, and temperature dependence that is distinct from the [0.33 0 L] oxygen ordering peak, indicating there is no clear relation between the chain layer and the [0.30 0 L] CDW order. Moreover, the [0.30 0 L] peak is shown to result from a spatial modulation of the energy of the Cu $2p$ to $3d_{x^2-y^2}$ transition, unlike the [0.33 0 L] oxygen ordering peak, which is described by a spatial modulation of the Cu valence. The former is consistent with RSXS measurements in stripe ordered 214 cuprates [2], which is also described by the energy shift model, suggesting a common origin to the CDW order that is generic to the cuprates.

4.3 Results

4.3.1 Measurement

Resonant scattering measurements were performed at the Canadian Light Source's Resonant Elastic and Inelastic X-ray Scattering (REIXS) beamline [168] using linearly polarized light in both σ and π scattering geometries, as depicted in Fig. 4.1(b). The sample orientation was confirmed by detection of [0 0 1], [$\pm$1 0 2], and [0 $\pm$1 2] Bragg reflections at 2.05 keV. XAS was measured using total fluorescence yield (TFY).

[1] The peaks in Ref. [22] are observed at H=0.31 and K=0.31 and not at H=0.30 and K=0.30 as in our measurements. At present, we cannot determine whether this difference is due to the different doping levels of the samples (a truly intrinsic effect) or some minor differences in the alignment of the crystals in the two studies.

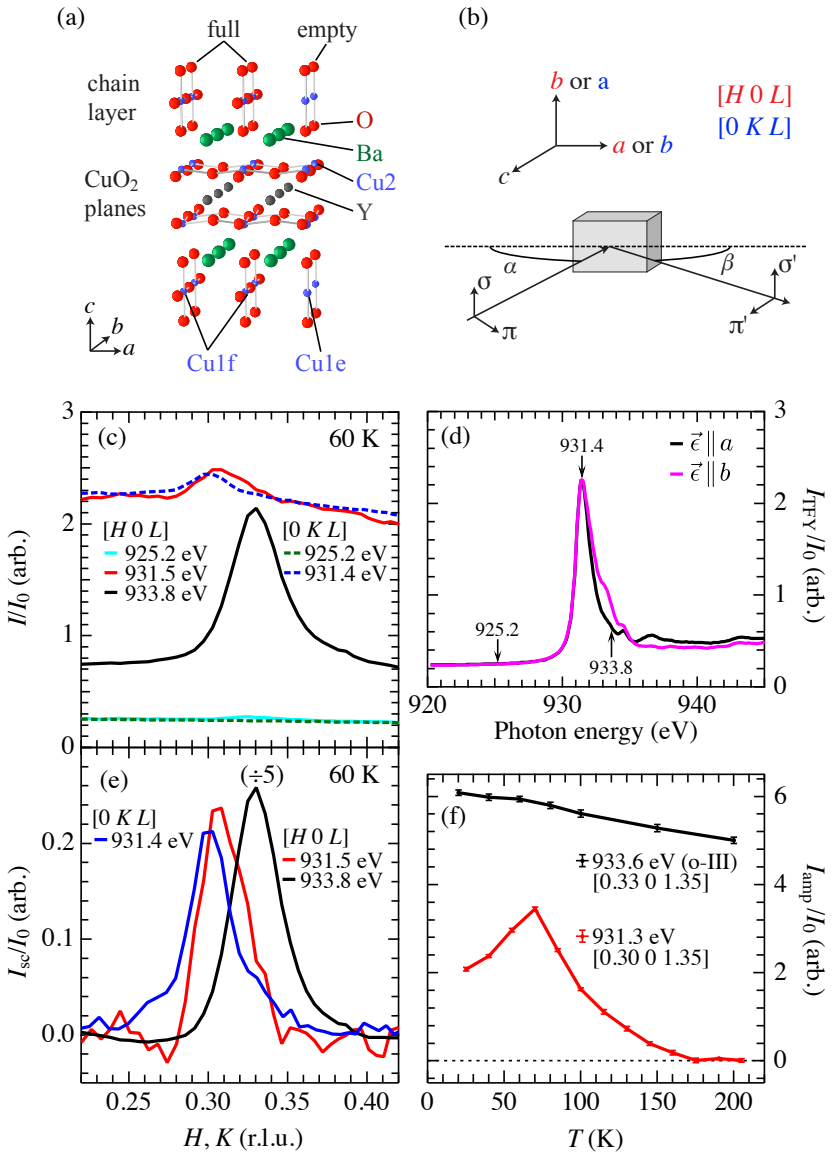

Figure 4.1 – (a) The crystal structure of ortho-III ordered YBCO. (b) A schematic of the experiment geometry. (c) [H 0 L] and [0 K L] scans at $T = 60$ K measured using sigma polarized light through the [0.30 0 1.4] and [0 0.30 1.4] superlattice peaks, which appear when the photon energy is tuned to the peak of the XAS (∼931.4 eV). The ortho-III oxygen ordering superlattice peak is seen at [0.33 0 L] and is most prominent around 933.8 eV. (d) The x-ray absorption with polarization along the a and b axes measured using total fluorescence yield. (e) The scattering intensity with fluorescence background subtracted. (f) The temperature dependence of the amplitudes of the [0.30 0 1.35] and [0.33 0 1.35] peaks. r.l.u., reciprocal lattice units.

The measured intensity of H and K scans through the [0.30 0 1.4] and [0 0.30 1.4] peaks at 60 K is shown in Fig. 4.1(c) for the incident photon energies indicated in Fig. 4.1(d). These superlattice reflections are observed above a large x-ray fluorescence background, similar to measurements from Ref. [22]. In addition, there is also a peak at [0.33 0 L] that is evident at higher photon energy.

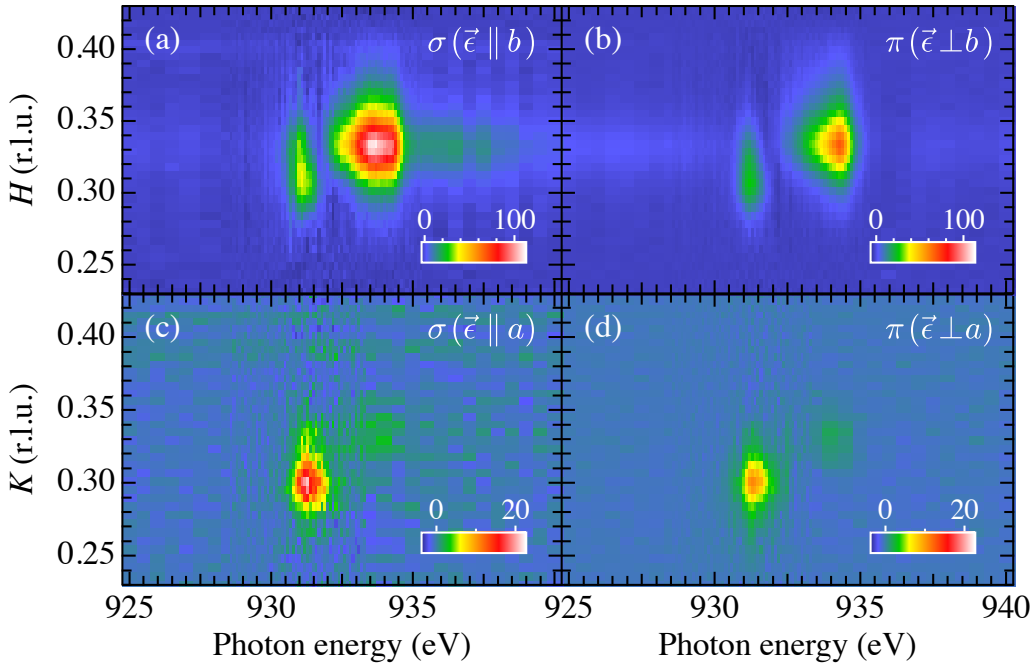

Figure 4.2 – The [H 0 L] [(a) and (b)] and [0 K L] [(c) and (d)] normalized scattering intensity, I_{sc}/I_0, in arbitrary units. The scattering intensity was measured with σ [(a) and (c)] and π [(b) and (d)] incident photon polarization at T = 60 K. r.l.u., reciprocal lattice units.

The scattering intensity, I_{sc}, was determined by fitting the fluorescence background to a polynomial and subtracting it from the data [Fig. 4.1(e)]. This procedure was repeated as a function of photon energy and for both σ and π incident photon polarizations, as shown in Fig. 4.2. In Fig. 4.2(a) and Fig. 4.2(b), two peaks at H=0.30 and H=0.33 are observed that resonate at different energies and have a different polarization dependence. Due to the large width of both peaks, they overlap in H forming one broad asymmetric peak, which is particularly evident around the peak in the x-ray absorption (931.4 eV). In contrast, the peak at [0 0.30 1.4], shown in Fig. 4.2(c) and Fig. 4.2(d), resonates at 931.3 eV with only a small signature of the peak at ∼0.33, likely due to residual (<3%) twinning of the sample. From these scans at 60 K, the correlation lengths of the peaks

are $\xi(K{=}0.30) \simeq 42$ Å , $\xi(H{=}0.30) \simeq 40$ Å, and $\xi(H{=}0.33) \simeq 37$ Å. Consistent with previous work [22, 23], the amplitude of the [0.30 0 L] reflection is first distinguished from the fluorescence background at ∼160 K, peaks near T_c, and decreases for $T < T_c$, as shown in Fig. 4.1(f). In contrast, the [0.33 0 L] peak amplitude exhibits a gradual T dependence with no notable features at T_c or 160 K.

4.3.2 Analysis

Analysis of the energy and polarization dependence of the integrated scattering intensities (Fig. 4.3) demonstrates that the $H{=}0.30$ and $K{=}0.30$ peaks are due to modulations in the CuO_2 planes, whereas the $H{=}0.33$ peaks are due to ortho-III ordering in the chain layer. To model the scattering intensity of the $H{=}0.33$ peak, we followed the procedure in Ref. [84] which illustrated that the scattering intensity and polarization dependence of the oxygen order superstructure in ortho-II ordered YBCO (full–empty–full–empty chains) could be calculated by accounting for the impact of the oxygen dopants on the Cu1 d states in the full and empty chains.

This was done by experimentally determining the energy dependence of the atomic scattering tensor, F_i, for Cu in full, $F_{\mathrm{Cu1f}}(\omega)$, and empty, $F_{\mathrm{Cu1e}}(\omega)$, chains using polarization dependent x-ray absorption measurements in YBCO prepared with either an entirely full ($YBa_2Cu_3O_7$) or an entirely empty ($YBa_2Cu_3O_6$) chain layer. Here we use the same analysis for the $H = 0.33$ peak with $F_{\mathrm{Cu1f}}(\omega)$ and $F_{\mathrm{Cu1e}}(\omega)$ from Ref. [84] and $I_{\mathrm{sc,o\text{-}III}}(H{=}0.33, \vec{\epsilon}) = |f_{\mathrm{Cu1f}}(\omega, \vec{\epsilon}) + f_O - f_{\mathrm{Cu1e}}(\omega, \vec{\epsilon})|^2$. As shown in Fig. 4.3(a), this analysis reproduces the energy and polarization dependence of the $H = 0.33$ peak, providing confirmation that this peak is dominated by the oxygen order in the chain layer.

In contrast, both the polarization and energy dependence of the $H{=}0.30$ and $K{=}0.30$ peaks are consistent with a spatial modulation of the Cu $3d_{x^2-y^2}$ states in the CuO_2 planes. First, one must note that the incident π and σ polarizations couple to different components of the scattering tensor. For σ polarization, the photon polarization is entirely along the $b(a)$ axis for the $H(K) = 0.30$ peak and is therefore sensitive to the $bb(aa)$ components of the scattering tensor. However, for π polarized light, the polarization has components along both the a and c axes that depend on the scattering geometry. For modulations of Cu $3d_{x^2-y^2}$ states, $f_{aa,\mathrm{Cu2}} \simeq f_{bb,\mathrm{Cu2}} >> f_{cc,\mathrm{Cu2}}$ and $I_{\mathrm{sc}}(\pi\pi')/I_{\mathrm{sc}}(\sigma\sigma') = [\sin(\alpha)\sin(\beta)\Delta f_{aa}]^2$, where α and β are the angles of the incident and scattered light relative to the sample surface [see Fig. 4.1(b)] [2]. For the values of α and β in our measurement, one would expect

[2] We assume only $\sigma\sigma'$ or $\pi\pi'$ scattering is allowed (no magnetic or anisotropic tensor susceptibility scattering.)

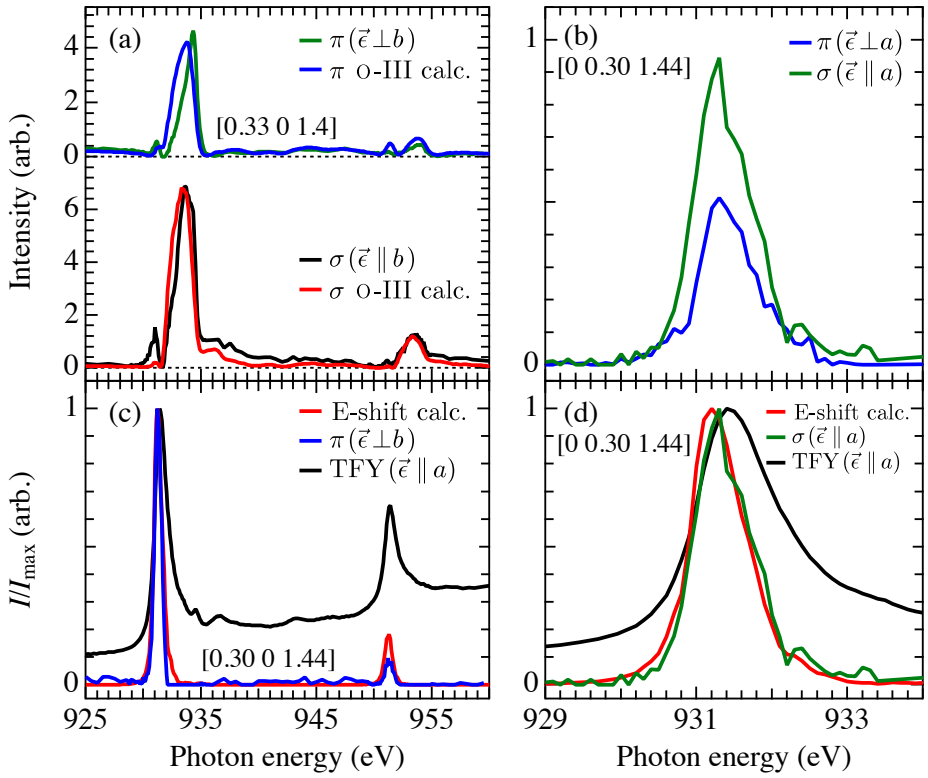

Figure 4.3 – (a) The measured energy dependence of the [0.33 0 1.4] oxygen ordering peak with σ and π polarized incident light along with the calculated spectra for ortho-III oxygen ordering of the chain layer. (b) The energy dependence of the [0 0.30 1.44] peak measured with σ and π polarized light. (c) The energy dependence of the [0.30 0 1.44] peak (blue) with π polarized light compared to the energy shift model calculation. The energy shift calculation captures the correct peak position and energy width of the scattering intensity. (d) The energy shift model calculation compared to the [0 0.30 1.44] peak with σ polarized light.

the ratio of $I_{sc}(\pi\pi')/I_{sc}(\sigma\sigma') = 0.46$ for a modulation of Cu $3d_{x^2-y^2}$ states. As shown in Fig. 4.3(b), the $K = 0.30$ peak is in good agreement with this ratio.

A final intriguing aspect of the energy dependence of the scattering intensity is that the line shape can be described by a simple phenomenological model for the scattering intensity based on a spatial modulation of the *energy* of the Cu $2p$ to $3d_{x^2-y^2}$ transition. The energy of this transition is determined by the energy of the $3d_{x^2-y^2}$ states, as well as the core hole energy and the interaction energy of the core hole with the d electrons, all of which may be spatially modulated. This energy shift model was recently shown to account for the

energy dependence of the scattering intensity of the [1/4 0 L] charge stripe ordering peak in $La_{1.475}Nd_{0.4}Sr_{0.125}CuO_4$, unlike models based on lattice displacements or charge density modulations [2]. Although in YBCO we do not know the structure factor that accounts for the [0.30 0 L] and [0 0.30 L] peaks, we can naively invoke the same energy shift model and assume that $I_{sc}[0.30\ 0\ L](\omega) \propto I_{sc}[0\ 0.30\ L](\omega) \propto |f_{Cu2a}(\hbar\omega + \Delta E) - f_{Cu2b}(\hbar\omega - \Delta E)|^2$, where Cu2a and Cu2b represent two sites in the CuO_2 planes with $f(\omega)$ that is identical apart from a small energy shift $\pm\Delta E$ at each site. Following previous work, $f_{Cu2}(\omega)$ can be determined from the experimentally measured x-ray absorption spectra [95, 96, 2]. In this case, the XAS with polarization oriented along the a-axis of the sample is used since it is dominated by the Cu $3d_{x^2-y^2}$ states of the CuO_2 planes with minimal chain contribution. As shown in Fig. 4.3(c) and Fig. 4.3(d), the energy shift model is in excellent agreement with the experiment, capturing the correct energy dependence and peak position, which peaks ~0.1 eV below the L_3 peak of the x-ray absorption. Note, for this calculation ΔE=0.1 eV was used[3].

4.4 Discussion

Although the energy shifts, and thus the scattering, may ultimately be caused by a modulation in Cu valence, the microscopic origin of the energy shifts is currently unclear. An important implication of the energy shift model is that the resonant scattering provides only indirect evidence for charge density (valence) modulations—the success of the energy shift model allows one to infer there is a charge density modulation since this must occur if the electronic structure is spatially modulated [2]. In contrast, the energy dependence of the ortho-III oxygen order peak ($H = 0.33$) is described "directly" in terms of a large change in valence between Cu in the full and empty chains. However, since we cannot presently estimate the magnitude of the charge density modulation from the energy shifts, it is conceivable that a modulation of charge is not the central feature of the newfound density wave order in YBCO (and also stripes in 214 cuprates). In such a case, the energy shifts may in fact be a signature of a novel electronic state, such as a valence bond solid [2]. Alternately, the energy shifts may result from weak-coupling, Fermi surface reconstruction descriptions of density wave order in the cuprates. Regardless of the origin, the success of the energy shift model may imply that the temperature dependence of the peak amplitudes results from a temperature dependent energy shift that peaks at T_c, providing an apparent link between the energy shifts and superconductivity.

[3] As discussed in Ref. [2], the line shape is insensitive to the magnitude of ΔE provided $\Delta E < 0.2$ eV. As such, ΔE should not be considered a fitting parameter.

Moreover, the applicability of the energy shift model to the resonant scattering intensity of charge stripe order in 214 cuprates and YBCO indicates that the CDW order likely shares a common origin in the two material systems. This commonality stands in contrast to important differences between the density wave order in YBCO and stripe ordered 214 cuprates. In 214 cuprates, the charge order is stabilized by the LTT structural phase [25, 88], has an incommensurability that plateaus at high doping at the commensurate value of $2\delta = 0.25$ [200, 179] and is understood to be unidirectional in nature (i.e. stripes). In YBCO, while there is no LTT phase, one might expect that the orthorhombic structure of YBCO would preferentially stabilize stripe order propagating along the a or b axes, perhaps with a period locked to the oxygen ordering in the chain layer of YBCO. However, no clear link between structure and the H and $K = 0.30$ peaks is observed in our measurements. Rather, the incommensurate value of the $2\delta = 0.30$ peaks relative to the commensurate oxygen ordering peak at $H = 0.33$, the similar magnitude of the scattering intensity of the H and K peaks and the presence of the $H = 0.30$ peaks in samples with weak oxygen order (only very short range ortho-V order) [22], indicate that the structural distortions are not an essential ingredient for CDW order in YBCO. Additionally, the existence of peaks along both H and K would seem to favor 2D checkerboard order. However, if the connection to the lattice is indeed weak, domains of unidirectional stripes oriented along both a and b may describe the CDW order in YBCO.

Finally, in addition to structural distortions, which may provide pinning centres commensurate with the lattice, disorder can also provide random pinning centres for density wave order and has been shown to enhance spin density wave and CDW order in 214 cuprates [201, 202, 203]. Moreover, 214 cuprates are intrinsically disordered owing to the chemical cation substitution (e.g., Sr for La) near the CuO_2 planes used to dope away from half filling. This makes it difficult to disentangle the role of disorder from the intrinsic physics of 214 cuprates. In contrast, the presence of CDW order in high-purity, oxygen ordered YBCO provides a strong indication that density wave order is in fact an intrinsic feature of underdoped cuprates.

Chapter 5

Orbital symmetry of charge density wave order in $La_{1.875}Ba_{0.125}CuO_4$ and $YBa_2Cu_3O_{6.67}$

An older version of this chapter is available in pre-print form.[4]

5.1 Overview

Recent theories of charge density wave (CDW) order in high temperature superconductors have predicted a primarily d CDW orbital symmetry. Here, we report on the orbital symmetry of CDW order in the canonical cuprate superconductors $La_{1.875}Ba_{0.125}CuO_4$ (LBCO) and $YBa_2Cu_3O_{6.67}$ (YBCO), using resonant soft x-ray scattering and a model mapped to the CDW orbital symmetry. From measurements sensitive to the O sublattice, we conclude that LBCO has predominantly s' CDW orbital symmetry, in contrast to the d orbital symmetry recently reported in other cuprates. Additionally, we find that the C_4 orbital symmetry of the Cu sublattice scattering is approximately preserved in LBCO and broken in YBCO. This work highlights orbital symmetry as an additional key property of CDW order that distinguishes the different cuprate families. We discuss how the CDW symmetry may be related to the "1/8–anomaly" and to static spin ordering.

5.2 Introduction

Charge density wave (CDW) order in underdoped cuprates has recently been revealed as an important and generic competitor to superconductivity (SC).[25, 176, 32, 22, 23, 2, 204, 73, 72] A significant property of CDW order is that it can exhibit both *inter* and *intra* unit cell symmetry breaking.[179, 205] Specifically, CDW order can occur with d rather than s or s' orbital symmetry.[206, 207, 106, 119, 75, 54, 120, 117, 116, 208, 209] Here, we report resonant soft x-ray scattering measurements of $La_{1.875}Ba_{0.125}CuO_4$ (LBCO) and $YBa_2Cu_3O_{6.67}$ (YBCO) that are resolved onto the O $2p_{x(y)}$ and Cu sublattices and mapped to the CDW symmetry. Our main finding is that LBCO has primarily s' symmetry CDW with a secondary d component, distinguishing it from the predominant d symmetry CDW observed in other cuprates.[117, 116] We propose that the s' symmetry in LBCO may be related to the "1/8–anomaly" and that it favours static spin ordering more than d symmetry. Additionally, we find that C_4 orbital symmetry of the Cu sublattice scattering is approximately preserved in LBCO and broken in YBCO. Moreover, in YBCO the symmetry is broken to different degrees along the a and b crystal axes, suggesting either exotic checkerboard order or domains of stripes. Finally, we present and discuss implications of energy dependent scattering from the O $2p_{x(y)}$ sublattices in LBCO.

Stimulated by theory,[75, 54] resonant soft x-ray scattering (RSXS) in YBCO and $Bi_2Sr_{2-x}La_xCuO_{6+\delta}$ (Bi-2201),[117] and scanning tunnelling microscopy (STM) measurements in $Bi_2Sr_2CaCu_2O_{8+\delta}$ (Bi-2212) and $Ca_{2-x}Na_xCuO_2Cl_2$ (Na-CCOC) [116] have recently reported that d symmetry characterizes the CDW order in the CuO_2 planes. In this d-symmetry CDW state, the modulation of charge (or a related microscopic quantity) on O p_x and O p_y sites is out of phase, as depicted in Fig. 5.1b for a commensurate, bond-centered CDW. An important question is whether d-symmetry CDW order is a generic property of underdoped cuprates and, specifically, if it also occurs in the canonical stripe-ordered La-based cuprates. There are many similarities in the CDW order of the La-based cuprates and other cuprates (eg. Bi-2212, YBCO) such as an enhancement in CDW intensity at doping levels near $p = 1/8$,[175, 210, 211, 212] competition with SC and a common spectroscopic signature to the resonant scattering intensity.[2, 1] However, these similarities are at odds with important differences such as the doping dependence of the CDW incommensurability.[175, 204, 211, 212, 30, 213, 200, 73] Perhaps most significantly, static spin density wave (SDW) order commensurate with CDW order is only observed in the La-based cuprates. Accordingly, it is not yet clear whether stripe order in the La-based cuprates and CDW order in other cuprates are slightly different manifestations of a common order or truly distinct phases.

Here, we have resolved the orbital symmetry and microscopic character of CDW order in

LBCO and YBCO using a RSXS technique where the incident photon polarization is varied relative to the material's crystallographic axes and the crystal is simultaneously rotated about the CDW ordering wavevector $\boldsymbol{Q}$, as illustrated in Fig. 5.1a. This special scattering geometry was used in Ref. [117] to study Cu sublattice scattering in YBCO and Bi-2201. Here, we utilize it at the O K edge for LBCO to determine the relative strength, phase relation and energy dependence of scattering from two O sublattices comprised of O atoms with Cu–O–Cu bonds either parallel ($O_{\parallel}$) or perpendicular ($O_{\perp}$) to $\boldsymbol{Q}$ (see Fig. 5.1b). The proportion of d to s' symmetry was characterized from O K edge measurements in LBCO using a polarization dependent RSXS model developed with parameters directly related to the d and s' symmetry components Δ_d and $\Delta_{s'}$. Additionally, RSXS measurements sensitive to the Cu sublattice were used to assess the degree of rotational C_4 symmetry on Cu sites in LBCO and YBCO.

Prior to discussing our results, we first describe the polarization dependent RSXS model which is used in this analysis and then parametrize the model in terms of the symmetry components of the CDW order. Within this framework, the CDW orbital symmetries in LBCO and YBCO are elucidated from the experimental data.

5.3 Polarization dependent resonant x-ray scattering

On an x-ray absorption edge, the resonant elastic x-ray scattering intensity is given by:

$$I(\boldsymbol{\epsilon}_i, \omega, \boldsymbol{Q}) \propto \left| \boldsymbol{\epsilon}_f^* \cdot T(\omega, \boldsymbol{Q}) \cdot \boldsymbol{\epsilon}_i \right|^2, \tag{5.1}$$

where ω is the angular frequency, $\boldsymbol{Q}$ is the momentum transfer, $\boldsymbol{\epsilon}_i$ and $\boldsymbol{\epsilon}_f$ are the incident and scattered polarization, respectively, and

$$T(\omega, \boldsymbol{Q}) = \sum_n F_n(\omega) e^{-i\boldsymbol{Q}\cdot\boldsymbol{r}_n} = \begin{bmatrix} t_{aa} & t_{ab} & t_{ac} \\ t_{ba} & t_{bb} & t_{bc} \\ t_{ca} & t_{cb} & t_{cc} \end{bmatrix} \tag{5.2}$$

is a tensor equivalent of the structure factor – a sum over site index n of the atomic scattering form factor, $F_n(\omega)$, with atomic positions r_n. The form factor is given by $F_n(\omega) = F_n^0(\omega) + F_n^{\mathrm{R}}(\omega)$, where $F_n^0(\omega)$ and $F_n^{\mathrm{R}}(\omega)$ are non-resonant and resonant contributions, respectively. The resonant part, $F_n^{\mathrm{R}}(\omega)$, is strongly enhanced on an x-ray absorption edge and has a symmetry that captures the local symmetry of electronic structure. For instance, at the Cu L edge, which probes the Cu $2p \rightarrow 3d$ transition, a Cu atom in tetragonal CuO_2

planes would have C_4 rotational symmetry and

$$F^{\mathrm{R}}_{\mathrm{Cu}}(\omega) = \begin{bmatrix} f^{\mathrm{R}}_{aa}(\omega) & 0 & 0 \\ 0 & f^{\mathrm{R}}_{bb}(\omega) & 0 \\ 0 & 0 & f^{\mathrm{R}}_{cc}(\omega) \end{bmatrix}, \tag{5.3}$$

where $f^{\mathrm{R}}_{aa}(\omega) = f^{\mathrm{R}}_{bb}(\omega) \gg f^{\mathrm{R}}_{cc}(\omega)$. When summed over n, the resulting symmetry of $T(\omega, \boldsymbol{Q})$ involves both intra and inter unit cell symmetries – symmetry associated with the average form factor, $\overline{F^{\mathrm{R}}_n}(\omega)$ and the orbital symmetry of the CDW modulation.

By scattering at photon energies corresponding to the Cu L (931.4 eV) and O K (528.3 eV) absorption edges, we can resolve the CDW order into the Cu and O sublattices, which occupy the "sites" and "bonds", respectively, of a single-band CDW model.[75]

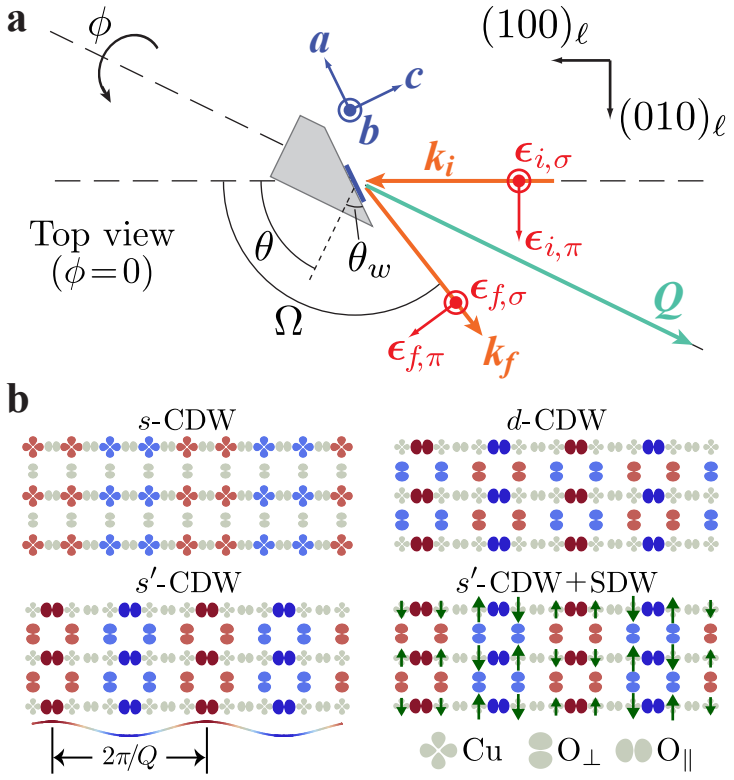

Figure 5.1 – Experimental setup and visualization of CDW order. **a.** Scattering geometry in laboratory frame, ℓ. **b.** CDW order with s, s' and d orbital symmetries, illustrated for a bond-centered, commensurate, and unidirectional CDW. Green arrows are spins in the lower right panel.

At the O K edge, the O sublattice can be further subdivided into two sublattices, O_x and O_y, having different symmetries of $\overline{F_n^R}(\omega)$. Since O $2p$ holes are primarily in σ-bonded $2p_x$ or $2p_y$ orbitals, it follows that one sublattice of O will have $f_{aa}^R \neq 0$ and $f_{bb}^R \simeq 0$ and the other will have $f_{aa}^R \simeq 0$ and $f_{bb}^R \neq 0$, at least at the O pre-edge photon energies of interest. Referencing to the CDW wavevector, $\boldsymbol{Q} = (H\ 0\ 0)$ or $(0\ K\ 0)$, these two O sublattices can be denoted as σ-bonded parallel ($O_\parallel$) or perpendicular ($O_\perp$) to $\boldsymbol{Q}$ (see Fig. 5.1b). The components of $T(\omega, \boldsymbol{Q})$ can also be referenced relative to $\boldsymbol{Q}$. We henceforth refer to the diagonal, in-plane components of $T(\omega, \boldsymbol{Q})$ as $t_\perp$ and $t_\parallel$, which sum over $O_\perp$ and $O_\parallel$, respectively [eg., $t_\parallel = \sum_n f_{aa,n} e^{-iHn}$ and $t_\perp = \sum_n f_{bb,n} e^{-iHn}$ for $\boldsymbol{Q} = (H\ 0\ 0)$].

The components of $T(\omega, \boldsymbol{Q})$ can be determined by varying $\boldsymbol{\epsilon}_f$ and $\boldsymbol{\epsilon}_i$ relative to the crystallographic axes of the sample. As detailed in section 5.9, this is realized experimentally by a combination of rotating the sample azimuthally by an angle, ϕ, about a fixed $\boldsymbol{Q}$ and rotating the incident polarization $\boldsymbol{\epsilon}_i$ between σ and π (see Fig. 5.1a). Additionally, since the CDW peak in the cuprates is broad in L, a wide range of measurement geometries can access the CDW peak and thus probe the components of $T(\omega, \boldsymbol{Q})$.

5.4 Model parametrization

We now turn to investigating the symmetry of CDW order through the symmetry of $T(\omega, \boldsymbol{Q})$ which provides insight into the microscopic character of the CDW order. To see why this is, we first consider the simple case of CDW order with a sinusoidal modulation of charge density ($s + s'$ symmetry) on a tetragonal CuO_2 plane. In this scenario, one would expect to have $|t_\perp| = |t_\parallel| \gg |t_{cc}|$, at both the Cu L and O K edges, mirroring the $d_{x^2-y^2}$ symmetry of F^R. In other words, the scattering tensor, T, can to first order remain C_4 symmetric even though a unidirectional stripe-like modulation breaks the C_4 symmetry of the lattice. If the average electronic structure were instead orthorhombic ($\overline{f_\perp^R} \neq \overline{f_\parallel^R}$), $|t_\perp| \neq |t_\parallel|$ might be expected to occur. However, this could also occur if $\overline{f_\perp^R} = \overline{f_\parallel^R}$ combined with a CDW state with a different orbital symmetry (eg. $d + s'$) that modulates the a and b components of $F_n(\omega)$ to different degrees. These differing possibilities highlight how $T(\omega, \boldsymbol{Q})$ is linked to the underlying symmetry of the CDW order.

To quantify this link, we have parametrized CDW order with mixed orbital symmetries into the single band model from Ref. [75]. The charge modulation amplitude Δ_{ij} (or some other quantity related to CDW order such as an energy shift)[2, 1] on bonds connecting

nearest neighbour Cu sites i and j, is given by:

$$\Delta_{ij} = \sum_{\boldsymbol{Q}^*} \left[\frac{1}{V} \sum_{\boldsymbol{k}} e^{i\boldsymbol{k}\cdot(\boldsymbol{r}_i - \boldsymbol{r}_j)} \Delta_{\boldsymbol{Q}^*}(\boldsymbol{k}) \right] e^{i\boldsymbol{Q}^*\cdot(\boldsymbol{r}_i + \boldsymbol{r}_j)/2}, \tag{5.4}$$

where V is volume and $\boldsymbol{Q}^*$ are the wavevectors of the CDW order. For 1D stripes, $\boldsymbol{Q}^*$ is given by either $(\pm Q_m\ 0\ 0)$ or $(0\ \pm Q_m\ 0)$ whereas checkerboard order has both $(\pm Q_m\ 0\ 0)$ and $(0\ \pm Q_m\ 0)$. In this prescription, $i = j$ corresponds to Cu sites and $i \neq j$ corresponds to O sites (bonds between Cu sites). $\Delta_{\boldsymbol{Q}^*}(\boldsymbol{k})$ captures the symmetry of the CDW state and can contain both site-centred (Δ_s) and bond-centred (Δ_d and $\Delta_{s'}$) symmetry components. As shown in section 5.8, this model can be mapped onto the O sites and related to the components of $T(\omega, \boldsymbol{Q})$, giving

$$\frac{\Delta_d}{\Delta_{s'}} = \frac{t_\parallel/t_\perp - 1}{t_\parallel/t_\perp + 1}. \tag{5.5}$$

Inspection of Eq. 5.5 shows that for pure d-CDW and s'-CDW orders, $t_\parallel/t_\perp$ has the same magnitude (=1), but with opposite sign. A mixed d and s' state would have $|t_\parallel/t_\perp| \neq 1$. In regions with $|t_\parallel/t_\perp| < 1$ (> 1), the sign of $\Delta_d/\Delta_{s'}$ is negative (positive), giving rise to an anti-phase (in-phase) relation between the d and s' symmetry components. Fig. 5.2f illustrates the mapping between $t_\parallel/t_\perp$ and $\Delta_d/\Delta_{s'}$ for O atoms in the CuO_2 plane. We note that Eq. 5.5 applies to both stripe and checkerboard order indicating that, at least in this prescription, $t_\parallel/t_\perp$ does not clearly distinguish checkerboard order from stripes.

The Cu L edge measurements are more difficult to interpret within this description. Most directly, the scattering intensity at the Cu L edge should be sensitive to the site-centered s symmetry component of the CDW order. However, the O-centered s' and d symmetry components may also influence the symmetry of scattering at the Cu L edge (Cu $2p \rightarrow 3d$ transition) by inducing different energy shifts on the Cu core electrons.[54]

5.5 Results

5.5.1 Polarization dependent RSXS in LBCO

In Fig. 5.2, we investigate the ϕ (Figs. 5.2a and 5.2b) and L (Figs. 5.2c and 5.2d) dependence of RSXS from CDW order in LBCO at the O K and Cu L edges in order to determine the magnitude and sign of $t_\parallel/t_\perp$. The dependence on ϕ of I_π/I_σ constrains both the magnitude and sign of $t_\parallel/t_\perp$ whereas the dependence on L constrains its magnitude

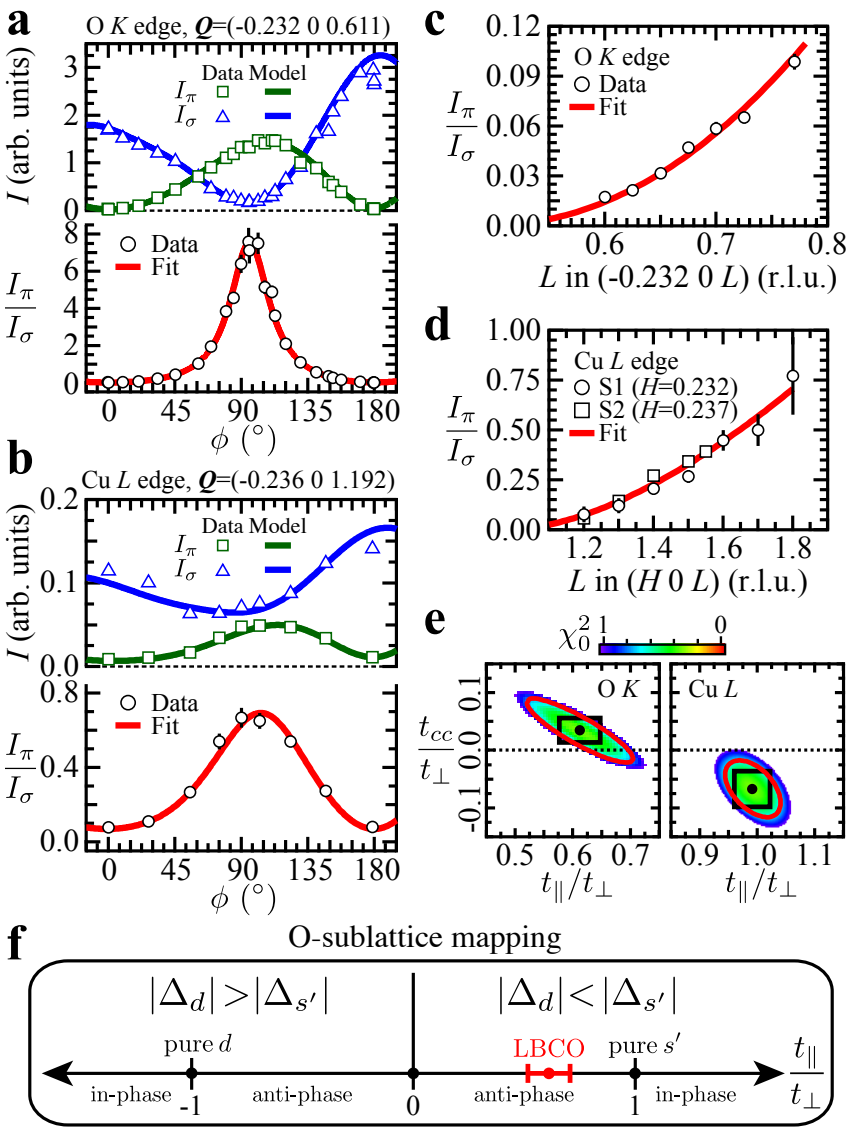

Figure 5.2 – The ϕ and L dependent RSXS for CDW order in LBCO at the O K and Cu L edges. **a-b.** Measured I_π (□), I_σ (△), and I_π/I_σ (◯) vs. ϕ at the O K (528.3 eV) and Cu L (931.3 eV) edges. **c-d.** I_π/I_σ vs. L at the O K and Cu L edges. Simultaneous fitting (red lines) the I_π/I_σ data in **a** and **c** (**b** and **d**) gives $t_\parallel/t_\perp = 0.612$ and $t_{cc}/t_\perp = 0.034$ ($t_\parallel/t_\perp = 0.991$ and $t_{cc}/t_\perp = -0.067$) for the O K (Cu L) edge. The blue and green lines in **a** and **b** are calculated using these parameters. **e.** Colour map of χ_0^2 with minima (best fit) shown as black dots and the 95% CI from least-squares fitting shown as black rectangles. The red ellipses are contours of constant χ_0^2 defining a 95% confidence *region*. **f.** O-sublattice mapping of $t_\parallel/t_\perp$ to $\Delta_d/\Delta_{s'}$ based on Eq. 5.5.

(this is illustrated in Fig. 5.6). A simultaneous fit of I_π/I_σ for both the ϕ (Fig. 5.2a, lower panel) and L (Fig. 5.2c) dependence in LBCO at the O K edge gives $t_\parallel/t_\perp = 0.612 \pm 0.035$ and $t_{cc}/t_\perp = 0.034 \pm 0.021$. In Fig. 5.2a, we show that calculations (solid lines) of the ϕ dependence using these parameters are in excellent agreement with the measured I_π (green squares) and I_σ (blue triangles), providing confidence that all relevant factors such as surface geometry and absorption corrections have been properly taken into account within the model. The reported errors represent 95% confidence intervals (CI) as determined by standard nonlinear least-squares fitting. In Fig. 5.2e, maps of the reduced chi-squared statistic, χ_0^2, for the O K (left) and Cu L (right) edges illustrate more appropriate 95% confidence *regions* of parameter space (red ellipses), defined as contours of constant χ_0^2.

The ratio $|t_\parallel/t_\perp| < 1$ indicates that the O scattering tensor in LBCO breaks C_4 symmetry with a smaller modulation for the $O_\parallel$ sublattice than for the $O_\perp$ sublattice. This result indicates that the Zhang-Rice singlet description of the electronic structure of the cuprates is inadequate for the stripe phase. We cannot rule out that $|t_\parallel/t_\perp| < 1$ results simply from an asymmetry in $\overline{F_R}$ associated with the low-temperature tetragonal (LTT) phase transition in LBCO, which cants the CuO_6 octahedra making each CuO_2 plane orthorhombic. However, this would require $\overline{f_\parallel^R}/\overline{f_\perp^R} = 0.612$, which is difficult to reconcile with the small octahedral tilts of the LTT phase. In contrast, if we interpret our results in terms of orbital symmetry as outlined above, $|t_\parallel/t_\perp| < 1$ is evidence that CDW order in LBCO has mixed, anti-phase $d + s'$ symmetry with a dominant s' symmetry: $\Delta_d/\Delta_{s'} = -0.241 \pm 0.027$. This dominant s' symmetry CDW stands in contrast to the dominant d symmetry CDW reported in YBCO, Bi-2201, Bi-2212, and Na-CCOC.[117, 116]

Although a clear asymmetry between $t_\parallel$ and $t_\perp$ is observed at the O K edge in LBCO, a similar asymmetry is not observed at the Cu L edge. Rather, the ϕ and L dependence of I_π/I_σ is consistent with $|t_\parallel| = |t_\perp| \gg |t_{cc}|$. A simultaneous fit of the ϕ (Fig. 5.2b, lower panel) and L (Fig. 5.2d) dependence at the Cu L edge gives $t_\parallel/t_\perp = 0.991 \pm 0.015$ and $t_{cc}/t_\perp = -0.067 \pm 0.015$, indicating that $\overline{f_\perp^R} = \overline{f_\parallel^R}$ on Cu sites and that the scattering tensor asymmetry observed on the O sublattice does not impart a similar asymmetry onto the Cu $2p \rightarrow 3d$ transition. Most simply, this may be understood as resulting from the Cu L edge measurement being most sensitive to the s or s' symmetry components of the CDW order with only a weak sensitivity to the smaller d component identified by the O K edge measurement. We note that the L dependence was measured in two LBCO samples with slightly different incommensurability and mounted differently (sample S1 was on a wedge and S2 was on a flat plug). These two samples exhibit similar L dependence (Fig. 5.2d) and were both included in the fitting.

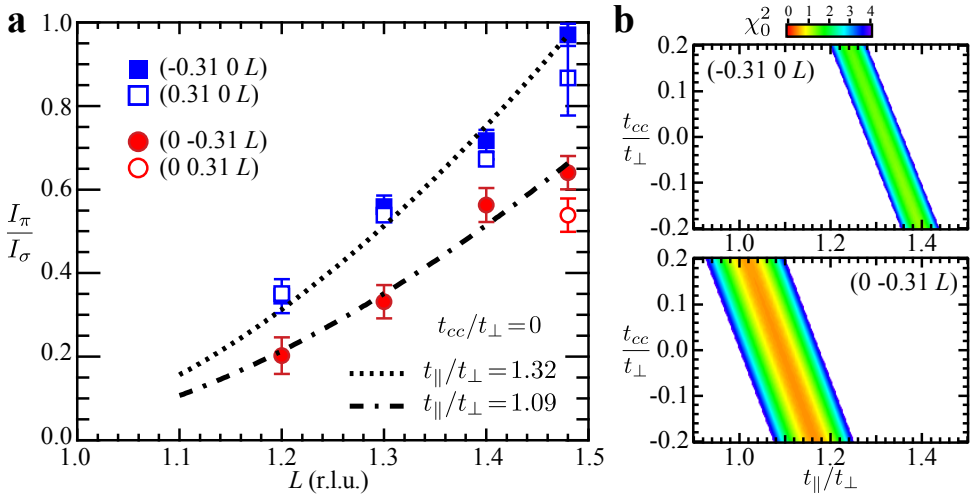

Figure 5.3 – Cu L edge scattering in YBCO. **a.** I_π/I_σ vs. L for the CDW peaks measured along $\boldsymbol{Q} = (\pm 0.31\ 0\ L)$ (blue) and $\boldsymbol{Q} = (0\ \pm 0.31\ L)$ (red) at 931.3 eV. The peaks along H have larger I_π/I_σ than those along K, giving different asymmetries in $t_\parallel/t_\perp$ for these directions. Fits to the data (dashed lines) are for $t_{cc} = 0$. **b.** Maps of χ_0^2 show linear regions of acceptable fit parameters for H (top) and K (bottom).

5.5.2 Cu L edge investigation of YBCO

Turning to YBCO, the L dependence of I_π/I_σ (Fig. 5.3) for $\boldsymbol{Q} = (0\ \pm 0.31\ L)$ is consistent with $|t_\parallel/t_\perp| \simeq 1$, similar to LBCO. In contrast, the $(\pm 0.31\ 0\ L)$ peaks exhibit larger values of I_π/I_σ than the $(0\ \pm 0.31\ L)$ peaks, corresponding to $|t_\parallel/t_\perp| > 1$. Specifically, fitting the data with $t_{cc} = 0$ gives $|t_\parallel/t_\perp| = 1.091 \pm 0.154$ for $(0 \pm 0.31\ L)$ and 1.317 ± 0.087 for $(\pm 0.31\ 0\ L)$. If we allow for $t_{cc} \neq 0$, the fit is under-constrained and linear regions in parameter space (Fig. 5.3b) provide acceptable fits to the data. However, one can reasonably assume that the CDW order is dominated by the CuO_2 planes and thus that t_{cc} is small relative to $t_\perp$.[2] Imposing the constraint that $|t_{cc}/t_\perp| \leq 0.2$ gives $1.01 \leq |t_\parallel/t_\perp| \leq 1.17$ for $(0 \pm 0.31\ L)$ and $1.24 \leq |t_\parallel/t_\perp| \leq 1.39$ for $(\pm 0.31\ 0\ L)$.

These measurements show that the orbital symmetry of CDW order differs along H and K in YBCO, providing further evidence that a simple checkerboard order is not applicable to YBCO.[204, 214] Although an exotic form of checkerboard order may explain this, a simpler view is that there are domains of stripe-like CDW order with different orbital symmetries in YBCO.

For the CDW peak along K in YBCO, the observation of $|t_\parallel/t_\perp| \simeq 1$ is consistent with the simplest picture of an s symmetry component dominating the scattering from

the Cu sublattice. However, since it is not presently evident how d symmetry impacts the Cu L edge measurement, a d symmetry component cannot be ruled out. This conclusion differs from the recent interpretation of the ϕ dependence of the $\boldsymbol{Q} = (0\ 0.31\ 1.5)$ peak (at the Cu L edge) in YBCO as evidence of dominant d symmetry CDW order, based on a plausible microscopic model.[117] In the framework presented here, the clearest evidence for dominant d symmetry would be the observation of $t_{\parallel}/t_{\perp} < 0$ at the O K edge. Future work is needed to determine if this indeed occurs in YBCO or other cuprates.

In contrast to the peaks along K, those along H do exhibit a more pronounced asymmetry ($|t_{\parallel}/t_{\perp}| \neq 1$) that may be evidence for a sizeable d symmetry component to the CDW order in YBCO. However, quantifying the relative components of Δ_d, Δ_s and $\Delta_{s'}$ requires a more detailed understanding of how these components influence the Cu L edge RSXS.

5.5.3 O K edge energy dependence of RSXS in LBCO

The energy dependence of the CDW scattering intensity at the O K edge has been analyzed in the past on either the $O_{\perp}$ or the $O_{\parallel}$ sublattice.[95, 96, 1, 215, 216] Here we present the energy dependence of both sublattices. As shown in Fig. 5.4, when scaled to equal intensity at 528.3 eV, both I_{π} (probing $O_{\parallel}$) and I_{σ} (probing $O_{\perp}$) exhibit very similar energy dependence. These measurements indicate that although the O K edge exhibits a significant asymmetry in the magnitude of scattering from $O_{\perp}$ and $O_{\parallel}$, this asymmetry does not manifest as a strong difference in the energy dependence. For σ-polarization, this energy dependence was previously shown to result from a spatial modulation in the energy of the O $1s \rightarrow 2p$ transition giving $f_n(\omega) = f(\omega + \Delta\omega_n)$, or more generally $f_n(\omega) = \overline{f}(\omega) + \Delta\omega_n \frac{\partial f(\omega)}{\partial \omega}$.[1] These measurements are also consistent with this phenomenological energy shift model, indicating that the $O_{\perp}$ and $O_{\parallel}$ sublattices are both subject to energy shifts. At present, it is unclear whether an alternate description of the energy dependence based on dynamical nesting would capture the measured polarization and energy dependence.[216]

As previously shown, the measured energy dependence does not correspond *directly* to modulations in charge density;[1] although it may be a signature of charge density modulations,[117] it could also arise due to modulations in other electronic structure parameters such as exchange interactions, the Cu–O hopping or the charge transfer energy. Identifying the microscopic origin of the RSXS energy dependence requires further investigation. To this end, we note that despite the good overall agreement between I_{π} and I_{σ} at the O K edge, the scaled scattering intensity is higher for I_{π} than for I_{σ} at 529.5 eV. This indicates that a model more sophisticated than the single parameter energy shift model is

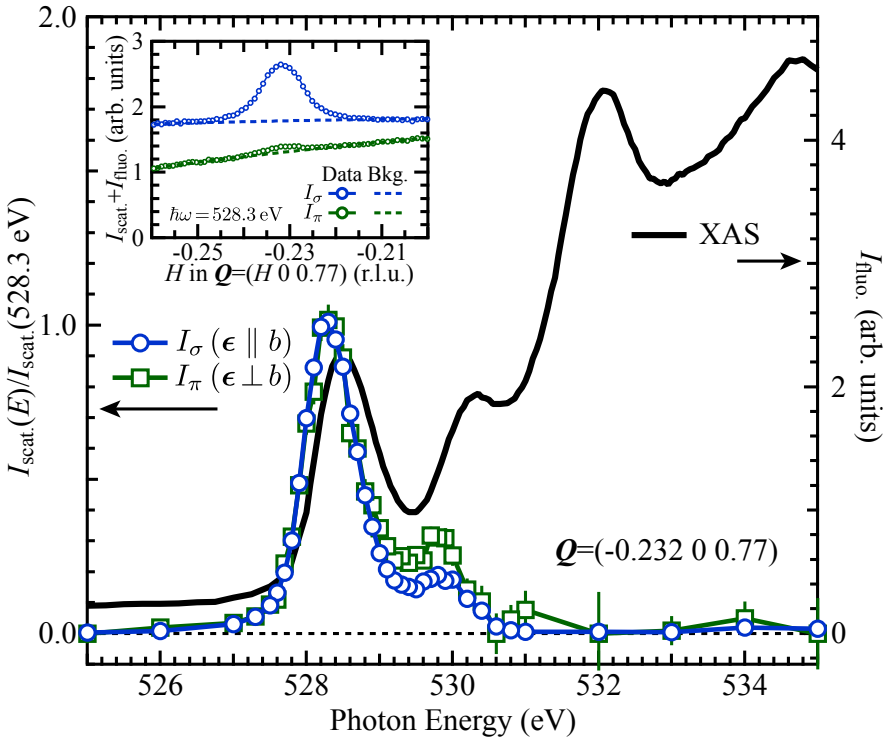

Figure 5.4 – Photon energy dependence at the O K edge of the (-0.232 0 0.77) CDW scattering intensity in LBCO with σ (blue) and π (green) incident polarization. The scattering intensities for the two polarizations, which measure the $O_\perp$ and $O_\parallel$ sublattices respectively, are scaled to 1 at 528.3 eV and compared to x-ray absorption (black) measured by total fluorescence yield with $\boldsymbol{\epsilon} \parallel \boldsymbol{a}$. Inset: Measured intensity as a function of H showing the scattering intensity along with the x-ray fluorescence background $I_{\text{fluo.}}$. The background is fit and subtracted to determine $I_{\text{scat.}}$.

needed to account for the detailed energy dependence of both I_π and I_σ and may provide a clue to the origin of the energy shifts. Specifically, the 529.5 eV peak appears to be more isotropic ($t_\parallel \simeq t_\perp$) than the lower energy peak at 528.3 eV. This difference in asymmetry may be related to how states at different energies hybridize with the Cu 3d states. The 529.5 eV peak is closer in energy to the upper Hubbard band (UHB) peak in the X-ray absorption spectrum (XAS) at 530.2 eV, which is present in the O K XAS due to strong mixing between the O 2p and Cu 3d states. In contrast, the lower energy states at 528.3 eV would be present in a doped charge-transfer insulator even in the absence of O 2p–Cu 3d hybridization. Accordingly, the C_4 symmetric character of the Cu edge scattering may be reflected more strongly at the UHB than at states closer to E_F.

5.6 Discussion

The observation of dominant s' symmetry CDW order in LBCO should be contrasted with existing evidence for predominantly d symmetry CDW in Bi-2212 and Na-CCOC.[116] If we assume both STM and RSXS have similar sensitivity to the CDW symmetry, our measurements highlight CDW orbital symmetry as an additional property of CDW order distinguishing the La-based cuprates from other cuprate families. This difference may be related to the spin ordering properties of these different families - only in the La-based cuprates does static SDW order develop with an incommensurability that is clearly related to the CDW order ($\delta_{\text{charge}} = 2\delta_{\text{spin}}$).[25, 175]. The related δ_{charge} and δ_{spin} in La-based cuprates is generally associated with a correlation between the local charge and the local anti-ferromagnetic (AF) ordering.[25] For example, in a valence bond-solid description of stripes, bond-order (CDW) and SDW order can be related, as shown in Fig. 5.1b, wherein bonds are correlated with the local AF order and sufficiently weak bonds connect ferromagnetically aligned spins.[19]

We now consider how this local charge/AF correlation is influenced by different CDW orbital symmetries. For an s' symmetry CDW, the local charge/AF order for bonds parallel and perpendicular to $\boldsymbol{Q}$ are modulated in-phase. This would naturally accommodate static SDW order consistent with observations in La-based cuprates (a commensurate, bond-centered s'-CDW+SDW order of this type is depicted in Fig. 5.1b).[25, 91] In contrast, d symmetry bond order would have local charge/AF order for bonds parallel and perpendicular to $\boldsymbol{Q}$ modulated out-of-phase with each other. Accordingly, a d symmetry CDW may prohibit static SDW order that is commensurate with the CDW, or conversely static SDW order may prohibit d symmetry CDW. This notion of a relation between CDW symmetry and static SDW order is consistent with existing theories. A recent study of CDW order in a three-orbital model that develops both spin and charge stripe order,[118] reports a predominantly s' symmetry CDW with a d/s' proportion similar in magnitude to our findings in LBCO. In contrast, theories that have reported a d symmetry CDW order have yet not exhibited both static SDW and CDW orders,[119, 75, 54, 120, 121] as found in La-based cuprates.

Finally, we speculate on the role of CDW symmetry in the competition between CDW order and superconductivity, for which various pictures have recently been proposed.[217, 63, 218, 219, 220] We note that T_c is more strongly suppressed around $p = 1/8$ in LBCO than in other cuprate families. One possibility is that this greater competition may ultimately be rooted in the symmetry of the CDW order, which may have a greater pair-breaking effect for s' symmetry than for d symmetry.

5.7 Methods

RSXS and x-ray absorption spectroscopy (XAS) measurements at the Cu L and O K edges were performed using the in-vacuum four-circle diffractometer[168] at the Canadian Light Source's REIXS beam line on single-crystal samples of $YBa_2Cu_3O_{6.67}$ (T_c = 64.5 K, p = 0.116) and $La_{1.875}Ba_{0.125}CuO_4$ ($T_c \approx 4$ K). The LBCO crystals were previously annealed in an $^{17}O_2$ environment.[221] Reciprocal lattice units (r.l.u.) were defined using the lattice constants a=3.84 Å, b=3.88 Å, c=11.74 Å for YBCO and a=b=3.787 Å, c=13.24 Å for LBCO. The YBCO sample was polished and two LBCO samples were cleaved in air prior to measurement.

The crystallographic orientation of the samples was verified in the diffractometer using appropriate structural Bragg peaks at ∼2 keV. LBCO samples were mounted separately to flat and wedge-shaped sample plugs. The first sample (S1) exhibited CDW peaks at $\boldsymbol{Q}$ = (±0.232 0 L), whereas the second sample (S2) had them at $\boldsymbol{Q}$ = (±0.237 0 L), indicating a slight difference in doping (incommensurability). For the O K (Cu L) edge azimuthal rotation experiment on LBCO, the wedge angle θ_w was 53° (34°) (see Fig. 5.1a). The formula defining these wedge angles is derived in Section A.2.

Due to a limited motion range on the ϕ motor, manual rotations of ϕ were performed with an in-vacuum screwdriver. Photographs through a levelled telescope were used to measure ϕ, yielding uncertainties of $\sim 1°$, and referenced to $\phi = 0°$ as set by the crystallographic orientation. The measurements on LBCO were performed at $T = 22$ K whereas those on YBCO were at 60 K and 160 K. The vacuum chamber pressure for all measurements was $P < 1 \times 10^{-9}$ Torr. X-ray absorption was measured by total fluorescence yield. Additional details about background subtractions, peak fitting, model calculations and parameter estimation are contained in section 5.10.

5.8 Orbital symmetry of CDW order on oxygen sites

Following Ref. [75], non s-wave symmetry CDW order in a single-band model of the CuO_2 planes can be parameterized by Δ_{ij}, which characterizes the charge modulation (or some other quantity related to charge order such as an energy shift)[2, 1] on bonds connecting nearest neighbour Cu sites i and j:

$$\Delta_{ij} = \sum_{\boldsymbol{Q}^*} \left[\frac{1}{V} \sum_{\boldsymbol{k}} e^{i\boldsymbol{k}\cdot(\boldsymbol{r}_i - \boldsymbol{r}_j)} \Delta_{\boldsymbol{Q}^*}(\boldsymbol{k}) \right] e^{i\boldsymbol{Q}^*\cdot(\boldsymbol{r}_i + \boldsymbol{r}_j)/2}, \tag{5.6}$$

where V is volume and $\boldsymbol{Q}^*$ are the wave vectors of the CDW order: $\boldsymbol{Q}^* = (\pm Q_m,\, 0,\, 0)$ or $(0,\, \pm Q_m,\, 0)$ for 1D stripes and $\boldsymbol{Q}^* = (\pm Q_m,\, 0,\, 0)$ and $(0,\, \pm Q_m,\, 0)$ for checkerboard order. In this prescription, $\boldsymbol{r}_i$ indexes the Cu sites so that Δ_{ii} corresponds to Cu sites and Δ_{ij} with $i \neq j$ corresponds to bonds between Cu sites (i.e. O sites). Including the s, s' and d symmetry terms,

$$\Delta_{\boldsymbol{Q}^*}(\boldsymbol{k}) = \begin{cases} \Delta_s + \Delta_{s'}(\cos k_x a + \cos k_y b) + \Delta_d(\cos k_x a - \cos k_y b) & \boldsymbol{Q}^* = (\pm Q_m, 0, 0) \\ \Delta_s + \Delta_{s'}(\cos k_x a + \cos k_y b) - \Delta_d(\cos k_x a - \cos k_y b) & \boldsymbol{Q}^* = (0, \pm Q_m, 0) \end{cases} \tag{5.7}$$

giving rise to spatial modulations of Δ_{ij} given in Fig. 5.1b.

This model identifies two distinct sublattices for the bonds, ij: one set of bonds, A, having $\boldsymbol{r}_j = \boldsymbol{r}_i \pm a\hat{x}$ and the other set, B, having $\boldsymbol{r}_j = \boldsymbol{r}_i \pm b\hat{y}$. For these two sublattices, a stripe state with $\boldsymbol{Q}^* = (\pm Q_m,\, 0,\, 0)$ has

$$\begin{aligned} \Delta_{iA} &= (\Delta_{s'} + \Delta_d)\cos[Q_m(r_{ix} + a/2)] \\ \Delta_{iB} &= (\Delta_{s'} - \Delta_d)\cos[Q_m r_{ix}], \end{aligned} \tag{5.8}$$

whereas a checkerboard with $\boldsymbol{Q}^* = (\pm Q_m,\, 0,\, 0)$ and $\boldsymbol{Q}^* = (0,\, \pm Q_m,\, 0)$ has

$$\begin{aligned} \Delta_{iA} &= (\Delta_{s'} + \Delta_d)\cos[Q_m(r_{ix} + a/2)] + (\Delta_{s'} - \Delta_d)\cos[Q_m r_{iy}] \\ \Delta_{iB} &= (\Delta_{s'} - \Delta_d)\cos[Q_m r_{ix}] + (\Delta_{s'} + \Delta_d)\cos[Q_m(r_{iy} + b/2)]. \end{aligned} \tag{5.9}$$

Translating this model into bond order on the O atoms, one can associate Δ_{iA} and Δ_{iB} with O atoms having holes in $2p_x$ and $2p_y$ orbitals, respectively. Next, we assume that $\Delta_{iA(B)}$ are proportional to modulations in the atomic scattering form factor $\Delta F_{O,iA(B)}(\omega)$ giving

$$\Delta F_{O,iA}(\omega) = C(\omega) \begin{bmatrix} \Delta_{iA} & 0 & 0 \\ 0 & 0 & 0 \\ 0 & 0 & 0 \end{bmatrix} \quad \text{and} \quad \Delta F_{O,iB}(\omega) = C(\omega) \begin{bmatrix} 0 & 0 & 0 \\ 0 & \Delta_{iB} & 0 \\ 0 & 0 & 0 \end{bmatrix}, \tag{5.10}$$

where $C(\omega)$ is a proportionality constant common to $\Delta F_{O,iA}(\omega)$ and $\Delta F_{O,iB}(\omega)$. For scattering at the O K edge in LBCO, the assumption that the energy dependence factorizes from the modulation amplitude and is common to the A and B sublattices seems justified given the approximate proportionality between the I_π and I_σ scattering (see Fig. 5.4). Then, for a measured $\boldsymbol{Q} = (Q_m\ 0\ L)$,

$$t_\parallel = t_{aa} = \frac{C(\omega)}{N}\sum_i(\Delta_{s'} + \Delta_d)\cos[Q_m(r_{ix} + a/2)]e^{iQ_m(r_{ix}+a/2)} \text{ and} \tag{5.11}$$

$$t_\perp = t_{bb} = \frac{C(\omega)}{N}\sum_i(\Delta_{s'} - \Delta_d)\cos[Q_m r_{ix}]e^{iQ_m r_{ix}}, \tag{5.12}$$

where r_{ix} is the position of the Cu sites. Combining Eqs. 5.11 and 5.12 gives

$$\frac{t_\parallel}{t_\perp} = \frac{\Delta_{s'} + \Delta_d}{\Delta_{s'} - \Delta_d}, \tag{5.13}$$

which is written in terms of $\Delta_d/\Delta_{s'}$ in Eq. 5.5, parametrizing how the experimental observables, $t_\parallel$ and $t_\perp$, can be mapped to the symmetry of the CDW order for O sites in the CuO_2 plane.

5.9 Polarization Dependent Scattering Model

5.9.1 Model derivation and effect of absorption correction

The expression for the polarization dependent scattering intensity (Eq. 5.1) references the incident and scattered photon polarization vectors relative to the crystallographic orientation of the sample. To see how variation of the experimental geometry (see Fig. 5.1a) affects Eq. 5.1, we express the photon polarization in the laboratory reference frame (denoted by the subscript ℓ) and Eq. 5.1 is rewritten as

$$I(\boldsymbol{\epsilon}_i, \omega, \boldsymbol{Q}) \propto \left|\boldsymbol{\epsilon}^*_{f,\ell} \cdot RT(\omega, \boldsymbol{Q})R^\top \cdot \boldsymbol{\epsilon}_{i,\ell}\right|^2, \tag{5.14}$$

where R is a rotation matrix that rotates the sample ($T(\omega, \boldsymbol{Q})$ is still referenced to the crystallographic axes) into the geometry necessary to satisfy the Bragg condition for a particular photon energy $\hbar\omega$ and momentum transfer $\boldsymbol{Q}$, and can also rotate the sample azimuthally (ϕ) about $\boldsymbol{Q}$.[117] For photon detection without polarization sensitivity, both $\boldsymbol{\epsilon}_{f,\sigma}$ and $\boldsymbol{\epsilon}_{f,\pi}$ scattering contribute to the scattering intensity, giving $I(\boldsymbol{\epsilon}_i) = I_{\boldsymbol{\epsilon}_i,\sigma'} + I_{\boldsymbol{\epsilon}_i,\pi'}$.

In calculating the expected scattering intensity for a given symmetry of T using Eq. 5.14, the rotations that the sample and photon polarization undergo relative to the lab reference frame must be specified. We incorporate a lab reference frame with $\boldsymbol{k}_i$ along the $(1\ 0\ 0)_\ell$ direction and the scattering plane being orthogonal to the $(0\ 0\ 1)_\ell$ direction, giving $\boldsymbol{\epsilon}_{i,\sigma}$ $= (0\ 0\ 1)_\ell$ and $\boldsymbol{\epsilon}_{i,\pi} = (0\ 1\ 0)_\ell$. The sample can be mounted on a wedge, defined by a wedge angle, θ_w, ($\theta_w = 0$ corresponds to a flat surface, i.e. no wedge) that can be rotated azimuthally about $(0\ 1\ 0)_\ell$ by an angle ϕ. The azimuthally rotated wedge can then be rotated by an angle θ about the $(0\ 0\ 1)_\ell$ axis. For $\theta_w = 0$, $\phi = 0$ and $\theta = 0$, the samples are mounted such that the crystalline axes c // $(0\ 1\ 0)_\ell$ and a [b] along $(1\ 0\ 0)_\ell$ for investigation of $(H\ 0\ L)$ [$(0\ K\ L)$] peaks. These rotations can be expressed as a rotation matrix R acting on T given by

$$R = R(\theta)_{001}R(\phi)_{010}R(\theta_w)_{001}R_O, \tag{5.15}$$

where, for example, $R(\theta)_{001}$ rotates the sample by an angle θ about the $(0\ 0\ 1)_\ell$ axis and R_O provides an initial orientation of the sample to give $c \parallel (0\ 1\ 0)_\ell$ and a or b along $(1\ 0\ 0)_\ell$. The scattered photon polarization, $\boldsymbol{\epsilon}_f$, is determined by $\boldsymbol{\epsilon}_i$ and $RTR^\top$ and can be expressed in terms of $\boldsymbol{\epsilon}_{f,\sigma}$ and $\boldsymbol{\epsilon}_{f,\pi}$ as

$$\boldsymbol{\epsilon}_f = \frac{(\boldsymbol{\epsilon}^*_{f,\sigma}\cdot RTR^\top\cdot\boldsymbol{\epsilon}_i)\boldsymbol{\epsilon}_{f,\sigma} + (\boldsymbol{\epsilon}^*_{f,\pi}\cdot RTR^\top\cdot\boldsymbol{\epsilon}_i)\boldsymbol{\epsilon}_{f,\pi}}{|(\boldsymbol{\epsilon}^*_{f,\sigma}\cdot RTR^\top\cdot\boldsymbol{\epsilon}_i)\boldsymbol{\epsilon}_{f,\sigma} + (\boldsymbol{\epsilon}^*_{f,\pi}\cdot RTR^\top\cdot\boldsymbol{\epsilon}_i)\boldsymbol{\epsilon}_{f,\pi}|}. \tag{5.16}$$

where $\boldsymbol{\epsilon}_{f,\sigma} = (0\ 0\ 1)_\ell$, $\boldsymbol{\epsilon}_{f,\pi} = (-\sin\Omega\ \cos\Omega\ 0)_\ell$ and Ω is the detector angle relative to the incident beam. The scattering intensity can be determined without knowledge of $\boldsymbol{\epsilon}_f$ by

$$I(\boldsymbol{\epsilon}_i,\omega,\boldsymbol{Q}) \propto \left|\boldsymbol{\epsilon}^*_{f,\sigma}\cdot RT(\omega,\boldsymbol{Q})R^\top\cdot\boldsymbol{\epsilon}_i\right|^2 + \left|\boldsymbol{\epsilon}^*_{f,\pi}\cdot RT(\omega,\boldsymbol{Q})R^\top\cdot\boldsymbol{\epsilon}_i\right|^2. \tag{5.17}$$

When comparing experimental results to model calculations, it is also important to account for the polarization dependent x-ray absorption cross-section, $\mu(\omega,\boldsymbol{\epsilon})$, of the incident and scattered photons. This is a minor correction in more electronically isotropic materials, but can have a significant impact in the cuprates, where the absorption coefficient along the a, b and c axes varies considerably. To account for geometry dependent attenuation of the incident and scattered x-rays, Eq. 5.17 must be corrected according to

$$I_{\text{abs}}(\boldsymbol{\epsilon}_i,\omega,\boldsymbol{Q}) \propto \frac{I(\boldsymbol{\epsilon}_i,\omega,\boldsymbol{Q})}{\mu_i + \mu_f\frac{\sin\alpha}{\sin\beta}}, \tag{5.18}$$

where α and β are the angles of the incident and scattered beam relative to the sample surface in the scattering plane and μ_i and μ_f are the linear absorption coefficients of the

incident and scattered photons respectively. These are given by

$$\mu_i \propto \mathrm{Im}\left(\boldsymbol{\epsilon}_i^* R\overline{F}R^\top \boldsymbol{\epsilon}_i\right) \text{ and} \tag{5.19}$$

$$\mu_f \propto \mathrm{Im}\left(\boldsymbol{\epsilon}_f^* R\overline{F}R^\top \boldsymbol{\epsilon}_f\right), \tag{5.20}$$

where $\overline{F}$ is the scattering tensor averaged over all atomic sites (O, Ba, Cu, ...) and includes both resonant and non-resonant contributions. Mirroring the polarization dependent x-ray absorption in the cuprates [105, 84, 1], $\mathrm{Im}(\overline{f_{aa}}) \simeq \mathrm{Im}(\overline{f_{bb}})$ and we estimate $\mathrm{Im}(\overline{f_{cc}})/\mathrm{Im}(\overline{f_{aa}}) \simeq 0.74$ at the O K edge (528.3 eV) in LBCO, 0.45 at the Cu L edge (931.4 eV) in LBCO and 0.66 at the Cu L edge (931.4 eV) in YBCO. [84, 1] For these estimates in LBCO, we assume that the absorption coefficient is similar to that of LNSCO, where polarization dependent XAS is available.

The effect of the absorption correction on the ϕ and L dependence of the model are illustrated in Fig. 5.5 for LBCO at the O K edge. The calculation without any absorption correction (Eq. 5.17) is shown as thin solid lines. The effect of including the absorption correction (Eq. 5.18) is shown with dashed lines. For the usual case where the sample surface is parallel to the wedge surface, the dashed line would be the ideal calculation. However, cleaving the sample LBCO S1 yielded a surface that was not parallel to the sample holder (this can also occur for intentionally miscut surfaces), affecting the angles α and β that enter into Eq. 5.18. The actual surface orientation was estimated with an optical microscope and included in the model calculations, shown as thick lines. The ϕ dependence of I_π and I_σ (Fig. 5.5a) changes significantly when the absorption correction and the orientation of the surface are incorporated. Examination of Fig. 5.5a illustrates that modelling the azimuthal dependence of I_π and I_σ directly (as shown in Fig. 5.2a) requires a full characterization of the experimental geometry and the effect of absorption on the incident and scattered photons.

When evaluating the ratio of I_π and I_σ, however, the important differences seen in Fig. 5.5a are largely factored out, as shown in Figs. 5.5b and 5.5c. The effect of the absorption correction is modest, on the order of $\sim$ 5%-15% near $\phi = 0°, 97°, 180°$, but can be important in accurately determining the parameters $t_\parallel/t_\perp$ and $t_{cc}/t_\perp$. The effect of the angled surface is seen to be less important in calculating the ratios of I_π and I_σ (Figs. 5.5b and 5.5c). This highlights that our estimate of the sample surface orientation (due to the cleave) is not important in the determination of $t_\parallel/t_\perp$ and $t_{cc}/t_\perp$ from fits to the ratio I_π/I_σ.

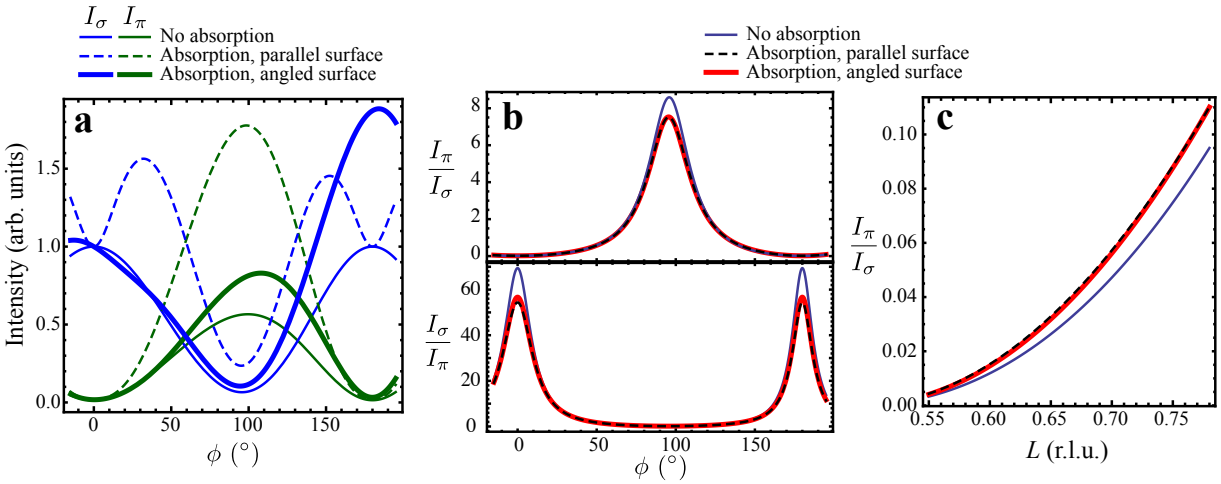

Figure 5.5 – Model calculations of the ϕ and L dependence of the scattering intensity in LBCO at the O K edge ($t_\parallel/t_\perp = 0.612$, $t_{cc}/t_\perp = 0.034$). **a.** I_π and I_σ vs. ϕ calculated by Eq. 5.17 (no absorption, thin line) and Eq. 5.18 (absorption) for a parallel surface (dashed line) and the angled surface of the measured sample (thick line). The ratios of I_π and I_σ vs. ϕ (**b**) and L (**c**).

5.9.2 Influence of CDW orbital symmetry and c axis scattering contributions on model

The sensitivity of the model to ϕ and the scattering geometry is most readily understood through calculations for representative sets of parameters corresponding to different CDW orbital symmetries. In Fig. 5.6 we show the ϕ and L dependence of I_π/I_σ calculated according to Eq. 5.18 for values of $t_\parallel/t_\perp = \pm 1, \pm 0.612, \pm 0.612^{-1}$. We can interpret these cases using Eq. 5.5 (see Fig. 5.2f for a mapping between $t_\parallel/t_\perp$ and $\Delta_d/\Delta_{s'}$). The case $t_\parallel/t_\perp = +1$ (-1) corresponds to pure s' (d) CDW symmetry (red lines in Fig. 5.6). We see that d symmetry (red, dashed) would give rise to $\sim 3.3\times$ larger maximum in I_π/I_σ than s' symmetry (red, solid) and the maximum in ϕ would be located at $\phi \approx 71°$ rather than $\phi \approx 99°$. The case $t_\parallel/t_\perp = +0.612$ (-0.612) corresponds to $\Delta_d/\Delta_{s'} = -0.241$ (-0.241^{-1}). This is an *anti-phase*, mixed d and s' state, with mostly s' (d) symmetry, which would appear experimentally as a maximum in I_π/I_σ near $\phi \approx 79°$ $(\phi \approx 96°)$. The mostly d symmetry (black, dashed) case would give rise to a $\sim 2\times$ larger maximum in I_π/I_σ than mostly s' symmetry (black, solid). Similarly, $t_\parallel/t_\perp = +0.612^{-1}$ (-0.612^{-1}) corresponds to $\Delta_d/\Delta_{s'} = 0.241$ (0.241^{-1}). This is an *in-phase*, mixed d and s' state, with mostly s' (d) symmetry. Again, the different peak positions and maximum values of I_π/I_σ would distinguish between the mostly s' and d cases.

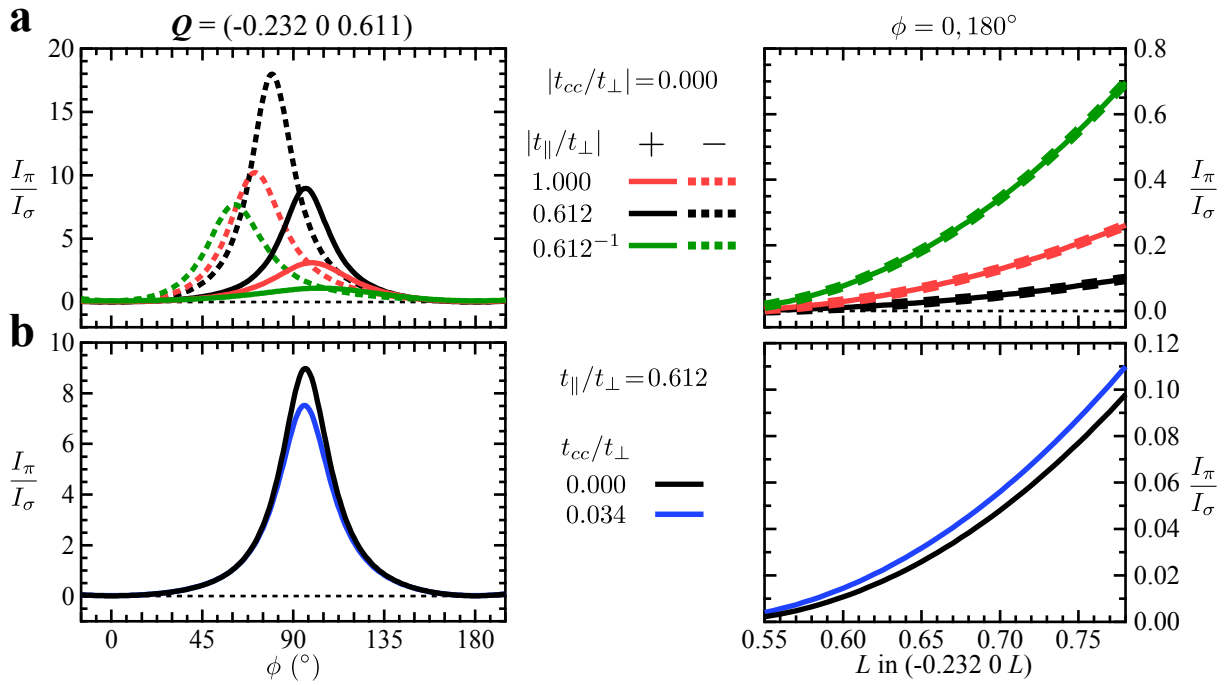

Figure 5.6 – Model calculations for different cases of orbital symmetry in LBCO at the O K edge. **a.** Calculated ϕ (left panels) and L (right panels) dependence of I_π/I_σ showing sensitivity to the sign and magnitude of $t_\parallel/t_\perp$. **b.** Calculated ϕ and L dependence of I_π/I_σ demonstrating sensitivity to the c axis contribution $t_{cc}/t_\perp$ of T. The blue curve is the best fit to the data.

From this discussion and examination of Fig. 5.6a, it becomes apparent that the ϕ dependence is sensitive to the sign and magnitude of $t_\parallel/t_\perp$. In contrast, the L dependence is sensitive to the magnitude but not the sign of $t_\parallel/t_\perp$. Combining both types of measurements enhances the reliability of experimentally determining the sign and magnitude of $t_\parallel/t_\perp$, ultimately enabling the determination of $\Delta_d/\Delta_{s'}$. This sensitivity to the magnitude and sign of $\Delta_d/\Delta_{s'}$ affirms that polarization dependent resonant soft x-ray scattering is a powerful tool in discerning the symmetry of CDW order in the cuprates.

In Fig. 5.6b, we illustrate how a c axis contribution to the scattering influences the model calculation. The blue curves are the best fit to the experimental data on LBCO at the O K edge. The effect of a non-zero $t_{cc}/t_\perp$ is modest and similar in magnitude to the effect of the absorption correction seen in Figs. 5.5b and 5.5c. This highlights the importance of including a full geometry dependent absorption correction in the model, as not doing so could lead to erroneous determinations of $t_\parallel/t_\perp$ and $t_{cc}/t_\perp$.

5.10 Experimental data

Here we provide the experimental data that was used to determine the ϕ and L dependences of I_σ and I_π shown in Fig. 5.2. Fig. 5.7 shows the ϕ dependence of I_σ and I_π in LBCO at the O K edge ($\boldsymbol{Q} = (-0.232\ 0\ 0.611)$, $\hbar\omega = 528.3$ eV). For each scan, the detector position (at angle Ω) was kept constant and the crystal was rotated about the vertical axis ($\perp$ to the scattering plane) by $\pm 15°$. I_σ and I_π were determined by first subtracting the x-ray fluorescence background ($I_{\text{fluo.}}$) using a polynomial fit that excluded the peak region and then fitting the resulting data ($I_{\text{scat.}}$) with a Lorentzian curve whose amplitude is reported in Fig. 5.2a. Figs. 5.7a and 5.7b show this analysis procedure for a representative set of measurements. Fig. 5.7c shows a projected view of the background-subtracted I_σ and I_π data for the full range of ϕ used in fitting to the scattering model.

Here we plot this data against $\Delta\theta = \theta - \theta_0$, where θ_0 is the center of the peak as identified by peak fitting. Due to a slight misalignment of the a and c crystal axes during sample mounting ($\sim 0.6°$ about wedge normal), the scattering geometry gradually shifted away from the nominal scattering geometry as ϕ was varied. This movement was small enough that minor adjustments to the instrument's χ angle ($< 1.5°$) could be used to reposition the CDW peak in the scattering plane, but it did moderately shift the apparent peak position in θ as ϕ was adjusted (the maximum deviation was $\sim 1°$). By plotting against $\Delta\theta$, we account for these minor shifts.

The measurement scheme we have employed (Ω remains fixed while θ is rotated) has the advantage of faster data collection speed and reduced noise, but a consequence is that the H, K and L indices all vary to differing degrees that depend on ϕ. These scans thus correspond to cuts in $\boldsymbol{Q}$ space, as illustrated in Fig. 5.8a, that depend on ϕ. Fig. 5.8b shows a projection onto the H–K plane of these same cuts. As can be seen, a scan at $\phi = 0°$ is mostly along H, with no K and some L variation, whereas one at $\phi = 90°$ is mostly along K, with some H and L variation.

In Fig. 5.8c, we present the same data as in Fig. 5.7 but here we have converted θ values into H, K and L indices and plotted the normalized sum of I_π and I_σ scattering in the H–K plane. H and K were shifted by H_0 and K_0 in order to account for the shifts in θ discussed above (ie. the data is plotted against ΔH and ΔK). The normalization is to the sum of the fit amplitudes of the I_π and I_σ data. In this form, the data can be fit to a Lorentzian function $I = A\left[(\Delta H/\gamma_H)^2 + (\Delta K/\gamma_K)^2 + 1\right]^{-1}$, where A is the amplitude and $\gamma_{(H,K)}$ is the HWHM. The H and K correlation lengths are related to $\gamma_{(H,K)}$ according to $\xi_{(H,K)} = (a, b)/(2\pi\gamma_{(H,K)})$. Fitting the normalized $I_\pi + I_\sigma$ data with this functional form (see Fig. 5.8d) gives $\xi_H \approx 215$ Å and $\xi_K \approx 184$ Å. These correlation lengths and their $\sim 17\%$ anisotropy appear consistent with prior hard x-ray scattering data on LBCO.[94]

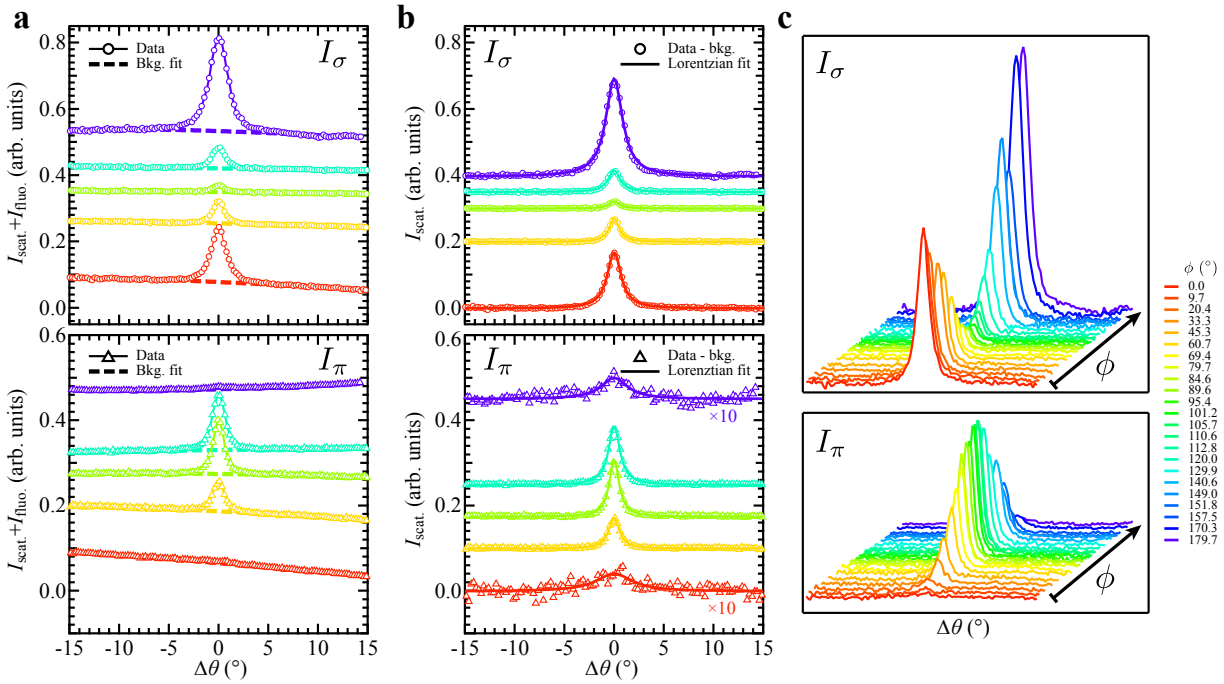

Figure 5.7 – Scans through the CDW peak as a function of ϕ for LBCO at the O K edge. **a.** Normalized intensity of scattering and x-ray fluorescence (open symbols) for incident σ (top panel) and π (bottom panel) photon polarization and polynomial background fit (dashed lines) for select ϕ values. **b.** Background-subtracted scattering intensity I_σ (open circles) and I_π (open triangles), and corresponding Lorenztian fits (solid lines). In **a** and **b** the data is offset vertically for clarity. **c.** Projected view of background-subtracted I_σ (top) and I_π (bottom) vs. ϕ for full range of measured angles. ϕ values are indicated in legend on right.

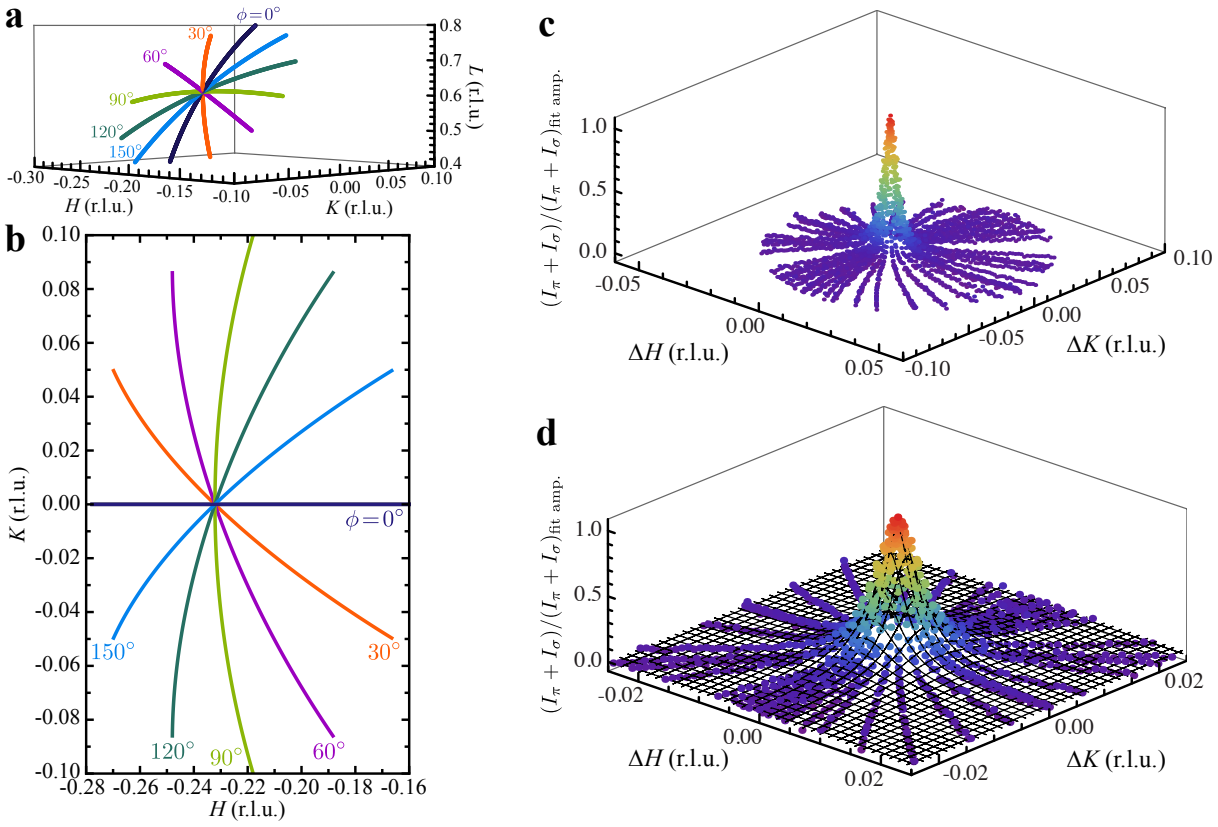

Figure 5.8 – Cuts in $\boldsymbol{Q}$ space and ϕ dependence of $I_\pi + I_\sigma$ in H–K plane. **a.** Depiction of cuts in H, K, and L when θ is varied by $\pm 15°$ and Ω is kept fixed for indicated ϕ values. **b.** Projection of these cuts onto the H–K plane. **c.** $I_\pi + I_\sigma$ data, normalized to the sum of their fit amplitudes, plotted in H–K plane, and shifted to the origin. **d.** A Lorentzian fit (mesh) to the data giving the reported correlation lengths in H and K.

Fig. 5.9 shows the photon energy dependence of I_σ and I_π vs. H for LBCO at the O K edge with $\boldsymbol{Q} = (H\ 0\ 0.77)$. Similar to the ϕ dependent data, the x-ray fluorescence background was first subtracted using a polynomial fit excluding the peak region (the backgrounds shown in Fig. 5.7a are representative of this procedure). Lorentzian fits were then used to determine the scattering intensities reported in Fig. 5.4.

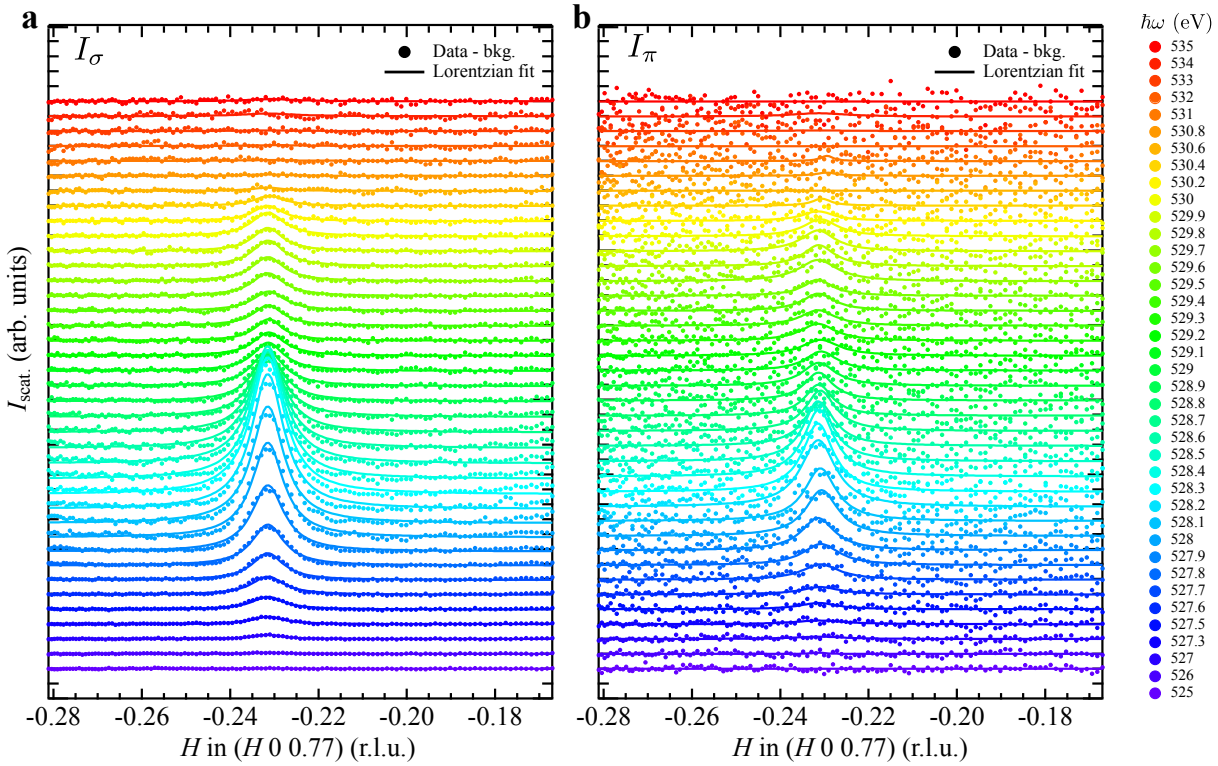

Figure 5.9 – Energy dependence of CDW scattering peak in LBCO at the O K edge for σ (**a**) and π (**b**) incident photon polarization. Solid lines are Lorenztian fits to the background-subtracted data (filled circles). Photon energy indicated in legend on the right. Data are offset for clarity.

Fig. 5.10 shows the ϕ dependence of I_σ (top panels) and I_π (lower panels) of LBCO at the Cu L edge, $\boldsymbol{Q} = (-0.236\ 0\ 1.192)$, $\hbar\omega = 931.4$ eV. As was done for the O K edge, the x-ray fluorescence background was subtracted using a polynomial fit excluding the peak region. Similar to the O K edge ϕ rotation data, we plot the Cu L edge data against $\Delta\theta$ to account for shifts in the scattering geometry as ϕ was varied (in this case, a maximum shift in θ of $\sim 5^\circ$ and χ corrections up to $\sim 4^\circ$ were used, although the mounting error was *smaller* for this measurement [$\sim 0.4^\circ$], there is a greater sensitivity to mounting errors at 931.4 eV as compared to 528.5 eV). In addition to scans with Ω-fixed, we performed scans with $\Omega = 2\theta$ and these are plotted against $\Delta\Omega$. These latter scans correspond to continually measuring the same arc in the H–L plane whereas the Ω-fixed scans correspond to arcs that vary with ϕ, as shown in the right panels of Fig. 5.10. The I_π and I_σ values reported in Fig. 5.2b are the average Lorenztian fit amplitude of both types of scan.

Fig. 5.11 shows the L dependence of I_σ and I_π vs. H of LBCO at the Cu L edge, $\boldsymbol{Q} = (0.232\ 0\ L)$, $\hbar\omega = 931.3$ eV (top panels) and at the O K edge, $\boldsymbol{Q} = (-0.232\ 0\ L)$, $\hbar\omega = 528.3$ eV (bottom panels). Similar to the ϕ dependent data, the x-ray fluorescence background was subtracted using a polynomial fit excluding the peak region. Lorentzian fits were then used to determine the scattering intensities reported in Figs. 5.2c and 5.2d.

Fig. 5.12 shows the L dependence of I_σ and I_π of YBCO at the Cu L edge ($\hbar\omega = 931.3$ eV) for the CDW peak along $\pm H$ and $\pm K$. In this case the background subtraction was accomplished by subtracting the measured x-ray fluorescence at 160 K from the measurement at 60 K. Figs. 5.12a and 5.12b show a representative set of such backgrounds. Lorentzian fits were then used to determine the scattering intensities reported in Fig. 5.3.

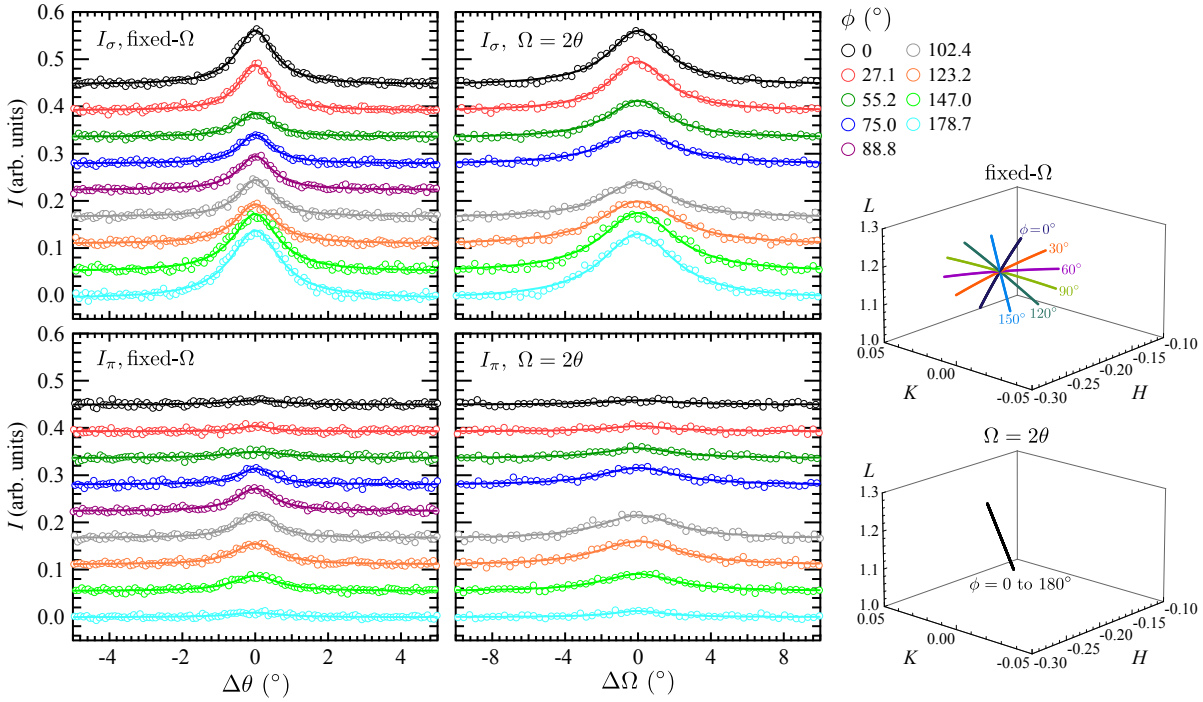

Figure 5.10 – Scans through the CDW peak as a function of ϕ for LBCO at the Cu L edge. The top (bottom) panels are for I_σ (I_π) and the left (middle) panels are for fixed-Ω (Ω = 2θ) scans at the ϕ values indicated in the top right legend. The cuts through $\boldsymbol{Q}$ space for fixed-Ω and Ω = 2θ scans are illustrated in the lower right;

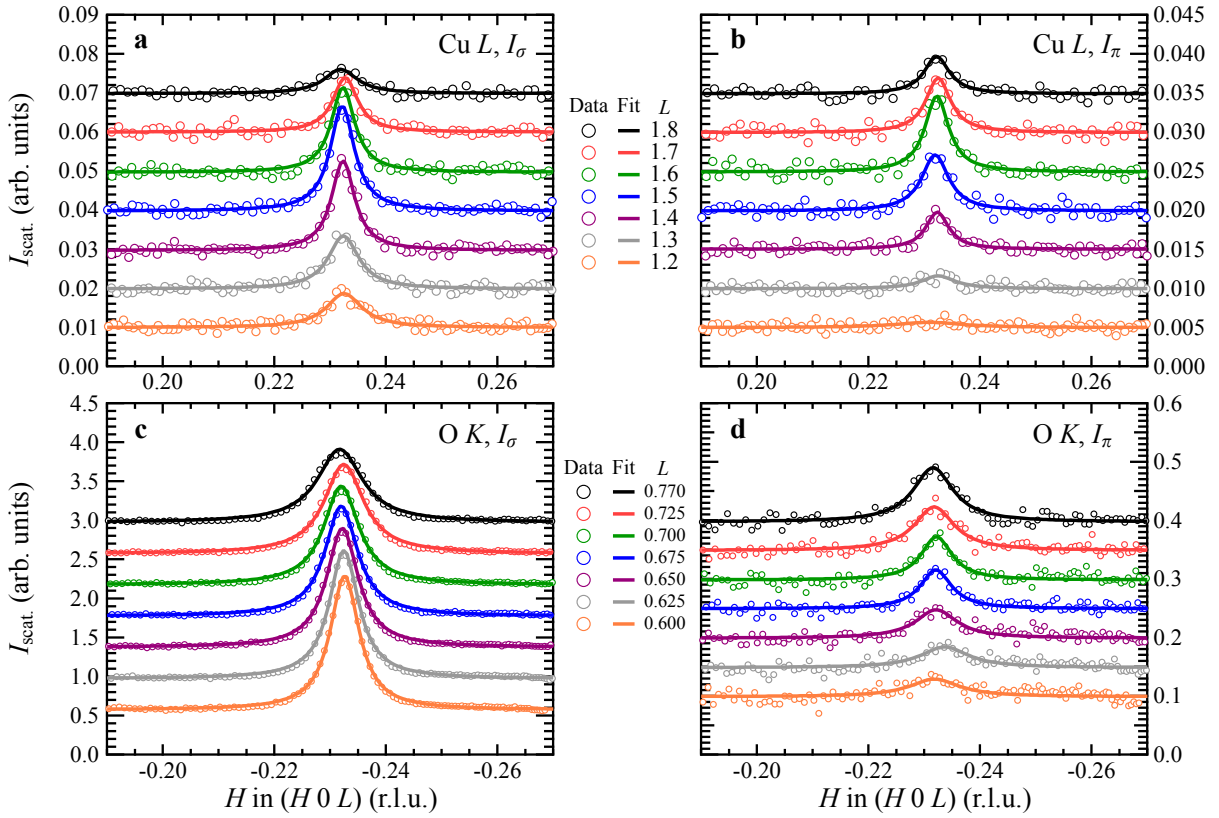

Figure 5.11 – L dependence of CDW scattering intensity in LBCO at the Cu L edge (**a**: I_σ and **b**: I_π vs. H) and O K (**c**: I_σ and **d**: I_π vs. H) edges. Open circles are background-subtracted data and solid lines are Lorenztian fits. Data are offset for clarity.

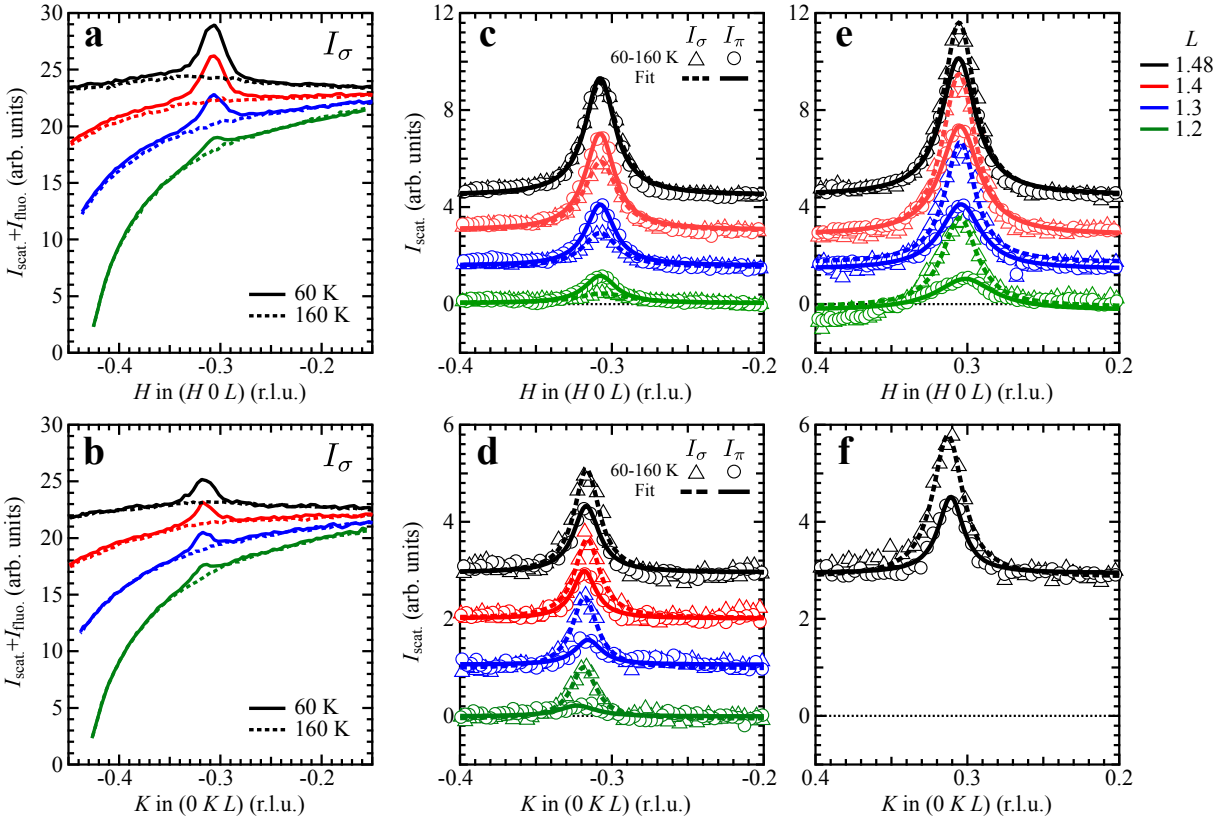

Figure 5.12 – L dependence of CDW scattering intensity in YBCO at the Cu L edge for scans along H (top row) and K (bottom row). **a-b**. Normalized intensity of scattering and x-ray fluorescence for incident σ polarization along H (**a**) and K (**b**) at 60 K (solid lines) and 160 K (dashed lines). **c-f**. Background-subtracted scattering intensity (60-160 K) for σ (open triangles) and π (open circles) incident photon polarization along $-H$ (**c**), $-K$ (**d**), $+H$ (**e**) and $+K$ (**f**). Dashed (solid) lines are Lorenztian fits to I_σ (I_π). L values are indicated in legend on right. Data in **c-f** are offset for clarity.

5.11 Parameter estimation and confidence regions

The parameters $t_\parallel/t_\perp$ and $t_{cc}/t_\perp$ were determined by unconstrained, weighted least-squares fitting of the experimental data to $I(\boldsymbol{\epsilon}_{i,\pi}, \omega, \boldsymbol{Q})/I(\boldsymbol{\epsilon}_{i,\sigma}, \omega, \boldsymbol{Q})$, as defined by Eq. 5.18. These were the only free parameters in the fit. For LBCO at the O K edge, both the ϕ and L dependent data were fit simultaneously. This simultaneous fit narrowed the confidence regions (CR) as compared to fitting either dataset individually. Since the ϕ dependence at the Cu L edge in YBCO and LBCO were not measured here, the fits in those cases are to the L dependence. Fitting to the L dependence alone does not determine the signs of $t_\parallel/t_\perp$ and $t_{cc}/t_\perp$ (see Fig. 5.6a), but can still constrain their absolute values and their relative sign (ie., $t_\parallel/t_\perp$ and $t_{cc}/t_\perp$ will either have the same or opposite sign).

Although least-squares fitting provides standard errors for the best fit parameters, an examination of χ_0^2, the reduced chi-squared statistic, throughout the parameter space identified that the 95% confidence intervals defined by the standard errors (rectangular regions in Fig. 5.2e) underestimated the regions of high confidence. The high confidence regions were better described by contours of constant χ_0^2, appearing as ellipses in the $t_\parallel/t_\perp$ – $t_{cc}/t_\perp$ plane for the LBCO O K and Cu L edge data. The contours were selected to represent regions where there was a 95% (or higher) likelihood that the model described the experimental data. To illustrate this point and the level of confidence with which the reported values $t_\parallel/t_\perp$ and $t_{cc}/t_\perp$ are given, we show here how the model calculations vary across the parameter space in regions around the best fit parameters. This analysis is shown in Fig. 5.13 for LBCO at the O K edge, Fig. 5.14 for LBCO at the Cu L edge, and Fig. 5.15 for YBCO at the Cu L edge.

We caution that the absolute values of χ_0^2 reported here should not be over-interpreted as the formal definition of χ_0^2 requires that weights be calculated from true variances (ie. σ from a normal distribution of repeated measurements). Here, we used statistical errors from fitting the CDW peak to estimate the variance, which can lead to $\chi_0^2 < 1$, indicating that the experimental uncertainty underestimates the variance. Although the magnitudes of χ_0^2 are affected by this detail, one can still use this statistic as a means of identifying regions of parameter space where the model yields good agreement with the data. It is in this sense that we have opted to define the high confidence regions of parameter space where the model agrees with the data.

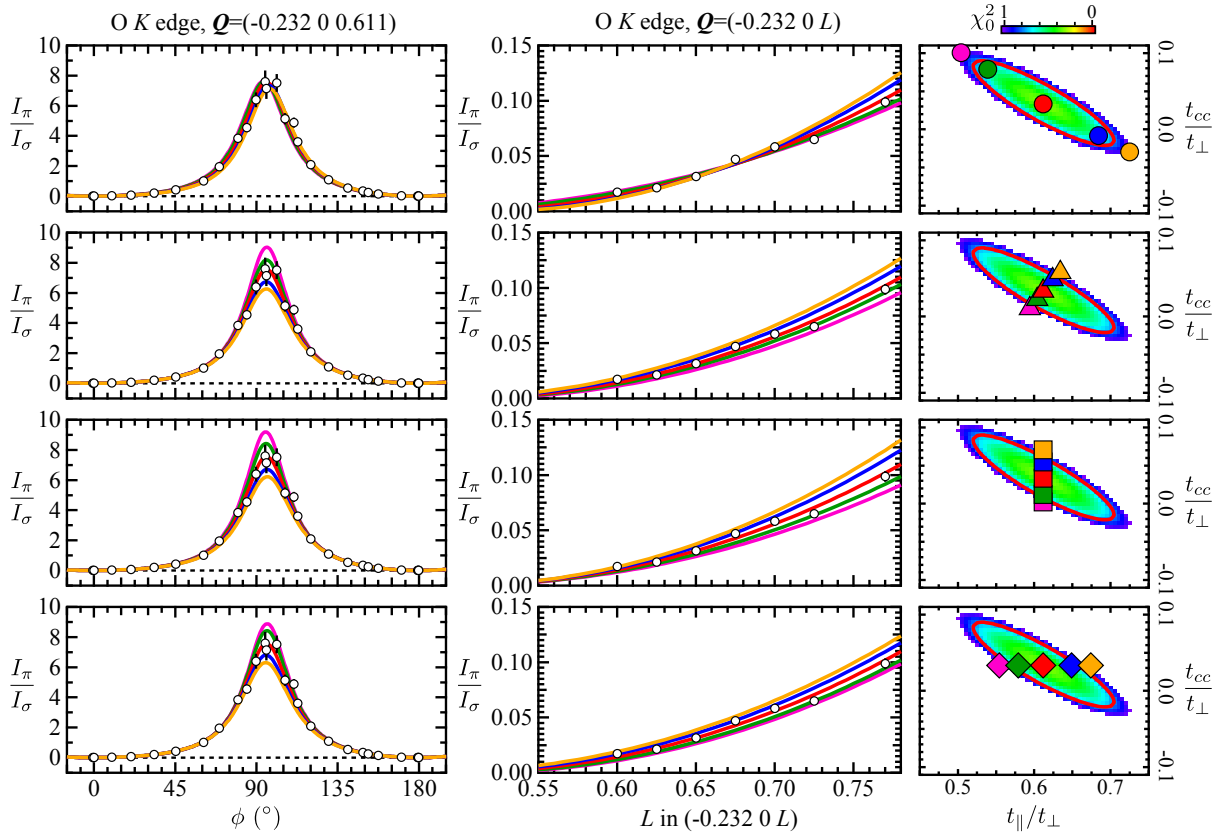

Figure 5.13 – LBCO O K edge ϕ (left panels) and L dependence (middle panels) of measured I_π/I_σ (open symbols) compared to the model calculations (coloured lines) based on Eq. 5.18 at the points indicated by coloured symbols on the maps of χ_0^2 in the $t_\parallel/t_\perp$ – $t_{cc}/t_\perp$ parameter space (right panels). Each row corresponds to exploring the parameter space of the model along a particular direction (ie., diagonal, vertical, horizontal). The red ellipse (right panels) is a contour of constant χ_0^2 that defines a region in the $t_\parallel/t_\perp$ – $t_{cc}/t_\perp$ plane where there is a 95% (or higher) likelihood that the experimental data is described by the model. The maps of χ_0^2 are truncated at values greater than 1, emphasizing the region of good agreement.

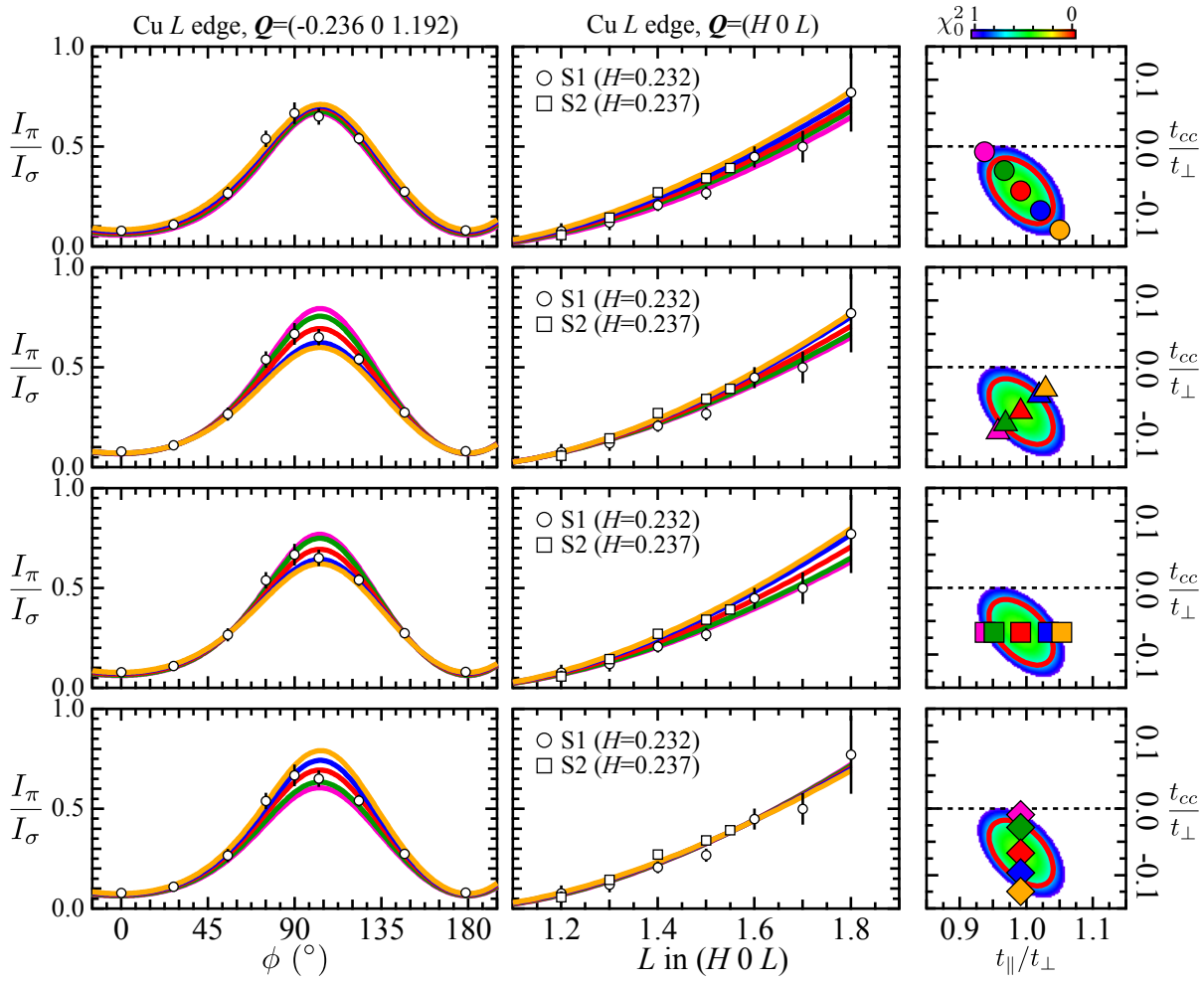

Figure 5.14 – LBCO Cu L edge ϕ (left panels) and L dependence (middle panels) of measured I_π/I_σ (open symbols) compared to the model calculations (coloured lines) based on Eq. 5.18 at the points indicated by coloured symbols on the maps of χ_0^2 in the $t_\parallel/t_\perp$ – $t_{cc}/t_\perp$ parameter space (right panels). Each row corresponds to exploring the parameter space of the model along a particular direction (ie., diagonal, vertical, horizontal). The red ellipse (right panels) is a contour of constant χ_0^2 that defines a region in the $t_\parallel/t_\perp$ – $t_{cc}/t_\perp$ plane where there is a 95% (or higher) likelihood that the experimental data is described by the model. The maps of χ_0^2 are truncated at values greater than 1, emphasizing the region of good agreement.

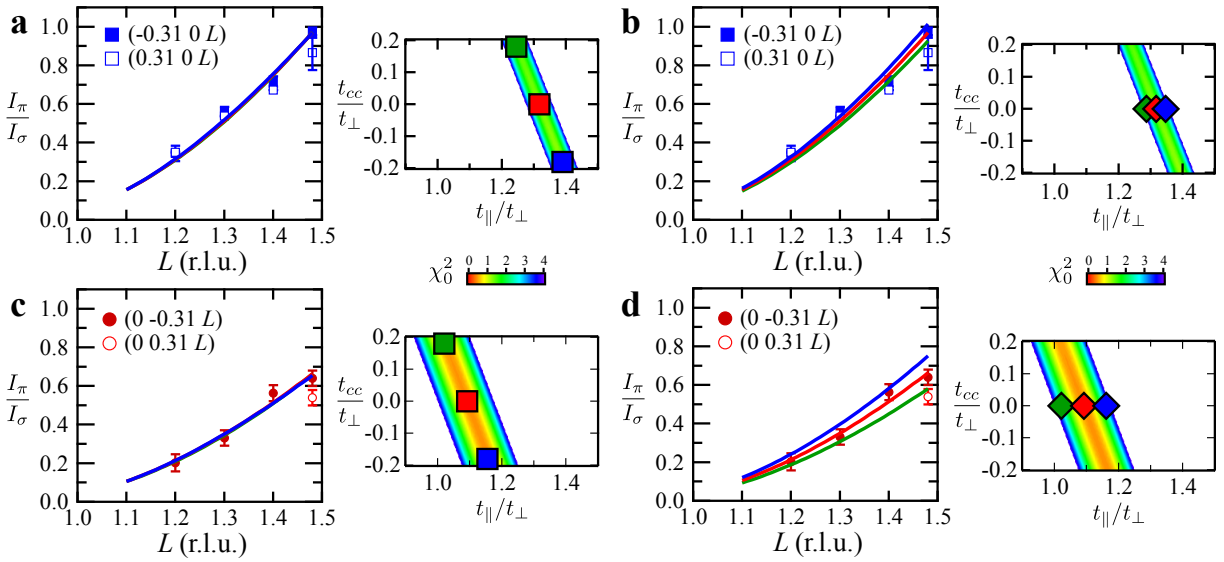

Figure 5.15 – L dependence of the model calculations based on Eq. 5.18, for YBCO at the Cu L edge, at the points indicated in the colour maps of χ_0^2 in the $t_\parallel/t_\perp$ – $t_{cc}/t_\perp$ parameter space. The parameter space of the model is explored for the CDW peak along H (**a-b**) and K (**c-d**) in the diagonal (left panels) and horizontal (right panels) directions. The maps of χ_0^2 are truncated at values greater than 4 to highlight the region of good agreement.

Lastly, we illustrate the confidence with which the sign of $t_\parallel/t_\perp$ is reported for LBCO at the O K edge. An examination of χ_0^2 over a larger region of the parameter space is shown in right panel of Fig. 5.16. Here χ_0^2 is truncated above $\chi_0^2 = 30$. The value of χ_0^2 outside the plotted region was found to be very large. The same 95% confidence region reported in Fig. 5.2e and shown above (Fig. 5.13) is shown in light green to provide a sense of scale for the parameter space. In addition to the global minimum at $t_\parallel/t_\perp = 0.612$ and $t_{cc}/t_\perp = 0.034$, we find a local minimum in χ_0^2 with a small and negative $t_\parallel/t_\perp$ and a relatively large and negative $t_{cc}/t_\perp$. As shown in Fig. 5.16, this local minimum has a considerably higher χ_0^2 than the global minimum (right panel) and is a poor fit to the data along ϕ (left panel) and L (center panel). A similar examination of χ_0^2 throughout the parameter space for the Cu L edge data in LBCO reveals very high values of χ_0^2 for $t_\parallel/t_\perp < 0$ and plots of the model for these values are in very poor agreement with the measured ϕ dependence (not shown). We therefore have a high degree of confidence that $t_\parallel/t_\perp > 0$, ruling out a dominant d symmetry to the CDW order in LBCO.

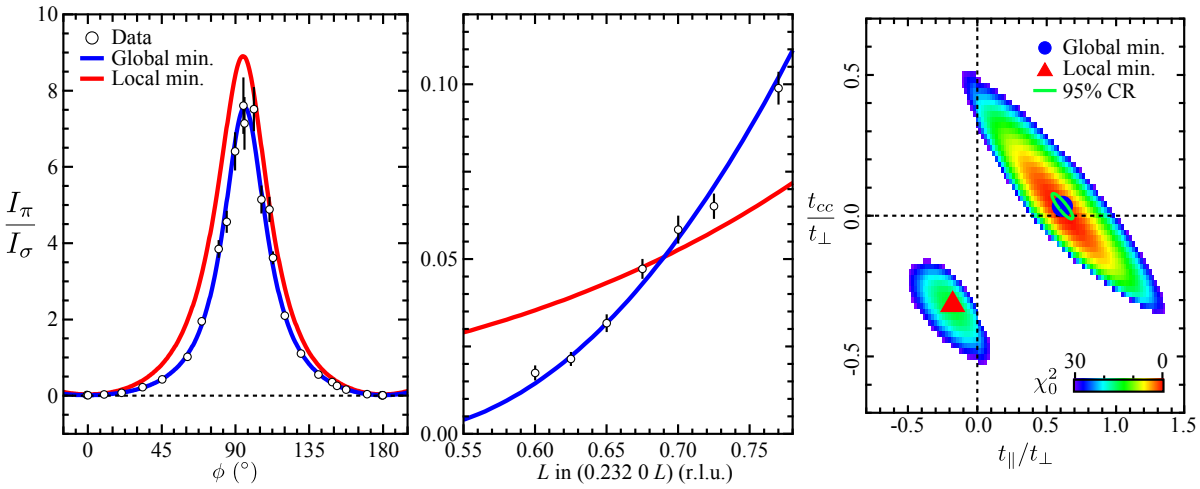

Figure 5.16 – Comparison of global minimum in χ_0^2 with $t_\parallel/t_\perp > 0$ with local minimum having $t_\parallel/t_\perp < 0$ for LBCO at the O K edge. Model calculations plotted against ϕ (left panel) and L (center panel) for the global and local minima indicated by coloured symbols in the right panel. The colour map of χ_0^2 is truncated above $\chi_0^2 = 30$. The 95% confidence region (CR), shown as a light green ellipse, is the same as in Figs. 5.2e and 5.13. The global minimum matches the data, whereas the local minimum with $t_\parallel/t_\perp < 0$ (corresponding to $|\Delta_d| > |\Delta_{s'}|$) is a poor match.

Chapter 6

Impact of Quenched Oxygen Disorder on Charge Density Wave Order in $YBa_2Cu_3O_{6+x}$

This chapter has been adapted from Ref. [3]

6.1 Overview

The competition between superconductivity and charge density wave (CDW) order in underdoped cuprates has now been widely reported, but the role of disorder in this competition has yet to be fully resolved. A central question is whether disorder sets the length scale of the CDW order, for instance by pinning charge density fluctuations or disrupting an otherwise long range order. Using resonant soft x-ray scattering, we investigate the sensitivity of CDW order in $YBa_2Cu_3O_{6+x}$ (YBCO) to varying levels of oxygen disorder. We find that quench cooling $YBCO_{6.67}$ ($YBCO_{6.75}$) crystals to destroy their o-V and o-VIII (o-III) chains decreases the intensity of the CDW superlattice peak by a factor of 1.9 (1.3), but has little effect on the CDW correlation length, incommensurability, and temperature dependence. This reveals that while quenched oxygen disorder influences the CDW order parameter, the spatial extent of the CDW order is insensitive to the level of quenched oxygen disorder and may instead be a consequence of competition with superconductivity.

6.2 Introduction

Charge density wave (CDW) order has been solidified as a generic property and principal competitor to superconductivity (SC) in underdoped cuprate superconductors through its observation in $YBa_2Cu_3O_{6+x}$ (YBCO),[22, 23, 2, 204, 214, 32, 222] Bi-based, [82, 176, 30, 72, 73], La-based,[215] and Hg-based cuprates.[74] Despite important differences in crystal structure and levels of disorder in these cuprates,[48] the spatial extent of CDW order is relatively short range in all cases. The origin of this common short range character is not currently understood. A widely held view is that disorder plays the role of either pinning charge density fluctuations or disrupting an otherwise long-range order.[112, 113, 114] These possibilities have been used to describe the effect of disorder and impurities in the cuprates. For example, apical oxygen vacancies in $Bi_{2+y}Sr_{2-y}CaCu_2O_{8+x}$ (Bi2212) were argued to pin a CDW checkerboard state.[223] The substitution of spinless Zn atoms for Cu atoms in YBCO was argued to disrupt [enhance] CDW [spin density wave (SDW)] correlations in the vicinity of the Zn defects.[214] Within such interpretations, the common short range character of CDW order in the cuprates is associated with each material's specific defect properties and crystal structure. However, it is also possible that such descriptions only apply due to the high defect strength, masking a more generic and intrinsic origin of this length scale, such as the competition of CDW order with superconductivity.[55, 56]

To address this question, we turn to high-purity, oxygen ordered YBCO. With regards to defects, YBCO represents a special case in the cuprates since stoichiometric, ultra-high purity crystals can be grown with low levels of cation disorder.[45] Doping of the CuO_2 planes occurs by the addition of oxygen atoms into the chain layer, which can organize into a number of ortho-ordered phases depending on the oxygen content.[108, 109, 110] Disorder in these CuO chains have been shown by microwave conductivity studies of quasiparticle scattering in $YBCO_{6.5}$ to be the dominant source of weak-limit scattering,[224] indicating that the most influential defects in YBCO reside in the chain layer.[48] As previously established, the oxygen ordered states can be intentionally destroyed by heating YBCO crystals to modest temperatures and subsequently quench cooling to prevent the formation of chain order.[110, 115, 111, 224] This allows for individual crystals of YBCO to be investigated with varying degrees of disorder.

In this chapter, this means of controlling disorder in YBCO is exploited to study the effect of quenched disorder on CDW order in the cuprates using resonant soft x-ray scattering (RSXS). Our main finding is that disordering the chains decreases the CDW scattering intensity, but has little impact on the CDW correlation length (ξ^{CDW}), incommensurability or T dependence. This reveals that while disorder influences the CDW order parameter, the length scale of the CDW order is insensitive to the level of disorder. We argue that

this observation is difficult to reconcile with simple pictures of disorder-induced pinning or of order nucleating around defects and suggest that the short range character of the CDW order has an intrinsic origin, possibly rooted in the competition between CDW order and superconductivity. We also discuss how the disorder effect studied here can be contrasted to disorder effects in other cuprates.

RSXS and x-ray absorption spectroscopy (XAS) measurements were performed at the Canadian Light Source's REIXS beamline [168] using high purity single crystals of YBCO with o-V ($T_c = 64.5$ K, $p = 0.116$, $x = 0.667$), o-VIII ($T_c = 65.5$ K, $p = 0.118$, $x = 0.667$) and o-III ($T_c = 75.2$ K, $p = 0.133$, $x = 0.75$) oxygen ordering.[45, 199] The samples were oriented with the ac plane parallel to the scattering plane (with the c-axis normal to the sample surface). The orientation was confirmed using (0 0 2) and ($\pm$1 0 2) Bragg reflections at 2 keV. Scattering was performed with σ polarized light and XAS was measured by total fluorescence yield (TFY).

6.3 Results

In Fig. 6.1(a), RSXS measurements of the CDW peak are shown at 65 K, at $L \simeq 1.48$ and at a photon energy of 931.3 eV, corresponding roughly to the maximum in CDW scattering intensity at the Cu L_3 edge.[22, 1] The fluorescence background and scattering contributions from nearby oxygen order peaks (off resonance but still visible) were subtracted using a scan at high T, as shown in Fig. 6.2(a) for the o-V $YBCO_{6.67}$ sample. This procedure was susceptible to a larger error for the ordered o-III $YBCO_{6.75}$ sample due to the overlap of the o-III superstructure reflection ($H = -0.33$) with the CDW peak ($H = -0.31$). The correlation lengths [$\xi_a = a/(2\pi \mathrm{HWHM}_H)$], T dependence (see Fig. 6.3) and incommensurability, as determined by Lorentzian peak fits to the background subtracted data, all vary somewhat weakly with doping and are consistent with previous and more recent work.[204, 212, 211] The measured peak widths were not appreciably influenced by the detector resolution.[1] Note that in addition to determining the T dependence with fitting of Q-scans, we have also monitored the detector count rate while the sample cooled below T_{CDW}, as shown in the solid lines of Fig. 6.3(a). Here we have subtracted a constant value for the fluorescence background, which from measurements at (-0.25 0 1.48) (away from the CDW peak) are found to be weakly temperature dependent over the temperature range of interest. Accordingly, we find the shape of the cooling curves to be consistent with the peak fitting results.

[1] The estimated resolution in the H direction at $Q = (-0.31\ 0\ 1.48)$ is $\Delta H \leq 0.019$ r.l.u.

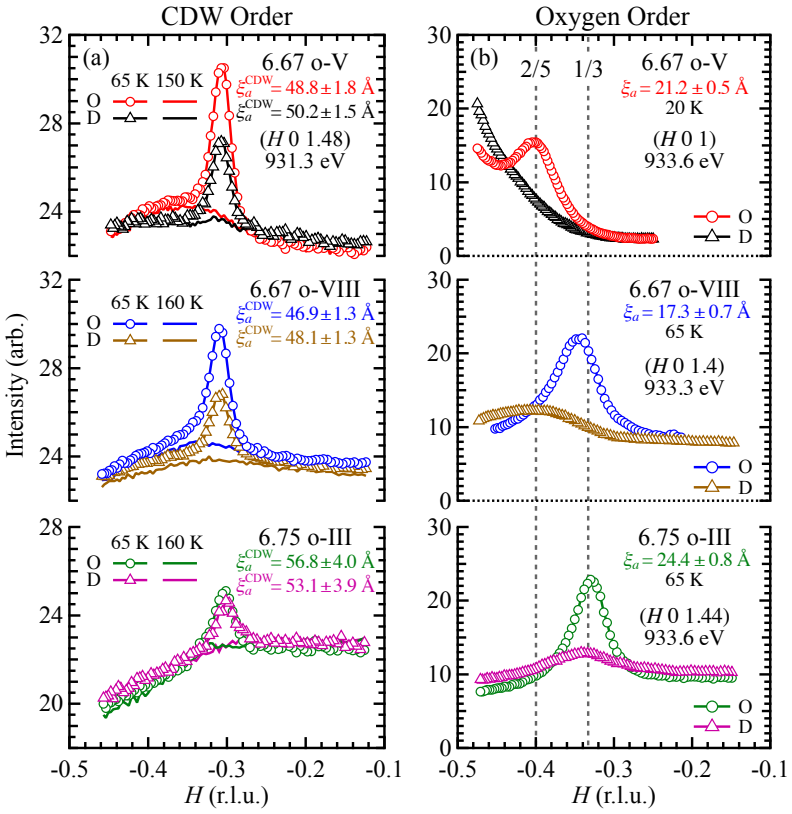

Figure 6.1 – $(H\ 0\ L)$ scans through the (a) CDW peaks and (b) oxygen chain ordering superstructure peaks in o-V, o-VIII and o-III ordered YBCO before (O) and after (D) heating the samples to disorder the oxygen in the chain layer. In panel (a) a small contribution of the oxygen order superstructure reflection is still visible for the oxygen ordered states at the photon energy 931.3 eV, where CDW order is most pronounced. The correlation lengths ξ_a^{CDW} given in (a) are for the ordered and disordered states of the crystals and the ortho structure correlation lengths ξ_a in (b) are for the ordered state.

After measurement in the ortho ordered state, the ortho phase was disordered by heating to ∼100 °C (above the oxygen ordering temperature). Despite oxygen atoms being mobile at this temperature, the kinetics of oxygen incorporation at the surface are very slow, so no change in sample stoichiometry is expected.[224] During this process, the pressure in the chamber was maintained below 6×10^{-9} Torr, ensuring a clean sample environment and no surface contamination. The samples were maintained at 100 °C long enough for the oxygen order superstructure reflection to disappear (∼30 to 60 min) and cooled back down to room temperature in ∼7 min (dictated by the maximum cooling rate of the instrument)

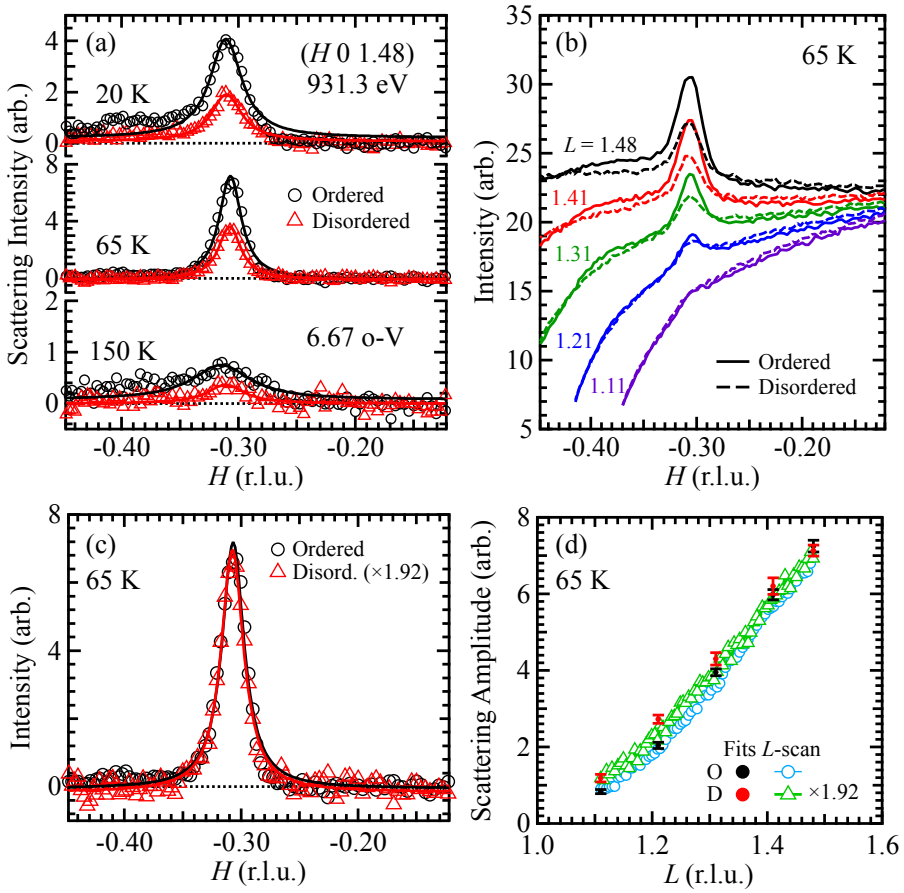

Figure 6.2 – CDW scattering intensity in o-V ordered YBCO before and after quench cooling. (a) Background subtracted scattering intensity at select temperatures. Solid lines are Lorentzian fits. (b) (H 0 L) scans at various L values. (c) and (d) The H and L dependence of the CDW scattering intensity at 65 K scaled to match peak intensities. The peak width and position (c) and L dependence (d) are the same in the oxygen ordered and disordered states.

to quench in the oxygen disorder. The degree of oxygen order is characterized by the intensity and width of the ortho order superstructure peaks along the a-axis, shown in Fig. 6.1(b). The correlation length along the b-axis, which is known to be larger,[23] was not measured here. In the ortho VIII ordered YBCO, the o-VIII ordering peak is replaced by weak o-V order at $H = -0.4$ upon quenching. Similarly, the quenching procedure destroys the o-V phase in the ortho V crystal and nearly eliminates the o-III phase of the ortho III crystal.

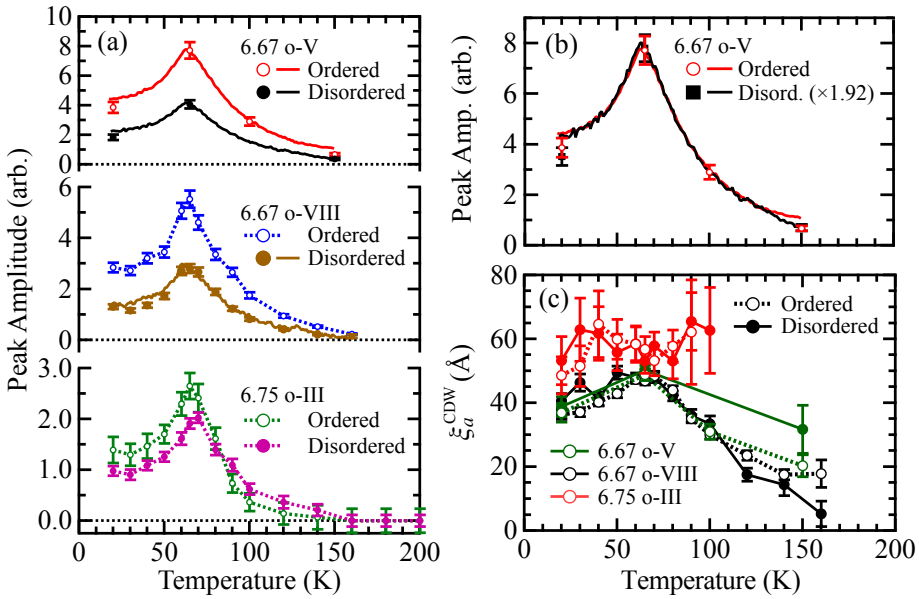

Figure 6.3 – (a) The T dependence of the CDW peak amplitude in oxygen ordered and disordered states. Solid lines (o-V and o-VIII disordered) are the scattering amplitude measured upon cooling and markers are Lorentzian fit amplitudes. Dotted lines connect markers in the cases where scattering amplitude was not measured upon cooling. (b) The T dependence of the CDW peak amplitude in the o-V sample scaled to equal intensity at 65 K. The T dependence is unchanged by disordering the chains. (c) The T dependence of ξ_a^{CDW} of the CDW peak in the ordered and disordered states.

We find that disordering the chains results in a decrease in CDW peak intensity [Fig. 6.1(a)], but essentially no change in the CDW peak incommensurability (Q position) [Fig. 6.2(c)], temperature dependence [Fig. 6.3(a)] or correlation length (either in-plane, ξ_a^{CDW} [Fig. 6.3(c)], or out-of-plane, ξ_c^{CDW} [Fig. 6.2(d)]). This is most clearly seen in the $x = 0.667$ o-V sample, where scaling the background-subtracted CDW scattering intensity after quenching by a constant factor of ∼1.9 provides an excellent match to the H, L [Fig. 6.2(c) and 6.2(d)] and T dependence [Fig. 6.3(b)] of the CDW peak in the original oxygen ordered state. Since no change in the L dependence of the peak is observed [Fig. 6.2(b) and 6.2(d)], we find that oxgyen disorder has a negligible impact on ξ_c^{CDW}.[2]

[2]The data suggests that $\xi_c^{\mathrm{CDW}} < c$ in both cases, consistent with the hard x-ray results in Ref. [23], but we cannot determine a reliable value given the limited Q-space.

6.4 Discussion

6.4.1 Interpretation

The disorder-independent incommensurability, ξ^{CDW} and T dependence argue against a strong role of the chain order periodicity in stabilizing the CDW order, consistent with the previous observations of distinct Q, energy and temperature dependence for the CDW and chain superstructure peaks.[2] In addition, the change in CDW intensity does not appear to be associated with a change in the hole doping in the CuO_2 planes upon disordering the chains. A change in hole doping might be expected since disordering the oxygen atoms can reduce the chain length – affecting the charge transfer to the CuO_2 planes by reducing the number of Cu atoms in the full chains that are coordinated by 4 oxygen atoms (2 apical and 2 in the chain layer) and increasing the number of Cu that are coordinated by only 3 oxygen atoms. However, XAS measurements (consistent with Refs. [194, 84]) before and after the quenching procedure, shown in Fig. 6.4, indicate that the hole doping change induced by disordering the chains is negligible, at least in the o-V sample. Moreover, under the premise that the CDW peak is most intense around $p=1/8$,[22] underdoping the $x=0.75$ sample would presumably enhance the CDW order, whereas the measured effect is a modest decrease in intensity by a factor of $\sim$1.3.

Consequently, rather than a change of hole doping in the CuO_2 planes, the decrease in CDW scattering intensity likely results from a change in the defect structure of the materials, specifically how the O disorder in the chain layer influences the CuO_2 planes. These defects include point-like defects due to the ends of finite length chainlets and also

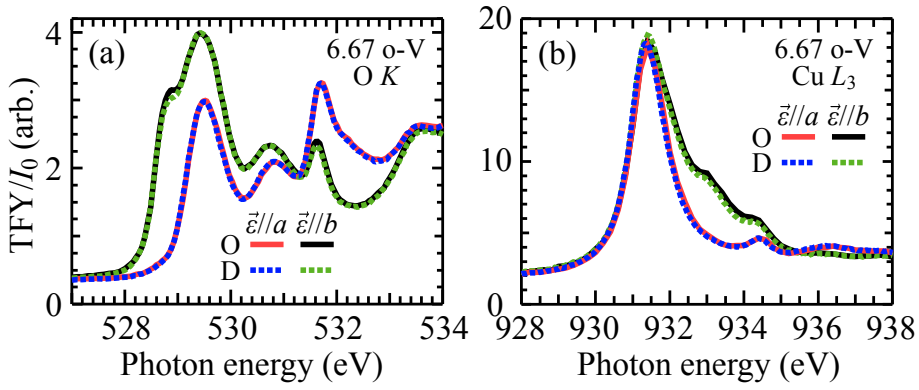

Figure 6.4 – (a) O K and (b) Cu L_3 edge XAS of the o-V sample in the oxygen ordered (O) and disordered (D) states. Nominally, no change in orbital occupation in the CuO_2 planes is seen.

domain walls caused by phase slips in the chain ordering pattern. In the O ordered phase, the short correlation length of the chain order implies an already large density of both types of defects. Quenching the samples into an O disordered phase decreases the average length of the chainlets, increasing the density of weak, random point-like defects. However, since the chain order is originally short-range, quenching the samples into an O disordered phase can also decrease rather than increase the domain wall density (a fully-disordered, random O distribution in the chain layer would have a single o-I domain with no domain walls). Somewhat counter-intuitively then, depending on the interplay of increasing point defect density and decreasing domain wall density, disordering the chains may result in more or less disorder in the CuO_2 planes. In short, although the oxygen atoms in the chain go from being ortho ordered to disordered after quench cooling, it is not yet clear whether the resultant decrease in CDW intensity is due to an increase or decrease in defect density in the CuO_2 planes. Future work to determine the proportion of these defects is needed to clarify this point. We also note that the variation in disorder here is unlikely to correspond to a variation in the strength of point-like defects, making it unclear how our measurements correspond to existing theoretical models of disorder effects on CDW order.[112, 113]

We note that the measured ξ^{CDW} (at $\sim T_c$) both here and in a wider range of dopings is only weakly dependent on the excess oxygen content.[212, 211] Since the level of oxygen disorder varies considerably in the investigated range of samples, a substantial doping dependence to ξ^{CDW} would be expected if oxygen disorder were setting the length scale of the CDW order.

6.4.2 Comparison to Zn doping

The effect of O disorder shown here should be compared with the effect of Zn-impurities on the CDW order in YBCO.[214] Blanco-Canosa *et al.* [214] also found that Zn doping decreases the CDW peak intensity, like our O disorder measurements. But, unlike O disorder, Zn-impurities decrease the correlation length and significantly change the T dependence of the CDW order. This was argued to be consistent with spatially inhomogeneous CDW order, with CDW order suppressed in regions around the Zn impurities, where incommensurate SDW order is enhanced. However, it is not clear that a similar description can be applied to O disorder since Zn doping introduces a spinless impurity in the CuO_2 planes that is a much stronger defect than O defects in the chain layer and results in strong pair breaking scattering, suppression of superconductivity, a slowing of spin fluctuations and of static, incommensurate SDW order. Moreover, the lack of dependence on ξ^{CDW} and T dependence for our O disorder measurements are difficult to reconcile with a simple

inhomogeneity model, where the volume fraction of CDW order is decreased when the O in the chain layer is disordered. Since ξ^{CDW} is not impacted by the O disorder, this scenario would require a domain size larger than the CDW correlation length. Given that the defect density is high in the O disordered state, and that the correlation length in the ortho ordered states is in fact less than that of the CDW order [the O order is short range, see Fig. 6.1(b)], it is unclear how CDW domains would form around O defects.

6.4.3 Possible origins

It is also difficult to reconcile the independence on oxygen disorder of the CDW T dependence and correlation length with pinning of CDW order that would be fluctuating in the absence of disorder, since the temperature evolution of the fluctuations should depend on the level of disorder.[114] Rather, these measurements suggest that the short range nature of the CDW order ($\xi^{\mathrm{CDW}} < 60$ Å) could have an intrinsic origin related to the competition between CDW order and SC rather than being a result of sample disorder. For instance, it has been shown that the gradual, concave T dependence of the CDW order shown in Fig. 6.3 can result from angular fluctuations of a multi-dimensional order parameter comprised of biaxial CDW order and superconductivity.[56] Although the impact of disorder on this model has not been investigated, it is plausible that disorder can affect the CDW peak amplitude without having a strong effect on the angular fluctuations that govern the CDW T dependence and possibly the correlation length.

Although a detailed explanation for the O disorder dependence is yet not evident, in the absence of a change in CDW volume fraction or pinning, it is reasonable to consider the reduction of the CDW peak intensity as being associated with a reduction in the magnitude of the CDW order parameter. As previously demonstrated, the CDW peak intensity at the Cu L edge is associated with a spatial modulation in the Cu $2p$ to $3d$ transition energies ΔE, which for small modulations scales as ΔE^2.[2, 1] Accordingly, the magnitude of these energy modulations, which are presumably proportional to the CDW order parameter, could be affected by quenched oxygen disorder (and full details of how quench cooling alters the defect structure). In this context, we note that the CDW order is more strongly reduced by disorder in the $YBCO_{6.67}$ samples than it is in the $YBCO_{6.75}$ sample. Although, we should caution that the level of disorder is not well calibrated between samples, it is curious that the larger change in the magnitude of the CDW order occurs in samples where the CDW peaks are most intense. Naively one may have expected CDW order to be more susceptible to disorder at doping levels where the order is weaker.

6.4.4 Broader comparison to other cuprates

Finally, we address how these results on YBCO can be understood in the broader context of CDW order in the cuprates. We showed here that the degree of oxygen disorder in YBCO does not determine ξ^{CDW}, suggesting a more intrinsic origin for the short range character of the CDW order. Although YBCO represents a case of relatively weak disorder, the implication that disorder is not the dominant factor in determining ξ^{CDW} may be applicable to other cuprates. This may explain why across the various cuprate families, where the type of defects and their importance varies considerably (e.g. cation substition, oxygen vacancies, lattice distortions),[48] ξ^{CDW} is of the same order of magnitude (e.g. 20-30 Å in Bi-2201,[73] $\simeq$ 20 Å in Hg-1201,[74] and 50-175 Å in LBCO[175]). Rather than an emphasis on disorder, an understanding of the competition between CDW order and superconductivity, and how this competition is influenced by the electronic and crystalline structure (e.g. Fermi surface topology, interlayer coupling), may clarify how the CDW order differs in the various cuprate families.

Chapter 7

Doping evolution of charge density wave order in $YBa_2Cu_3O_{6+x}$

7.1 Overview

The recent observation of CDW order in underdoped YBCO by hard and soft x-ray scattering across a variety of hole dopings has solidified CDW order as an important phase that onsets below the pseudgap and above the superconducting transition, and persisting deep into the superconducting state. The interpretation of how these electronic and quantum mechanical ordering phenomena compete, coexist and ultimately form is still a subject of much debate. Establishing how the characteristics of CDW order vary across the phase diagram is essential to framing this debate. In this chapter, I report such a study for the CDW order in YBCO. I will present a phase diagram and the doping dependence of several quantities (incommensurability, correlation length, peak intensity, temperature dependence) that combine my observations with those from other groups.[212, 211, 204] Notably, I report the observation of CDW order at $p = 0.058$, near the anti-ferromagnetic insulator to superconductor transition, with a propagation direction along the b axis but not along the a axis. At this doping level, static incommensurate spin density wave (SDW) order is known to form along a in YBCO.[225] Combined with a notable deviation between the a and b axis correlation lengths at low doping, this helps to establish the competition between spin ordering in CDW order in YBCO. Moreover, it acts as a clear demonstration of unidirectional CDW order in YBCO. Also identified is a subtle deviation from linearity in the doping evolution of the incommensurability, which decreases with doping, opposite to La-based cuprates and opposite to the incommensurability of spin order.

7.2 Experimental results

Resonant soft x-ray scattering experiments on 7 samples of $YBa_2Cu_3O_{6+x}$ with varying oxygen contents and degrees of oxygen ordering were conducted at the Canadian Light Source's REIXS beamline. Orientation of the crystals was performed at ~ 2 keV using (0 0 2) or (0 0 4) and ($\pm$1 0 2) or (0 $\pm$1 2) Bragg peaks. All RSXS data presented here is for vertically polarized incident photons (σ-polarization) at a photon energy of 931.3 eV, or about 0.1 eV below the maximum in the XAS for the Cu L_3 edge. These experiments were performed over a 3 year period, consisting of 12 "beamtimes", so great care had to be taken to ensure the reliability of the reported parameters. Despite a significant effort to ensure the reliability and consistency of the data and the extracted parameters, there may still be important experimental uncertainties that could influence some of the presented results. These limitations are discussed at length in section 7.4.2.

7.2.1 $YBa_2Cu_3O_{6+x}$ samples

The properties and origins of the investigated $YBa_2Cu_3O_{6+x}$ crystals are listed in Table 7.1. All but one of the samples were provided by Ruixing Liang, Doug Bonn and Walter Hardy from the University of British Colombia (UBC). The other was provided by Santiago Blanco-Canosa (and collaborators) from the Max-Planck-Institut (MPI) für Festkörperforschung, Heisenbergstraße in Stuttgart, Germany. As noted in Table 7.1, most of the samples were polished. Although the CDW order could be detected by RSXS with and without polishing (eg. in $YBa_2Cu_3O_{6.67}$ o-VIII and $YBa_2Cu_3O_{6.75}$ o-III), polishing was preferable to remove surface imperfections (see Fig. 2.13), as discussed in section 2.3.3. The $YBa_2Cu_3O_{6.99}$ sample was previously etched and studied by x-ray absorption at Taiwan's National Synchrotron Radiation Research Center, as reported in Ref. [84]. Chain ordering and de-twinning was performed by the crystal growers.

The superconducting transition temperatures T_c were determined using DC susceptibility measurements.[1] The measurements are presented and discussed in section 7.2.3. The corresponding hole concentrations were then obtained using previously established mapping between T_c and p in Ref. [199]. Note that the units of p denoted as "holes/Cu" in this chapter refers to holes per *planar* copper atom.

Note, throughout this chapter the following notation will be adopted when discussing the chain order state of the YBCO samples:

[1] Except for the sample $YBCO_{6.5}$ (A). Here T_c was taken for the nominal composition.

Table 7.1: $YBa_2Cu_3O_{6+x}$ sample properties

Sample	Chains	T_c (K)	p (holes/Cu)	Polished?	Origin
$YBCO_{6.335}$	o-I	12.6 ± 2	0.058 ± 0.003	Yes	UBC
$YBCO_{6.5}$ (A)	o-II	56.0 ± 3	0.096 ± 0.008	Yes	UBC
$YBCO_{6.5}$ (A)	o-IId	53.0 ± 3	0.089 ± 0.008	Yes	UBC
$YBCO_{6.5}$ (B)	o-II	59.9 ± 3	0.105 ± 0.008	No	MPI
$YBCO_{6.67}$	o-V	65.3 ± 1	0.117 ± 0.003	Yes	UBC
$YBCO_{6.67}$	o-VIII	66.3 ± 1	0.119 ± 0.003	Yes & No	UBC
$YBCO_{6.75}$	o-III	77.1 ± 2	0.134 ± 0.003	Yes & No	UBC
$YBCO_{6.99}$	o-I	90.1 ± 2	0.181 ± 0.003	Yes & Br etched	UBC

1. o-I indicates a fully disordered chain layer.

2. o-II, o-III, o-V, and o-VIII denote robust chain order in the form of an identifiable peak (even if the correlation length of the order is modest, as shown in chapter 6).

3. o-IId, o-IIId, o-Vd, and o-VIIId will denote that the chains have been *disordered*, by the quench cooling process discussed in chapter 6.

7.2.2 Resonant scattering data

A representative sampling of RSXS measurements of the CDW order in $YBa_2Cu_3O_{6+x}$ is shown in Fig. 7.1. Measurements at temperatures corresponding to the high temperature background, the onset temperature, T_{CDW}^{on}, and the scattering intensity maximum, T_{CDW}^{max}, are shown. From visual inspection, there is a clear doping dependence to the peak intensity (relative to the background) and the peak position, although the widths appear somewhat comparable in all cases. Note that the data is coloured according to temperature with a common scale across all panels. The photon energy is 931.3 eV and the wavevector direction is indicated in each panel. The full set of temperatures-series are presented in section 7.4.1.1.

For these measurements, the scan mode was a θ-scan. This entails keeping the detector position fixed high angle ($2\theta \sim 170°$) and rocking the θ motion, as was discussed in section 5.10. This scan type produces more points on either side of the peak than an H-scan does, making it much simpler to perform reliable background subtractions. It also allows the L

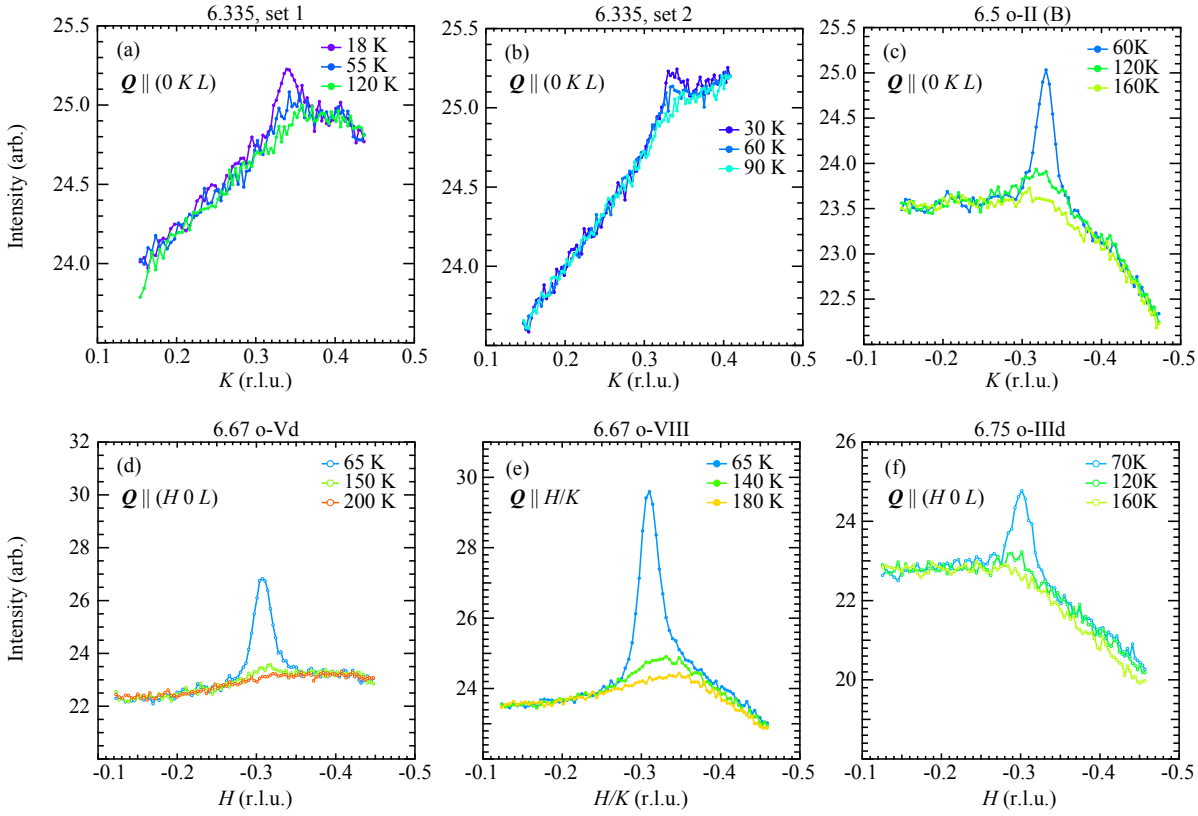

Figure 7.1 – Raw RSXS data of CDW scattering peak showing $T_{\mathrm{CDW}}^{\mathrm{on}}$ and $T_{\mathrm{CDW}}^{\mathrm{max}}$in (a-b) $YBa_2Cu_3O_{6.335}$, (c) $YBa_2Cu_3O_{6.5}$, (d)-(e)$YBa_2Cu_3O_{6.67}$, and (f) $YBa_2Cu_3O_{6.75}$. The chain ordering state as well as the scattering wavevector direction is indicated in each panel. The data are coloured according to temperature with a common colour scale across all panels.

value at the peak position to be slightly higher than for an H-scan, increasing the signal to noise ratio (SNR) by a modest amount. In a few test cases, the extracted peak positions, widths and amplitudes were in good agreement for both scan methods. The L index (near the peak) for these measurements was $L \approx 1.45$.

The high temperature backgrounds shown in Fig. 7.1 are due primarily to x-ray fluorescence from the samples. This can be seen by a calculation of the geometry dependence of the x-ray fluorescence, as illustrated in section 7.4.1.3. Scattering from chain ordering can also contribute to the background. Chain order causes a resonance at nearby $\boldsymbol{Q}$ and E, as discussed in chapter 4. In such cases, a high temperature measurement was used to

subtract the chain contribution. This procedure was also used when the high temperature subtraction caused no noticeable artifacts. For cases where the background measurement was not suitable for subtraction, polynomial fitting was used in its place. Additional details of the background subtraction are discussed in section 7.4.2.1.

The background-subtracted RSXS measurements are shown in Fig. 7.2 at $\sim T_{\mathrm{CDW}}^{\mathrm{max}}$. The left panel is for samples with oxygen-ordering in the chain layer and the right panel is for disordered chains. A common axis is used for scans taken along (H 0 L) and (0 K L). The data are offset vertically for clarity. The vertical scale is common for all panels and the peak intensities may be compared (cautiously) in this way. The associated uncertainties in the vertical scales is quite large, owing to difficulties in comparing scattering amplitudes across experimental beamtimes and samples. See section 7.4.2.3 for a discussion of the uncertainties involved in making this comparison possible.

For $YBCO_{6.335}$, the CDW scattering peak along K is barely present above the noise in the fluorescence background [Fig. 7.1 (a)]. No peak was detected along H. At best, the peak along K has a SNR of $\sim$ 1.8, sufficiently high to resolve, but very near the detection limit. For this sample T_{c} is lower than the base temperature of the instrument, so it is possible the peak would have continued to grow in intensity at lower temperature 13 K. The identification of a $T_{\mathrm{CDW}}^{\mathrm{max}}$ in this case was attributed a large error. The *actual* data point with a maximum was taken as $T_{\mathrm{CDW}}^{\mathrm{max}}$ $T_{\mathrm{CDW}}^{\mathrm{on}}$ was identified as the average onset temperature found in two experiments: one performed in August 2013 (set 1) and the other in September 2014 (set 2), both shown in Fig. 7.1.

For $YBCO_{6.5}$ o-II, the CDW scattering peak is seen along H and K in two samples, labeled A and B. In both cases, the scattering intensity is clearly stronger along K, by a factor of $\sim 2-3$, as shown in Fig. 7.2. Also, the peak along K has a larger incommensurability than the one along H.

A special mention needs to be made about $YBCO_{6.5}$ sample (A) with disordered o-II chains. There is limited data from this sample (notably lacking a full temperature dependence), but where possible data from its study has been included in the phase diagram. It was not possible to disorder the chains on this sample inside the diffractometer, since the quench cooling procedure was too slow and robust o-II order reformed in the time it took to cool the sample. Instead, the sample was enclosed in an evacuated quartz tube, heated up in a furnace at 200 °C for 2.5 hours and then quench-cooled by dumping into an ice bath prior. After this procedure, the sample was mounted and loaded into the chamber in as fast a time as possible ($\sim$ 4 hours). It is estimated from Ref. [109] that the formation rate of the o-II order at room temperature is sufficiently slow that this should not have allowed the chains to reform. This is affirmed by the measurement of a significantly degraded o-II

chain peak in this state (see Fig. 7.17). For this oxygen content, the presence of o-II chains is known to influence T_c and hence p. Values from Ref. [199] were taken for T_c and p for the ordered and disordered states of $YBCO_{6.5}$ (A) o-II and o-IId. This provides data for two dopings in the phase diagram in the low-doped regime.

For $YBCO_{6.67}$ o-V, the CDW scattering peak is seen along H and K. Reliable (comparable) data for both was only measured after disordering the o-V chains, and is shown in Fig. 7.2 (b). Here we can see $\xi_a < \xi_b$ and $I_H > I_K$.

For the $YBCO_{6.67}$ o-VIII sample that was investigated, a chain ordering peak of comparable strength was identified along H and K, suggesting that the sample was twinned, at least in the region that was measured. Inspection of the sample with polarized light under a microscope suggest some light twinning in various spots of this sample. Unfortunately, the RSXS measurements were likely performed on such a spot. Consequently, H and K could not be distinguished and the scattering arises from a mixture of CDW order along both directions. That said, the position (amplitude) of this peak appears quite near the average of ξ_a and ξ_b (I_H and I_K) for the 6.67 o-Vd sample, suggesting very similar properties in its CDW order, despite the different chain orders.

For $YBCO_{6.75}$ o-III, the CDW scattering peak is seen along H and K. The scattering intensity is very slightly stronger along H and there is little difference in the peak position, suggesting $I_H \approx I_K$ and $\xi_a \approx \xi_b$.

The full temperature series shown in section 7.4.1.1 was analyzed by first performing background subtractions and then fitting the result with a Lorentzian function. In Fig. 7.3 the temperature dependence of the fit amplitude is shown. Here the fit amplitudes have been normalized to their maximum value and are shown as open circles. In cases where the circles are not connected, cooling curves are shown as solid lines. These are obtained by fixing the scattering geometry to $\boldsymbol{Q}_{\mathrm{CDW}}$ and recording the total flux as the system cools slowly from high T to base temperature, as described in section 6.3. The peak widths have minima at $T \sim T_c$.

In Fig. 7.3, the gray (pink) striped regions denote T_c ($T_{\mathrm{CDW}}^{\mathrm{on}}$). The measurement of T_c is described in next section (section 7.2.3). $T_{\mathrm{CDW}}^{\mathrm{on}}$ and its uncertainty was set according to the first detectable peak with a generous uncertainty spanning the neighbouring measurements. If the first detectable peak was sufficiently above the detection limit, then the midpoint between it and the next higher T was set as $T_{\mathrm{CDW}}^{\mathrm{on}}$. $T_{\mathrm{CDW}}^{\mathrm{max}}$ was taken from the scan exhibiting the strongest scattering peak, with an uncertainty given by the temperature spacing of the neighbouring scans. The uncertainties in $T_{\mathrm{CDW}}^{\mathrm{on}}$ are discussed further in section 7.4.2.6.

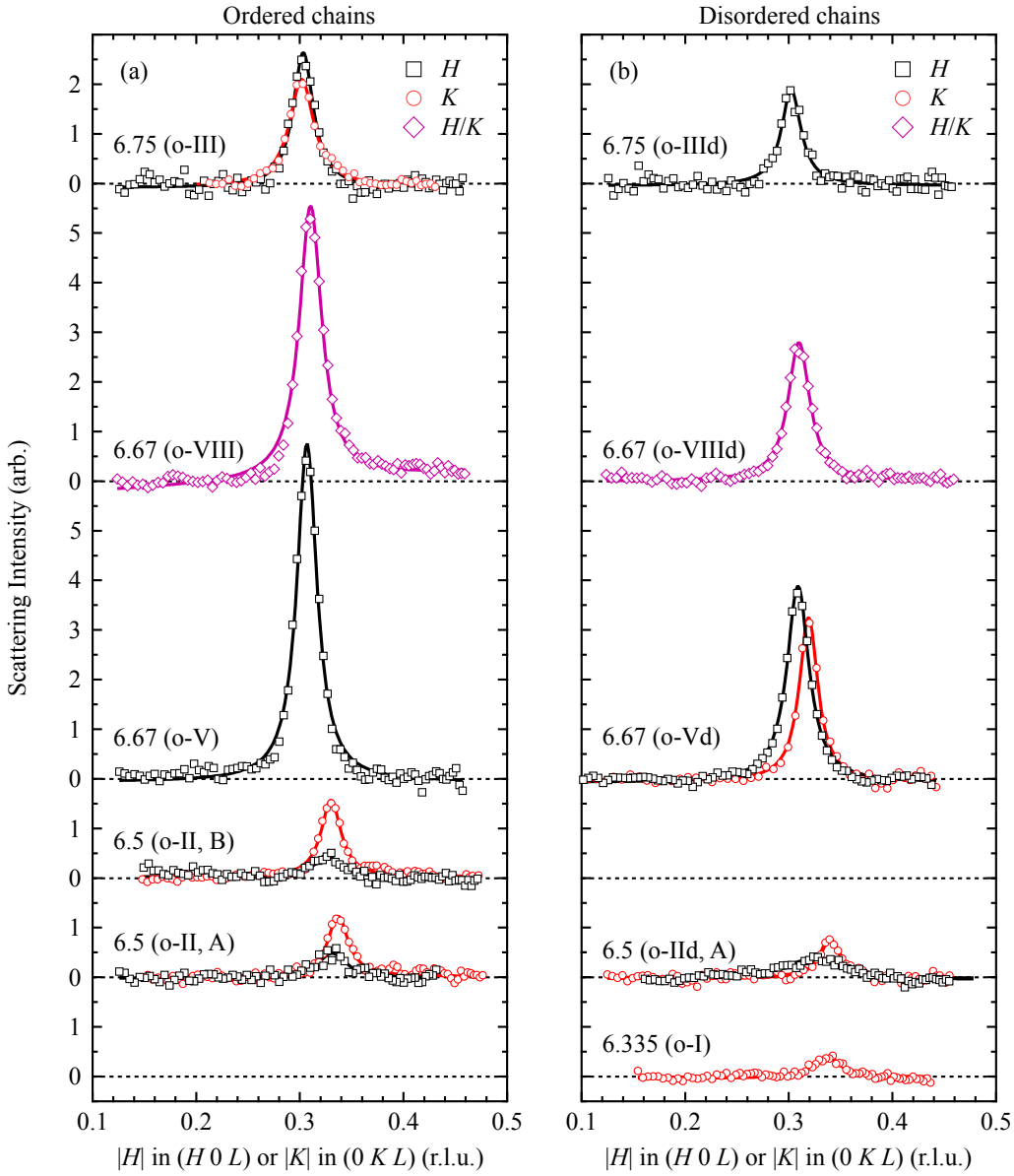

Figure 7.2 – Doping dependence background-subtracted RSXS peak from CDW order in samples with oxygen-ordered chains (a) and with the chains disordered or absent (b). Open black squares (red circles) are background-subtracted RSXS along H (K). The purple diamonds are for a twinned sample. Solid lines are Lorentzian fits. This data and the corresponding fits are used to extract the peak incommensurability (Fig. 7.6 and Fig. 7.7), correlation length (Fig. 7.8) and maximal peak intensities (Fig. 7.9).

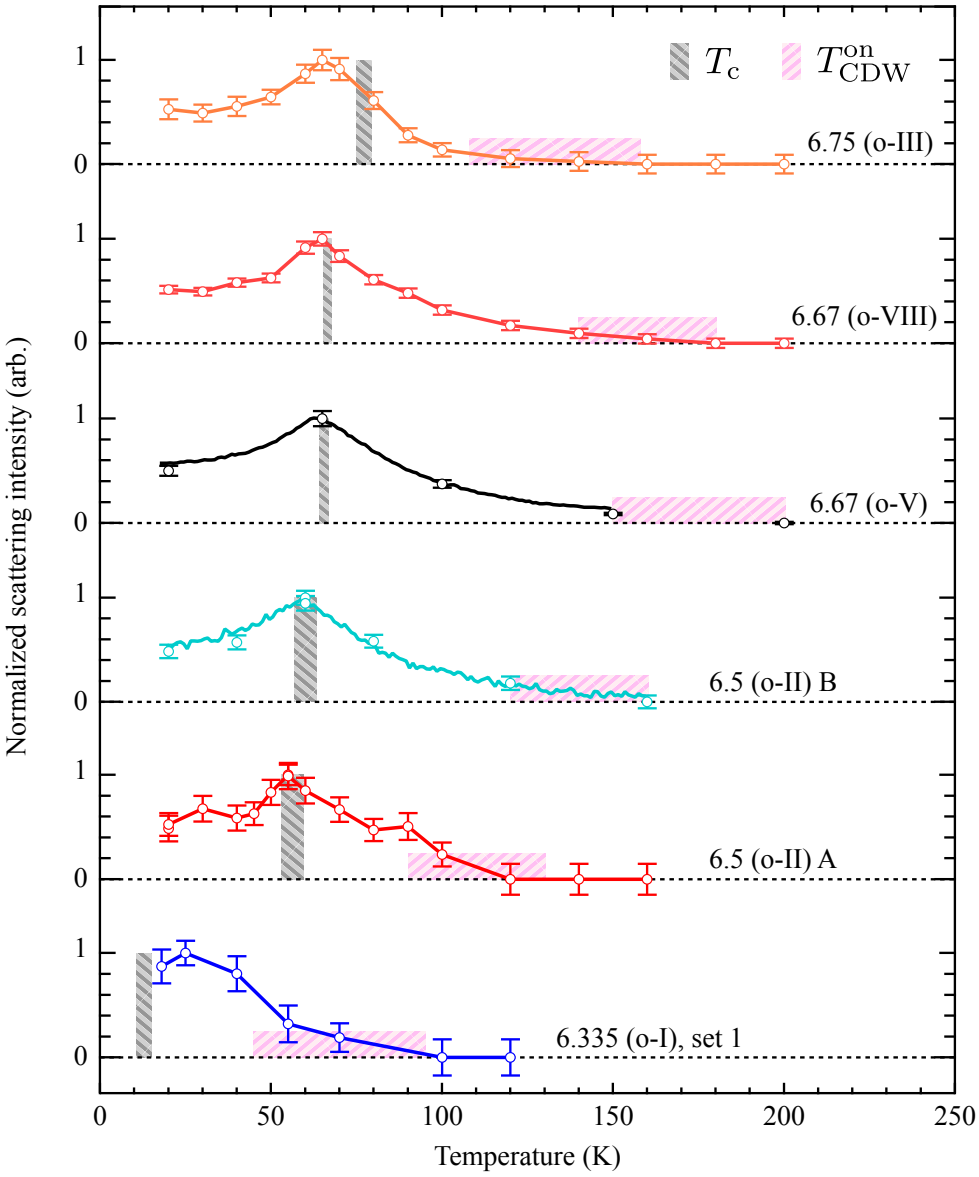

Figure 7.3 – Temperature dependence of CDW scattering amplitude for $YBa_2Cu_3O_{6+x}$with $x = 6.335,\ 6.5,\ 6.67,$ and 6.75. Open circles denote scattering amplitudes determined by background-subtracted Lorentzian fits to the CDW peak. Solid continuous lines (6.5 o-II and 6.67 o-V) are cooling scans as described in the text with a constant background subtracted. The data have been normalized to 1 at their maxima. T_c and T_{CDW}^{on} are denoted by gray and pink boxes (width denotes uncertainty, height is only for visual clarity), respectively. Values of T_c were recorded by DC susceptibility as shown in Fig. 7.4.

7.2.3 Measurement of T_c

The DC magnetic susceptibility of the $YBa_2Cu_3O_{6+x}$ samples was used to measure T_c, as shown in Fig. 7.4. The samples were zero field cooled and slowly heated up in a 10 Oe field. The magnetic field was coarsely aligned with the c axis. In Fig. 7.4, the magnetic moment was normalized to -1 at low T and the resulting -5% crossing was defined as T_c (indicated by the horizontal dashed line in Fig. 7.4).

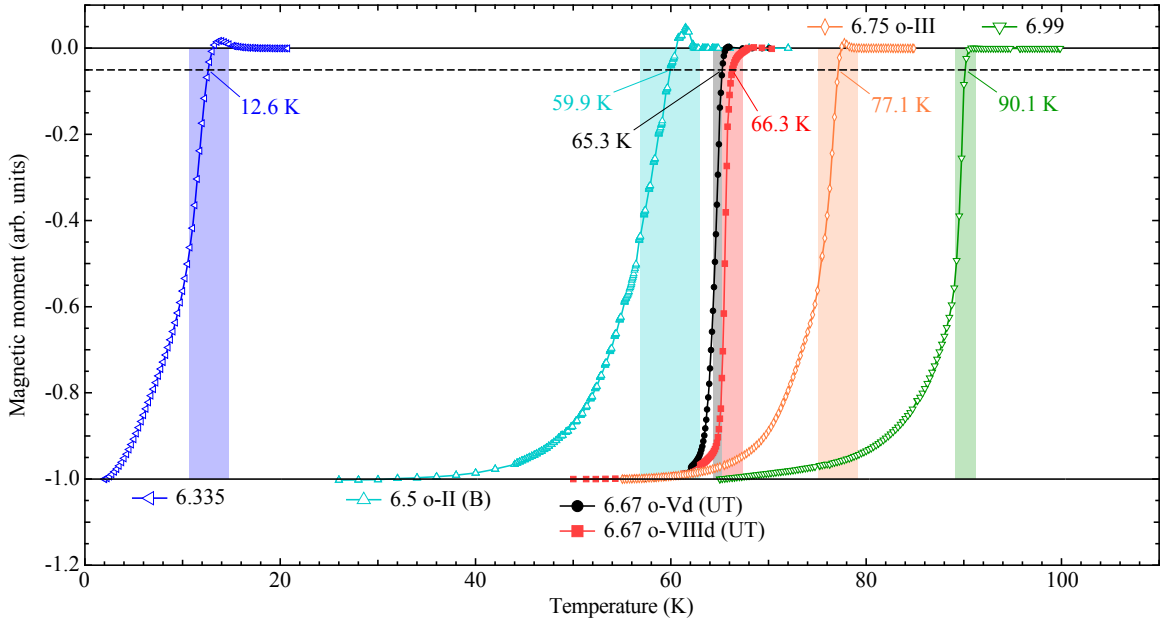

Figure 7.4 – Normalized DC magnetic susceptibility of $YBa_2Cu_3O_{6+x}$ samples. T_c is indicated at the -5% crossing (dashed line).

The $YBCO_{6.67}$ samples were measured at the Univeristy of Toronto (indicated as UT in Fig. 7.4) with a Quantum Design magnetic property measurement system (MPMS) operating in DC scan mode. For the other samples, measurements were performed at the University of Waterloo's WatLab with a Quantum Design MPMS3 operating in VSM mode (vibrating sample magnetometer). For both instruments, samples were loaded into a straw and held in place with cotton and two bent pieces of straw. Most samples had values of T_c in agreement with the expected value within 1-2 K. The $YBCO_{6.99}$ and $YBCO_{6.335}$ samples had slightly larger deviations from their expected T_c. This may be due to long-timescale oxygen diffusion, given that these were grown less recently than the other samples (they

sat in a desiccator at room temperature for a period of ~ 7 years). Under this premise, the $YBCO_{6.99}$ ($YBCO_{6.335}$) sample would have lost (gained) some oxygen content over time, causing T_c to increase from the expected value in both cases.

As evidenced in Fig. 7.4, there were some difficulties associated with the measurements performed in the VSM mode leading to small positive moments in the vicinity of T_c. These are suspected to be artifacts of the VSM scan mode, as discussed in section 7.4.2.4. Error bars were chosen generously to account for these challenges. Further discussion of the uncertainties in the mapping between T_c and p is presented in section 7.4.2.5

7.2.4 Phase diagram

We can now examine trends in the doping evolution of T_{CDW}^{on}, T_{CDW}^{max}, $\delta_{a,b}$, $\xi_{a,b}$, and $I_{H,K}^{max}$. In addition to data from this work, these extracted parameters and their p dependence will be compared with data published in recent studies performed by hard x-ray (HXR) and soft x-ray (SXR) diffraction. Taken as whole, this gives us a wider perspective on the competing phases across the hole doped side of cuprate superconductors. Notably, this updated phase diagram expands the extent of known CDW order down to $p \sim 0.058$, very near the AF insulator phase and in coexistence with robust incommensurate SDW order.

7.2.4.1 CDW onset and maximum temperatures

In Fig. 7.5 a phase diagram has been constructed showing T_{CDW}^{on}, T_{CDW}^{max}, T_c, T_N, T^* and T_{SDW} for $YBa_2Cu_3O_{6+x}$. The solid symbols are from this work. Open symbols and lines are taken from references given in the figure. The T_{CDW}^{on} and T_{CDW}^{max} domes are parabolic fits to all of the plotted data. For T_{CDW}^{on} (T_{CDW}^{max}) the maximum is at $p \sim 0.120$ ($p \sim 0.119$) and has a value of $\sim$155 K ($\sim$67 K).

These fits suggest a termination of the CDW order in the range $0.045 < p < 0.055$, coincident with the termination of T_N and the onset of T_c. At high p, the termination is likely between $0.163 < p < 0.181$, based on the observation of CDW order at $p = 0.163$,[212] but not at $p = 0.181$ (this work) nor at $p = 0.189$ (Ref. [212]). This range encompasses optimal doping for $YBa_2Cu_3O_{6+x}$.

For much of the phase diagram it can be seen that T_{CDW}^{max} tracks T_c ($0.85 < p < 1.25$). Curiously, a deviation from T_c is apparent above $p = 0.13$ both from this work and in Ref. [212]. For the point at $p = 0.058$ it is unclear whether T_{CDW}^{max} and T_c are coincident since the measurement could not be performed at sufficiently low T.

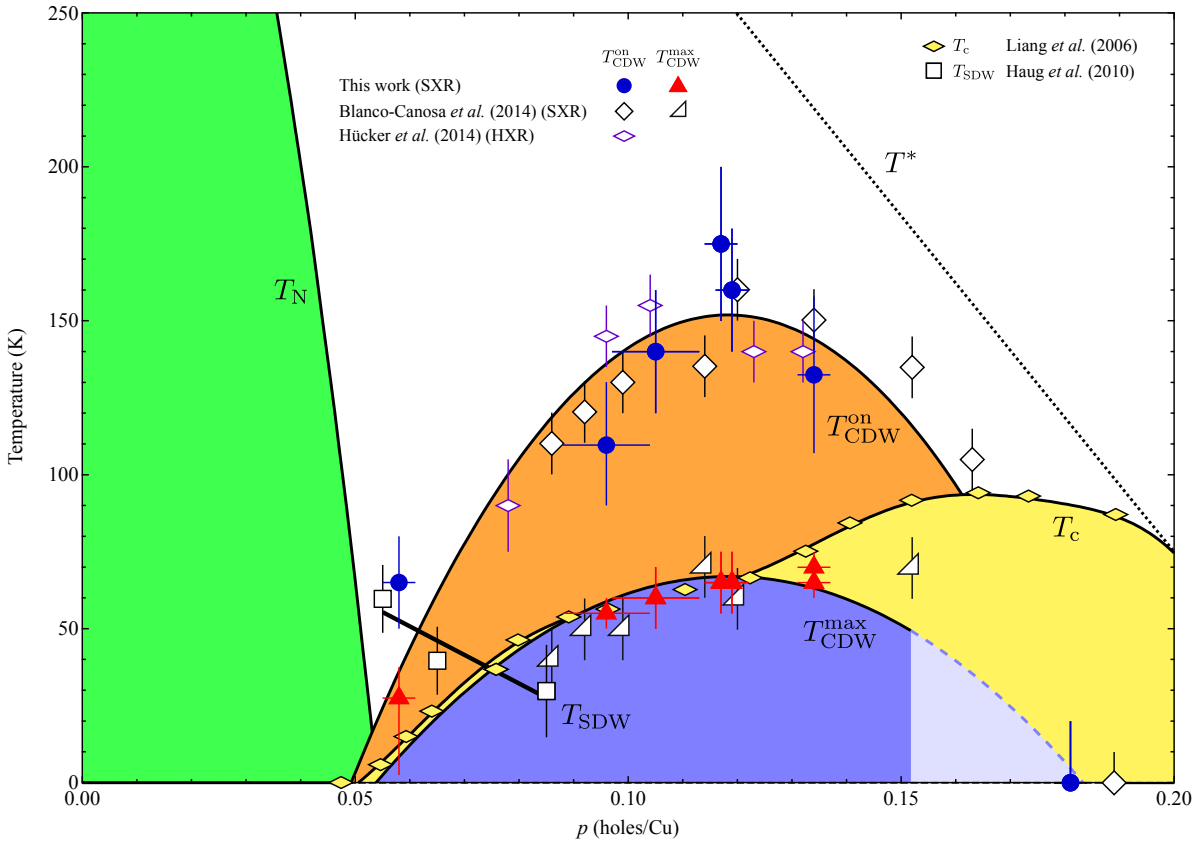

Figure 7.5 – $YBa_2Cu_3O_{6+x}$ phase diagram, highlighting spin and charge ordering onset temperatures in contrast T_c. The CDW onset temperature, T_{CDW}^{on} forms a dome centered at $p = 0.12 \pm 0.01$. T_{CDW}^{max} tracks T_c for much of the phase diagram, but appears to diverge at $p > 0.13$. For T_{CDW}^{on} and T_{CDW}^{max}, the solid symbols are from this work and the open symbols were taken from Blanco-Canosa *et al.* (2014),[212] and Hücker *et al.* (2014).[211] T_c is from Liang *et al.* (2006).[199] T_N and T_{SDW} are from Haug *et al.* (2010).[225]

In the region $p < 0.09$, incommensurate (commensurate) SDW order along H (K) was detected in $YBa_2Cu_3O_{6+x}$ by neutron scattering,[225] with onset temperature T_{SDW} as shown in Fig. 7.5 ranging between $\sim$ 60 K and $\sim$ 30 K. There are now at least three independent observations of CDW order (along K only) in this low-doped region of the phase diagram, providing confidence that superconductivity, SDW order and CDW order do coexists at low p in $YBa_2Cu_3O_{6+x}$.

7.2.4.2 Incommensurability

The peak position, directly related to the incommensurability, δ, of the CDW with the underlying crystal lattice, has been studied as a function of p. In Fig. 7.6, a compilation of data from this work as well as others is presented. On a wide scale, there is a robust decrease in δ with increasing p in $YBa_2Cu_3O_{6+x}$. This, as noted previously,[211, 212] is opposite to the trends in La-based cuprates. δ_{CDW} and δ_{SDW} for LBCO are shown for comparison. In LBCO and other La-based cuprates, the spin and charge incommensurability are related by $\delta_{CDW} \approx 2\delta_{SDW}$. This is notably opposite to the observed δ_{CDW} and δ_{SDW} trends in $YBa_2Cu_3O_{6+x}$, which have opposite sign in the low p region.

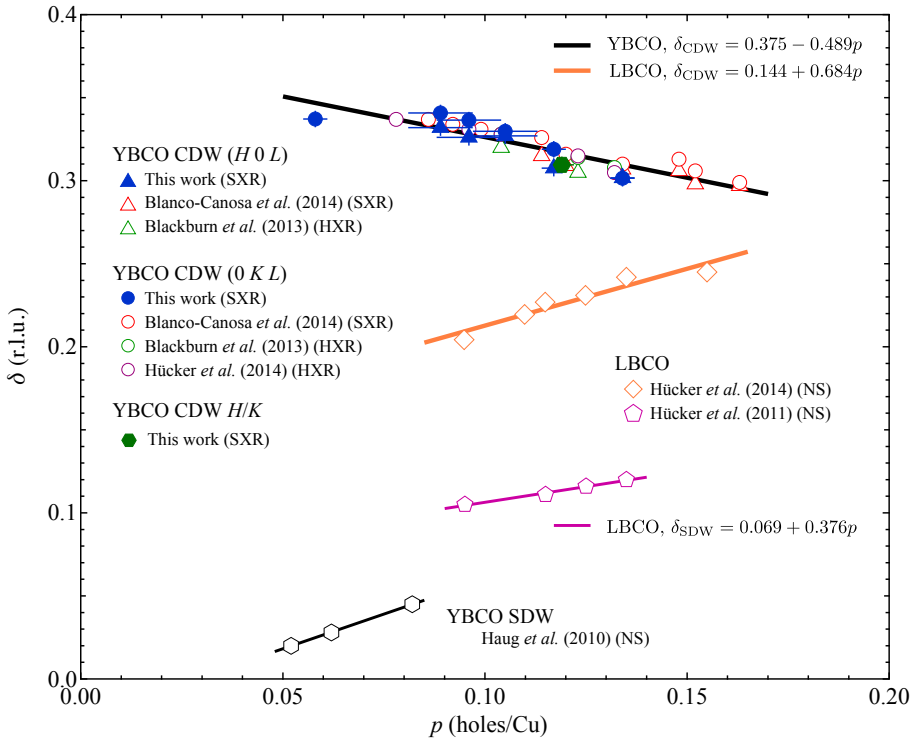

Figure 7.6 – Doping evolution of CDW (SDW) wavevector incommensurability, δ_{CDW} (δ_{SDW}), in $YBa_2Cu_3O_{6+x}$ and $La_{2-x}Ba_xCuO_4$. Triangles (circles) denote δ_a (δ_b) and filled symbols are from this work. Straight lines are linear fits in the region of available data. In $La_{2-x}Ba_xCuO_4$ a relationship of $2\delta_{SDW} \approx \delta_{CDW}$ exists, but in $YBa_2Cu_3O_{6+x}$ the slopes for δ_{CDW} and δ_{SDW} have opposite signs. Open symbols were digitized from Blanco-Canosa *et al.* (2014),[212] Blackburn *et al.* (2013),[204] Hücker *et al.* (2014),[211], Hücker *et al.* (2011),[175] and Haug *et al.* (2010).[225]

In Fig. 7.7, we focus on δ for CDW order in $YBa_2Cu_3O_{6+x}$. At this smaller scale, there appears to be some deviation from the linear trend shown in Fig. 7.6, with $\delta_{a,b}$ mostly being above (below) the fit line at $p < 0.11$ ($p > 0.11$). This is illustrated with the pink (gray) shaded regions, which serve as guides to the eye for δ_a (δ_b). These guides were obtained with sigmoid fits, giving their S-shapes. Despite the debatable applicability of the sigmoid fit, there are also robust differences in δ_a and δ_b, as identified earlier in the background-subtracted data (Fig. 7.2). Generally speaking, $\delta_b > \delta_a$ over all p. To the best of my knowledge, this deviation from linearity has not previously been noted. There appears to be a robust increase in the rate of change of δ over $0.11 < p < 0.13$.

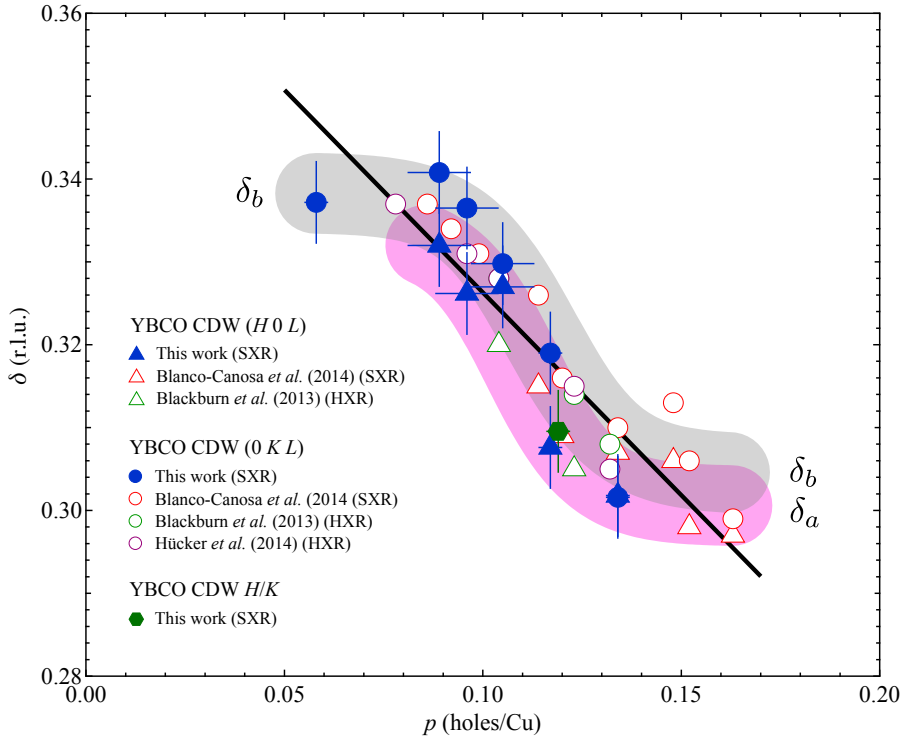

Figure 7.7 – Comparison of CDW incommensurability δ_a [δ_b] for peaks along wavevectors parallel to (H 0 L) [(0 K L)], shown as triangles [circles]. The shaded regions have a width of 0.01 r.l.u. (2× the estimated uncertainty) and guide the eye for δ_a (magenta) and δ_b (gray). The black line is the same linear fit as in Fig. 7.6. This closer view suggests that the p evolution of δ_{CDW} deviates slightly from linearity, as discussed in the text. Filled symbols are from this work whereas open symbols were digitized from Blanco-Canosa *et al.* (2014),[212] Blackburn *et al.* (2013),[204] and Hücker *et al.* (2014).[211]

It would be very interesting to know if δ_b and δ_a converge for low or high p. This might be expected at low p, since the a and b lattice constants of $YBa_2Cu_3O_{6+x}$ converge giving a tetragonal crystal structure. Conversely, it might be surprising at high p, given the maximal difference in a and b there. Given the scatter in the data, we can make conservative estimates of the difference $\delta_b - \delta_a$. For this estimate, I use the sigmoid fits to evaluate δ_a and δ_b. A constant uncertainty level of ± 0.005 r.l.u. was used. The reasons for this uncertainty level are discussed in section 7.4.2.1. I then estimate that $\delta_b - \delta_a$ is 0.006 ± 0.007 r.l.u. on average for all p, 0.004 ± 0.007 r.l.u. at low and high p, and 0.008 ± 0.007 r.l.u. near $p = 0.12$. At low and high p, there is then a 72% probability that $\delta_b > \delta_a$ and a 46% probability that $\delta_b = \delta_a$ (within ± 0.005 r.l.u.). At this stage, neither probability level is sufficiently high to make a conclusive claim, either way, so the question remains open.

7.2.4.3 Correlation length

The CDW correlation length, ξ_{CDW}, has also been studied as a function of p. In Fig. 7.8, a compilation of data from this work (solid symbols) as well data from other groups (open symbols) is presented. Here, the ξ_{CDW} is taken at $T \sim T_c$, within ~ 5 K usually. As was done for the incommensurability, the scattering data with wavevectors aligned to H and K can be considered together or separately. In Fig. 7.8 (a) we take the first view. Here the ξ_{CDW} appears to have a dome-like shape with a maximum at $p = 0.11$. The shaded region is the 99% confidence band (CB) of a parabolic fit (solid black line) to the data. Yet, when viewed this way, there are some pretty significant outliers and the fact that a peak is not seen along H at low p is ignored.

In Fig. 7.8 (b), we take the second view and fit ξ_a and ξ_b separately (the fits were unweighted). In this view, we note that there are now two domes with maxima at $p = 0.11$ and $p = 0.125$. These domes are not coincident at low p, but overlap at higher p. Specifically, ξ_a and ξ_b largely overlap for $p > 0.125$ and $\xi_b > \xi_b$ for $0.058 < p < 0.125$. This view also captures the fact that CDW order aligned with the a-axis should disappear by $p \sim 0.08$ – indeed, no CDW order along H has been reported at this doping, with the reported observation here at $p \sim 0.089$ in the o-IId sample being the lowest reported doping with a detected peak along H.

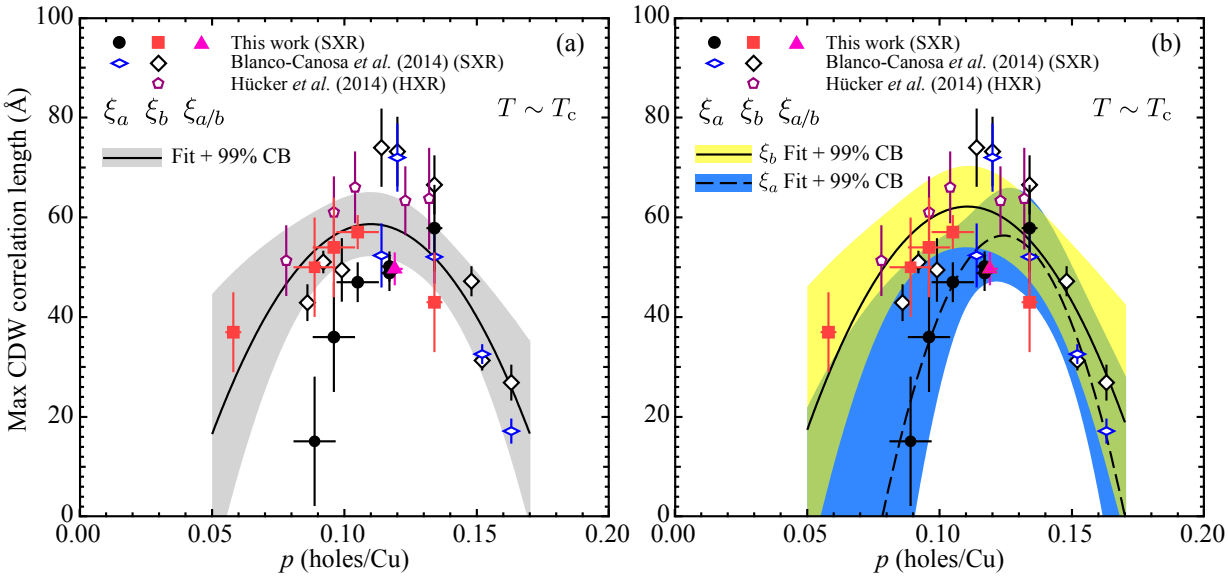

Figure 7.8 – The maximum CDW correlation length across the phase diagram of $YBa_2Cu_3O_{6+x}$. Correlation lengths are for $T \sim T_c$. (a) Values of ξ_a and ξ_b are considered together. This gives an overall picture of a dome-like correlation length across the phase diagram with a maximum at $p = 0.11$, as shown by a parabolic fit (black line) and its 99% confidence band. (b) Values of ξ_a and ξ_b are now fit separately, giving the dashed (solid) line for ξ_a (ξ_b) and corresponding blue (yellow) 99% CB. Regions of overlap appear dark yellow/green. This gives two domes that are not coincident at low p, but overlap at higher p. The ξ_b (ξ_a) dome peaks at $p = 0.11$ ($p = 0.125$). Filled symbols are from this work and open symbols were digitized from Blanco-Canosa *et al.* (2014),[212] and Hücker *et al.* (2014).[211]

7.2.4.4 Scattering intensity

In Fig. 7.9 a phase diagram of the CDW scattering amplitude is presented. Here a distinction between ordered (a) and disordered (b) chains is made because, as discussed in chapter 6 the CDW scattering amplitude decreases when chains are disordered. The gray and red shaded regions are guides to the eye for scattering along H and K, respectively. It should be noted that considerable flexibility exists as to how one can choose to draw these guides, given the sparsity of data. These guides were drawn using a simultaneous fit to all the datasets using a Lorentzian function with independent widths and amplitudes, but a global peak position. It should also be noted that making this intensity comparison possible required cross-calibration of scattering intensities across beamtimes spanning a

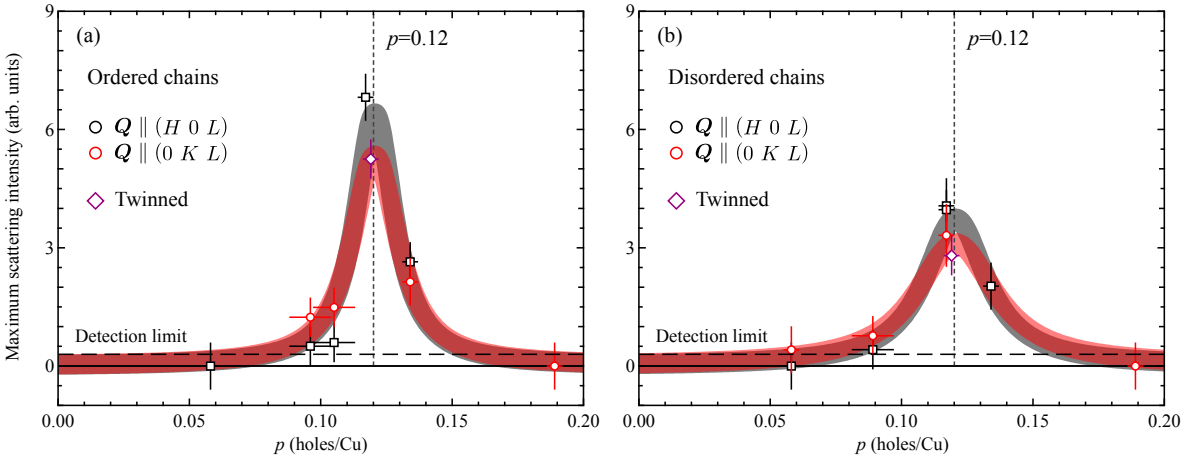

Figure 7.9 – Maximum CDW scattering intensity across the phase diagram for peaks along $(H\ 0\ L)$ and $(0\ K\ L)$ for cases where chain order is (a) present and (b) absent/minimal. The data indicates that peaks along $(0\ K\ L)$ are stronger for $p < 0.110$. This trend appears to reverse in the vicinity of $p = 0.120$, but this data is presently inconclusive for higher p. The vertical dashed line denotes $p = 0.12$ and the horizontal dashed line denotes the experimental detection limit. The shaded regions are guides to the eye.

3 year period and there could be major uncertainties resulting from this procedure. See section 7.4.2.3 for a discussion of the relevant uncertainties. Despite these challenges, we can attempt to draw some observations from this data.

The peak intensities along H and K both grow as p approaches $p = 0.12$ and then drop back down. In the region $p < 0.11$, the scattering intensity is stronger along K than along H. In the vicinity of $p = 0.12$ the peaks along H are generally stronger than along K, regardless of the presence of chain order. When all the data is considered together, the maximum in scattering intensity appears to occur at $p \sim 0.12$. At present, it is not possible to determine if there is a systematic difference between the peak position for H and K from this intensity data.

7.3 Discussion

The present study confirms much of the existing work on the doping evolution of CDW order in $YBa_2Cu_3O_{6+x}$ [22, 204, 212, 211] while also extending the extent of CDW order to lower p and providing updated phase diagrams. Importantly, the qualitative and quantitative agreement of independent measurements on different samples by different groups in the reported trends for the CDW incommensurability, correlation length, scattering amplitude, and onset/max temperatures (where overlap exists) provide confidence in the overall correctness of the constructed phase diagram. In addition, comparisons of the CDW characteristics for propagation directions parallel to the a and b crystal axes reveal important differences in the scattering intensity and correlation length in this low-doped regime. These observations further constrain the possible interpretations of the phase diagram and make some important implications.

Based on three independent observations of CDW order for $p < 0.082$, the low-doped region appears to support the coexistence of CDW order and incommensurate SDW order along H.[225] Interestingly, below $p \sim 0.09$ the CDW order persists along K but is not detectable along H. This is reflected in the faster drop off in ξ_a identified in Fig. 7.8 (b) towards lower p. This indicates that the incommensurate SDW and CDW order along H ($\boldsymbol{a}^*$) compete more strongly than the commensurate AF order and incommensurate CDW order along K ($\boldsymbol{b}^*$). As hypothesized in chapter 5, the incommensurate SDW in LBCO may play a role in favouring (or being more compatible) with s' symmetry CDW order. Along the same lines, it may be that the CDW symmetry at low doping in YBCO also prefers to exhibit s' symmetry, due to this competing incommensurate SDW order, even though YBCO reportedly exhibits d symmetry at higher doping.[117]

From Fig. 7.7, it also appears that the incommensurability along H and K deviates slightly from linearity. The magnitude of the charge order wavevectors have recently been linked experimentally to the separation between "hot spots" on the Fermi arcs of underdoped cuprates.[72, 73] This observed deviation from linearity would then suggest that the evolution of the Fermi arcs, and hence separation between hot spots, should gradually accelerate and subsequently decelerate in the vicinity of $p = 0.115$. Although I am not aware of any theoretical calculations that show this effect, it could be a very subtle feature that is omitted when displaying a coarser variation in p.

It should be noted that, in Bi-2212, a substantial drop in δ_a occurs at $p \sim 0.1$ (see Fig. 2H in Ref. [72]). Based on the magnitude of the jump, from $\delta_a \sim 0.3$ to $\delta_a \sim 0.25$, it is speculated that for $p < 0.1$ ($p > 0.1$) the character of the CDW order in Bi-2212 is similar to YBCO (LBCO). A similar, yet more subtle, effect could be occurring in YBCO. This could

ultimately be tied to the symmetry character of the CDW order varying across the phase diagram in response to changes in the degree of static and/or fluctuating SDW correlations. Future work systematically investigating the CDW symmetry across the phase diagram of $YBa_2Cu_3O_{6+x}$ would be needed to address this hypothesis.

Also potentially relevant for future calculations of Fermi arcs and understanding of the electronic structure of $YBa_2Cu_3O_{6+x}$ is the observed difference $\delta_b - \delta_a$. On average I find $\delta_b - \delta_a = 0.006 \pm 0.007$ r.l.u., but the data could also be consistent with $\delta_b - \delta_a$ tending towards 0 at low and high p with a maximum of $\delta_b - \delta_a = 0.008 \pm 0.007$ r.l.u. at $p \sim 0.12$. These features could potentially be revealed as subtle variations of the shape (asymmetry) of the Fermi arcs in the doping range where CDW order is present.

7.4 Supplementary information

In this section, supplementary data, a fluorescence calculation and additional discussions regarding uncertainties in the measurements and analysis techniques will be presented. There is quite a bit of information contained herein, most of which has already been summarized or alluded to in the main text. Descriptions of the data here will be sparse and only provided where clarification is needed.

7.4.1 Supplementary data

7.4.1.1 Temperature series

The presented RSXS scans in Fig. 7.1 were meant to illustrate the high temperature background, a scan corresponding approximately to $T_{\mathrm{CDW}}^{\mathrm{on}}$, and a scan corresponding to $T_{\mathrm{CDW}}^{\mathrm{max}}$. Here, the complete temperature series are presented. Fig. 7.10 presents the raw form with the background still intact (note that this figure spans multiple pages).

To present the background-subtracted data and the corresponding Lorentzian fits, I have found it most useful to offset vertically the data, otherwise there is too much overlap to evaluate fit quality. This makes for very tall figures, so these are presented filling a page each.

Figure 7.10 – *Note: this figure spans multiple pages.* The measured temperature evolution of the CDW scattering peak for (a) $YBa_2Cu_3O_{6.335}$, (b)-(c) $YBa_2Cu_3O_{6.5}$, (d)-(e)$YBa_2Cu_3O_{6.67}$, and (f)-(g) $YBa_2Cu_3O_{6.75}$. The chain ordering state as well as the scattering wavevector direction is indicated in each panel. The data are coloured according to temperature with a common colour scale across all panels.

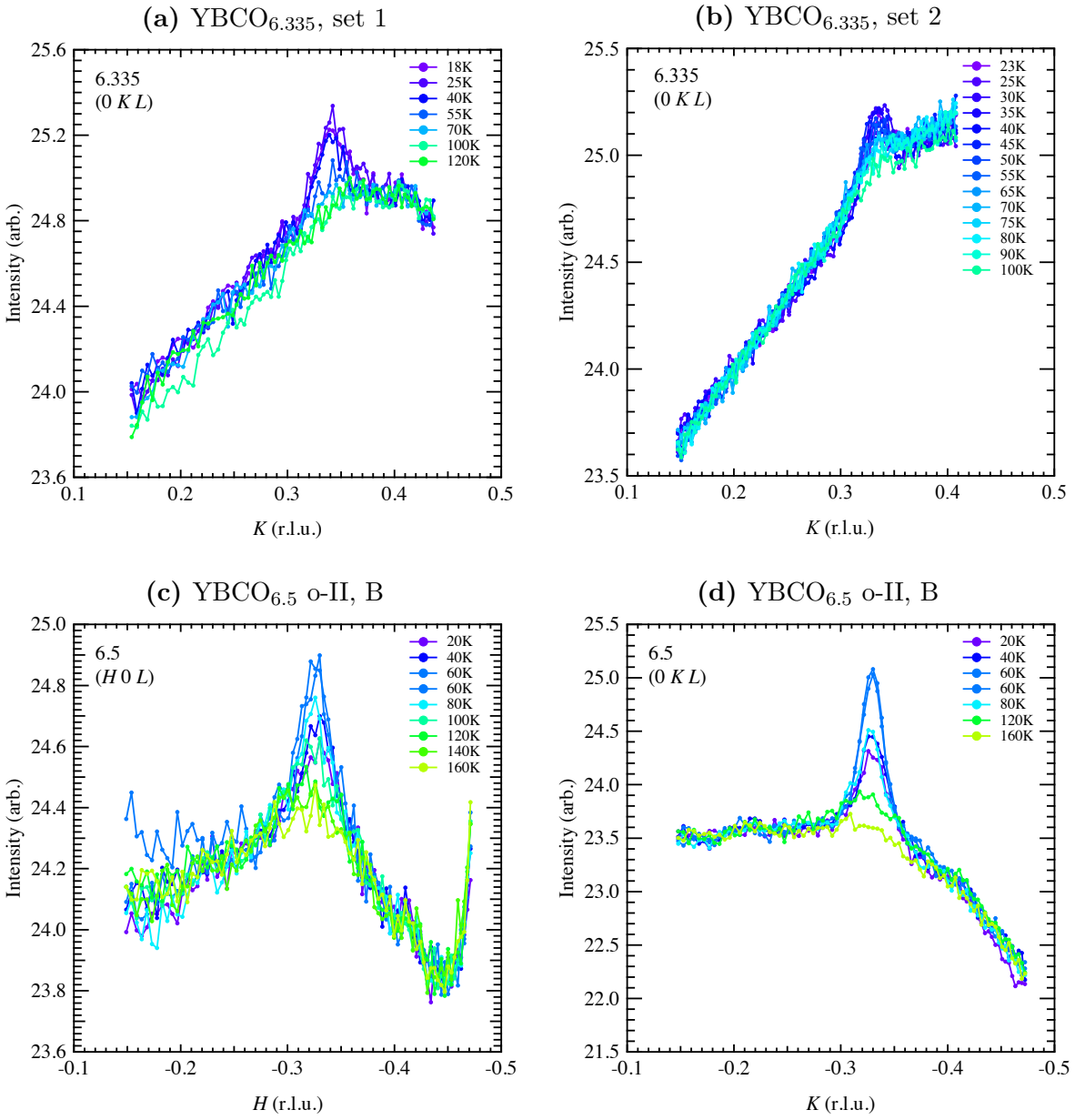

(e) $YBCO_{6.67}$ o-V

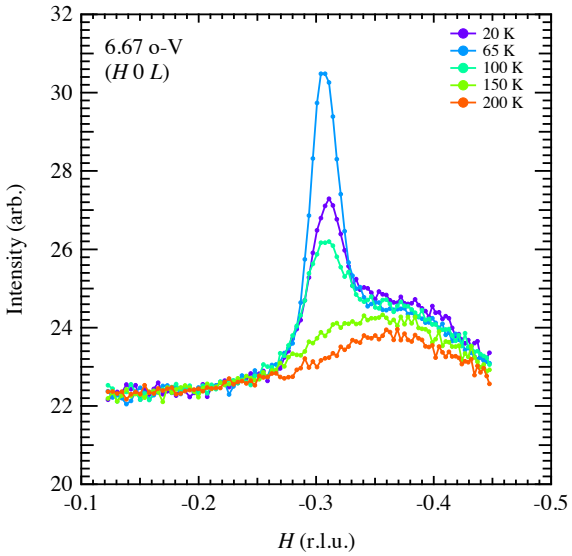

(f) $YBCO_{6.67}$ o-Vd

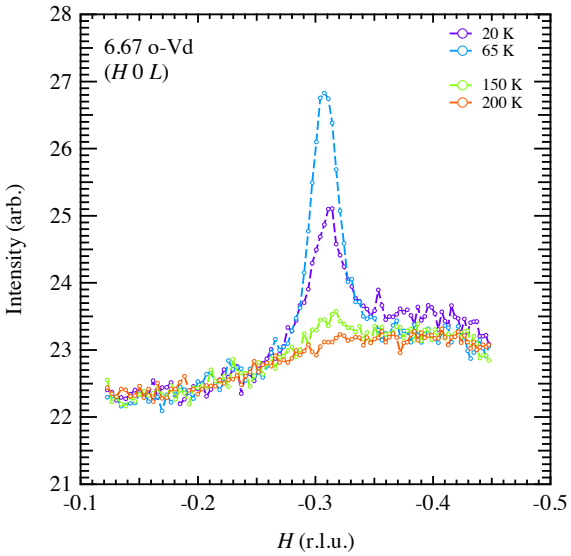

(g) $YBCO_{6.67}$ o-VIII

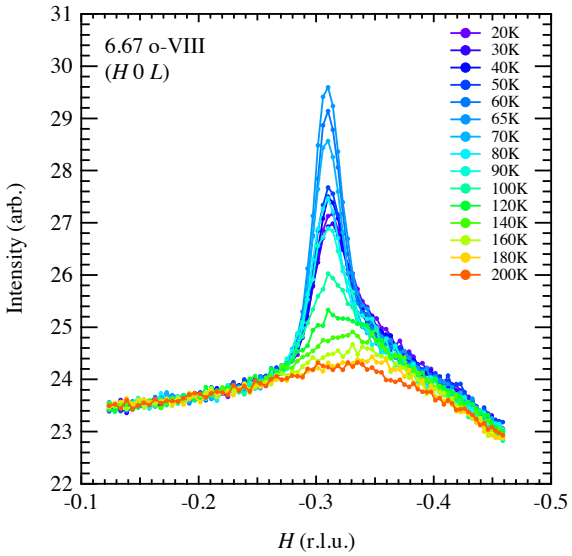

(h) $YBCO_{6.67}$ o-VIIId

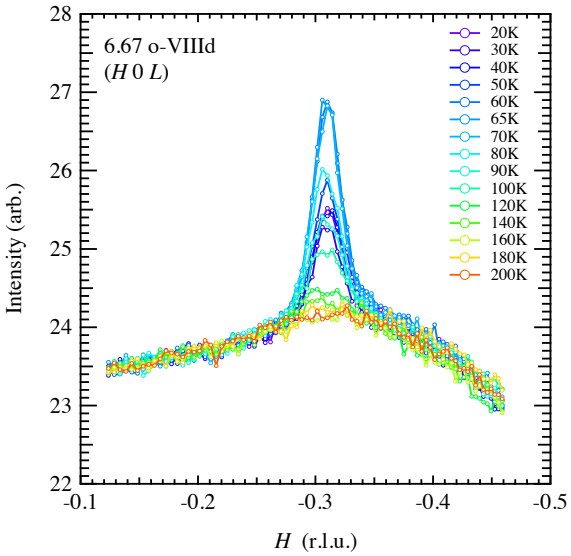

(i) $YBCO_{6.75}$ o-III

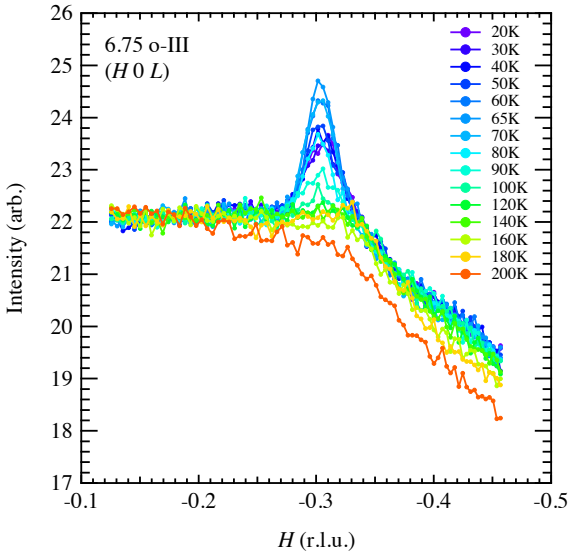

(j) $YBCO_{6.75}$ o-IIId

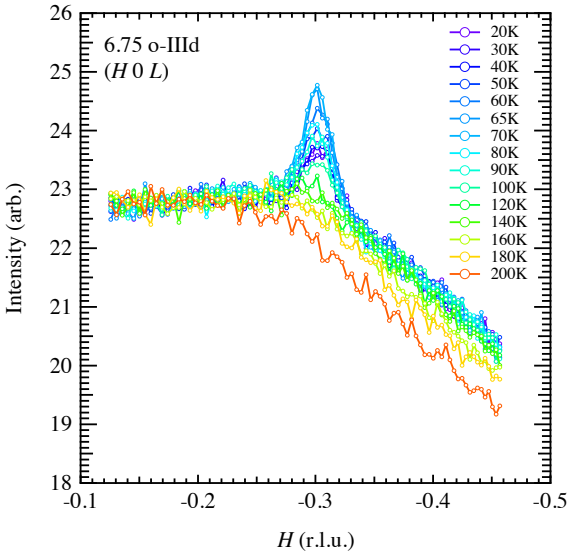

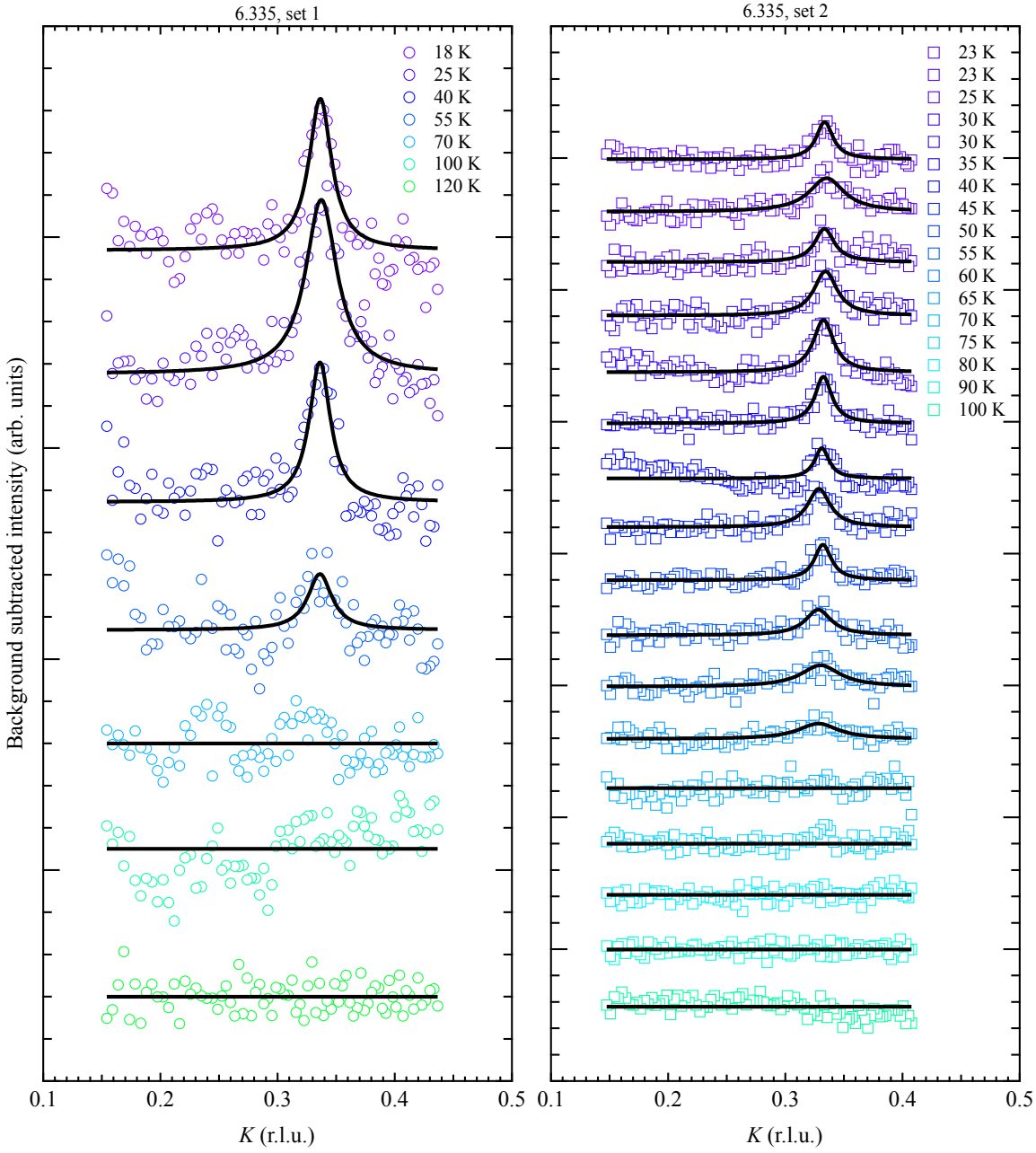

Figure 7.11 – Background subtracted data and fits for $YBCO_{6.335}$. Left and right panels are for two measurements performed at different beamtimes. CDW onset temperature taken from average value from both sets. SNR was better during set 1 measurements, but temperature spacing was coarser due to time constraints.

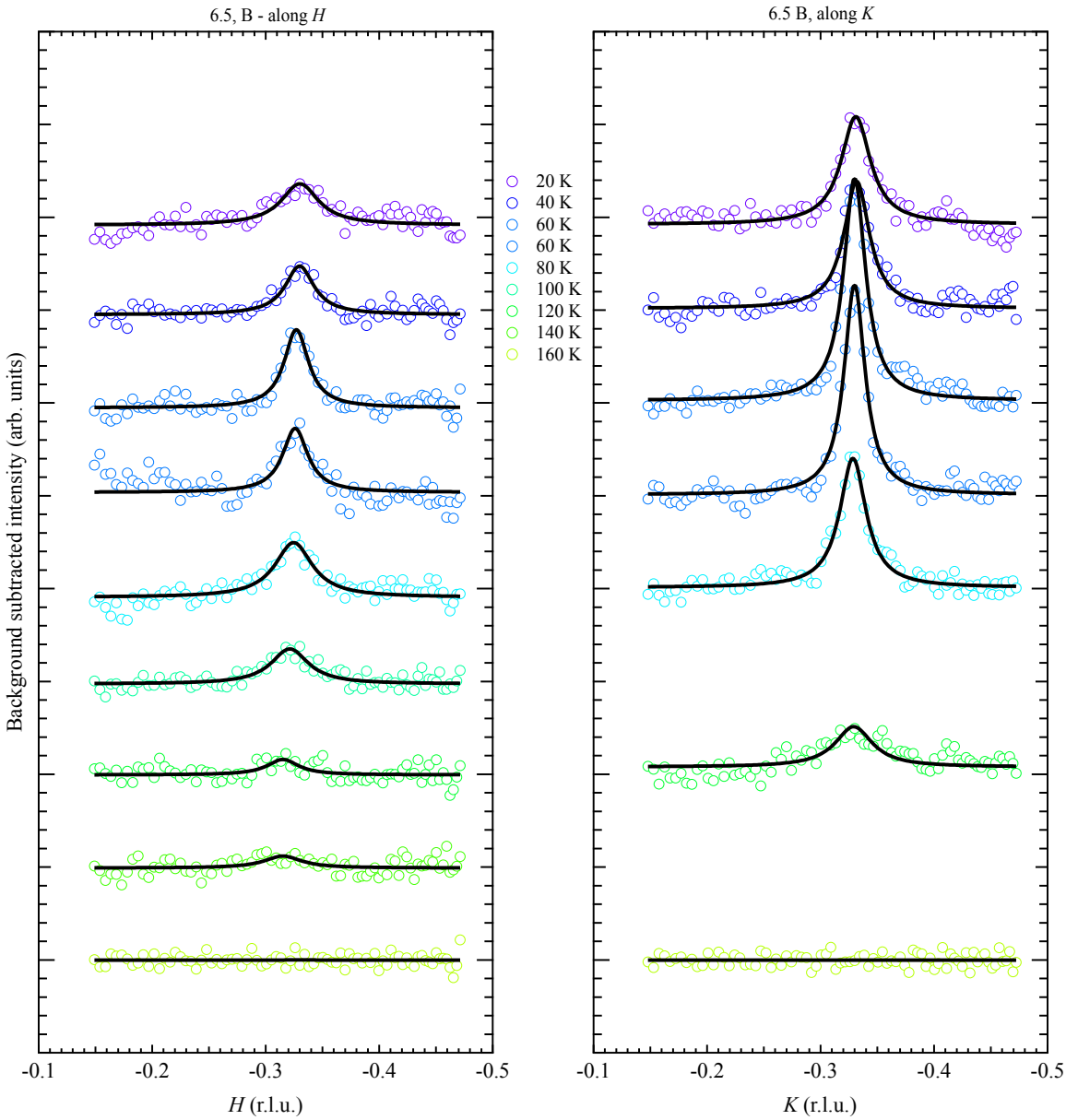

Figure 7.12 – Background subtracted data and fits for $YBCO_{6.5}$, sample B. The temperature evolution of peak along H (K) is shown in the left (right) panel.

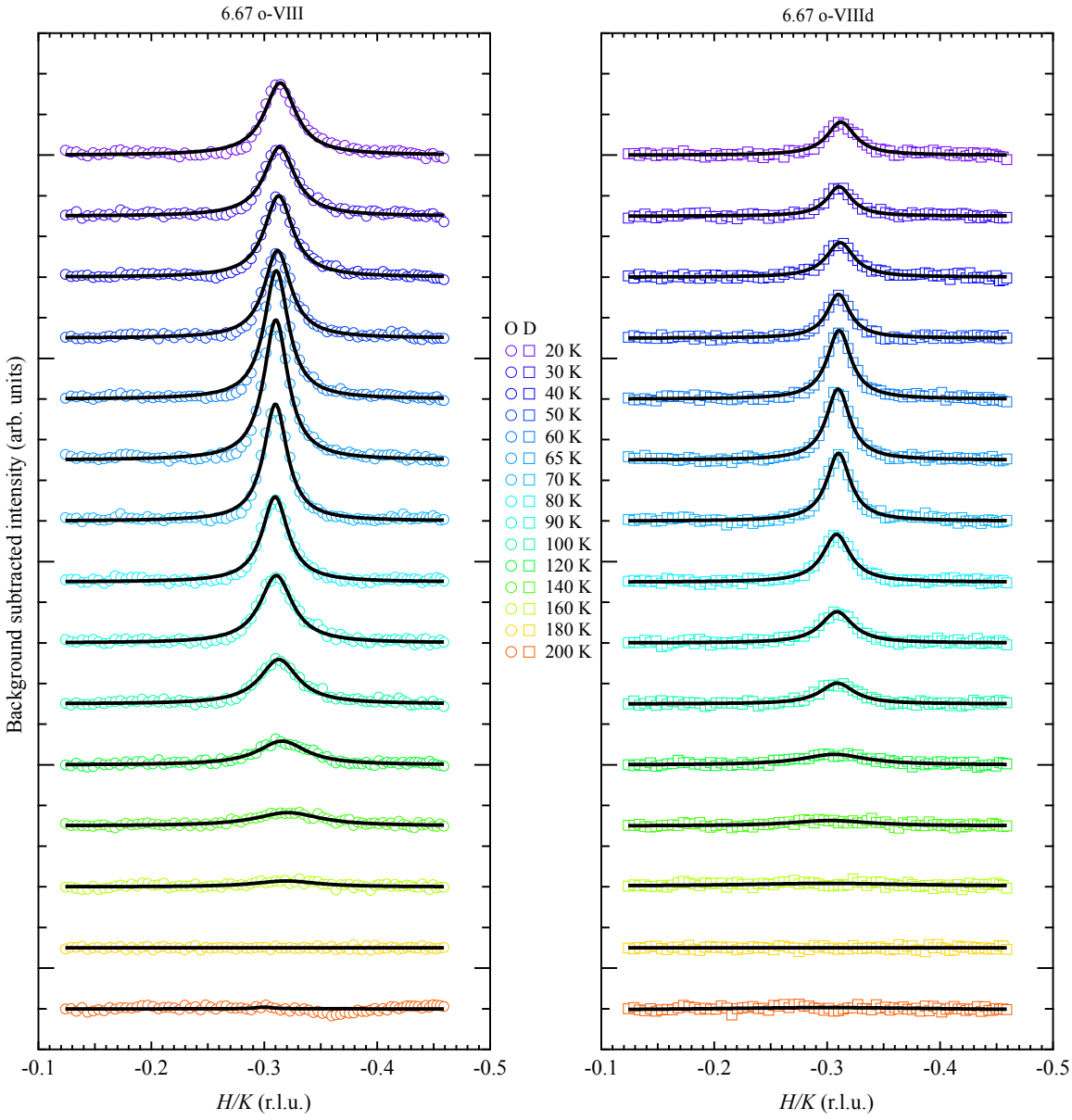

Figure 7.13 – Background subtracted data and fits for $YBCO_{6.67}$ o-VIII and o-VIIId. The temperature evolution of peak along H/K (twinned sample) for the ordered (disordered) state of the chains is shown in the left (right) panel.

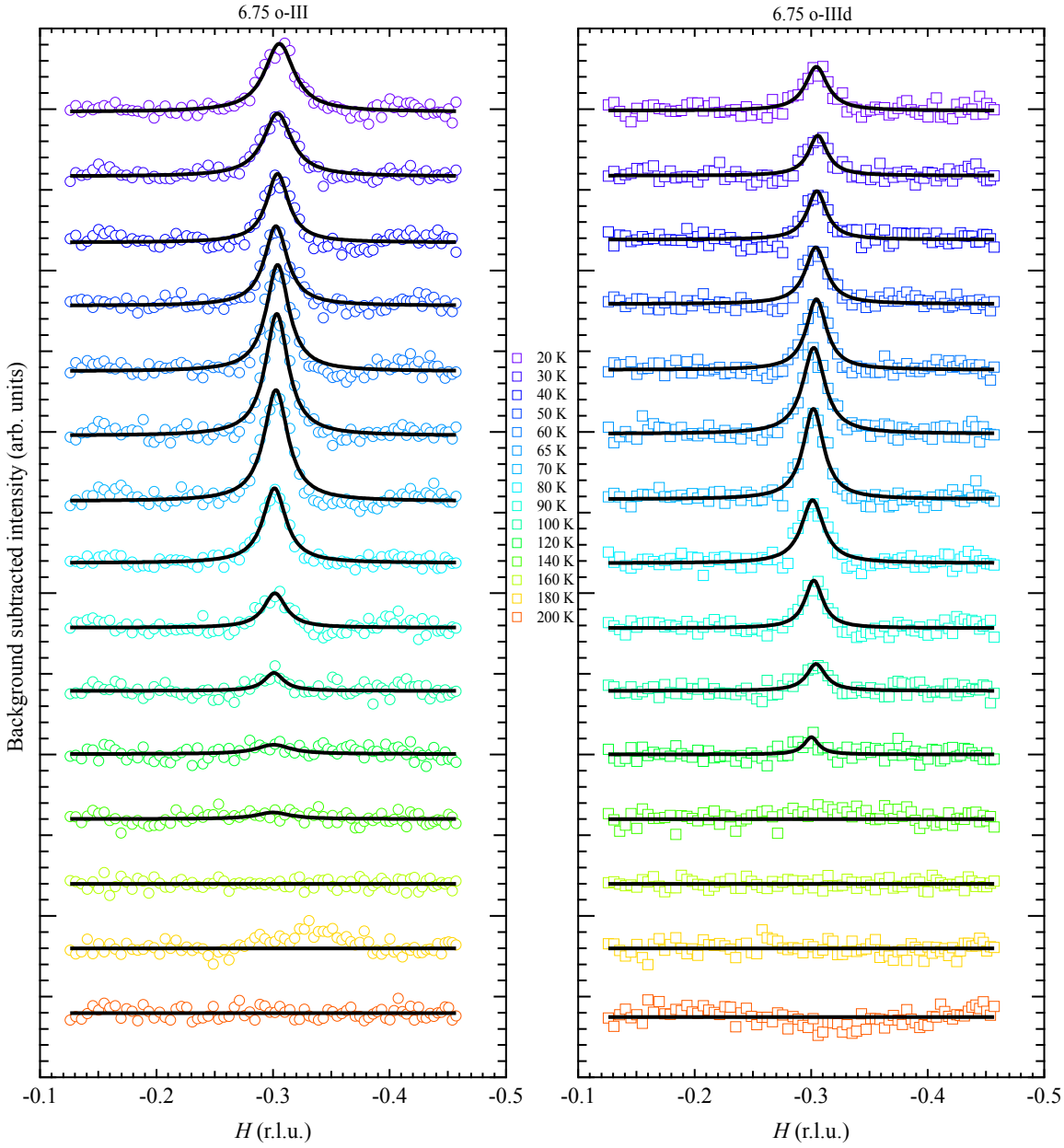

Figure 7.14 – Background subtracted data and fits for $YBCO_{6.75}$ o-III and o-IIId. The temperature evolution of peak along H for the ordered (disordered) state of the chains is shown in the left (right) panel.

7.4.1.2 X-ray absorption data

As a very coarse means of verifying the overall doping levels of the samples and sample orientation, one can evaluate the x-ray absorption with the incident photon polarization along the a or b crystal axes and compare the spectra to the literature.[84] In Fig. 7.15, the XAS at the Cu L_3 edge for the investigated samples is shown for both $\boldsymbol{\epsilon} \parallel a$ (left panel) and $\boldsymbol{\epsilon} \parallel b$ (right panel). Unfortunately, a failure to measure the XAS over a wide enough range at the time of the experiment now prevents a proper normalization of some of the data (the correct procedure is to normalize far away from the edge, in the pre- and post-edges; eg. at 910 eV and 990 eV). Nevertheless, by normalizing to the maximum at the Cu L_3 and in the pre-edge, we can see that the doping evolution is largely in agreement with the literature. As oxygen content increases a shoulder develops at around 933.6 eV, most notable for $\boldsymbol{\epsilon} \parallel b$, but also for the 6.75 and 6.99 samples for $\boldsymbol{\epsilon} \parallel a$. Note that this XAS was recorded using total fluorescence yield (TFY). Self-absorption effects are likely present, affecting this comparison slightly. Self-absorption can influence the lineshape, generally by enhancing the shoulder features relative to the maximum.

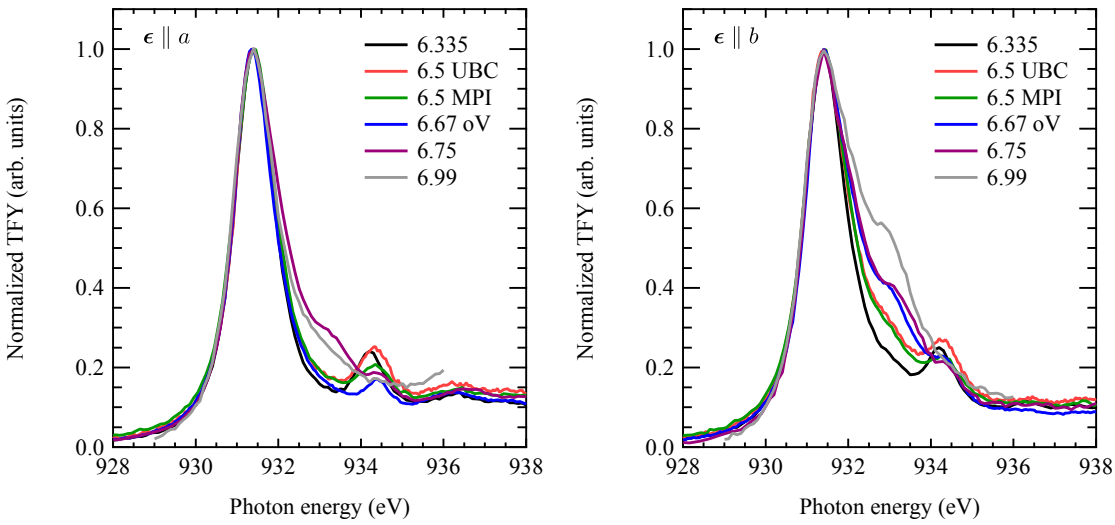

Figure 7.15 – Cu L_3 edge x-ray absorption for investigated samples. Left (right) panel is for an incident photon polarization parallel to a (b). The data are normalized to their maximum and in the pre-edge; this is not ideal but a lack of wide-range XAS prevents are more accurate normalization for all the measurements. Nevertheless, the observed doping evolution is largely consistent with the literature XAS on $YBa_2Cu_3O_{6+x}$.[84]

7.4.1.3 Fluorescence background calculation

As mentioned in section 7.2.2, the background upon which the resonant scattering signal rests is largely dominated by x-ray fluorescence from the sample. Neglecting the effect of nearby chain-ordering scattering peaks, the geometry dependence of the fluorescence can be modelled and compared to the experimental observation. One such calculation and corresponding set of data is shown in Fig. 7.16.

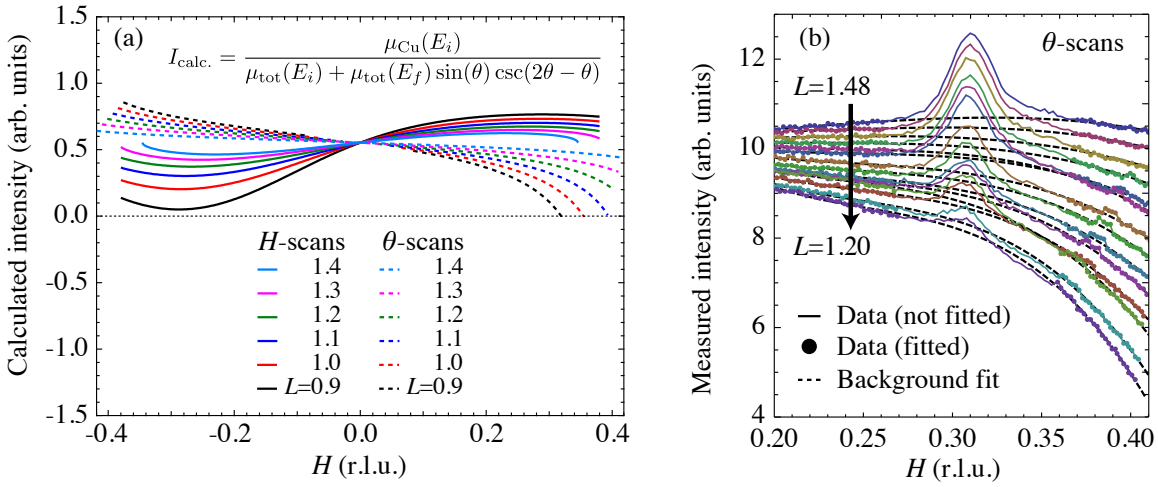

Figure 7.16 – (a) Fluorescence background calculation for $YBa_2Cu_3O_{6+x}$ showing the estimated background's variation with L, which alters the scattering geometry. For the θ-scan, the L value denotes L at the position $H = \pm 0.31$. (b) A set of θ-scans on $YBa_2Cu_3O_{6.67}$ where L varies from 1.48 to 1.2 in 0.02 increments. Dashed lines are polynomial fits to the background (filled circles) excluding the peak region (solid lines). The background variation seen in (b) agrees qualitatively with the calculated backgrounds (light blue, magenta and green) in (a).

The calculations in Fig. 7.16 (a) are performed according to the inset equation. μ_{Cu} and μ_{tot} are the x-ray attenuation coefficients for the Cu atoms in YBCO and all atoms in YBCO, respectively, evaluated at 931.3 eV. The angles $(\theta, 2\theta)$ define the scattering geometry and depend on whether an H-scan or θ-scan is performed, thus giving different shapes to the background. H-scans (solid lines) follow a straight line in $\boldsymbol{Q}$-space with fixed K and L, requiring motions of both θ and 2θ. The θ-scans (dashed lines) correspond to a fixed 2θ position and only a motion in θ, which traces an arc in $\boldsymbol{Q}$-space with varying H and L. The calculations for the θ-scan at positive H are in quite good qualitative agreement with the experimentally measured θ-scan background shown in Fig. 7.16 (b),

where one should just focus on the dashed lines. These are polynomial fits to the data (circles) excluding the peak region (lines). These types of calculations have been useful in finding good experimental geometries with relatively flat backgrounds.

7.4.1.4 Disordering of o-II chains

As mentioned in section 7.2.2, the $YBa_2Cu_3O_{6.5}$ sample A was measured both with robust o-II chain order and with a degraded o-II order. This has a measurable impact on p, so this data from disordered sample actually enabled the study of the CDW characteristics at a different p using the same sample. In Fig. 7.17, the data showing the disordering of the o-II chains is presented. The timeline of the experiments is as follows.

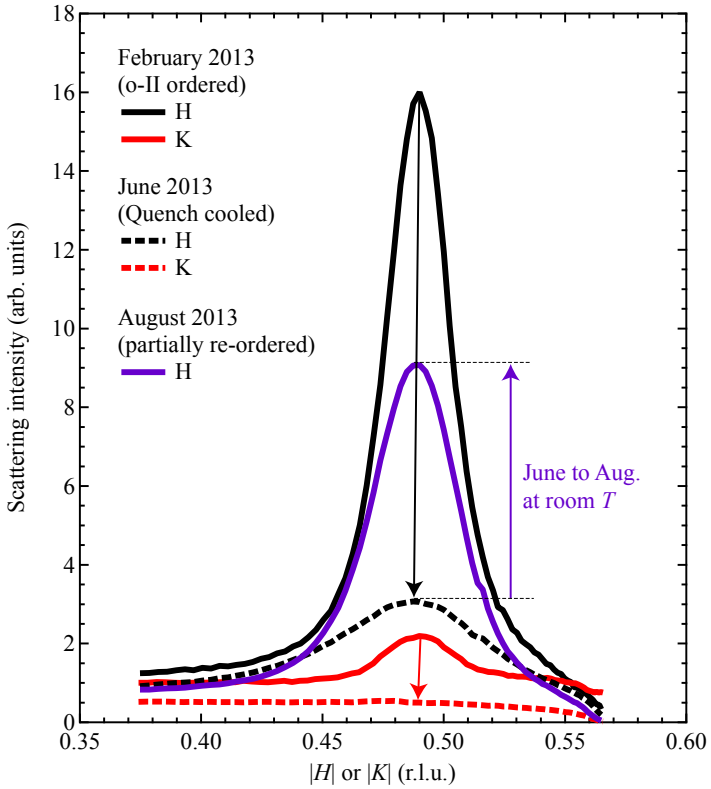

Figure 7.17 – o-II chain peak in ordered and disordered $YBCO_{6.5}$ A. The timeline for the experiments and the quench cooling procedure are discussed in the text.

Initial measurements were performed in February of 2013. There robust o-II chain ordering was detected along H. A small peak was also seen along K, likely due to light twinning of the sample. These are the solid black (H) and red (K) lines in Fig. 7.17. During this experiment, an attempt to quench cool the sample was made in a similar way as described in Chapter 6. Essentially, the sample was heated in the scattering chamber under vacuum sufficiently long that the chain peak disappeared. The heater was then turned off and the cryostat operated at maximum power to cool the sample. This procedure was fast enough to destroy o-III, o-VIII, and o-V chains in other samples, but the o-II chains reformed too quickly and the resulting state of the sample still exhibited robust o-II order, $\sim 90\%$ as intense as the original o-II order.

The plan was then to disorder the chains outside of the scattering chamber by first placing the sample in an evacuated quartz tube and heating it in a furnace and then submersing the tube into an ice bath to quench cool the sample. In June 2013, this procedure was performed 4 hours before the sample could be eventually transferred into the scattering chamber. The data corresponding to the remaining o-II order is shown in dashed lines in Fig. 7.17. Comparing the dashed lines to the solid lines reveals that the procedure was indeed successful. Unfortunately, due to an error in accounting for the cross-calibration of scattering intensities between beamtimes, this was not realized at the time (!), and it was instead believed the sample was still well ordered, so very few measurements were performed on it.[2] By the next experimental beamtime in August, the chains had partially re-ordered up to about 50% of their original amount (purple line), just due to being kept at room temperature for a sufficiently long period of time.

Despite a failure to fully characterize the sample in its disordered state, there was still *some* data that could be extracted from the experiments, and I have included as much as I could in the phase diagram since these provide crucial additional data points in the low-doped regime.

[2] In Fig. 7.17 this cross-calibration has been implemented.

7.4.2 Discussion of experimental uncertainties

The data presented here are a selection from experiments that spanned the March 2012 to January 2015 timeframe. A significant effort was made to ensure consistency between these experiments, yet there are some aspects of the measurements that cannot readily be controlled and even those that can will have some uncertainty associated with them. The net effect of these controlled and uncontrolled variables is an imperfect reproducibility of measurements of the same samples in nominally identical conditions. As a result, only those results which could be reliably extracted and checked for consistency across experiments were kept and are presented in this chapter.

Despite these efforts, there may still be important errors (systematic or otherwise) in some of the results. To account for this, generous error bars were assigned to the reported parameters. In this section, I will cover all the significant sources of error that I am aware of and provide my rationale for the reported uncertainties.

7.4.2.1 Peak position (incommensurability)

One of the important parameters studied in this chapter is the peak position, providing a measure of the CDW incommensurability. The uncertainty in this parameter for all reported data was set at ± 0.005 r.l.u. to cover a variety of possible sources of error influencing the peak position. This corresponds to $\sim 1.5\%$ uncertainty in the reported CDW incommensurability across the phase diagram. Here, I address the rationale for this uncertainty level, which comes from consideration of errors in the lattice constants, the calibration of the scattering geometry, and the background subtraction and peak fitting procedures.

Lattice constants — The momentum transfer $\boldsymbol{Q}$ has been expressed here, and throughout this thesis, with the convention of expressing the Miller indices (H, K, L) in units of $(\frac{2\pi}{a}, \frac{2\pi}{b}, \frac{2\pi}{c})$. Consequently, the derived peak positions, and hence the reported CDW incommensurability, depend on the a, b, and c lattice constants. In YBCO, a, b, and c all vary with sample composition and temperature. For the data presented here, estimates of these lattice constants, based on expected nominal sample stoichiometry and adjusting for expected thermal contraction, were used. Unfortunately, these values could not be readily verified, so they are essentially a "best guess", bringing into question what effect these guesses may play in the observed incommensurability trends. Through a sensitivity analysis, it is possible to demonstrate that the maximum potential variation in reported peak positions due these guesses is less than 1%, reflecting the fact that a and b vary less than 1% over $0.3 < x < 0.9$.[226] For instance, if one uses the lattice constants for $YBa_2Cu_3O_{6.9}$

to define $\boldsymbol{Q}$ in $YBa_2Cu_3O_{6.3}$, the apparent locations of a (hypothetical) CDW peak along H (K) would differ from the true position by 0.68% (−0.85%). The uncertainties caused by such effects for the data in Fig. 7.7 are estimated to range primarily from 0% to 0.4%. This corresponds, conservatively, to a maximum uncertainty of ±0.0015 r.l.u. due to possible errors in the lattice constants used.

Scattering geometry and crystal orientation — The geometry of the diffractometer (see Fig. 2.6), namely the angles θ and 2θ, obviously play an essential role in determining the peak positions since (H K L) indices map directly to $(\theta, 2\theta)$. For these experiments, the angle 2θ was defined using the beam direction and a photodiode detector with a narrow slit, giving $< 0.01°$ error. A structural Bragg peak with a specular scattering geometry was then used to define θ as half of 2θ. The precision of this latter step gives an uncertainty in θ of $\pm 0.15°$, equivalent to ±0.0013 r.l.u. in the H and K indices of peaks located at (± 0.31 0 L) or (0 ± 0.31 L), with $L = 1.48$. Note that refraction effects were neglected.[3] Consequently, with conservative rounding, there is approximately a maximum uncertainty of ±0.0015 r.l.u. from the crystal orientation step.

Background subtraction and peak fitting — All of the x-ray scattering data on YBCO was collected with the MCP detector (see Fig. 2.8) that also collects a considerable amount of x-ray fluorescence. This generally produced smoothly varying, temperature independent backgrounds. In cases where this background measurement was in good agreement with the other data in a given T-series, a smoothed version of the background was subtracted from all the scans. Occasionally the high temperature background did not match perfectly for the full T-series, likely due to drifts in the beamline energy or the beam spot on the sample. To account for this, the most frequent operation was simply a constant offset applied to the background, but occasionally the background was scaled by a small factor. The differences between offsetting or scaling the background were typically very minute.

If subtraction of the high temperature background resulted in noticeable artifacts (eg. dips, humps or slopes) even with offsets or scales, then it was preferable to fit the backgrounds using order 3 to 6 polynomials. Here the fit was done in regions excluding the peak. The polynomial order was varied to best match the fluorescence background of a given experimental geometry and sample, but never between scans with the same geometry (ie. any given T-series used the same polynomial order). This background varies due to differences in the experimental geometry.[4] Comparisons between this subtraction

[3] The index of refraction of $YBa_2Cu_3O_{6+x}$ at 2000 eV is 0.9996, so the resulting error in θ is correspondingly $< 0.04\%$, sufficiently small to neglect.

[4] The dependence on scattering geometry and representative calculations of this fluorescence background are illustrated in Fig. 7.16.

method and the high temperature background subtraction (when possible) did not reveal any major quantitative differences, validating both approaches.

The most difficult background subtractions were for the $YBCO_{6.75}$ and $YBCO_{6.67}$ samples with o-III (o-VIII) ordered chains. Here the chain order peaks are very near the CDW peak, so care needed to be taken to remove the influence of the chain peak on the CDW peak. Comparing different methods and background subtractions for these samples yielded differences in peak positions and amplitudes on the order of ± 0.003 r.l.u. and 5%, respectively. I take these errors as high limits and apply them (conservatively) to all samples. As a final note, the uncertainties reported by the statistical errors from least-squares fitting were typically an order magnitude lower than this, so they are being neglected.

Final estimate — Finally, to arrive at an estimate for the uncertainty due to all these factors, I have taken the average of their direct addition (0.006 r.l.u.) and their addition in quadrature (0.004 r.l.u), giving a global uncertainty of ± 0.005 r.l.u in the peak positions. Although this estimate is not statistically rigorous (I know of no proper way to combine these errors since they are not related in a straightforward manner), I note that this value is larger than any individual source of error by a factor of at least 1.5 and no more than 3.5, representing a fairly conservative (but not overly so) estimate.

7.4.2.2 Peak width (correlation length)

The peak widths and corresponding correlation lengths have uncertainties that range from 6% to 20%. This is largely dictated by the statistics of the peak fitting and varies with the signal to noise ratio of the CDW scattering peak. For instance, the uncertainty in $YBCO_{6.335}$ is quite large since the signal to noise (SNR) ratio is ~ 1.8, whereas it is much small for $YBCO_{6.67}$, since the SNR is ~ 15. The reliability of the background subtraction also influenced this uncertainty, so for the difficult cases mentioned above, the uncertainty was increased accordingly.

The fitting function used consistently across data sets was a Lorentzian function of the form $f(x) = y_0 + A/[1 + ((x - x_0)/\gamma)^2]$, where y_0 is a constant offset, A is the amplitude, x is either the H or K index, x_0 is the centroid and γ is the half width at half-maximum (HWHM). γ is related to the correlation length according to $\xi_{(H,K)} = (a, b)/(2\pi\gamma_{(H,K)})$. Note that Gaussian fits tended to overestimate the width and not fit as well as a Lorentzian. The data also fits well to a squared Lorentzian, which has a negligible impact on the $\xi^{\max}$ for all cases except the 6.67 samples (due to their higher SNR). In those cases, the squared Lorentzian would decrease γ (increase ξ) by up to $\sim 10\%$ as compared to the reported values. For consistency, this has not been corrected, but the effect on Fig. 7.8 would be

to raise the cluster of points near $p = 0.12$ (filled circles and squares) by amounts ranging from 2 to 6 Å. While this does support a very slight maximum in ξ around $p = 0.12$ from this data, it does not significantly affect the overall trend nor the relatively weak doping-dependence of ξ across the phase diagram.

Another factor to consider is the possible effect of instrumental resolution broadening. The instrumental resolution depends on energy and scattering geometry, so we will just consider the relevant case here. All of the presented data were collected on the MCP detector with a 25.4 mm diameter. A rather simplistic calculation of the instrumental resolution for high-L geometries ($L \approx 1.48$) at 931.3 eV, produces an estimated resolution of 0.016 r.l.u. (0.006 r.l.u.) for the MCP (channeltron detector: 10 mm slit).[5] These estimated resolutions are approximately 2/3 (1/4) of the minimum peak width, suggesting there may be an issue with resolution broadening for the MCP detector and the narrowest peaks ($p \sim 0.12$, $T \sim T_c$). However, measurements of the CDW scattering peak on the MCP and on the channeltron detector consistently produced peak widths that agreed within their margins of error, even for the narrowest peaks. In my estimation, this observation rules out a significant broadening effect and indicates that my simplistic resolution estimate is likely inaccurate. Consequently, resolution broadening has not been corrected for. I expect that doing so would increase the reported correlation lengths by less than 5%.

As a final note, the reported correlation lengths are only weakly sensitive to errors in lattice constants ($< 1\%$), temperature (negligible variation within ± 10 K of T_c or T_{CDW}^{max}), or crystal orientation ($< 2\%$), all of which fall below the statistical uncertainty, the effect of the background subtraction and errors due to the fitting function.

7.4.2.3 Peak amplitude

Comparing the scattering amplitudes for samples measured at different beamtimes was particularly challenging. The most important uncertainty comes from uncontrollable as-

[5] For this estimate, I simply take the width of the detectors and calculate the corresponding H or K value at either edge of the detector to estimate the "width" of the detector in r.l.u. for geometries near the peak. This overlooks the details of how resolution broadening should correctly be estimated. A realistic treatment would require first mapping the 2-dimensional detector surface to (H K L) indices, producing a surface in momentum space. It is this surface which should be convolved with the peak in momentum space. This could possibly be done numerically with an assumed "true" peak shape. This kind of calculation should more realistically indicate at what peak width the detector resolution has a quantifiable impact. In terms of de-convolving the existing data, an additional complication is that the surface actually changes gradually for every set of scattering angles, and each data point would then correspond to a slightly different integration of the peak. It is not clear to me how one might expect to handle this situation besides neglecting the changes in the surface shape.

pects of the experimental setup (beamline changes, storage ring, detector sensitivity, etc.). These can lead to large influences on the recorded intensity and the noise level of the data, despite normalizing the detector current to the incident flux (as measured by a gold mesh, upstream from the scattering chamber). To account for these changes, I compared x-ray absorption data as well as scattering data with similar scattering geometries across all relevant experiments and determined scaling factors that optimized both the comparability of the x-ray absorption spectra and the x-ray fluorescence backgrounds of the momentum space scans. These scaling factors have a large associated errors, since often this scaling could not optimize both comparisons simultaneously. I found that the needed scaling factors could vary by 10% to 30%. Overall, this is the dominant source for the large error bars in Fig. 7.9. Besides applying % errors of this magnitude, I also added uncertainty to the points very near the detection threshold to account for their relatively low SNR.

There are other relevant factors that could also affect the uncertainty in the amplitude. One is that the scattering intensity depends on photon energy and L (peaking at half-integer values). The photon energy was controlled between experiments as best as possible, but the possibility exists that the energy is offset by ± 0.1 eV, which translates to errors of $\pm 5\%$ in the scattering intensity (see Fig. 4.3). Differences in the L index could account for underestimating the peak amplitude in some cases since occasionally L was less than 1.48. Using Fig. 6.2 (d) to model the L dependence for all samples, this would suggest an maximum possible underestimate of $\sim 15\%$ (comparing $L = 1.4$ to $L = 1.48$).

Also, the peak amplitudes were extracted using the fitting amplitude from the Lorentzian function defined above. As noted, a squared Lorentzian function also could fit the data, with differences only being noticeable for the $x = 0.67$ samples. In those cases, the reported peak amplitude would diminish by about 1% using the squared Lorenztian. Finally, there could be small errors if the measurement temperature was offset from the ideal maximum, but this would be expected to be quite small and certainly less than the presented errors.

It should be mentioned that a different analysis method was also tested to evaluate the trends presented in Fig. 7.9. By dividing the peak amplitude by the background level, any differences in normalization factors between different experiments could in principle be eliminated. This analysis produced results very similar to those in Fig. 7.9. Although this procedure emphasized the uncertainty in the beamline energy, noise level, and statistics of peak fitting rather than the scaling factors mentioned above, it still produced both qualitatively similar results and a very similar global fit result with a peak at $p = 0.122$ and similar trends for the doping dependence. This provides confidence that the scaling factors were determined appropriately and are not unduly distorting the presented trends. I preferred to present the scaled amplitudes rather than the peak to background ratios as the errors are more conservative and more easily quantified.

7.4.2.4 Measurement of T_c

As discussed previously, the DC susceptibility measurements from U. of T. were performed in DC scan mode whereas those at U. of W. were performed in VSM mode. The DC scan mode produced a smooth transition between a clear diamagnetic response and none, just above T_c. With the VSM mode, artifacts (in the form of a positive signal) appeared in the data as the diamagnetic signal disappeared upon heating. Unfortunately, this made it more difficult to assess T_c from these measurements. To understand why, I will provide a brief explanation of the different scan modes.

The DC scan mode scans the sample height through an assembly of two counter-wound superconducting quantum interference devices (SQUIDs), such that the profile resulting from a magnetic material passing through them has a peaky structure on top of a background. With repeated measurements and fits to this peak function, an amplitude proportional to the magnetic moment can be extracted. As the signal becomes weaker and weaker, this method gradually finds that the scans resemble the background signal and so there is a smooth transition to zero magnetic moment.

The VSM scan mode also scans the sample height, but at each height interval it oscillates the sample (hence the name "vibrating sample magnetometer") and uses a lock-in amplifier to determine the magnitude and phase of the resulting signal. The magnetic field is still DC, but as the sample height oscillates, the SQUID picks up this oscillation. In principle, this approach can allow the system to track extremely weak signals. Despite this, close inspection of the data showed that very near T_c, the lock-in amplifier lost its phase lock but still reported a non-zero magnetic moment. Eventually, the system settled down and the magnetic moment was reported as zero. Although I suspect that there is no real magnetic moment (positive or negative) in this region of positive response, I have allowed for rather generous error bars in the reported values of T_c to account for the possibility that this is wrong.

Note that there is a high cost associated with using these MPMS instruments, so I had little choice but to use the available data despite the obvious issue I found with using the VSM mode. Also note that at the time of the these measurements, the MPMS3 had very recently been installed and was undergoing commissioning. It did not yet have the necessary software to operate in DC scan mode, which would have been preferable.

7.4.2.5 Conversion of T_c to p

With the values of T_c obtained as described above, the hole concentration was determined by digitization of the previously published mapping between T_c and p.[199] The errors on

T_c were converted to equivalent errors in p from this mapping. Given that interpolation was needed and that digitization itself can introduce small errors, I then increased the uncertainty in p by at least 0.001 holes/Cu for all samples. In most cases this led to ± 0.003 holes/Cu as the uncertainty level. For the sample $YBCO_{6.5}$ (B), it was a larger value of ± 0.008 holes/Cu, mostly due to a larger error on T_c. Note that T_c for the sample $YBCO_{6.5}$ (A) was not measured, but rather just taken as the nominal T_c for this stoichiometry. This seems justified given the close match between this T_c and T_{CDW}^{max} shown in Fig. 7.3. Nevertheless, I also gave sample $YBCO_{6.5}$ (A) the relatively large uncertainty of ± 0.008 holes/Cu.

7.4.2.6 Measurement of T_{CDW}^{on}

The CDW onset temperature was taken as the temperature at which the peak was first resolvable by direct inspection of the raw data in comparison to a reference high-T scan. The uncertainty was then set to span the two neighbouring points in the T-series. In some cases, this underestimated T_{CDW}^{on} a bit too strongly, so the midpoint between a scan with a resolvable peak and one without was taken as T_{CDW}^{on} while their T span (or a slightly expanded span) represented the uncertainty. For the $YBCO_{6.335}$ data, T_{CDW}^{on} was determined in this way for two datasets and then averaged (with error propagation) to produce the range shown in Fig. 7.3.

Chapter 8

Conclusion

8.1 Summary of results and significance

An overarching motivation for this thesis has been to clarify the nature of charge ordering in cuprate superconductors in order to guide theoretical efforts to understand how this phase may compete with superconductivity. In this regard, a few key conclusions can be drawn from the experiments and analysis.

The charge density wave in La-based cuprates was shown to be consistent with a small charge modulation amplitude. This conclusion arises from the ability to describe the scattering processes from Cu and O sublattices in $La_{2-x-y}Nd_ySr_xCuO_4$ via a model of spatially modulated orbital energies. Crucially, this model does not explicitly include modulations in hole doping, yet it successfully describes the observed resonance profiles. This indicates that the different sites in the lattice have atomic scattering form factors with similar spectral weight distributions, providing indirect evidence for nonzero, yet minimal, charge modulations. As compared to a half-filled charge stripe, this more nuanced perspective on charge ordering in La-based cuprates points towards theoretical models that emphasize bond order with minimal charge modulations, such as a valence bond solid, and argues against the robust forms of charge stripe order that is seen in the nickelates and identified in early mean-field theories.

Resonance profiles from the newfound incommensurate CDW order in $YBa_2Cu_3O_{6+x}$ were also shown to be described by spatially modulated orbital energies. In contrast, the valence modulation experienced by Cu atoms in the chain layer of YBCO is well described by calculations involving sites with different doping, and hence different spectral weight

distributions in their atomic form factors. This reveals the energy shifts as a distinguishing characteristic between the CDW in the CuO_2 planes and the valence modulation in the CuO chains. That this energy shift model applies to $YBa_2Cu_3O_{6+x}$ as well as La-based cuprates, despite their important structural differences, provides clear evidence that structural peculiarities are not central to the charge ordering, helping to dispel long-standing beliefs that charge order in La-based is a special case associated with the LTT distortion. This observation argues that charge order is a generic feature of the cuprate phase diagram associated with the physics of the CuO_2 plane. Indeed, it has been shown and is now widely recognized that charge ordering is a ubiquitous phenomenon in the cuprates.

Recent theories of charge ordering have provided a framework for describing CDW order with mixed orbital symmetry and predicted a dominant d form factor, as identified by analysis of STM data on Bi-2212 and Na-CCOC. Here, scattering measurements in a special experimental geometry were used to elucidate the orbital symmetry in $La_{2-x}Ba_xCuO_4$ and constrain the possible symmetry configurations for $YBa_2Cu_3O_{6+x}$. It was revealed that $La_{2-x}Ba_xCuO_4$ exhibits a dominant s' symmetry with a secondary d component. For $YBa_2Cu_3O_{6+x}$, the orbital symmetry could not be resolved quantitatively, but it was shown that it differs from $La_{2-x}Ba_xCuO_4$ and that it is also different for the a and b orientations of the CDW in $YBa_2Cu_3O_{6+x}$. The difference between $La_{2-x}Ba_xCuO_4$ and other cuprates, including $YBa_2Cu_3O_{6+x}$, is argued to be related to the static spin ordering, which seems to favour s' over d symmetry. This distinction also appears in theoretical models; for example, a recent 3-band Hubbard model calculation develops a s'-CDW alongside static spin order, whereas models that do not develop static spin order tend to develop a d-CDW. Microscopically, this indicates that bond modulations correlate with local AF order.

An important aspect of CDW order in $YBa_2Cu_3O_{6+x}$ and other cuprates is the spatial extent of CDW order, which remains relatively short range across many cuprate families. To address disorder in the chain layer as a potential factor setting the length scale of CDW order in $YBa_2Cu_3O_{6+x}$, three crystals with different compositions and types of chain order were studied before and after disordering the chains. It was shown that neither the correlation lengths, temperature evolution, or peak incommensurability were affected by the disruption of chain order, which alters the density of point-like oxygen defects and chainlet endpoint defects. The CDW order was nonetheless affected by this change, evidenced by a decrease in the scattering intensity associated with the magnitude orbital energy modulations. Altogether, this argues against defects pinning the CDW order or disrupting an otherwise long-range order and points towards a competition-mediated length scale as the origin for the CDW length scale in cuprates.

Finally, an effort to characterize CDW order across the phase diagram of $YBa_2Cu_3O_{6+x}$ was undertaken. CDW order was detected in a sample with a hole doping as low as

$p = 0.058$ (T_c= 12.6 K) for order along the b axis but not along the a axis, providing clear evidence for unidirectional CDW order at this low doping, near the AF insulator to superconductor transition. An inequivalence in the correlation length for order along a and b was identified for $p < 0.12$, suggesting that CDW order along a may be disrupted by competition with static incommensurate spin correlations. The CDW incommensurability decreases with increasing p, opposite of La-based cuprates and incommensurate spin ordering. Although this has been so far approximated as linear, here a subtle deviation from linearity was identified, with an inflection point around $p \sim 0.11$. These results extend the range of CDW order in the phase diagram of $YBa_2Cu_3O_{6+x}$. They also reveal important differences between the characteristics of the CDW order oriented along the a and b crystal axes, arguing for unidirectional order.

As has been shown, the cuprate problem is multifaceted and complex. Despite 3 decades of research into these materials, no single theory has unified our understanding of their physics and basic fundamental questions remain unsolved. What is the pairing mechanism? Does Mott-Hubbard or quantum critical physics form a better basis for describing the cuprates? Are the various orders intertwined or competing? Although this work does not resolve these deep questions, it has revealed various important details which will guide efforts to address them. Specifically, this work has helped to establish charge ordering as a generic and central feature of the cuprate phase diagram. Any unified theory of cuprate physics will need to explain not only superconductivity but also the co-existing and competing charge order, thus constraining its various microscopic details: short range character, temperature evolution, family-dependent CDW orbital symmetry (related to spin ordering), small charge modulation amplitudes, spatially modulated orbital energies, and a likely unidirectional nature. Altogether, this contributes significantly to narrowing the focus on the cuprate problem and guiding future efforts to resolve this great challenge in condensed matter physics.

8.2 Future work

A few projects come to mind when considering what else could still be done to exploit RSXS and answer questions regarding the nature of CDW order in the cuprates. Firstly, I think there is a potential to discover a doping evolution to the CDW symmetry in LBCO and YBCO. These experiments would be challenging but potentially quite insightful. If indeed the symmetry of the CDW varies as a function of doping, it may be possible to relate this directly to a variation in the character of the spin ordering. It would also be worth investigating if the CDW symmetry varies with temperature across T_c. If it did, it

would provide additional clues as to how CDW order and superconductivity compete.

With regards to the influence of disorder on CDW order, additional work is warranted as a major question remains: does the presence or absence of chain order correspond to more or less effective disorder on the CuO_2 plane? Theoretical models have yet to provide certainty on this matter, as simulations typically involve impurity sites placed directly in the CuO_2 plane, a scenario not quite analogous to the chain layer disorder. Experimentally, it may yet be worthwhile to revisit the case of $YBa_2Cu_3O_{6.5}$ with and without o-II order. Although the phase diagram work suggests the difference in the a and b properties of the CDW is most directly related to static spin ordering at lower hole doping, it is possible that the more robust o-II chain ordering also influences the CDW properties. This study may also represent a potentially more viable theoretical playground than the other sample compositions, given the half-filled nature of the chain layer.

There are also opportunities in developing more sophisticated modelling techniques to describe the O K edge resonance profile. In particular, I believe it should be possible to use interpolation schemes to model the doping evolution of the x-ray absorption in the pre-edge, and thus approximate the atomic scattering form factors for arbitrary p. For this, it would be ideal to measure x-ray absorption using electron yield on vacuum-cleaved samples with, well characterized, Sr content x near the 1/8 level, since the literature data are too coarse in x to reliably extrapolate to $p \pm \delta p$ for small δp. With such data and a corresponding model, it may be possible to demonstrate an approximate equivalence between an energy shift model and a hole modulation for small δp. In this scenario the shift in spectral weight (hole modulation) could be minimal while still providing enough of an energy shift ΔE to produce a detectable scattering intensity, providing a conceptually straightforward way to understand the energy shift model. This approach should in principle be amenable to extracting quantitative values for δp and ΔE, advancing our understanding of the microscopic nature of the CDW order.

Finally, a suitable microscopic description of how charge or energy modulations on O sites may influence the Cu sites needs to be developed. This is extremely relevant to interpreting the symmetry of the CDW order from Cu L edge scattering, since how the CDW symmetry components on O sites maps to the Cu sites depends on the electronic structure of the CuO_2 plane. Given the location in momentum space of the CDW scattering peak (O sublattice scattering is practically impossible), this may represent the best opportunity for determining the CDW symmetry in $YBa_2Cu_3O_{6+x}$. It is thus crucial to develop an appropriate electronic picture within which to make quantitative estimates for the CDW symmetry components.

APPENDICES

Appendix A

Useful formulae and calculations

A.1 Relation between Miller indices and $(\theta, 2\theta)$ in a 2-circle scattering geometry

We begin with the Laue equations written in Eq. 2.1. Recall that $\boldsymbol{a}_1$, $\boldsymbol{a}_2$ and $\boldsymbol{a}_3$ are the primitive vectors of the crystal lattice and H, K and L are Miller indices for a reciprocal lattice vector $\boldsymbol{G}$ that satisfies $\boldsymbol{G} = H\boldsymbol{b}_1 + K\boldsymbol{b}_2 + L\boldsymbol{b}_3$, where $\boldsymbol{b}_1$, $\boldsymbol{b}_2$ and $\boldsymbol{b}_3$ are the basis vectors for the reciprocal lattice.[143]

$$\begin{aligned} \boldsymbol{a}_1 \cdot (\boldsymbol{k}' - \boldsymbol{k}) &= 2\pi H \\ \boldsymbol{a}_2 \cdot (\boldsymbol{k}' - \boldsymbol{k}) &= 2\pi K \\ \boldsymbol{a}_3 \cdot (\boldsymbol{k}' - \boldsymbol{k}) &= 2\pi L \end{aligned} \tag{A.1}$$

Working in the lab reference frame, rotations of the sample about the center of a four-circle diffractometer have the effect of rotating the primitive vectors. The rotation rotation matrix for our four-circle diffractometer that gives this rotation is $R = R_\theta \cdot R_\chi \cdot R_\phi$, written fully as:

$$R = \begin{pmatrix} \cos(\theta)\cos(\phi) - \sin(\theta)\sin(\chi)\sin(\phi) & -\sin(\theta)\cos(\chi) & \sin(\theta)\sin(\chi)\cos(\phi) + \cos(\theta)\sin(\phi) \\ \cos(\theta)\sin(\chi)\sin(\phi) + \sin(\theta)\cos(\phi) & \cos(\theta)\cos(\chi) & \sin(\theta)\sin(\phi) - \cos(\theta)\sin(\chi)\cos(\phi) \\ -\cos(\chi)\sin(\phi) & \sin(\chi) & \cos(\chi)\cos(\phi) \end{pmatrix}. \tag{A.2}$$

We define the beam direction as $\hat{x}$, the sample normal when $\theta = 0$ as $\hat{y}$, and the vertical direction as $\hat{z}$. This definition gives $\boldsymbol{k} = \frac{2\pi E}{hc}\hat{x}$ and $\boldsymbol{k}' = \frac{2\pi E}{hc}[\cos(\omega)\hat{x} + \sin(\omega)\hat{y}]$, where I am now using ω instead of 2θ to avoid confusing notation, E is the photon energy in eV, and hc is Planck's constant times the speed of light in vacuum.[1] Thus $\boldsymbol{Q} = \boldsymbol{k}' - \boldsymbol{k} = \frac{2\pi E}{hc}[(-1+\cos(\omega))\hat{x} + \sin(\omega)\hat{y}]$. For an orthorhombic crystal mounted with its a axis aligned to $-\hat{x}$, its b axis aligned to $\hat{z}$ and its c axis aligned to $\hat{y}$ (lattice constants a, b, and c), Eq. A.1 becomes

$$\begin{aligned} R \cdot (-\hat{x}) \cdot (\boldsymbol{k}' - \boldsymbol{k}) &= 2\pi H/a \\ R \cdot (+\hat{z}) \cdot (\boldsymbol{k}' - \boldsymbol{k}) &= 2\pi K/b \\ R \cdot (+\hat{y}) \cdot (\boldsymbol{k}' - \boldsymbol{k}) &= 2\pi L/c \end{aligned} \tag{A.3}$$

[1] Note that when c appears as hc, it is the speed of the light, whereas when it appears as L/c, it is the lattice constant.

For a diffractometer operating in 2-circle mode, we can set χ and ϕ to 0, thus simplifying Eq. A.3 considerably. First, we find that $K = (0\ 0\ 1) \cdot (\boldsymbol{k}' - \boldsymbol{k}) = 0$, reducing the problem from 3 to 2 dimensions. The two remaining equations are then given by:

$$-\frac{hc}{E}\frac{H}{a} = \cos(\theta - \omega) - \cos(\theta) \tag{A.4}$$

$$-\frac{hc}{E}\frac{L}{c} = \sin(\theta - \omega) - \sin(\theta). \tag{A.5}$$

Dividing Eq. A.4 by Eq. A.5, we arrive at

$$\frac{H}{L}\frac{c}{a} = \tan\left(\frac{\omega}{2} - \theta\right). \tag{A.6}$$

Adding the square of Eq. A.4 to the square of Eq. A.5, we arrive at

$$\left(\frac{hc}{E}\right)^2 \left(\frac{H^2}{a^2} + \frac{L^2}{c^2}\right) = 2 - 2\cos(\omega), \tag{A.7}$$

which can be re-written using the trigonometric identity $2 - 2\cos(x) = 4\sin^2(x/2)$ and taking the square root of both sides

$$\frac{hc}{2E}\sqrt{\frac{H^2}{a^2} + \frac{L^2}{c^2}} = \sin\left(\frac{\omega}{2}\right). \tag{A.8}$$

Eq. A.8 is just a 2-dimensional formulation of Bragg's Law, $n\lambda = 2d\sin(\theta_B)$. We can see this by using the relations $\lambda = \frac{hc}{E}$, $\sqrt{\frac{H^2}{a^2} + \frac{L^2}{c^2}} = \frac{1}{d}$, $n = 1$, and $\sin(\frac{\omega}{2}) = \sin(\theta_B)$.

The equations Eq. A.6 and Eq. A.8 can be used to solve for (θ, ω) for a desired (H, L). This is how Eq. 2.2 and Eq. 2.3 were derived in the main text. Note, a different notation was used ($\omega \to 2\theta,\ \theta \to \theta_s,\ L \to K,\ c \to b$). Explicitly, in this notation, the relations are:

$$\omega = 2\sin^{-1}\left(\frac{hc}{2E}\sqrt{\left(\frac{H}{a}\right)^2 + \left(\frac{L}{c}\right)^2}\right) \tag{A.9}$$

$$\theta = \frac{\omega}{2} - \tan^{-1}\left(\frac{H}{L}\frac{c}{a}\right), \tag{A.10}$$

Interestingly, when deriving Bragg's Law from the Laue equations, we realize that Bragg's Law fails to relate θ to the Miller indices. For any Bragg peak with $H = 0$, this does not matter, as we have a specular condition and $\theta = \omega/2$ by definition. It also does not matter for measurements of crystalline powders (with all possible orientations fulfilled), as then the definition of θ is meaningless. For diffraction from single crystals, however, one certainly needs to use the Laue formulation!

A.2 Wedge angle for azimuthal rotation experiment

In chapter 5 an azimuthal rotation experiment was performed to rotate sample about $\boldsymbol{Q}_{\mathrm{CDW}}$. For this a wedge-shaped azimuthal sample plug had to be made with the correct surface angle. See Fig. 5.1 for the geometry. Here I will derive the formula for this angle.

The wedge acts as an additional rotation that occurs before ϕ, χ or θ, so the rotation matrix with the wedge included is given by $R = R_\theta \cdot R_\chi \cdot R_\phi \cdot R_w$, where R_w will provide a rotation about the $\hat{z}$ axis in the positive θ direction of magnitude θ_w. This can be simplified using the substitutions $\theta = \omega/2$ and $\chi = 0$. The former ensures that the axis of rotation of ϕ is aligned with $\boldsymbol{Q}$ (specular geometry with $\theta_w = 0$), while the latter limits the possible solutions to those only involving θ_w. The rotation matrix is then given by:

$$R = \begin{pmatrix} \cos(w)\cos\left(\frac{\omega}{2}\right)\cos(\phi) - \sin(w)\sin\left(\frac{\omega}{2}\right) & -\sin(w)\cos\left(\frac{\omega}{2}\right)\cos(\phi) - \cos(w)\sin\left(\frac{\omega}{2}\right) & \cos\left(\frac{\omega}{2}\right)\sin(\phi) \\ \sin(w)\cos\left(\frac{\omega}{2}\right) + \cos(w)\sin\left(\frac{\omega}{2}\right)\cos(\phi) & \cos(w)\cos\left(\frac{\omega}{2}\right) - \sin(w)\sin\left(\frac{\omega}{2}\right)\cos(\phi) & \sin\left(\frac{\omega}{2}\right)\sin(\phi) \\ -\cos(w)\sin(\phi) & \sin(w)\sin(\phi) & \cos(\phi) \end{pmatrix}. \quad \text{(A.11)}$$

We then evaluate the system Eq. A.3 using Eq. A.11 and find that it reduces to

$$\begin{aligned} -\frac{H}{a} &= 2\sin(\theta_w)\sin\left(\frac{\omega}{2}\right)\frac{E}{hc} \\ \frac{K}{b} &= 0 \\ \frac{L}{c} &= 2\cos(\theta_w)\sin\left(\frac{\omega}{2}\right)\frac{E}{hc} \end{aligned} \quad \text{(A.12)}$$

The wedge angle is thus found easily, giving

$$\theta_w = -\tan^{-1}\left(\frac{H}{L}\frac{c}{a}\right). \quad \text{(A.13)}$$

The sign is not important for manufacturing the wedge. However, some care should be taken when defining $\phi = 0$ in this system. Whether the wedge angle adds to θ or subtracts from θ at $\phi = 0$ turns out to be important for comparison to model calculations that incorporate absorption effects, since these can cause the scattering intensity for $\phi = 0°$ and $\phi = 180°$ to differ.

A.3 Photon path lengths

The maximum path length $p_{\max}$ (cm) that photons of energy E can traverse through air while retaining a fraction $f = I/I_0$ of their initial flux can be approximated by

$$p_{\max} = -\ln(f)(\rho\mu(E))^{-1}, \tag{A.14}$$

where $\mu(E)$ is the x-ray attenuation coefficient (cm^2/g) and $\rho = 4.64444 \times 10^{-4} P/T$ is the density of dry air (g/cm^3) with pressure P (Torr) and temperature T (K). Table A.1 shows $p_{\max}$ for 100 eV photons passing through dry air at room temperature calculated at pressures ranging from atmospheric pressure to UHV. Note that higher energy photons have larger $p_{\max}$ than calculated here, since $\mu(100 \text{ eV}) > \mu(E > 100 \text{ eV})$ for dry air.

Table A.1: Maximum path length $p_{\max}$ that 100 eV photons can traverse through dry air while maintaining $I/I_0 > f$ as a function of pressure. Calculated for $T = 20°$C.

P (Torr)	$p_{\max}$ (cm) $f = 0.50$	$p_{\max}$ (cm) $f = 0.99$
760	1.19×10^{-2}	1.72×10^{-4}
100	9.02×10^{-2}	1.31×10^{-3}
1	9.02	1.31×10^{-1}
10^{-3}	9.02×10^{3}	1.31×10^{2}
10^{-6}	9.02×10^{6}	1.31×10^{5}
10^{-9}	9.02×10^{9}	1.31×10^{8}

As a practical example, if we want to build a 20 m long beamline (at room temperature) and we want less than 1% flux loss for 100 eV photons, using Eq. A.14, we find that P must be less than 6.54×10^{-5} Torr. This illustrates one fundamental reason why soft x-ray beamlines typically operate in UHV conditions for all of their optical components. Other reasons are the need to be connected to the storage ring, which is kept under UHV, and to minimize contamination on optical components. The generally much smaller experimental endstations can in principle be designed to operate at higher pressures with consideration of these flux losses.

References

[1] Achkar, A.J., He, F., Sutarto, R., Geck, J., Zhang, H., Kim, Y.J., & Hawthorn, D.G., Resonant X-Ray Scattering Measurements of a Spatial Modulation of the Cu $3d$ and O $2p$ Energies in Stripe-Ordered Cuprate Superconductors. *Phys. Rev. Lett.* **110**, 017001 (2013), DOI: 10.1103/PhysRevLett.110.017001.

[2] Achkar, A.J., Sutarto, R., Mao, X., He, F., Frano, A., Blanco-Canosa, S., Le Tacon, M., Ghiringhelli, G., Braicovich, L., Minola, M., Moretti Sala, M., Mazzoli, C., Liang, R., Bonn, D.A., Hardy, W.N., Keimer, B., Sawatzky, G.A., & Hawthorn, D.G., Distinct Charge Orders in the Planes and Chains of Ortho-III-Ordered $YBa_2Cu_3O_{6+\delta}$ Superconductors Identified by Resonant Elastic X-ray Scattering. *Phys. Rev. Lett.* **109**, 167001 (2012), DOI: 10.1103/PhysRevLett.109.167001.

[3] Achkar, A.J., Mao, X., McMahon, C., Sutarto, R., He, F., Liang, R., Bonn, D.A., Hardy, W.N., & Hawthorn, D.G., Impact of Quenched Oxygen Disorder on Charge Density Wave Order in $YBa_2Cu_3O_{6+x}$. *Phys. Rev. Lett.* **113**, 107002 (2014), DOI: 10.1103/PhysRevLett.113.107002.

[4] Achkar, A.J., He, F., Sutarto, R., McMahon, C., Zwiebler, M., Hucker, M., Gu, G.D., Liang, R., Bonn, D.A., Hardy, W.N., Geck, J., & Hawthorn, D.G., Orbital symmetry of charge density wave order in La1.875Ba0.125CuO4 and YBa2Cu3O6.67. arXiv:1409.6787v1 [cond-mat.supr-con].

[5] Bednorz, J. & Müller, K., Possible high T_c Superconductivity in the Ba–La–Cu–O system. *Zeitschrift für Physik B Condensed Matter* **64**, 189–193 (1986), DOI: 10.1007/BF01303701.

[6] Carbotte, J.P., Properties of boson-exchange superconductors. *Rev. Mod. Phys.* **62**, 1027–1157 (1990), DOI: 10.1103/RevModPhys.62.1027.

[7] Bardeen, J., Cooper, L.N., & Schrieffer, J.R., Theory of Superconductivity. *Phys. Rev.* **108**, 1175–1204 (1957), DOI: 10.1103/PhysRev.108.1175.

[8] Bardeen, J., Cooper, L.N., & Schrieffer, J.R., Microscopic Theory of Superconductivity. *Phys. Rev.* **106**, 162–164 (1957), DOI: 10.1103/PhysRev.106.162.

[9] Van Harlingen, D.J., Phase-sensitive tests of the symmetry of the pairing state in the high-temperature superconductors–Evidence for $d_{x^2-y^2}$ symmetry. *Rev. Mod. Phys.* **67**, 515–535 (1995), DOI: 10.1103/RevModPhys.67.515.

[10] Matthias, B.T., Empirical Relation between Superconductivity and the Number of Valence Electrons per Atom. *Phys. Rev.* **97**, 74–76 (1955), DOI: 10.1103/PhysRev.97.74.

[11] Pickett, W., Electronic structure of the high-temperature oxide superconductors. *Rev. Mod. Phys.* **61**, 433–512 (1989), DOI: 10.1103/RevModPhys.61.433.

[12] Dagotto, E., Correlated electrons in high-temperature superconductors. *Rev. Mod. Phys.* **66**, 763–840 (1994), DOI: 10.1103/RevModPhys.66.763.

[13] Timusk, T. & Statt, B., The pseudogap in high-temperature superconductors: an experimental survey. *Reports on Progress in Physics* **62**, 61 (1999), DOI: 10.1088/0034-4885/62/1/002.

[14] Hashimoto, M., Vishik, I.M., He, R.H., Devereaux, T.P., & Shen, Z.X., Energy gaps in high-transition-temperature cuprate superconductors. *Nature Phys.* **10**, 483–495 (2014), DOI: 10.1038/nphys3009.

[15] Buchanan, M., Mind the pseudogap. *Nature* **409**, 8–11 (2001), DOI: 10.1038/35051238.

[16] van Delft, D. & Kes, P., The discovery of superconductivity. *Physics Today* **63**, 38 (2010), DOI: 10.1063/1.3490499.

[17] Uchida, S., Copper Oxide Superconductors. In *High Temperature Superconductivity*, Vol. 213 of *Springer Series in Materials Science*, (pages 23–59) (Springer Japan, 2015), ISBN 978-4-431-55299-4, DOI: 10.1007/978-4-431-55300-7_3.

[18] Hull, J.R., Applications of high-temperature superconductors in power technology. *Reports on Progress in Physics* **66**, 1865 (2003), DOI: 10.1088/0034-4885/66/11/R01.

[19] Sachdev, S., *Colloquium:* Order and quantum phase transitions in the cuprate superconductors. *Rev. Mod. Phys.* **75**, 913–932 (2003), DOI: 10.1103/RevModPhys.75.913.

[20] Norman, M.R. & Pépin, C., The electronic nature of high temperature cuprate superconductors. *Reports on Progress in Physics* **66**, 1547 (2003), DOI: 10.1088/0034-4885/66/10/R01.

[21] Taillefer, L., Scattering and Pairing in Cuprate Superconductors. *Annual Review of Condensed Matter Physics* **1**, 51–70 (2010), DOI: 10.1146/annurev-conmatphys-070909-104117.

[22] Ghiringhelli, G., Le Tacon, M., Minola, M., Blanco-Canosa, S., Mazzoli, C., Brookes, N.B., De Luca, G.M., Frano, A., Hawthorn, D.G., He, F., Loew, T., Moretti Sala, M., Peets, D.C., Salluzzo, M., Schierle, E., Sutarto, R., Sawatzky, G.A., Weschke, E., Keimer, B., & Braicovich, L., Long-Range Incommensurate Charge Fluctuations in (Y,Nd)$Ba_2Cu_3O_{6+x}$. *Science* **337**, 821–825 (2012), DOI: 10.1126/science.1223532.

[23] Chang, J., Blackburn, E., Holmes, A.T., Christensen, N.B., Larsen, J., Mesot, J., Liang, R., Bonn, D.A., Hardy, W.N., Watenphul, A., Zimmermann, M.v., Forgan, E.M., & Hayden, S.M., Direct observation of competition between superconductivity and charge density wave order in $YBa_2Cu_3O_{6.67}$. *Nature Phys.* **8**, 871–876 (2012), DOI: 10.1038/nphys2456.

[24] Fradkin, E. & Kivelson, S.A., High-temperature superconductivity: Ineluctable complexity. *Nature Phys.* **8**, 864–866 (2012), DOI: 10.1038/nphys2498.

[25] Tranquada, J.M., Sternlieb, B.J., Axe, J.D., Nakamura, Y., & Uchida, S., Evidence for stripe correlations of spins and holes in copper oxide superconductors. *Nature* **375**, 561–563 (1995), DOI: 10.1038/375561a0.

[26] Damascelli, A., Hussain, Z., & Shen, Z.X., Angle-resolved photoemission studies of the cuprate superconductors. *Rev. Mod. Phys.* **75**, 473–541 (2003), DOI: 10.1103/RevModPhys.75.473.

[27] Tranquada, J., Neutron Scattering Studies of Antiferromagnetic Correlations in Cuprates. In *Handbook of High-Temperature Superconductivity*, edited by J.R. Schrieffer & J.S. Brooks, (pages 257–298) (Springer New York, 2007), ISBN 978-0-387-35071-4, DOI: 10.1007/978-0-387-68734-6_6.

[28] Fink, J., Schierle, E., Weschke, E., & Geck, J., Resonant elastic soft x-ray scattering. *Reports On Progress In Physics* **76**, 056502 (2013), DOI: 10.1088/0034-4885/76/5/056502.

[29] Blackburn, E., X-ray diffraction studies of charge density waves in cuprate superconductors: A brief review. *Physica B: Condensed Matter* (2014), DOI: 10.1016/j.physb.2014.11.055.

[30] Fujita, K., Schmidt, A.R., Kim, E.A., Lawler, M.J., Lee, D.H., Davis, J.C., Eisaki, H., & Uchida, S., Spectroscopic Imaging Scanning Tunneling Microscopy Studies of Electronic Structure in the Superconducting and Pseudogap Phases of Cuprate High-T_c Superconductors. *J. Phys. Soc. Jpn.* **81**, 011005 (2012), DOI: 10.1143/JPSJ.81.011005.

[31] Warren, W., Walstedt, R., Brennert, G., Cava, R., Tycko, R., Bell, R., & Dabbagh, G., Cu spin dynamics and superconducting precursor effects in planes above T_c in $YBa_2Cu_3O_{6.7}$. *Phys. Rev. Lett.* **62**, 1193–1196 (1989), DOI: 10.1103/PhysRevLett.62.1193.

[32] Wu, T., Mayaffre, H., Krämer, S., Horvatić, M., Berthier, C., Hardy, W.N., Liang, R., Bonn, D.A., & Julien, M.H., Magnetic-field-induced charge-stripe order in the high-temperature superconductor $YBa_2Cu_3O_y$. *Nature* **477**, 191–194 (2011), DOI: 10.1038/nature10345.

[33] Fink, J., Nücker, N., Pellegrin, E., Romberg, H., Alexander, M., & Knupfer, M., Electron energy-loss and x-ray absorption spectroscopy of cuprate superconductors and related compounds. *Journal of Electron Spectroscopy and Related Phenomena* **66**, 395–452 (1994), DOI: 10.1016/0368-2048(93)01857-B.

[34] Cooper, S.L., Reznik, D., Kotz, A., Karlow, M.A., Liu, R., Klein, M.V., Lee, W.C., Giapintzakis, J., Ginsberg, D.M., Veal, B.W., & Paulikas, A.P., Optical studies of the a-, b-, and c-axis charge dynamics in $YBa_2Cu_3O_{6+x}$. *Phys. Rev. B* **47**, 8233–8248 (1993), DOI: 10.1103/PhysRevB.47.8233.

[35] Sutherland, M., Hawthorn, D.G., Hill, R.W., Ronning, F., Wakimoto, S., Zhang, H., Proust, C., Boaknin, E., Lupien, C., Taillefer, L., Liang, R., Bonn, D.A., Hardy, W.N., Gagnon, R., Hussey, N.E., Kimura, T., Nohara, M., & Takagi, H., Thermal conductivity across the phase diagram of cuprates: Low-energy quasiparticles and doping dependence of the superconducting gap. *Phys. Rev. B* **67**, 174520 (2003), DOI: 10.1103/PhysRevB.67.174520.

[36] Ando, Y., Komiya, S., Segawa, K., Ono, S., & Kurita, Y., Electronic Phase Diagram of High-T_c Cuprate Superconductors from a Mapping of the In-Plane Resistivity Curvature. *Phys. Rev. Lett.* **93**, 267001 (2004), DOI: 10.1103/PhysRevLett.93.267001.

[37] Nagaoka, T., Matsuda, Y., Obara, H., Sawa, A., Terashima, T., Chong, I., Takano, M., & Suzuki, M., Hall Anomaly in the Superconducting State of High- T_c Cuprates: Universality in Doping Dependence. *Phys. Rev. Lett.* **80**, 3594–3597 (1998), DOI: 10.1103/PhysRevLett.80.3594.

[38] Wang, Y., Li, L., & Ong, N., Nernst effect in high-T_c superconductors. *Phys. Rev. B* **73**, 024510 (2006), DOI: 10.1103/PhysRevB.73.024510.

[39] Doiron-Leyraud, N., Proust, C., LeBoeuf, D., Levallois, J., Bonnemaison, J.B., Liang, R., Bonn, D.A., Hardy, W.N., & Taillefer, L., Quantum oscillations and the Fermi surface in an underdoped high-T_c superconductor. *Nature* **447**, 565–568 (2007), DOI: 10.1038/nature05872.

[40] Chakravarty, S., Quantum oscillations and key theoretical issues in high temperature superconductors from the perspective of density waves. *Reports on Progress in Physics* **74**, 022501 (2011), DOI: 10.1088/0034-4885/74/2/022501.

[41] Barišić, N., Badoux, S., Chan, M.K., Dorow, C., Tabis, W., Vignolle, B., Yu, G., Béard, J., Zhao, X., Proust, C., & Greven, M., Universal quantum oscillations in the underdoped cuprate superconductors. *Nature Phys.* **9**, 761–764 (2013), DOI: 10.1038/nphys2792.

[42] Rao, C.N.R. & Ganguli, A.K., Structural aspects of superconducting cuprates. *Acta Crystallographica Section B* **51**, 604–618 (1995), DOI: 10.1107/S0108768194014655.

[43] Kastner, M., Birgeneau, R., Shirane, G., & Endoh, Y., Magnetic, transport, and optical properties of monolayer copper oxides. *Rev. Mod. Phys.* **70**, 897–928 (1998), DOI: 10.1103/RevModPhys.70.897.

[44] Gu, G., Takamuku, K., Koshizuka, N., & Tanaka, S., Large single crystal Bi-2212 along the c-axis prepared by floating zone method. *Journal of Crystal Growth* **130**, 325–329 (1993), DOI: 10.1016/0022-0248(93)90872-T.

[45] Liang, R., Bonn, D.A., & Hardy, W.N., Growth of high quality YBCO single crystals using $BaZrO_3$ crucibles. *Physica C* **304**, 105 (1998), DOI: 10.1016/S0921-4534(98)00275-5.

[46] Shiohara, Y. & Endo, A., Crystal growth of bulk high-Tc superconducting oxide materials. *Materials Science and Engineering: R: Reports* **19**, 1–86 (1997), DOI: 10.1016/S0927-796X(96)00198-2.

[47] Phillips, J.C., Saxena, A., & Bishop, A.R., Pseudogaps, dopants, and strong disorder in cuprate high-temperature superconductors. *Reports on Progress in Physics* **66**, 2111 (2003), DOI: 10.1088/0034-4885/66/12/R02.

[48] Eisaki, H., Kaneko, N., Feng, D.L., Damascelli, A., Mang, P.K., Shen, K.M., Shen, Z.X., & Greven, M., Effect of chemical inhomogeneity in bismuth-based copper oxide superconductors. *Phys. Rev. B* **69**, 064512 (2004), DOI: 10.1103/PhysRevB.69.064512.

[49] Alloul, H., Bobroff, J., Gabay, M., & Hirschfeld, P., Defects in correlated metals and superconductors. *Rev. Mod. Phys.* **81**, 45–108 (2009), DOI: 10.1103/RevModPhys.81.45.

[50] Hubbard, J., Electron Correlations in Narrow Energy Bands. *Proceedings of the Royal Society of London A: Mathematical, Physical and Engineering Sciences* **276**, 238–257 (1963), DOI: 10.1098/rspa.1963.0204.

[51] Lee, P., Nagaosa, N., & Wen, X.G., Doping a Mott insulator: Physics of high-temperature superconductivity. *Rev. Mod. Phys.* **78**, 17–85 (2006), DOI: 10.1103/RevModPhys.78.17.

[52] Ogata, M. & Fukuyama, H., The $t-J$ model for the oxide high-T_c superconductors. *Reports on Progress in Physics* **71**, 036501 (2008), DOI: 10.1088/0034-4885/71/3/036501.

[53] Abanov, A., Chubukov, A.V., & Schmalian, J., Quantum-critical theory of the spin-fermion model and its application to cuprates: normal state analysis. *Advances in Physics* **52**, 119–218 (2003), DOI: 10.1080/0001873021000057123.

[54] Efetov, K.B., Meier, H., & Pépin, C., Pseudogap state near a quantum critical point. *Nature Phys.* **9**, 442–446 (2013), DOI: 10.1038/nphys2641.

[55] Sachdev, S. & Demler, E., Competing orders in thermally fluctuating superconductors in two dimensions. *Phys. Rev. B* **69**, 144504 (2004), DOI: 10.1103/PhysRevB.69.144504.

[56] Hayward, L.E., Hawthorn, D.G., Melko, R.G., & Sachdev, S., Angular Fluctuations of a Multicomponent Order Describe the Pseudogap of $YBa_2Cu_3O_{6+x}$. *Science* **343**, 1336–1339 (2014), DOI: 10.1126/science.1246310.

[57] Anderson, P.W., The Resonating Valence Bond State in La_2CuO_4 and Superconductivity. *Science* **235**, 1196–1198 (1987), DOI: 10.1126/science.235.4793.1196.

[58] Varma, C.M., Non-Fermi-liquid states and pairing instability of a general model of copper oxide metals. *Phys. Rev. B* **55**, 14554–14580 (1997), DOI: 10.1103/PhysRevB.55.14554.

[59] Berg, E., Fradkin, E., Kivelson, S.A., & Tranquada, J.M., Striped superconductors: how spin, charge and superconducting orders intertwine in the cuprates. *New Journal of Physics* **11**, 115004 (2009), DOI: 10.1088/1367-2630/11/11/115004.

[60] Fradkin, E., Kivelson, S.A., & Tranquada, J.M., Theory of Intertwined Orders in High Temperature Superconductors. *ArXiv e-prints* (2014), URL: http://arxiv.org/abs/1407.4480.

[61] Berg, E., Fradkin, E., & Kivelson, S.A., Charge-4e superconductivity from pair-density-wave order in certain high-temperature superconductors. *Nature Physics* **5**, 830–833 (2009), DOI: 10.1038/nphys1389.

[62] Fradkin, E., Kivelson, S.A., Lawler, M.J., Eisenstein, J.P., & MacKenzie, A.P., Nematic Fermi Fluids in Condensed Matter Physics. *Annual Review of Condensed Matter Physics* **1**, 153–178 (2010), DOI: 10.1146/annurev-conmatphys-070909-103925.

[63] Lee, P.A., Amperean Pairing and the Pseudogap Phase of Cuprate Superconductors. *Phys. Rev. X* **4**, 031017 (2014), DOI: 10.1103/PhysRevX.4.031017.

[64] Foulkes, W., Mitas, L., Needs, R., & Rajagopal, G., Quantum Monte Carlo simulations of solids. *Rev. Mod. Phys.* **73**, 33–83 (2001), DOI: 10.1103/RevModPhys.73.33.

[65] Sandvik, A., Evidence for Deconfined Quantum Criticality in a Two-Dimensional Heisenberg Model with Four-Spin Interactions. *Phys. Rev. Lett.* **98**, 227202 (2007), DOI: 10.1103/PhysRevLett.98.227202.

[66] Isakov, S.V., Hastings, M.B., & Melko, R.G., Topological entanglement entropy of a Bose-Hubbard spin liquid. *Nature Phys.* **7**, 772–775 (2011), DOI: 10.1038/nphys2036.

[67] White, S. & Scalapino, D., Density Matrix Renormalization Group Study of the Striped Phase in the 2D $t - J$ Model. *Phys. Rev. Lett.* **80**, 1272–1275 (1998), DOI: 10.1103/PhysRevLett.80.1272.

[68] Stoudenmire, E. & White, S.R., Studying Two-Dimensional Systems with the Density Matrix Renormalization Group. *Annual Review of Condensed Matter Physics* **3**, 111–128 (2012), DOI: 10.1146/annurev-conmatphys-020911-125018.

[69] Caffarel, M. & Krauth, W., Exact diagonalization approach to correlated fermions in infinite dimensions: Mott transition and superconductivity. *Phys. Rev. Lett.* **72**, 1545–1548 (1994), DOI: 10.1103/PhysRevLett.72.1545.

[70] Georges, A., Kotliar, G., Krauth, W., & Rozenberg, M., Dynamical mean-field theory of strongly correlated fermion systems and the limit of infinite dimensions. *Rev. Mod. Phys.* **68**, 13–125 (1996), DOI: 10.1103/RevModPhys.68.13.

[71] Orenstein, J. & Millis, A.J., Advances in the Physics of High-Temperature Superconductivity. *Science* **288**, 468–474 (2000), DOI: 10.1126/science.288.5465.468.

[72] da Silva Neto, E.H., Aynajian, P., Frano, A., Comin, R., Schierle, E., Weschke, E., Gyenis, A., Wen, J., Schneeloch, J., Xu, Z., Ono, S., Gu, G., Le Tacon, M., & Yazdani, A., Ubiquitous Interplay Between Charge Ordering and High-Temperature Superconductivity in Cuprates. *Science* **343**, 393–396 (2014), DOI: 10.1126/science.1243479.

[73] Comin, R., Frano, A., Yee, M.M., Yoshida, Y., Eisaki, H., Schierle, E., Weschke, E., Sutarto, R., He, F., Soumyanarayanan, A., He, Y., Le Tacon, M., Elfimov, I.S., Hoffman, J.E., Sawatzky, G.A., Keimer, B., & Damascelli, A., Charge Order Driven by Fermi-Arc Instability in $Bi_2Sr_{2-x}La_xCuO_{6+\delta}$. *Science* **343**, 390–392 (2014), DOI: 10.1126/science.1242996.

[74] Tabis, W., Li, Y., Le Tacon, M., Braicovich, L., Kreyssig, A., Minola, M., Dellea, G., Weschke, E., Veit, M.J., Ramazanoglu, M., Goldman, A.I., Schmitt, T., Ghiringhelli, G., Barišić, N., Chan, M.K., Dorow, C.J., Yu, G., Zhao, X., Keimer, B., & Greven, M., Connection between charge-density-wave order and charge transport in the cuprate superconductors. arXiv:1404.7658 [cond-mat.supr-con].

[75] Sachdev, S. & La Placa, R., Bond Order in Two-Dimensional Metals with Antiferromagnetic Exchange Interactions. *Phys. Rev. Lett.* **111**, 027202 (2013), DOI: 10.1103/PhysRevLett.111.027202.

[76] Tranquada, J.M., Stripes and superconductivity in cuprates. *Physica B: Condensed Matter* **407**, 1771–1774, proceedings of the International Workshop on Electronic Crystals (ECRYS-2011) (2012), DOI: 10.1016/j.physb.2012.01.026.

[77] Axe, J.D., Moudden, A.H., Hohlwein, D., Cox, D.E., & Mohanty, K.M., Structural phase transformations and superconductivity in $La_{2-x}Ba_xCuO_4$. *Phys. Rev. Lett.* **62**, 2751–2754 (1989), DOI: 10.1103/PhysRevLett.62.2751.

[78] Katano, S., Fernandez-Baca, J., Funahashi, S., Môri, N., Ueda, Y., & Koga, K., Crystal structure and superconductivity of $La_{2x}Ba_xCuO_4$ ($0.03 \leq x \leq 0.24$). *Physica C: Superconductivity* **214**, 64–72 (1993), DOI: 10.1016/0921-4534(93)90108-3.

[79] Sakita, S., Nakamura, F., Suzuki, T., & Fujita, T., Structural Transitions and Localization in $La_{2-x-y}Nd_ySr_xCuO_4$ with $p \sim 1/8$. *Journal of the Physical Society of Japan* **68**, 2755 (1999), DOI: 10.1143/JPSJ.68.2755.

[80] Hücker, M., Structural aspects of materials with static stripe order. *Physica C: Superconductivity* **481**, 3–14 (2012), DOI: 10.1016/j.physc.2012.04.035.

[81] McElroy, K., Simmonds, R.W., Hoffman, J.E., Lee, D.H., Orenstein, J., Eisaki, H., Uchida, S., & Davis, J.C., Relating atomic-scale electronic phenomena to wave-like quasiparticle states in superconducting $Bi_2Sr_2CaCu_2O_{8+\delta}$. *Nature* **422**, 592–596 (2003), DOI: 10.1038/nature01496.

[82] Hanaguri, T., Lupien, C., Kohsaka, Y., Lee, D.H., Azuma, M., Takano, M., Takagi, H., & Davis, J.C., A 'checkerboard' electronic crystal state in lightly hole-doped $Ca_{2-x}Na_xCuO_2Cl_2$. *Nature* **430**, 1001 (2004), DOI: 10.1038/nature02861.

[83] Smadici, Ş., Abbamonte, P., Taguchi, M., Kohsaka, Y., Sasagawa, T., Azuma, M., Takano, M., & Takagi, H., Absence of long-ranged charge order in $Na_xCa_{2-x}CuO_2Cl_2$ (x=0.08). *Phys. Rev. B* **75**, 075104 (2007), DOI: 10.1103/PhysRevB.75.075104.

[84] Hawthorn, D.G., Shen, K.M., Geck, J., Peets, D.C., Wadati, H., Okamoto, J., Huang, S.W., Huang, D.J., Lin, H.J., Denlinger, J.D., Liang, R., Bonn, D.A., Hardy, W.N., & Sawatzky, G.A., Resonant elastic soft x-ray scattering in oxygen-ordered $YBa_2Cu_3O_{6+\delta}$. *Phys. Rev. B* **84**, 075125 (2011), DOI: 10.1103/PhysRevB.84.075125.

[85] Tranquada, J.M., Axe, J.D., Ichikawa, N., Nakamura, Y., Uchida, S., & Nachumi, B., Neutron-scattering study of stripe-phase order of holes and spins in $La_{1.48}Nd_{0.4}Sr_{0.12}CuO_4$. *Phys. Rev. B* **54**, 7489–7499 (1996), DOI: 10.1103/PhysRevB.54.7489.

[86] Tranquada, J.M., Axe, J.D., Ichikawa, N., Moodenbaugh, A.R., Nakamura, Y., & Uchida, S., Coexistence of, and Competition between, Superconductivity and Charge-Stripe Order in $La_{1.6-x}Nd_{0.4}Sr_xCuO_4$. *Physical Review Letters* **78**, 338–341 (1997), DOI: 10.1103/PhysRevLett.78.338.

[87] Ichikawa, N., Uchida, S., Tranquada, J., Niemöller, T., Gehring, P., Lee, S.H., & Schneider, J., Local Magnetic Order vs Superconductivity in a Layered Cuprate. *Phys. Rev. Lett.* **85**, 1738–1741 (2000), DOI: 10.1103/PhysRevLett.85.1738.

[88] Fujita, M., Yamada, K., Hiraka, H., Gehring, P.M., Lee, S.H., Wakimoto, S., & Shirane, G., Static magnetic correlations near the insulating-superconducting phase boundary in $La_{2-x}Sr_xCuO_4$. *Phys. Rev. B* **65**, 064505 (2002), DOI: 10.1103/PhysRevB.65.064505.

[89] Christensen, N.B., McMorrow, D.F., Rønnow, H.M., Lake, B., Hayden, S.M., Aeppli, G., Perring, T.G., Mangkorntong, M., Nohara, M., & Takagi, H., Dispersive Excitations in the High-Temperature Superconductor $La_{2-x}Sr_xCuO_4$. *Phys. Rev. Lett.* **93**, 147002 (2004), DOI: 10.1103/PhysRevLett.93.147002.

[90] Fujita, M., Goka, H., Yamada, K., Tranquada, J.M., & Regnault, L.P., Stripe order, depinning, and fluctuations in $La_{1.875}Ba_{0.125}CuO_4$ and $La_{1.875}Ba_{0.075}Sr_{0.050}CuO_4$. *Phys. Rev. B* **70**, 104517 (2004), DOI: 10.1103/PhysRevB.70.104517.

[91] Christensen, N.B., Rønnow, H.M., Mesot, J., Ewings, R.A., Momono, N., Oda, M., Ido, M., Enderle, M., McMorrow, D.F., & Boothroyd, A.T., Nature of the Magnetic Order in the Charge-Ordered Cuprate $La_{1.48}Nd_{0.4}Sr_{0.12}CuO_4$. *Phys. Rev. Lett.* **98**, 197003 (2007), DOI: 10.1103/PhysRevLett.98.197003.

[92] Zimmermann, M.v., Vigliante, A., Niemöller, T., Ichikawa, N., Frello, T., Madsen, J., Wochne, P., Uchida, S., Andersen, N.H., Tranquada, J.M., Gibbs, D., & Schneider, J.R., Hard–X-ray diffraction study of charge stripe order in $La_{1.48}Nd_{0.4}Sr_{0.12}CuO_4$. *Europhys. Lett.* **41**, 629–634 (1998), DOI: 10.1209/epl/i1998-00204-2.

[93] Niemöller, T., Ichikawa, N., Frello, T., Hünnefeld, H., Andersen, N.H., Uchida, S., Schneider, J.R., & Tranquada, J.M., Charge stripes seen with X-rays in $La_{1.45}Nd_{0.4}Sr_{0.15}CuO_4$. *European Physical Journal B* **12**, 509–513 (1999), DOI: 10.1007/s100510051032.

[94] Kim, Y.J., Gu, G.D., Gog, T., & Casa, D., X-ray scattering study of charge density waves in $La_{2-x}Ba_xCuO_4$. *Phys. Rev. B* **77**, 064520 (2008), DOI: 10.1103/PhysRevB.77.064520.

[95] Abbamonte, P., Rusydi, A., Smadici, S., Gu, G.D., Sawatzky, G.A., & Feng, D.L., Spatially modulated 'Mottness' in $La_{2-x}Ba_xCuO_4$. *Nature Phys.* **1**, 155–158 (2005), DOI: 10.1038/nphys178.

[96] Fink, J., Schierle, E., Weschke, E., Geck, J., Hawthorn, D., Soltwisch, V., Wadati, H., Wu, H.H., Dürr, H.A., Wizent, N., Büchner, B., & Sawatzky, G.A., Charge ordering in $La_{1.8-x}Eu_{0.2}Sr_xCuO_4$ studied by resonant soft x-ray diffraction. *Phys. Rev. B* **79**, 100502 (2009), DOI: 10.1103/PhysRevB.79.100502.

[97] Moodenbaugh, A.R., Xu, Y., Suenaga, M., Folkerts, T.J., & Shelton, R.N., Superconducting properties of $La_{2-x}Ba_xCuO_4$. *Phys. Rev. B* **38**, 4596–4600 (1988), DOI: 10.1103/PhysRevB.38.4596.

[98] Wochner, P., Tranquada, J.M., Buttrey, D.J., & Sachan, V., Neutron-diffraction study of stripe order in La_2NiO_{4+} with $\delta = \frac{2}{15}$. *Phys. Rev. B* **57**, 1066–1078 (1998), DOI: 10.1103/PhysRevB.57.1066.

[99] Hannon, J.P., Trammell, G.T., Blume, M., & Gibbs, D., X-Ray Resonance Exchange Scattering. *Phys. Rev. Lett.* **61**, 1245–1248 (1988), DOI: 10.1103/PhysRevLett.61.1245.

[100] Jark, W. & Stöhr, J., A high-vacuum triple-axis-diffractometer for soft X-ray scattering experiments. *Nuclear Instruments and Methods in Physics Research Section A: Accelerators, Spectrometers, Detectors and Associated Equipment* **266**, 654–658 (1988), DOI: 10.1016/0168-9002(88)90459-7.

[101] Gau, T.S., Jean, Y.C., Liu, K.Y., Chung, C.H., Chen, C.K., Lai, S.C., Shu, C.H., Huang, Y.S., Chao, C.H., Lee, Y.R., Chen, C., & Chang, S.L., Soft X-ray diffractometer for synchrotron radiation. *Nuclear Instruments and Methods in Physics Research Section A: Accelerators, Spectrometers, Detectors and Associated Equipment* **466**, 569–575 (2001), DOI: 10.1016/S0168-9002(01)00200-5.

[102] Abbamonte, P., Venema, L., Rusydi, A., Sawatzky, G.A., Logvenov, G., & Bozovic, I., A Structural Probe of the Doped Holes in Cuprate Superconductors. *Science* **297**, 581–584 (2002), DOI: 10.1126/science.1070903.

[103] Grabis, J., Nefedov, A., & Zabel, H., Diffractometer for soft x-ray resonant magnetic scattering. *Review of Scientific Instruments* **74**, 4048–4051 (2003), DOI: http://dx.doi.org/10.1063/1.1602932.

[104] Chen, C.T., Sette, F., Ma, Y., Hybertsen, M.S., Stechel, E.B., Foulkes, W.M.C., Schulter, M., Cheong, S.W., Cooper, A.S., L. W. Rupp, J., Batlogg, B., Soo, Y.L., Ming, Z.H., Krol, A., & Kao, Y.H., Electronic states in $La_{2-x}Sr_xCuO_{4+\delta}$ probed by soft-x-ray absorption. *Phys. Rev. Lett.* **66**, 104–107 (1991), DOI: 10.1103/PhysRevLett.66.104.

[105] Chen, C., Tjeng, L., Kwo, J., Kao, H., Rudolf, P., Sette, F., & Fleming, R., Out-of-plane orbital characters of intrinsic and doped holes in $La_{2-x}Sr_xCuO_4$. *Phys. Rev. Lett.* **68**, 2543–2546 (1992), DOI: 10.1103/PhysRevLett.68.2543.

[106] Vojta, M. & Rösch, O., Superconducting d-wave stripes in cuprates: Valence bond order coexisting with nodal quasiparticles. *Phys. Rev. B* **77**, 094504 (2008), DOI: 10.1103/PhysRevB.77.094504.

[107] Beyers, R., Ahn, B.T., Gorman, G., Lee, V.Y., Parkin, S.S.P., Ramirez, M.L., Roche, K.P., Vazquez, J.E., Gür, T.M., & Huggins, R.A., Oxygen ordering, phase separation and the 60-K and 90-K plateaus in $YBa_2Cu_3O_x$. *Nature* **340**, 619–621 (1989), DOI: doi:10.1038/340619a0.

[108] Uimin, G., Order and disorder in the ensemble of Cu-O chain fragments in oxygen-deficient planes of $YBa_2Cu_3O_{6+x}$. *Phys. Rev. B* **50**, 9531–9547 (1994), DOI: 10.1103/PhysRevB.50.9531.

[109] Schleger, P., Hadfield, R.A., Casalta, H., Andersen, N.H., Poulsen, H.F., von Zimmermann, M., Schneider, J.R., Liang, R., Dosanjh, P., & Hardy, W.N., Random-Field Structural Transition in $YBa_2Cu_3O_{6.5}$? *Phys. Rev. Lett.* **74**, 1446–1449 (1995), DOI: 10.1103/PhysRevLett.74.1446.

[110] Andersen, N.H., von Zimmermann, M., Frello, T., Käll, M., Mønster, D., Lindgård, P.A., Madsen, J., Niemöller, T., Poulsen, H.F., Schmidt, O., Schneider, J.R., Wolf, T., Dosanjh, P., Liang, R., & Hardy, W.N., Superstructure formation and the structural phase diagram of $YBa_2Cu_3O_{6+x}$. *Physica C Superconductivity* **317-318**, 259–269 (1999), DOI: 10.1016/S0921-4534(99)00066-0.

[111] Zimmermann, M.v., Schneider, J.R., Frello, T., Andersen, N.H., Madsen, J., Käll, M., Poulsen, H.F., Liang, R., Dosanjh, P., & Hardy, W.N., Oxygen-ordering superstructures in underdoped $YBa_2Cu_3O_{6+x}$ studied by hard x-ray diffraction. *Phys. Rev. B* **68**, 104515 (2003), DOI: 10.1103/PhysRevB.68.104515.

[112] Robertson, J.A., Kivelson, S.A., Fradkin, E., Fang, A.C., & Kapitulnik, A., Distinguishing patterns of charge order: Stripes or checkerboards. *Phys. Rev. B* **74**, 134507 (2006), DOI: 10.1103/PhysRevB.74.134507.

[113] Del Maestro, A., Rosenow, B., & Sachdev, S., From stripe to checkerboard ordering of charge-density waves on the square lattice in the presence of quenched disorder. *Phys. Rev. B* **74**, 024520 (2006), DOI: 10.1103/PhysRevB.74.024520.

[114] Nie, L., Tarjus, G., & Kivelson, S.A., Quenched disorder and vestigial nematicity in the pseudogap regime of the cuprates. *Proc. Natl. Acad. Sci. U.S.A.* **111**, 7980–7985 (2014), DOI: 10.1073/pnas.1406019111.

[115] Liang, R., Bonn, D.A., & Hardy, W.N., Preparation and X-ray characterization of highly ordered ortho-II phase $YBa_2Cu_3O_{6.50}$ single crystals. *Physica C* **336**, 57 (2000), DOI: 10.1016/S0921-4534(00)00091-5.

[116] Fujita, K., Hamidian, M.H., Edkins, S.D., Kim, C.K., Kohsaka, Y., Azuma, M., Takano, M., Takagi, H., Eisaki, H., Uchida, S.i., Allais, A., Lawler, M.J., Kim, E.A., Sachdev, S., & Davis, J.C.S., Direct phase-sensitive identification of a *d*-form factor density wave in underdoped cuprates. *Proc. Natl. Acad. Sci. U.S.A.* **111**, E3026–E3032 (2014), DOI: 10.1073/pnas.1406297111.

[117] Comin, R., Sutarto, R., He, F., da Silva Neto, E., Chauviere, L., Frano, A., Liang, R., Hardy, W.N., Bonn, D., Yoshida, Y., Eisaki, H., Hoffman, J.E., Keimer, B., Sawatzky, G.A., & Damascelli, A., The symmetry of charge order in cuprates. arXiv:1402.5415 [cond-mat.supr-con].

[118] Fischer, M.H., Wu, S., Lawler, M., Paramekanti, A., & Kim, E.A., Nematic and spin-charge orders driven by hole-doping a charge-transfer insulator. arXiv:1406.2711 [cond-mat.str-el].

[119] Metlitski, M.A. & Sachdev, S., Quantum phase transitions of metals in two spatial dimensions. II. Spin density wave order. *Phys. Rev. B* **82**, 075128 (2010), DOI: 10.1103/PhysRevB.82.075128.

[120] Atkinson, W.A., Kampf, A.P., & Bulut, S., Charge Order in the Pseudogap Phase of Cuprate Superconductors. arXiv:1404.1335 [cond-mat.supr-con].

[121] Yamakawa, Y. & Kontani, H., Spin-Fluctuation-Driven Nematic Charge-Density-Wave in Cuprate Superconductors: Charge-Orbital-Spin Multimode Fluctuations Caused by Vertex Corrections. arXiv:1406.7520 [cond-mat.str-el].

[122] Vettier, C., Resonant elastic X-ray scattering: Where from? where to? *The European Physical Journal Special Topics* **208**, 3–14 (2012), DOI: 10.1140/epjst/e2012-01602-7.

[123] Sasaki, S., Analyses for a planar variably-polarizing undulator. *Nuclear Instruments and Methods in Physics Research Section A* **347**, 83–86 (1994), DOI: 10.1016/0168-9002(94)91859-7.

[124] Bilderback, D.H., Elleaume, P., & Weckert, E., Review of third and next generation synchrotron light sources. *Journal of Physics B: Atomic, Molecular and Optical Physics* **38**, S773–S797 (2005), DOI: 10.1088/0953-4075/38/9/022.

[125] Templeton, D.H. & Templeton, L.K., X-ray dichroism and polarized anomalous scattering of the uranyl ion. *Acta Crystallographica Section A* **38**, 62–67 (1982), DOI: 10.1107/S0567739482000114.

[126] Dmitrienko, V.E., Forbidden reflections due to anisotropic X-ray susceptibility of crystals. *Acta Crystallographica Section A* **39**, 29–35 (1983), DOI: 10.1107/S0108767383000057.

[127] Blume, M. & Gibbs, D., Polarization dependence of magnetic x-ray scattering. *Phys. Rev. B* **37**, 1779–1789 (1988), DOI: 10.1103/PhysRevB.37.1779.

[128] Kotani, A. & Shin, S., Resonant inelastic x-ray scattering spectra for electrons in solids. *Rev. Mod. Phys.* **73**, 203–246 (2001), DOI: 10.1103/RevModPhys.73.203.

[129] Ament, L.J.P., van Veenendaal, M., Devereaux, T.P., Hill, J.P., & van den Brink, J., Resonant inelastic x-ray scattering studies of elementary excitations. *Rev. Mod. Phys.* **83**, 705–767 (2011), DOI: 10.1103/RevModPhys.83.705.

[130] Carra, P. & Thole, B.T., Anisotropic x-ray anomalous diffraction and forbidden reflections. *Rev. Mod. Phys.* **66**, 1509–1515 (1994), DOI: 10.1103/RevModPhys.66.1509.

[131] Hill, J.P. & McMorrow, D.F., X-ray resonant exchange scattering: Polarization dependence and correlation functions. *Acta Crystallographica Section A* **52**, 236–244 (1996), DOI: 10.1107/S0108767395012670.

[132] Lovesey, S., Balcar, E., Knight, K., & Rodríguez, J.F., Electronic properties of crystalline materials observed in X-ray diffraction. *Physics Reports* **411**, 233–289 (2005), DOI: 10.1016/j.physrep.2005.01.003.

[133] Dmitrienko, V.E., Ishida, K., Kirfel, A., & Ovchinnikova, E.N., Polarization anisotropy of X-ray atomic factors and 'forbidden' resonant reflections. *Acta Crystallographica Section A* **61**, 481–493 (2005), DOI: 10.1107/S0108767305018209.

[134] Matteo, S.D., Resonant x-ray diffraction: multipole interpretation. *Journal of Physics D: Applied Physics* **45**, 163001 (2012), DOI: 10.1088/0022-3727/45/16/163001.

[135] Joly, Y., Matteo, S.D., & Bunău, O., Resonant X-ray diffraction: Basic theoretical principles. *The European Physical Journal Special Topics* **208**, 21–38 (2012), DOI: 10.1140/epjst/e2012-01604-5.

[136] Detlefs, C., Sanchez del Rio, M., & Mazzoli, C., X-ray polarization: General formalism and polarization analysis. *The European Physical Journal Special Topics* **208**, 359–371 (2012), DOI: 10.1140/epjst/e2012-01630-3.

[137] Hahn, T. (Editor), *International Tables for Crystallography*, Vol. A, Space-group symmetry, chapter 9 (Chester: International Union of Crystallography, 2006), first online edition, DOI: 10.1107/97809553602060000100.

[138] Thomas, J.M., Centenary: The birth of X-ray crystallography. *Nature* **491**, 186–187 (2012), DOI: 10.1038/491186a.

[139] Sumner, T., Dazzling History. *Science* **343**, 1092–1093 (2014), DOI: 10.1126/science.343.6175.1092.

[140] Marder, M.P., *Scattering and Structures*, chapter 3, (pages 43–75) (John Wiley & Sons, Inc., 2010), ISBN 9780470949955, DOI: 10.1002/9780470949955.ch3.

[141] Bragg, W.H. & Bragg, W.L., The Reflection of X-rays by Crystals. *Proceedings of the Royal Society of London A: Mathematical, Physical and Engineering Sciences* **88**, 428–438 (1913), DOI: 10.1098/rspa.1913.0040.

[142] Friedrich, W., Knipping, P., & Laue, M., Interferenzerscheinungen bei Röntgenstrahlen. *Annalen der Physik* **346**, 971–988 (1913), DOI: 10.1002/andp.19133461004.

[143] Prince, E. (Editor), *International Tables for Crystallography*, Vol. C, Mathematical, physical and chemical tables, chapter 1 (Chester: International Union of Crystallography, 2006), first online edition, DOI: 10.1107/97809553602060000103.

[144] spec: Software for Diffraction, URL: http://www.certif.com/content/spec/.

[145] Busing, W. & Levy, H., Angle calculations for 3-and 4-circle X-ray and neutron diffractometers. *Acta Crystallographica* **22**, 457–464 (1967), DOI: 10.1107/S0365110X67000970.

[146] Foldy, L.L., The Electromagnetic Properties of Dirac Particles. *Phys. Rev.* **87**, 688–693 (1952), DOI: 10.1103/PhysRev.87.688.

[147] Jackson, J.D., *Classical Electrodynamics* (Wiley, 1998), third edition, ISBN 047130932X, URL: http://www.worldcat.org/oclc/38073290.

[148] Altarelli, M., Resonant X-ray Scattering: A Theoretical Introduction. In *Magnetism: A Synchrotron Radiation Approach*, Vol. 697 of *Lecture Notes in Physics*, edited by E. Beaurepaire, H. Bulou, F. Scheurer, & J.P. Kappler, (pages 201–242) (Springer Berlin Heidelberg, 2006), ISBN 978-3-540-33241-1, DOI: 10.1007/3-540-33242-1_8.

[149] Sakurai, J.J., *Advanced Quantum Mechanics*, chapter 3, (pages 75–178) (Addison-Wesley, 1967), first edition, ISBN 0201067102, URL: http://www.worldcat.org/oclc/869733.

[150] Dirac, P.A.M., The Quantum Theory of the Electron. *Proceedings of the Royal Society of London. Series A* **117**, 610–624 (1928), DOI: 10.1098/rspa.1928.0023.

[151] Dirac, P.A.M., The Quantum Theory of the Emission and Absorption of Radiation. *Proceedings of the Royal Society of London. Series A* **114**, 243–265 (1927), DOI: 10.1098/rspa.1927.0039.

[152] Sakurai, J.J., *Advanced Quantum Mechanics*, chapter 2, (pages 21–64) (Addison-Wesley, 1967), first edition, ISBN 0201067102, URL: http://www.worldcat.org/oclc/869733.

[153] Blume, M., Magnetic scattering of x rays (invited). *Journal of Applied Physics* **57**, 3615–3618 (1985), DOI: 10.1063/1.335023.

[154] Lovesey, S. & Collins, S., *X-ray Scattering and Absorption by Magnetic Materials*. Oxford science publications (Clarendon Press, 1996), ISBN 9780198517375, URL: http://www.worldcat.org/oclc/283724551.

[155] Collins, S. & Bombardi, A., Resonant X-Ray Scattering and Absorption. In *Magnetism and Synchrotron Radiation*, Vol. 133 of *Springer Proceedings in Physics*,

edited by E. Beaurepaire, H. Bulou, F. Scheurer, & K. Jean-Paul, (pages 223–262) (Springer Berlin Heidelberg, 2010), ISBN 978-3-642-04498-4, DOI: 10.1007/978-3-642-04498-4_8.

[156] Wende, H. & Antoniak, C., X-Ray Magnetic Dichroism. In *Magnetism and Synchrotron Radiation*, Vol. 133 of *Springer Proceedings in Physics*, edited by E. Beaurepaire, H. Bulou, F. Scheurer, & K. Jean-Paul, (pages 145–167) (Springer Berlin Heidelberg, 2010), ISBN 978-3-642-04497-7, DOI: 10.1007/978-3-642-04498-4_5.

[157] Haverkort, M.W., Hollmann, N., Krug, I.P., & Tanaka, A., Symmetry analysis of magneto-optical effects: The case of x-ray diffraction and x-ray absorption at the transition metal $L_{2,3}$ edge. *Phys. Rev. B* **82**, 094403 (2010), DOI: 10.1103/PhysRevB.82.094403.

[158] Chantler, C.T., Theoretical Form Factor, Attenuation, and Scattering Tabulation for Z=1-92 from E=1-10 eV to E=0.4-1.0 MeV. *J. Phys. Chem. Ref. Data* **24**, 71–643 (1995), DOI: 10.1063/1.555974.

[159] Chantler, C.T., Detailed Tabulation of Atomic Form Factors, Photoelectric Absorption and Scattering Cross Section, and Mass Attenuation Coefficients in the Vicinity of Absorption Edges in the Soft X-Ray (Z=30–36, Z=60–89, E=0.1 keV–10 keV), Addressing Convergence Issues of Earlier Work. *Journal of Physical and Chemical Reference Data* **29**, 597–1056 (2000), DOI: 10.1063/1.1321055.

[160] National Institute of Standards and Technology: X-Ray Form Factor, Attenuation, and Scattering Tables, URL: http://www.nist.gov/pml/data/ffast/index.cfm.

[161] Henke, B., Gullikson, E., & Davis, J., X-Ray Interactions: Photoabsorption, Scattering, Transmission, and Reflection at E = 50-30,000 eV, Z = 1-92. *Atomic Data and Nuclear Data Tables* **54**, 181–342 (1993), DOI: 10.1006/adnd.1993.1013.

[162] The Center for X-ray Optics: X-Ray Interactions With Matter, URL: http://henke.lbl.gov/optical_constants/.

[163] Tabulated atomic scattering form factors and a Mathematica notebook to extract data, URL: https://github.com/AJAthesis/f1f2_AtomicDB.

[164] Newton, R.G., Optical theorem and beyond. *American Journal of Physics* **44**, 639–642 (1976), DOI: 10.1119/1.10324.

[165] Toll, J.S., Causality and the Dispersion Relation: Logical Foundations. *Phys. Rev.* **104**, 1760–1770 (1956), DOI: 10.1103/PhysRev.104.1760.

[166] A Mathematica notebook to calculate f1 from tabulated f2 atomic scattering form factors, URL: https://github.com/AJAthesis/KramersKronig_AtomicNIST/.

[167] Stavitski, E. & de Groot, F.M., The CTM4XAS program for EELS and XAS spectral shape analysis of transition metal L edges. *Micron* **41**, 687–694 (2010), DOI: 10.1016/j.micron.2010.06.005.

[168] Hawthorn, D.G., He, F., Venema, L., Davis, H., Achkar, A.J., Zhang, J., Sutarto, R., Wadati, H., Radi, A., Wilson, T., Wright, G., Shen, K.M., Geck, J., Zhang, H., Novák, V., & Sawatzky, G.A., An in-vacuum diffractometer for resonant elastic soft x-ray scattering. *Rev. Sci. Instrum.* **82**, 073104 (2011), DOI: 10.1063/1.3607438.

[169] Design of REIXS beamline, URL: http://exshare.lightsource.ca/REIXS/Pages/BLDesign.aspx.

[170] Basic Demonstration of OrientExpress for orienting a single crystal from a single Laue Photograph, URL: http://www.ccp14.ac.uk/tutorial/lmgp/orientexpress.htm.

[171] Zaanen, J. & Gunnarsson, O., Charged magnetic domain lines and the magnetism of high-T_c oxides. *Phys. Rev. B* **40**, 7391–7394 (1989), DOI: 10.1103/PhysRevB.40.7391.

[172] Poilblanc, D. & Rice, T.M., Charged solitons in the Hartree-Fock approximation to the large-U Hubbard model. *Phys. Rev. B* **39**, 9749–9752 (1989), DOI: 10.1103/PhysRevB.39.9749.

[173] Schulz, H.J., Domain walls in a doped antiferromagnet. *J. Phys. France* **50**, 2833–2849 (1989), DOI: 10.1051/jphys:0198900500180283300.

[174] Machida, K., Magnetism in La_2CuO_4 based compounds. *Physica C* **158**, 192–196 (1989), DOI: 10.1016/0921-4534(89)90316-X.

[175] Hücker, M., Zimmermann, M.v., Gu, G.D., Xu, Z.J., Wen, J.S., Xu, G., Kang, H.J., Zheludev, A., & Tranquada, J.M., Stripe order in superconducting $La_{2-x}Ba_xCuO_4$ ($0.095 \leq x \leq 0.155$). *Phys. Rev. B* **83**, 104506 (2011), DOI: 10.1103/PhysRevB.83.104506.

[176] Kohsaka, Y., Taylor, C., Fujita, K., Schmidt, A., Lupien, C., Hanaguri, T., Azuma, M., Takano, M., Eisaki, H., Takagi, H., Uchida, S., & Davis, J.C., An Intrinsic Bond-Centered Electronic Glass with Unidirectional Domains in Underdoped Cuprates. *Science* **315**, 1380–1385 (2007), DOI: 10.1126/science.1138584.

[177] LeBoeuf, D., Doiron-Leyraud, N., Levallois, J., Daou, R., Bonnemaison, J.B., Hussey, N.E., Balicas, L., Ramshaw, B.J., Liang, R., Bonn, D.A., Hardy, W.N., Adachi, S., Proust, C., & Taillefer, L., Electron pockets in the Fermi surface of hole-doped high-T_c superconductors. *Nature* **450**, 533–536 (2007), DOI: 10.1038/nature06332.

[178] Daou, R., Chang, J., LeBoeuf, D., Cyr-Choinière, O., Laliberté, F., Doiron-Leyraud, N., Ramshaw, B.J., Liang, R., Bonn, D.A., Hardy, W.N., & Taillefer, L., Broken rotational symmetry in the pseudogap phase of a high-T_c superconductor. *Nature* **463**, 519–522 (2010), DOI: 10.1038/nature08716.

[179] Vojta, M., Lattice symmetry breaking in cuprate superconductors: stripes, nematics, and superconductivity. *Advances in Physics* **58**, 699–820 (2009), DOI: 10.1080/00018730903122242.

[180] Read, N. & Sachdev, S., Valence-bond and spin-Peierls ground states of low-dimensional quantum antiferromagnets. *Phys. Rev. Lett.* **62**, 1694–1697 (1989), DOI: 10.1103/PhysRevLett.62.1694.

[181] Vojta, M. & Sachdev, S., Charge Order, Superconductivity, and a Global Phase Diagram of Doped Antiferromagnets. *Phys. Rev. Lett.* **83**, 3916–3919 (1999), DOI: 10.1103/PhysRevLett.83.3916.

[182] Fink, J., Soltwisch, V., Geck, J., Schierle, E., Weschke, E., & Büchner, B., Phase diagram of charge order in $La_{1.8-x}Eu_{0.2}Sr_xCuO_4$ from resonant soft x-ray diffraction. *Phys. Rev. B* **83**, 092503 (2011), DOI: 10.1103/PhysRevB.83.092503.

[183] Wilkins, S.B., Dean, M.P.M., Fink, J., Hücker, M., Geck, J., Soltwisch, V., Schierle, E., Weschke, E., Gu, G., Uchida, S., Ichikawa, N., Tranquada, J.M., & Hill, J.P., Comparison of stripe modulations in $La_{1.875}Ba_{0.125}CuO_4$ and $La_{1.48}Nd_{0.4}Sr_{0.12}CuO_4$. *Phys. Rev. B* **84**, 195101 (2011), DOI: 10.1103/PhysRevB.84.195101.

[184] Romberg, H., Alexander, M., Nücker, N., Adelmann, P., & Fink, J., Electronic structure of the system $La_{2-x}Sr_xCuO_{4+\delta}$. *Phys. Rev. B* **42**, 8768–8771 (1990), DOI: 10.1103/PhysRevB.42.8768.

[185] Nücker, N., Fink, J., Fuggle, J.C., Durham, P.J., & Temmerman, W.M., Evidence for holes on oxygen sites in the high-T_c superconductors $La_{2-x}Sr_xCuO_4$ and $YBa_2Cu_3O_{7-y}$. *Phys. Rev. B* **37**, 5158–5163 (1988), DOI: 10.1103/PhysRevB.37.5158.

[186] Hybertsen, M.S., Stechel, E.B., Foulkes, W.M.C., & Schlüter, M., Model for low-energy electronic states probed by x-ray absorption in high-T_c cuprates. *Phys. Rev. B* **45**, 10032–10050 (1992), DOI: 10.1103/PhysRevB.45.10032.

[187] Eskes, H. & Sawatzky, G.A., Doping dependence of high-energy spectral weights for the high-T_c cuprates. *Phys. Rev. B* **43**, 119–129 (1991), DOI: 10.1103/PhysRevB.43.119.

[188] de Groot, F., Multiplet effects in X-ray spectroscopy. *Coordination Chemistry Reviews* **249**, 31–63 (2005), DOI: 10.1016/j.ccr.2004.03.018.

[189] Quan, Y., Pardo, V., & Pickett, W.E., Formal Valence, 3*d*-Electron Occupation, and Charge-Order Transitions. *Phys. Rev. Lett.* **109**, 216401 (2012), DOI: 10.1103/PhysRevLett.109.216401.

[190] Kivelson, S.A., Bindloss, I.P., Fradkin, E., Oganesyan, V., Tranquada, J.M., Kapitulnik, A., & Howald, C., How to detect fluctuating stripes in the high-temperature superconductors. *Rev. Mod. Phys.* **75**, 1201–1241 (2003), DOI: 10.1103/RevModPhys.75.1201.

[191] Kohsaka, Y., Taylor, C., Wahl, P., Schmidt, A., Lee, J., Fujita, K., Alldredge, J.W., McElroy, K., Lee, J., Eisaki, H., Uchida, S., Lee, D.H., & Davis, J.C., How Cooper pairs vanish approaching the Mott insulator in $Bi_2Sr_2CaCu_2O_{8+\delta}$. *Nature* **454**, 1072–1078 (2008), DOI: 10.1038/nature07243.

[192] Millis, A.J. & Norman, M.R., Antiphase stripe order as the origin of electron pockets observed in 1/8-hole-doped cuprates. *Phys. Rev. B* **76**, 220503 (2007), DOI: 10.1103/PhysRevB.76.220503.

[193] Sebastian, S.E., Harrison, N., & Lonzarich, G.G., Towards resolution of the Fermi surface in underdoped high-T_c superconductors. *Reports on Progress in Physics* **75**, 102501 (2012), DOI: 10.1088/0034-4885/75/10/102501.

[194] Nücker, N., Pellegrin, E., Schweiss, P., Fink, J., Molodtsov, S.L., Simmons, C.T., Kaindl, G., Frentrup, W., Erb, A., & Müller-Vogt, G., Site-specific and doping-dependent electronic structure of $YBa_2Cu_3O_x$ probed by O 1*s* and Cu 2*p* x-ray-absorption spectroscopy. *Phys. Rev. B* **51**, 8529–8542 (1995), DOI: 10.1103/PhysRevB.51.8529.

[195] Edwards, H.L., Barr, A.L., Markert, J.T., & de Lozanne, A.L., Modulations in the CuO Chain Layer of $YBa_2Cu_3O_{7-\delta}$: Charge Density Waves? *Phys. Rev. Lett.* **73**, 1154–1157 (1994), DOI: 10.1103/PhysRevLett.73.1154.

[196] Grévin, B., Berthier, Y., & Collin, G., In-Plane Charge Modulation below T_c and Charge-Density-Wave Correlations in the Chain Layer in $YBa_2Cu_3O_7$. *Phys. Rev. Lett.* **85**, 1310 (2000), DOI: 10.1103/PhysRevLett.85.1310.

[197] Derro, D.J., Hudson, E.W., Lang, K.M., Pan, S.H., Davis, J.C., Markert, J.T., & de Lozanne, A.L., Nanoscale One-Dimensional Scattering Resonances in the CuO Chains of $YBa_2Cu_3O_{6+x}$. *Phys. Rev. Lett.* **88**, 097002 (2002), DOI: 10.1103/PhysRevLett.88.097002.

[198] Fujita, M., Goka, H., Yamada, K., & Matsuda, M., Competition between Charge- and Spin-Density-Wave Order and Superconductivity in $La_{1.875}Ba_{0.125-x}Sr_xCuO_4$. *Phys. Rev. Lett.* **88**, 167008 (2002), DOI: 10.1103/PhysRevLett.88.167008.

[199] Liang, R., Bonn, D.A., & Hardy, W.N., Evaluation of CuO_2 plane hole doping in $YBa_2Cu_3O_{6+x}$ single crystals. *Phys. Rev. B* **73**, 180505 (2006), DOI: 10.1103/PhysRevB.73.180505.

[200] Yamada, K., Lee, C.H., Kurahashi, K., Wada, J., Wakimoto, S., Ueki, S., Kimura, H., Endoh, Y., Shirane, G., Birgeneau, R.J., Greven, M., Kastner, M.A., & Kim, Y.J., Doping dependence of the spatially modulated dynamical spin correlations and the superconducting-transition temperature in $La_{2-x}Sr_xCuO_4$. *Phys. Rev. B* **57**, 6165–6172 (1998), DOI: 10.1103/PhysRevB.57.6165.

[201] Hirota, K., Neutron scattering studies of Zn-doped $La_{2-x}Sr_xCuO_4$. *Physica C Superconductivity* **357**, 61–68 (2001), DOI: 10.1016/S0921-4534(01)00195-2.

[202] Fujita, M., Enoki, M., & Yamada, K., Spin- and charge-density-wave orders in $La_{1.87}Sr_{0.13}Cu_{0.99}Fe_{0.01}O_4$. *J. Phys. Chem. Sol.* **69**, 3167–3170 (2008), DOI: 10.1016/j.jpcs.2008.06.049.

[203] Suchaneck, A., Hinkov, V., Haug, D., Schulz, L., Bernhard, C., Ivanov, A., Hradil, K., Lin, C.T., Bourges, P., Keimer, B., & Sidis, Y., Incommensurate Magnetic Order and Dynamics Induced by Spinless Impurities in $YBa_2Cu_3O_{6.6}$. *Phys. Rev. Lett.* **105**, 037207 (2010), DOI: 10.1103/PhysRevLett.105.037207.

[204] Blackburn, E., Chang, J., Hücker, M., Holmes, A.T., Christensen, N.B., Liang, R., Bonn, D.A., Hardy, W.N., Rütt, U., Gutowski, O., Zimmermann, M.v., Forgan,

E.M., & Hayden, S.M., X-Ray Diffraction Observations of a Charge-Density-Wave Order in Superconducting Ortho-II $YBa_2Cu_3O_{6.54}$ Single Crystals in Zero Magnetic Field. *Phys. Rev. Lett.* **110**, 137004 (2013), DOI: 10.1103/PhysRevLett.110.137004.

[205] Lawler, M.J., Fujita, K., Lee, J., Schmidt, A.R., Kohsaka, Y., Kim, C.K., Eisaki, H., Uchida, S., Davis, J.C., Sethna, J.P., & Kim, E.A., Intra-unit-cell electronic nematicity of the high-T_c copper-oxide pseudogap states. *Nature* **466**, 347–351 (2010), DOI: 10.1038/nature09169.

[206] Li, J.X., Wu, C.Q., & Lee, D.H., Checkerboard charge density wave and pseudogap of high-T_c cuprate. *Phys. Rev. B* **74**, 184515 (2006), DOI: 10.1103/PhysRevB.74.184515.

[207] Seo, K., Chen, H.D., & Hu, J., *d*-wave checkerboard order in cuprates. *Phys. Rev. B* **76**, 020511 (2007), DOI: 10.1103/PhysRevB.76.020511.

[208] Allais, A., Bauer, J., & Sachdev, S., Bond order instabilities in a correlated two-dimensional metal. arXiv:1402.4807 [cond-mat.str-el].

[209] Chowdhury, D. & Sachdev, S., Density wave instabilities of fractionalized Fermi liquids. arXiv:1409.5430 [cond-mat.str-el].

[210] Fujita, K., Kim, C.K., Lee, I., Lee, J., Hamidian, M.H., Firmo, I.A., Mukhopadhyay, S., Eisaki, H., Uchida, S., Lawler, M.J., Kim, E.A., & Davis, J.C., Simultaneous Transitions in Cuprate Momentum-Space Topology and Electronic Symmetry Breaking. *Science* **344**, 612–616 (2014), DOI: 10.1126/science.1248783.

[211] Hücker, M., Christensen, N.B., Holmes, A.T., Blackburn, E., Forgan, E.M., Liang, R., Bonn, D.A., Hardy, W.N., Gutowski, O., Zimmermann, M.v., Hayden, S.M., & Chang, J., Competing charge, spin, and superconducting orders in underdoped $YBa_2Cu_3O_y$. *Phys. Rev. B* **90**, 054514 (2014), DOI: 10.1103/PhysRevB.90.054514.

[212] Blanco-Canosa, S., Frano, A., Schierle, E., Porras, J., Loew, T., Minola, M., Bluschke, M., Weschke, E., Keimer, B., & Le Tacon, M., Resonant x-ray scattering study of charge-density wave correlations in $YBa_2Cu_3O_{6+x}$. *Phys. Rev. B* **90**, 054513 (2014), DOI: 10.1103/PhysRevB.90.054513.

[213] Wise, W.D., Boyer, M.C., Chatterjee, K., Kondo, T., Takeuchi, T., Ikuta, H., Wang, Y., & Hudson, E.W., Charge-density-wave origin of cuprate checkerboard visualized by scanning tunnelling microscopy. *Nature Phys.* **4**, 696 (2008), DOI: 10.1038/nphys1021.

[214] Blanco-Canosa, S., Frano, A., Loew, T., Lu, Y., Porras, J., Ghiringhelli, G., Minola, M., Mazzoli, C., Braicovich, L., Schierle, E., Weschke, E., Le Tacon, M., & Keimer, B., Momentum-Dependent Charge Correlations in $YBa_2Cu_3O_{6+\delta}$ Superconductors Probed by Resonant X-Ray Scattering: Evidence for Three Competing Phases. *Phys. Rev. Lett.* **110**, 187001 (2013), DOI: 10.1103/PhysRevLett.110.187001.

[215] Wu, H.H., Buchholz, M., Trabant, C., Chang, C.F., Komarek, A.C., Heigl, F., Zimmermann, M.v., Cwik, M., Nakamura, F., Braden, M., & Schüßler-Langeheine, C., Charge stripe order near the surface of 12-percent doped $La_{2-x}Sr_xCuO_4$. *Nature Commun.* **3**, 1023 (2012), DOI: 10.1038/ncomms2019.

[216] Benjamin, D., Abanin, D., Abbamonte, P., & Demler, E., Microscopic Theory of Resonant Soft-X-Ray Scattering in Materials with Charge Order: The Example of Charge Stripes in High-Temperature Cuprate Superconductors. *Phys. Rev. Lett.* **110**, 137002 (2013), DOI: 10.1103/PhysRevLett.110.137002.

[217] Chowdhury, D. & Sachdev, S., Feedback of superconducting fluctuations on charge order in the underdoped cuprates. arXiv:1404.6532 [cond-mat.str-el].

[218] Meier, H., Pépin, C., Einenkel, M., & Efetov, K.B., Cascade of phase transitions in the vicinity of a quantum critical point. *Phys. Rev. B* **89**, 195115 (2014), DOI: 10.1103/PhysRevB.89.195115.

[219] Pépin, C., de Carvalho, V.S., Kloss, T., & Montiel, X., Coexistence of pseudo-gap and charge order at the hot spots in cuprate superconductors. arXiv:1408.5908 [cond-mat.supr-con].

[220] Wang, Y. & Chubukov, A., Charge-density-wave order with momentum $(2Q, 0)$ and $(0, 2Q)$ within the spin-fermion model: Continuous and discrete symmetry breaking, preemptive composite order, and relation to pseudogap in hole-doped cuprates. *Phys. Rev. B* **90**, 035149 (2014), DOI: 10.1103/PhysRevB.90.035149.

[221] Grafe, H.J., Curro, N., Young, B., Vyalikh, A., Vavilova, J., Gu, G., Hcker, M., & Bchner, B., Charge order and low frequency spin dynamics in lanthanum cuprates revealed by Nuclear Magnetic Resonance. *The European Physical Journal Special Topics* **188**, 89–101 (2010), DOI: 10.1140/epjst/e2010-01299-6.

[222] LeBoeuf, D., Krämer, S., Hardy, W.N., Liang, R., Bonn, D.A., & Proust, C., Thermodynamic phase diagram of static charge order in underdoped $YBa_2Cu_3O_y$. *Nature Phys.* **9**, 79–83 (2013), DOI: 10.1038/nphys2502.

[223] Zeljkovic, I., Xu, Z., Wen, J., Gu, G., Markiewicz, R.S., & Hoffman, J.E., Imaging the Impact of Single Oxygen Atoms on Superconducting $Bi_{2+y}Sr_{2-y}CaCu_2O_{8+x}$. *Science* **337**, 320–323 (2012), DOI: 10.1126/science.1218648.

[224] Bobowski, J.S., Baglo, J.C., Day, J., Semple, L., Dosanjh, P., Turner, P.J., Harris, R., Liang, R., Bonn, D.A., & Hardy, W.N., Oxygen chain disorder as the weak scattering source in $YBa_2Cu_3O_{6.50}$. *Phys. Rev. B* **82**, 134526 (2010), DOI: 10.1103/PhysRevB.82.134526.

[225] Haug, D., Hinkov, V., Sidis, Y., Bourges, P., Christensen, N.B., Ivanov, A., Keller, T., Lin, C.T., & Keimer, B., Neutron scattering study of the magnetic phase diagram of underdoped $YBa_2Cu_3O_{6+x}$. *New Journal of Physics* **12**, 105006 (2010), DOI: 10.1088/1367-2630/12/10/105006.

[226] Andersen, N. H. and Lebech, B. and Poulsen, H. F., "The structural phase diagram and oxygen equilibrium partial pressure of $YBa_2Cu_3O_{6+x}$ studied by neutron powder diffraction and gas volumetry". *Physica C: Superconductivity* **172**, 31–42 (1990), DOI: 10.1016/0921-4534(90)90639-V.